TECHNISCHE
UNIVERSITÄT
WIEN
Vienna University of Technology

DISSERTATION

Characterization of radiation damage in detectors made from different silicon materials

Ausgeführt zum Zwecke der Erlangung des akademischen Grades einer Doktorin der technischen Wissenschaften

unter der Leitung von

Univ.Doz. Dipl.-Ing. Dr.techn Manfred Krammer
E 188
Atominstitut

eingereicht an der Technischen Universität Wien

Fakultät für Physik

Von

Katharina Kaska
Matrikelnr.: 0025729
Robert Blumstr. 19
3100 St. Pölten

Wien, am eigenhändige Unterschrift

Abstract

With the increase of luminosity in particle colliders like the Large Hadron Collider at CERN, new detector materials that can withstand the increase in radiation around the collision point are needed. In this study pad detectors made from three different types of silicon materials, standard Float Zone (FZ) silicon, Magnetic Czochralski (MCz) and epitaxial silicon (EPI), irradiated with 24 GeV/c protons, reactor neutrons and 200 MeV pions are investigated. A vast amount of data from samples irradiated together and measured with the same equipment at the same conditions could thus be collected and provides, for the first time, a proper base for a direct comparison of the development of macroscopic properties with fluence. The investigation is focused on the effective space charge $|N_{eff}|$, the maximum collected charge, the effective trapping times and the space charge sign.

For both FZ and MCz no difference in $|N_{eff}|$ is seen between proton and pion irradiated samples, whereas irradiation with neutrons was more damaging. MCz proves to be superior to FZ and EPI after irradiation with charged hadrons, but the lower resistivity in EPI leads to a clear advantage over both FZ and MCz after irradiation with reactor neutrons. For n-type EPI a thorough literature study and comparative measurements on 150 μm devices also shows that the decrease of $|N_{eff}|$ with layer thickness mentioned in previous studies was most likely rather due to slight differences in measurement setups for samples of various thickness than a result of the layer thickness itself. For p-type EPI no dependence of $|N_{eff}|$ on layer thickness is visible from measurements of 50, 75 and 150 μm samples.

Contrary to $|N_{eff}|$ the maximum collected charge after full depletion of the detector is not material dependent. Since, however, the voltage that can be applied to a detector in practical use is limited, not the maximum, but the charge collected at a certain voltage - in this case 300V - is investigated. At low irradiation fluences 150 μm EPI samples are clearly inferior to both FZ and MCz due to their lower thickness that reduces the number of charge carriers produced as a particle moves through the detector volume. At fluences above around 1 x $10^{15}\,cm^{-2}$ this shorter particle path as well as the higher carrier velocity at the same bias voltage on the other hand also reduces the possibility of charge carriers being trapped and therefore lost for the read-out signal, making the collected charge in EPI similar to that in MCz. After neutron irradiation, where EPI additionally shows a favorable development of the effective space charge with fluence, the thinner sample is superior to all other materials.

The effective electron and hole trapping times, measured by Transient Current Technique in this study, depend on the type of particle used for irradiation but not on the material. Compared to previous studies a far large number of data points from FZ, MCz and EPI samples could therefore be combined to determine the proportionality constant $\beta_{e,h}$ for 24 GeV/c protons, reactor neutrons and 200 MeV pions. Whereas no difference is seen between proton and pion irradiated samples, the increase of trapping with fluence is slower in neutron irradiated samples. For all particle types β_h is about 20-30 % higher than β_e.

TCT was also used to determine the space charge sign in irradiated silicon samples. As expected from previous studies samples from all silicon types showed negative space charge after high fluence irradiation with reactor neutrons. After proton irradiation negative space charge is introduced in FZ and positive space charge in EPI. For MCz previous results were contradictory. In this study it is shown that these contradictions are due to limited voltage ranges and different trapping times used for correcting the TCT curve. However, even measurements over a wider voltage range and a correction of the curves with values for τ_{eff} obtained here yield inconclusive result that point towards local field and space charge variations. This then prohibits the application of the space charge correction method used so far and makes further measurements with other methods like edge-TCT necessary to determine the real field distribution in MCz.

In the last chapter a methodological problem when determining the effective space charge is addressed. $|N_{eff}|$ is in most cases extracted from the kink in the capacitance-voltage curve that indicates full depletion is reached in the sample. In the same way the change in current and collected charge at depletion in the IV and QV curves can be evaluated to determine $|N_{eff}|$. In unirradiated samples and those irradiated to low fluences all three methods yield the same results. With increased particle fluence, however, not only the absolute values, but also the increase of $|N_{eff}|$ with fluence differs depending on the method used. While only few general trends can be observed and the underlying mechanism still needs to be determined, these findings at least urge some caution regarding the reliability of CV measurements at high fluences.

Kurzfassung

Die erhöhte Luminosität in Teilchenbeschleunigern wie dem CERN Large Hadron Collider macht die Entwicklung neuer Detektormaterialien nötig, die die erhöhte Strahlung rund um den Kollisionspunkt bewältigen können. In dieser Untersuchung werden einfache Siliziumdetektoren (Dioden) aus drei verschiedenen Arten von Silizium, Float Zone (FZ), Magnetic Czochralski (MCz) und epitaxial (EPI) Silizium, nach Bestrahlung mit 24 GeV/c Protonen, Reaktorneutronen und 200 MeV Pionen untersucht. Die große Menge an gewonnenen Daten von Detektoren, die zusammen bestrahlt wurden und mit denselben Messaufbauten untersucht wurden, kann zum ersten Mal eine breite, genau definierte Basis für einen direkten Vergleich der Entwicklung makroskopischer Parameter mit der Fluenz liefern. Die Untersuchung konzentriert sich auf die effektive Raumladung $|N_{eff}|$, die gesammelte Ladung und das Vorzeichen der Raumladung.

Für FZ und MCz konnte kein Unterschied in $|N_{eff}|$ zwischen Detektoren, die mit Protonen und Pionen bestrahlt wurden, festgestellt werden, während Neutronen zu stärkerer Schädigung führten. MCz stellte sich als überlegen gegenüber FZ und EPI nach Bestrahlung mit geladenen Hadronen heraus, während der niedrigere spezifische elektrische Widerstand in EPI klare Vorteile gegenüber FZ und MCz nach Bestrahlung mit Reaktorneutronen brachte. Für EPI-n zeigten eine gründliche Literaturstudie und Vergleichsmessungen überdies, dass die in anderen Publikationen postulierte Reduktion von $|N_{eff}|$ mit der Schichtdicke eher durch leichte Unterschiede im Messablauf für Detektoren verschiedener Dicke bedingt ist, als durch die Schichtdicke selbst. Für EPI-p zeigten meine Messungen an 50, 75 und 150 μm Detektoren keine Abhängigkeit von $|N_{eff}|$ von der Schichtdicke

Im Unterschied zu $|N_{eff}|$ hängt die maximale gesammelte Ladung über der Verarmungsspannung nicht vom Material ab. Da jedoch die Spannung, die in der praktischen Verwendung an einen Detektor angelegt werden kann, begrenzt ist, wird nicht das Maximum, sondern die Ladung bei einer bestimmten Spannung - in diesem Fall 300V - untersucht. Bei niedrigen Fluenzen sind 150 μm EPI Detektoren aufgrund ihrer geringeren Schichtdicke, die die Anzahl an Ladungsträgern limitiert, die ein Teilchen, das das Detektorvolumen durchquert, produzieren kann, deutlich schlechter als FZ und MCz. Bei Fluenzen über etwa 1 x 10^{15} cm^{-2} reduziert dieser kürzere Weg der einfallenden Teilchen jedoch auch die Wahrscheinlichkeit, dass Ladungsträger in Traps gefangen werden und für das Signal verloren gehen. Ein zusätzlicher Vorteil dünnerer Detektoren ist überdies das höhere Feld bei gleicher angelegter Spannung, das zu höheren Ladungsträgergeschwindigkeiten führt, die wiederum die Wahrscheinlichkeit für Trapping reduzieren. Obwohl $|N_{eff}|$ in EPI Detektoren, die mit hohen Protonenfluenzen bestrahlt wurden deutlich höher ist als in MCz und eine angelegte Spannung von 300V weit unter der Verarmungsspannung ist, ist daher die gesammelte Ladung in beiden Materialen sehr ähnlich. Nach Neutronenbestrahlung, bei der EPI zusätzlich eine günstigere Entwicklung von $|N_{eff}|$ aufweist, ist der dünnere Detektor allen anderen Materialien überlegen.

Die effektiven Trappingzeiten für Elektronen und Löcher, hier mit der Transient Current Technique gemessen, hängen von der Bestrahlungsart, aber nicht vom Detektormaterial ab. Im Vergleich zu früheren Studien konnte in dieser Arbeit eine große Anzahl an Daten von FZ, MCz und EPI Detektoren vereint werden, um die Proportionalitätskonstante $\beta_{e,h}$ für 24 GeV/c Protonen, Reaktorneutronen und 200 MeV Pionen zu bestimmen. Während zwischen mit Protonen und mit Pionen bestrahlten Detektoren kein Unterschied festgestellt werden konnte, zeigt sich in mit Neutronen bestrahlten Detektoren ein langsamerer Anstieg des Trappings mit der Fluenz. Für alle Bestrahlungsarten ist β_h etwa 20-30 % höher als β_e.

TCT Messungen wurden auch angewandt, um das Vorzeichen der Raumladung in bestrahlten Siliziumdetektoren zu bestimmen. Wie nach früheren Untersuchungen erwartet zeigten alle Materialien negative Raumladung nach der Bestrahlung mit Reaktorneutronen. Nach Protonenbestrahlung wird in FZ negative und in EPI positive Raumladung induziert. Für MCz waren die bisherigen Messungen widersprüchlich. Meine Arbeit zeigt nun deutlich, dass diese Widersprüche durch die Verwendung unterschiedlicher Trappingzeiten für die Korrektur der TCT Kurve und durch eingeschränkte Spannungsbereiche bedingt sind. Jedoch zeigen auch Messungen über größere Spannungsbereiche und eine Korrektur der Kurven mit Werten für τ_{eff}, wie sie in dieser Untersuchung bestimmt wurden, widersprüchliche Ergebnisse, die auf lokale Feld- und Raumladungsunterschiede hinweisen. Diese machen die Anwendung der bisher verwendeten sogenannten Space-Charge-Correction Methode zur Bestimmung der Raumladung unmöglich und weitere Messungen mit anderen Methoden, wie etwa edge-TCT, nötig, um die Feldverteilung in MCz zu bestimmen.

Im letzten Kapitel wird ein methodisches Problem im Zusammenhang mit der Bestimmung der effektiven Raumladung angesprochen. In den meisten Fällen wird $|N_{eff}|$ durch die Gradientenänderung in der CV-Kurve bestimmt. In gleicher Weise ist es auch möglich $|N_{eff}|$ durch die Änderung der IV und QV Kurven zu bestimmen. In unbestrahlten Detektoren und solchen, die mit niedrigen Fluenzen bestrahlt wurden, führen alle drei Methoden zum selben Ergebnis. Bei höheren Fluenzen ändert sich jedoch nicht nur der Absolutwert, sondern auch der Anstieg von $|N_{eff}|$ mit der Fluenz je nach Methode. Während nur wenige allgemeine Entwicklungen beobachtet werde können und die dahinterliegenden Mechanismen erst untersucht werden müssen, gebieten diese Ergebnisse zumindest etwas Vorsicht in Hinblick auf die Verlässlichkeit von CV Messungen bei hohen Fluenzen.

Acknowledgements

First and foremost I like to thank my supervisor Manfred Krammer for his immense patience and continuous support during this rather prolonged PhD project. My research at CERN was guided by Michael Moll, who never tired to discuss scientific and technical problems, no matter how small, and encouraged me to finish this thesis even after I had left Geneva and physics.

This research would never have been possible without the support of the technical staff at CERN. Maurice Glaser not only irradiated countless samples for me, but also willingly shared his expertise and practical knowledge. My thanks also to to Ian McGill and other members of the bonding lab at CERN for bonding so many samples so quickly.

My colleagues Julien Mekki and Nicola Pacifico provided many fruitful suggestions for my research and made working at CERN a great experience. Life in Geneva was greatly improved by meeting many nice and interesting people like Gry Tveten, Angela Brett, Nir Amram, Arely Cortéz and Sandrina Fernandes to name just a few. I also like to thank Herta Richter for being a great friend throughout our studies together in Vienna and our time as PhD students at CERN.

Contents

Chapter 1

Overview

In 2009 the Large Hadron Collider at CERN started its operation with an energy of 1.18 TeV per beam, thus making it the highes energy particle collider in the world superseding Tevatrons 0.98 TeV record. Over the following years the beam energy was increased up to 4 TeV per beam. After the planned shutdown during 2013 the collision energies will be increased to 7 TeV per beam for the restart in 2015 with an anticipated luminosity for proton-proton collisions of $L \approx 10^{34}\ cm^{-2}\ s^{-1}$. Bunches with 1.1 x 10^{11} protons will collide in the experiments with a bunch crossing time of 25 ns. [Eva08]

One of the main areas of research is testing and expanding the standard model for particle physics which is known to be incomplete as it can for instance not fully explain particle masses. Results of proton-proton collisions that imitate conditions shortly after the big bang could shed light on the issue. Two important steps towards testing the reliability of the standard model have so far been taken: in July 2012 the finding of a new boson in the 126 GeV range was reported that could be the long sought after Higgs boson, which however still has to be confirmed by further analysis. In November 2012 data analysis indicated that the possibility of there being supersymmetrical particles as an addition to the standard model is decreasing. Collision products are detected at four main experiments: ATLAS, CMS, LHC-B and ALICE. For registering collision events the experiments employ several different kinds of detectors assembled around the crossing point. For both ATLAS and CMS the innermost layer is made up of silicon detectors which are followed by electromagnetic and hadronic calorimeter and muon detector at the outer edges in beam direction [ATL08] [CMS08].

The innermost silicon trackers that are closest to the beam interaction point suffer most from radiation damage due to the high rate of particles. This will be an even greater issue for proper detector operation when the LHC luminosity will be increased in an upgrade planned for 2022. At the higher luminosity of $L \approx 10^{35}\ cm^{-2}\ s^{-1}$ the innermost silicon pixel layer situated only 4 cm away from the beam pipe will be hit by an expected particle fluence of 2 x $10^{16} cm^{-2}$ and the innermost silicon strip detectors will receive 1 x $10^{15} cm^{-2}$ in five years of operation, which is an order of magnitude higher than what is expected for

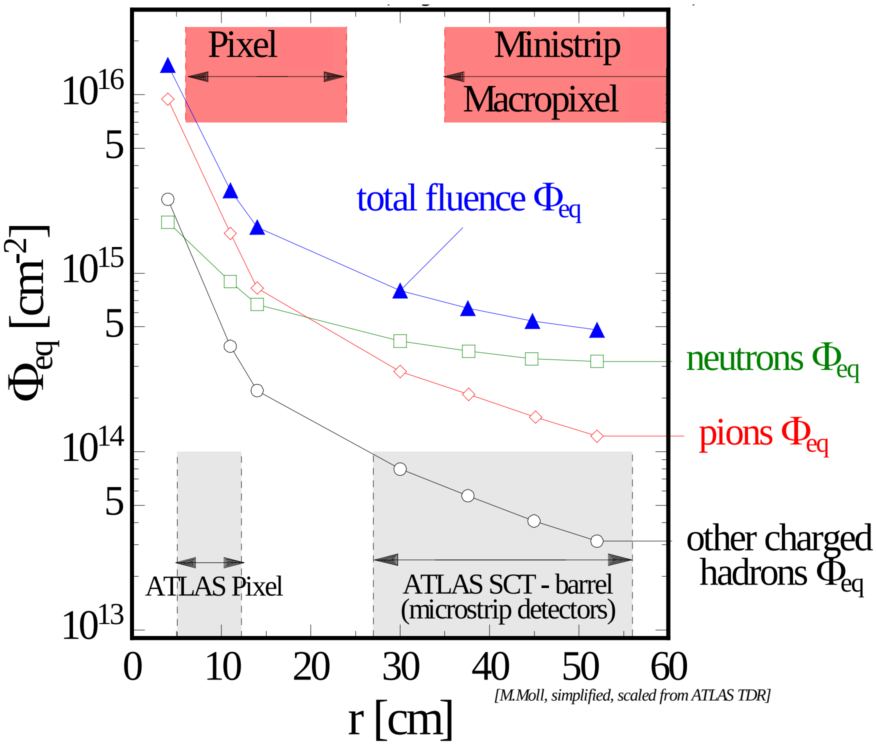

Figure 1.1: Simulation of the proton, neutron and pion as well as the combined fluence received in detector parts as a function of the distance from the interaction point (M. Moll, simplified, scaled from ATLAS TDR [Mol07]). The fluence is given in neuron equivalents (compare chapter 4.2).

the LHC [RD511]. Simulations for proton, neutron and pion fluences in dependence of the distance from the beam pipe for this luminosity are shown in Fig. 1.1. Close to the beam the fluence is mainly contributed by pions whereas protons and neutrons play a smaller role. In the strip detector region proton and pion fluences are reduced while neutron fluences stay more or less constant between a distance of 10 to 60 *cm* away from the beam pipe. For the luminosity upgrade therefore detectors are needed that can withstand this increased mixed particle fluence for the envisioned run time of the accelerator.

To address the problem of radiation damage in silicon devices the CERN RD50 collaboration for the development for radiation hard semiconductor detectors for very high luminosity colliders in 2002 proposed an R&D campaign targeted toward the requirements of the LHC luminosity upgrade [RD502]. Research is divided into five different projects [RD510]:

- Defect/Material Characterization
- Defect Engineering
- Pad Detector Characterization

- New Structures
- Full Detector Systems

Two main approaches towards radiation hard detectors can be distinguished: on the one hand the detector design is being looked into, where new devices like 3D detectors are developed and full detector systems simulating the application in real experiments are tested, on the other hand various detector materials and their macroscopic and microscopic properties are investigated.

Defect or material characterization is concerned with the investigation of microscopic defects in silicon by methods like Deep Level Transient Spectroscopy (DLTS) or Thermally Stimulated Current (TSC). Investigating defects that are the causes for macroscopic changes in detectors can help to improve research in defect engineering, where defects are introduced into the silicon lattice in order to improve detector performance. Pad detectors produced out of these silicon materials are then irradiated and their properties, like effective space charge, reverse current and charge collection efficiency, are tested and compared to standard Floating Zone (FZ) silicon material.

This thesis is mainly concerned with the material properties of different silicon types that are tested in the form of simple pad detectors. It has been shown by the CERN RD48 (ROSE) collaboration that the introduction of oxygen into the silicon bulk greatly improves the radiation hardness of the material when it comes to the development of the effective space charge [RD408] [Mol99] [Lin01a] [Lin01b]. In standard FZ silicon the oxygen concentrations that can be reached are limited by the production process. This limitation can be overcome by using a different production method (Magnetic Czochralski, MCz, silicon) that however for a long time had the disadvantage of leaving too many other impurities in the silicon and therefore reducing the resistivity to a level that made it not suitable for detector operation [Fre05]. After overcoming these difficulties MCz silicon went on to be one of the most studied materials in the field of defect engineering in recent years. In this study MCz samples will be compared to standard FZ devices to show the influence of high oxygen concentrations on macroscopic detector parameters important for read-out, like effective space charge and collected charge, as well as on the electric field in the device.

In this work, only in the case of epitaxial silicon (EPI) also device engineering is employed to alter detector properties. The active epitaxial layer is thinner than the 300 μm standard used for FZ and MCz. This has the advantage that the leakage current is reduced due to the smaller active volume, as is the depletion voltage that scales with the detector thickness. For the same reason trapping is reduced as the charge needs to travel a shorter distance. The disadvantage however is the smaller number of charge deposited by an incoming particle, which reduces the signal height in unirradiated detectors. Epitaxial silicon with a thickness of the active layer of 150 μm will be compared to other silicon types for all measurement methods as well to thinner samples for the development of the effective space charge.

The development of some detector parameters, especially the effective space charge, with fluence depends on the type of particle causing the damage. Since a mixed field is expected in real life detector operation, samples from all materials were irradiated with 24 GeV/c protons and reactor neutrons. Due to limitations in access to adequate particle sources, pion irradiation could only be performed on a subset of the total material range.

After a short introduction into the physics of silicon detectors (chapter 2), silicon growth techniques (chapter 3) and radiation damage in silicon (chapter 4), the experimental procedures and samples are described in chapter 5. Measurement results are grouped according to the most important detector parameters: effective space charge or depletion voltage (chapter 6), collected charge (chapter 7) and electric field and within it trapping time (chapter 8). In each chapter the three silicon materials FZ, MCz and EPI are first discussed separately and are then compared to each other for the three irradiation types, 24 GeV/c protons, reactor neutrons and 200 MeV pions. Chapter 9 discusses differences in the effective space charge obtained by different measurement methods. Finally chapter 10 gives a summary and conclusions.

Chapter 2

Basics of Silicon Detectors

In this chapter a short introductory overview of the basic properties of silicon diodes is given, starting with the description of a p-n junction (chapter 2.1). Then the voltage dependence of the capacitance and reverse current is explained (chapter 2.2) followed by a description of the signal formation (chapter 2.3). More detailed information on these topics can be found in [Sze81], [Spi05] or [Lut99].

2.1 p-n junction

In semiconductors like silicon the band gap between the valence and the conduction band is small enough to allow free electrons from broken bonds between neighboring atoms to enter the conduction band. In the valence band therefore a hole is created that together with the electron in the conduction band conducts electricity when an electric field is applied. Only very few electrons however are thermally excited at room temperature in intrinsic silicon, which limits the number of free charge carriers available for conduction.

To change the conductivity impurities can be introduced into the silicon lattice by a process called doping, changing it from an intrinsic to an extrinsic semiconductor. To produce n-type silicon with electrons as charge carriers, silicon atoms are replaced by elements with five valence electrons like phosphorus or arsenic or other so called shallow donors. Four of these electrons form covalent bonds with neighboring atoms while the fifth that is only loosely bound (45 and 54 meV respectively for the above mentioned elements [Sze85]) acts as conduction electron (compare Fig. 2.1 (a)). When the electron is removed from the donor atom, positively charged ions remain in the silicon lattice, leading to a positive space charge in n-type silicon.

To obtain p-type silicon shallow acceptors with only three valence electrons like boron are used. A hole is created by the missing electron that can be filled by an electron from a neighboring lattice atom, causing the hole to move. The free charge carriers in this case are therefore positively charged and the negative ions are left in the bulk (compare Fig. 2.1 (b)).

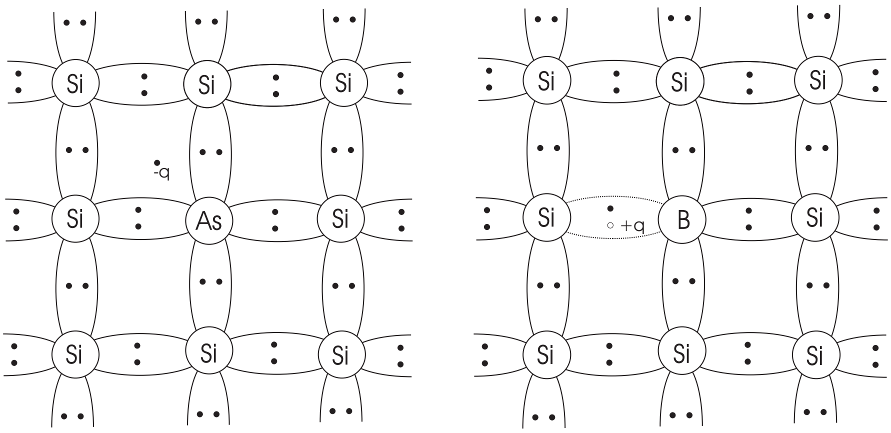

Figure 2.1: (a) Bonds in silicon doped with phosphorus. Phosphorus introduces an additional conduction electron -q thereby leaving a positively charged ion in the bulk, which creates n-type silicon with a positive space charge after removal of the free charge carriers. (b) Bonds in silicon doped with boron. Boron lacks one electron for creating a bond with the neighboring silicon atom, which can be interpreted as the creation of a positively charged hole +q. The negatively charged boron atom in the bulk creates negative space charge in depleted p-type silicon.

A p-n junction can be understood as n-type silicon with a Fermi level E_F close to the conduction band and a large number of free electrons that is brought in contact with p-type silicon (E_F close to the valence band, large number of free holes). When both types are joined this concentration gradient leads to diffusion and recombination of free charge carriers (compare Fig. 2.2). Electrons from the n-side silicon diffuse into the p-side, leaving positive donor ions uncompensated and vice versa. Thereby two space charge regions, positive on the n-side and negative on the p-side are formed. These space charge regions with their potential difference Φ_{bi} introduce a drift current in the direction opposite to the diffusion current, which, in steady state condition, leads to zero net current flow across the junction.

In silicon diodes one side is usually more heavily doped than the other, so for instance a p^+-n junction is formed, where p^+ describes a heavily doped p-type silicon [1]. The electric field in this kind of impurity distribution can be approximated by the one-sided abrupt junction model in a diode with thickness d (compare Fig. 2.3). Since overall charge neutrality has to be preserved, the depletion region with a width W has to extend further into the less heavily doped bulk. Furthermore one assumes a homogeneous space charge

---

[1] Compare Fig. 5.2 in chapter 5.1 for a schematics of the silicon diodes used in this work

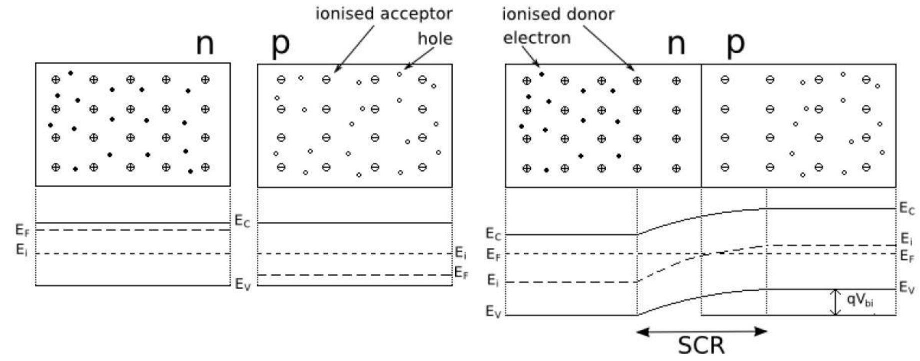

Figure 2.2: Creation of a p-n junction. n- and p-type silicon with their respective energy levels (left) are brought in contact (right). In equilibrium conditions the Fermi energy E_F has to be constant through the junction, the potentials are shifted according to the space charge build up.

density $\rho_{el} = q_0 N_{eff}$ in the depletion region, neglecting influences from diffusion from the n-type bulk close to the edges. The electric field can then be calculated from the Poisson equation

$$-\frac{d^2\Phi(x)}{dx^2} = \frac{q_0\, N_{eff}}{\epsilon\epsilon_0}. \tag{2.1}$$

where $N_{eff} = N_D - N_A$ is the difference between donors and acceptors in the space charge region and therefore the effective space charge, q_0 is the elementary charge and $\epsilon\epsilon_0 = 11.9$ is the dielectric constant in silicon [Lut99].

Integration with the boundary condition $E(W) = -\frac{d}{dx}\Phi(x\!=\!W) = 0$ gives an expression for the electric field $E(x)$ for $0 \leq x \leq W$ and $W \leq d$

$$E(x) = \frac{q_0 N_{eff}}{\epsilon\epsilon_0}(x - W) \tag{2.2}$$

with an absolute maximum at $x = 0$ and a linear decrease to E=0 at x=W.

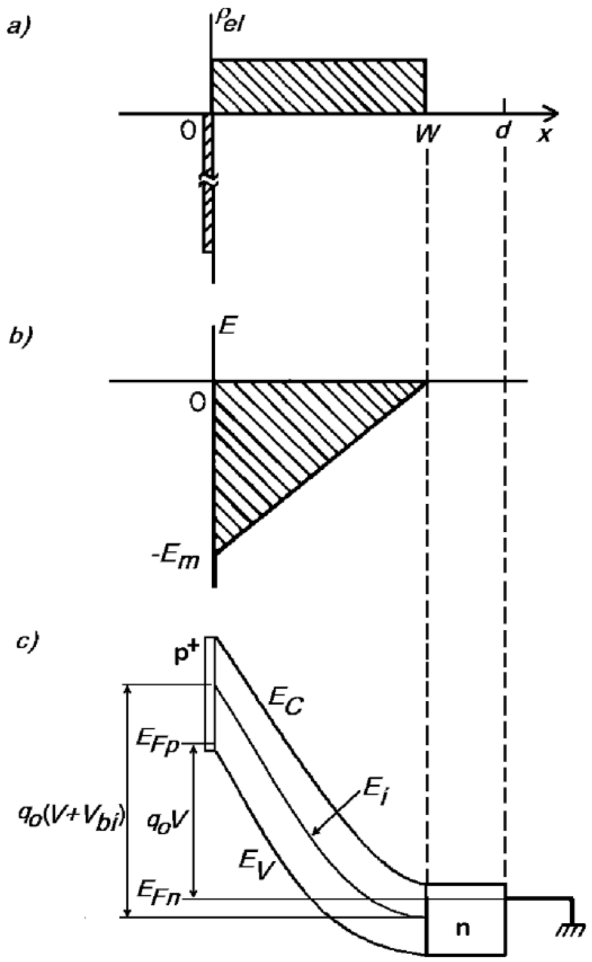

Figure 2.3: Schematics of an abrupt $p^+ - n$ junction in a diode of thickness d and depletion width W. (a) electric charge density ρ_{el} (b) electric field E with an absolute maximum E_m at $x = 0$ (c) electron potential energy $q_0\Phi$. q_0 is the elementary charge, V the bias voltage and V_{bi} the built-in voltage.

After a further integration with the boundary condition $\Phi(x = W) = 0$, again with $0 \leq x \leq W$ and $W \leq d$, the electric potential is obtained:

$$\Phi(x) = -\frac{1}{2}\frac{q_0 N_{eff}}{\epsilon\epsilon_0}(x - W)^2 \tag{2.3}$$

The depletion width $W(V)$ in a diode biased with a voltage V can then be expressed by

$$W(V) = \sqrt{\frac{2\epsilon\epsilon_0}{q_0|N_{eff}|}(V + V_{bi})} \tag{2.4}$$

under the boundary condition of $\Phi(x=0) = -V_{bi} - V$, where V_{bi} is the built-in voltage due to the potential difference Φ_{bi}.

The voltage at which the depletion region extends through the whole diode and therefore W=d is called *depletion voltage* V_{dep} and can be calculated from Eq. 2.4:

$$V_{dep} + V_{bi} = \frac{q_0}{2\epsilon\epsilon_0} |N_{eff}| d^2 \tag{2.5}$$

Since the internal voltage V_{bi} is usually much lower than the applied bias voltage, it can be neglected in most cases. In the following the effective space charge will be calculated from the depletion voltage alone via

$$|N_{eff}| = \frac{V_{dep} 2\epsilon\epsilon_0}{q_0 d^2} \tag{2.6}$$

2.2 Capacitance and reverse current

The capacitance of the depletion layer per unit area is defined as $C = dQ/dV$, where dQ is the incremental increase of charge per unit area if the applied voltage is increased by dV. dQ can be calculated using the equation for the charge in a diode with an area A modeled by an abrupt junction:

$$Q = q_0 N_{eff} A W(V) \tag{2.7}$$

Together with Eq. 2.4 it follows:

$$C(V) = \frac{dQ}{dW}\frac{dW}{dV} = \epsilon\epsilon_0 \frac{A}{W(V)} = A\sqrt{\frac{\epsilon\epsilon_0\, q_0\, |N_{eff}|}{2\,V}} \tag{2.8}$$

for $V \leq V_d$. The capacitance therefore decreases with $C \propto 1/\sqrt{V}$ and reaches the *end capacitance* or *geometrical capacitance*

$$C_{end} = \frac{\epsilon\epsilon_0 A}{d} \tag{2.9}$$

at full depletion, which explains the shape of the CV characteristics presented in chapter 6, where $logV$ vs. $logC$ is ploted to determine the depletion voltage in a diode.

The *leakage current* is the current that flows in a reverse biased diode. In an ideal diode it only consists of the diffusion current from undepleted areas, in reality however impurities introduced by imperfect manufacturing contribute. For the 2.5 x 2.5 and 5 x 5 mm^2 diodes used in this work the leakage current before irradiation was below $1nA$.

After irradiation, the leakage current increases due to damages in the surface oxide and the silicon bulk. In the following only the bulk current that arises from defects with energy levels close to the middle of the band gap will be taken into account. Since only defects in the space charge region contribute to the current, it scales with the depletion width and thus with the square root of the voltage (compare Eq. 2.4):

$$I_{bulk} \propto \sqrt{V} \tag{2.10}$$

The leakage current is temperature dependent and has to be normalized to the reference temperature $T_{ref} = 20°$ according to

$$I(T_{ref}) = I(T) \cdot \left(\frac{T_{ref}}{T}\right)^2 \exp\left(-\frac{E_g}{2\,k_B}\left[\frac{1}{T_{ref}} - \frac{1}{T}\right]\right). \tag{2.11}$$

where k_b denotes the Boltzmann constant and E_g the energy gap between valence and conduction band in silicon, for which a value of 1.21 eV was used in all calculations in this work. This value is higher than $E_g = 1.12\ eV$ [Sze85] as used in most previous publications and is the result of recent corrections suggested by Alexander Chilingarov, described in detail in [Chi11] and [Chi13].

2.3 Signal formation

Semiconductor detectors act like solid state ionization chambers. An incident particle transfers energy to the atomic electrons to form electron-hole pairs in the silicon bulk. The number of e-h pairs can be calculated by dividing the absorbed energy by the ionization energy. For high energy quanta with $E \gg E_g$ the ionization energy is roughly proportional to the band gap via [Spi05]

$$E_i \approx 2.8\,E_g + 0.6\,eV \tag{2.12}$$

For silicon the experimentally found ionization energy is about 3.6 eV compared to the band gap of 1.12 eV, so only about 30% of the incident energy goes into the signal charge whereas the rest is lost due to phonon excitation by which the momentum is conserved.

In the electric field created by applying a bias voltage to the detector, the electrons drift to the positive and the holes to the negative electrode. The induced current created by N charge carriers that is responsible for the signal in a pad detector can be described by Ramo's theorem in a one-dimensional approximation (since $d << \sqrt{A}$):

$$I_{e,h} = \pm \frac{q_0 N_{e,h}(t)}{d} v_{e,h}(t) \tag{2.13}$$

The drift velocity $v_{e,h}(t)$ depends on electric field and can be different for different positions within the detectors. For low electric fields it can be expressed by $v_{drift} = \mu_0 E$, where μ_0 is the charge carrier mobility, whereas in high electric field the drift velocity saturates $(v_{drift} = v_{sat})$.

For detector purposes it is more important to look at the collected charge than the current induced at a given moment, which can be achieved by integrating over the induced current. If the number of charge carriers is constant during their drift through the detector and no charge is lost, the induced charge is equal to the charge deposited by the incident particle:

$$Q = Q_0 = q_0 N_0 \tag{2.14}$$

In irradiated detectors however defects that can act as traps for electrons and holes transversing the silicon bulk can be created. The probability for a charge carrier to get trapped is proportional to the length of its path through the diode. After a drift length *dl* the number of charge carriers lost is therefore

$$dN_{e,h} = -\frac{N_{e,h}}{\lambda_{eff_{e,h}}} dl \tag{2.15}$$

where N is the number of elementary charges crossing the diode and $\lambda_{eff_{e,h}}$ is the effective carrier trapping distance.

If the thermal velocity of the charge carriers is much higher than the drift velocity, *dl* can be related to the effective trapping time $\tau_{eff_{e,h}}$ via $dl = v_{th_{e,h}} dt$

$$dN_{e,h} = -N_{e,h} \frac{v_{th_{e,h}}}{\lambda_{eff_{e,h}}} dt = -N_{e,h} \frac{1}{\tau_{eff_{e,h}}} dt \tag{2.16}$$

The initial number of charge carriers decreases therefore with

$$N_{e,h} = N_{0_{e,h}} \exp(-\frac{t}{\tau_{eff_{e,h}}}) \tag{2.17}$$

If the integration time of the read out signal is longer than the time needed for detrapping of the charge, it is still included in the measured signal. In standard measurement conditions however it is lost for the read-out. This phenomenon is described by the *Charge*

Collection Efficiency that describes the ratio between the charge collected in an irradiated detector Q and the deposited charge Q_0 that is equal to the charge collected in an unirradiated device.

Chapter 3

Silicon Growth Techniques

In this chapter the production steps from basic polysilicon material (chapter 3.1) to the different materials used in this work, float zone (FZ) (chapter 3.2) , magnetic Czochralski (MCz) (chapter 3.3) and epitaxial (EPI) (chapter 3.4) silicon, is discussed. A more detailed description can be found in [Sze85].

3.1 Polysilicon

To gain the very pure silicon needed for detectors from quartzite (SiO_2) or very pure sand two steps are necessary to remove the impurities (mainly Al_2O_3 and Fe_2O_3). It is first put in a furnace with a carbon source (coke, coal or wood chips), which leads to a main reaction of

$$SiC(solid) + SiO_2(solid) \rightarrow Si(solid) + SiO(gas) + CO(gas).$$

This Metalurgical Grade Silicion (MGS) with a purity of already 98% is then ground into powder and exposed to hydrogen chloride gas at 300 degrees:

$$Si(solid) + 3HCl(gas) \rightarrow SiHCl_3(gas) + H_2(gas).$$

From impurities in the silicon other chlorides with higher boiling points than $SiHCl_3$ that boils at 32°C can be formed. The mixture is therefore distilled repeatedly to reduce the concentration of impurities. For gaining Semiconductor Grade Silicon (SGS) the trichlorsilane gas is passed over a resistance-heated silicon rod that acts as the nucleation point for the deposition together with hydrogen gas:

$$SiHCl_3(gas) + H_2(gas) \rightarrow Si(solid) + 3HCl(gas).$$

The impurity concentration is thereby reduced to the parts-per-billion range [Sze85].

3.2 Float Zone

Most detectors used in HEP experiments are made from very pure FZ material which is not usually used in industry. The method for producing this type of of silicon was patented in 1962 [The62]. A highly pure polysilicon rod with a silicon seed at the bottom is placed in vacuum or inert gas like argon and rotated in an RF coil that melts it. From the seed a neck is grown to achieve a dislocation free crystal. The neck is then widened to the desired thickness (see Fig. 3.1). When the RF coil is moved upwards along the silicon rod a floating zone (hence the name) of molten polysilicon is created that solidifies into a single crystal.

Doping is achieved by changing the gas atmosphere: phosphine (PH_3) is added for n-type material, diborane (B_2H_6) for p-type. For doping the segregation coefficient k plays a role, i.e. the ratio of the concentration of impurities in the solid to the liquid. Phosphorus has a low k value and can therefore be segregated, but it also evaporates from the liquid, making it more difficult to have uniform distribution in the ingot.

Boron on the other hand tends to stay in the solid, so for achieving high resistivity the starting polysilicon rod has to have a low boron content. Impurities can be removed from the crystal by repeated melting and growing cycles, making it possible to produce high resistivity detectors [Amm84].

3.3 Czochralski Silicon

Czochralski silicon is the material mainly used in industry where very high purity is not important due to its cheaper production technique and better resistivity to thermal stress.

3.3.1 Standard Cz

The process was invented by Teal and Little [Tea50] based on research by J. Czochralski [Czo18] on crystallization velocities of metals. A schematic drawing of the pulling process applied in the production of Cz silicon can be seen in Fig. 3.2. The SGS silicon melt is contained in a silica crucible surrounded by a graphite susceptor and a RF coil, which can be rotated. A crystal pulling mechanism with a silicon seed is placed above the crucible

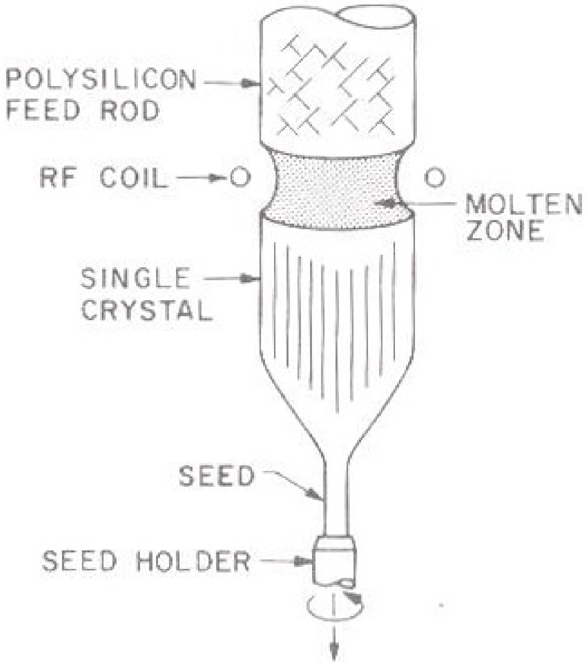

Figure 3.1: Schematic setup of a FZ process [Sze85]

and connected to another rotation mechanism. The atmosphere is controlled by a gas source, a flow control and an exhaust system.

The seed is dipped into molten polycrystalline silicon and gradually pulled upwards under constant rotation. By adjusting temperature and pulling speed the ingot is widened and a large single crystal is produced. During the production the silica crucible slowly dissolves into the molten silicon, releasing oxygen. Most of it leaves the melt as SiO gas, but the remainder is still enough to make Cz silicon far more oxygen rich than standard FZ. The production process also introduces carbon into the melt due to interaction of silicon oxide with carbon from the graphite susceptor. The overall homogeneity of Cz silicon strongly depends on the temperature, pulling and rotational speed and the atmosphere. Due to the impurities introduced during the production it is difficult to reach the resistivity needed in silicon detectors with this method.

3.3.2 Magnetic Cz

The basic production process is the same as for standard Cz silicon, but in addition a strong magnetic field is applied, either in vertical or horizontal direction. This helps to avoid mixing between the melt in the middle and on the edges of the furnace. It leads

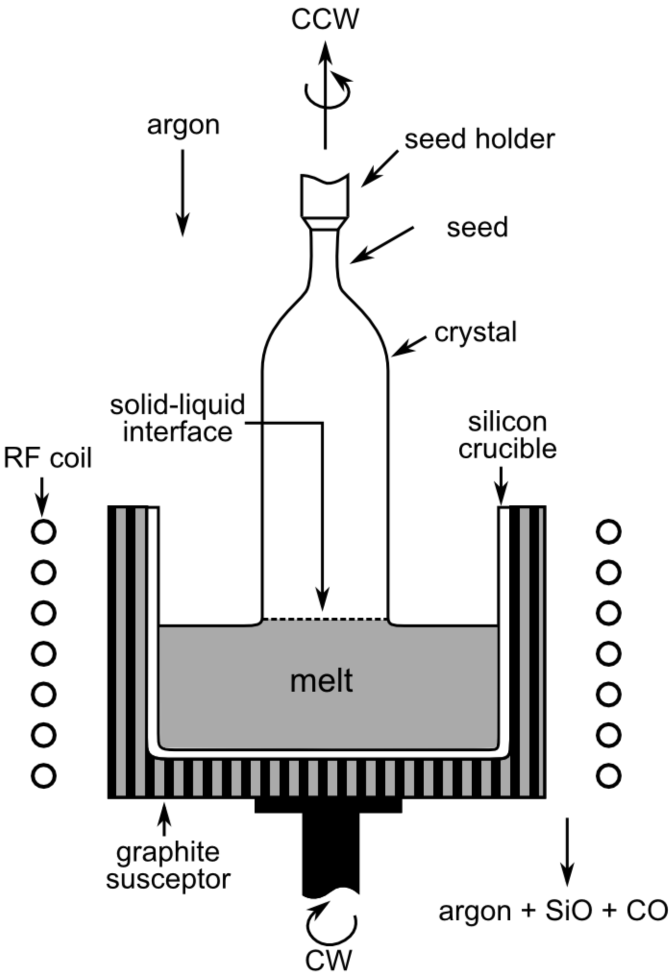

Figure 3.2: Schematic setup of a Cz process after [Sze85]

to a liquid silicon crucible around the center that traps much of the oxygen, reducing the oxygen content in the actual crystal and making the distribution of defects more homogeneous. Nevertheless the impurity concentration is still higher than in other silicon types, with (7-8) x $10^{17} cm^{-3}$ for oxygen and about $10^{16} cm^{-3}$ for carbon [Mol99]. The high oxygen concentration however has been shown to actually be advantageous when it comes to radiation hardness in silicon [Fre05].

3.4 Epitaxial silicon

For silicon production the most important epitaxial process is vapor phase epitaxy (VPE) where the seed crystal is a low resistivity substrate wafer upon which the active layer, whose crystal orientation follows that of the substrate, is deposited. The substrate layer of the epitaxial silicon produced by ITME [ITM] that was used in this work was low resistivity Cz silicon, whose low resistivity can be neglected, thereby reducing the active area of the detector to the epitaxial layer. As a silicon source various gaseous forms of silicon are used of which $SiCl_4$ (silicon tetrachloride) is the most studied. The typical reaction temperature is 1200 degrees, about 200 degrees under the melting point of silicon, as opposed to the before mentioned techniques that work with the liquid phase. For $SiCl_4$ the overall reaction is

$$SiCl_4(gas) + 2\,H_2(gas) \rightarrow Si(solid) + 4\,HCl(gas)$$

The growth rate is reduced by a competing reaction

$$SiCl_4(gas) + Si(solid) \rightarrow 2\,SiCl_2(gas)$$

If the $SiCl_4$ concentration is too high, it can therefore lead to etching of silicon rather than growing. The dopant is introduces in gaseous form together with the silicon tetracholoride. For n-type phosphoine (PH_3) and for p-type diborane (B_2H_6) is used.

The oxygen concentration in epitaxial material is higher than in standard FZ devices since oxygen from the Cz substrate can diffuse into the active layer. It is however very inhomogeneous distributed throughout the layer as Secondary Ion Emission Spectroscopy (SIMS) measurements have shown (compare Fig. 3.3).

3.5 Oxygenated Silicon

Research by the CERN RD48 (ROSE) collaboration, dedicated to improving radiation hardness by defect engeneering, has shown that increasing the oxygen concentration in silicon improves the radiation hardness of the material when it comes to the development of the effective space charge. In Czochralski silicon a high concentration of oxygen (up to $10^{18}\ cm^{-3}$) is present due to the production process that at the same time, however, also makes it difficult to achieve detector grade quality. It was therefore attempted to increase the oxygen concentration in detector grade FZ material by different techniques, of which oxygenation by difusion proved to be the most cost effective. Oxygen from a thick oxide layer grown by a prolonged oxidation step diffuses into the silicon bulk to achieve an almost homogeneous oxygen concentratons of over $10^{17}\ cm^{-3}$ throughout the bulk [RD408].

In this work only few DOFZ samples were used. However, the positive effect of oxygen in the bulk is also present in MCz and EPI silicon as described in the the previous chapters.

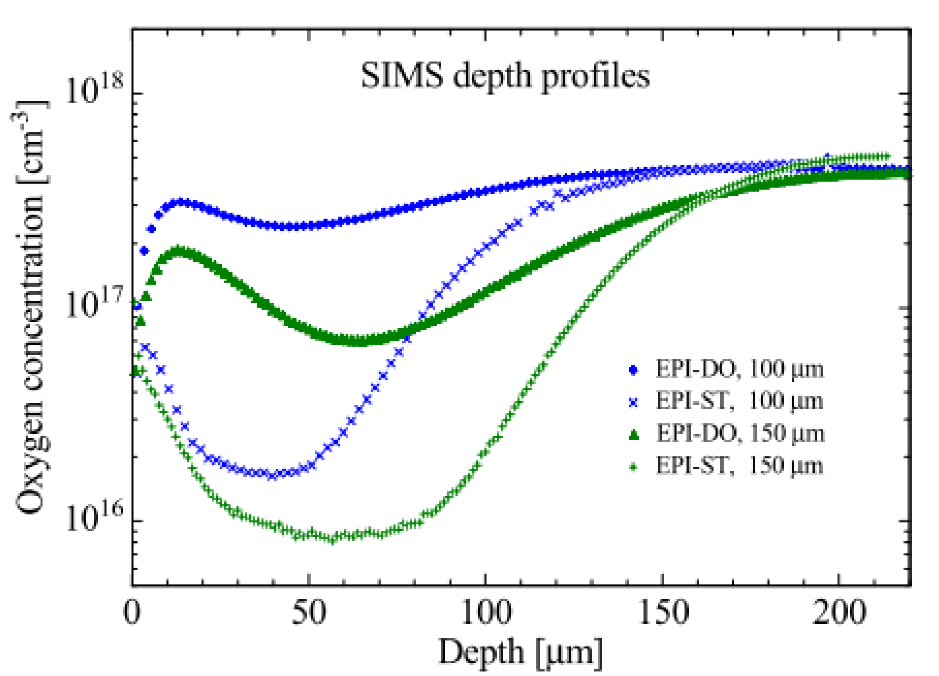

Figure 3.3: SIMS measurements to determine the oxygen concentrations in EPI silicon. In this plot taken from [Eck08] standard EPI and oxygenated EPI (EPI-DO). The investigated standard diodes were produced from the same wafer material as the ones used in this work.

Chapter 4

Radiation Damage

Radiation going through silicon devices not only creates electron-hole pairs that can be used for its detection, but can also interact with nuclei in the silicon lattice, causing permanent damage. One can differentiate between two types of damage in a silicon detector: surface and bulk damage. Surface damage refers to interaction of radiation with the SiO_2 layer and the SiO_2-Si interface via ionization. This can lead to charge accumulation and electric breakdown that deteriorates the performance of strip detectors.

The use of silicon as a detector material in high radiation environments is however mainly limited by the bulk damage caused by displacement of atoms in the silicon lattice. Depending on the impurities various defect types can be created by combinations of vacancies and impurity atoms that can, if they are electrically active, influence the macroscopic detector properties.

In the following first the damage mechanisms that lead to bulk damage are discussed (chapter 4.1). How damage caused by different particle types can be compared is then explained using the NEIL hypothesis (chapter 4.2). Finally an overview over the macroscopic effects of radiation damage in silicon diodes and their changes with time is given in chapters 4.3 and 4.4.

4.1 Damage mechanisms

Particles interacting with silicon can lose their energy either by ionization, interaction with the crystal lattice or nuclear reactions. Charge carriers quickly recombine in the silicon bulk, therefore ionizing energy loss is not of importance for the bulk damage. Energy is mainly lost due to non-ionizing energy loss and more specifically due to atom displacement since the creation rate for defects caused by nuclear reactions is low [Kra01] [Ž98].

The maximum energy transfer E_{max} from an incoming particle with mass m and energy

E to the so called Primary Knock-on Atom (PKA) with mass m_{Si} can be described using non-relativistic collision kinetics[1] by

$$\frac{E_{max}}{E} = \frac{4m \cdot m_{Si}}{(m + m_{Si})^2} \tag{4.1}$$

The minimum recoil energy needed to displace a silicon atom is about 15 eV. This threshold however depends on the direction of the recoil - towards a neighboring atom or between them - so the energy at which the displacement probability is about one half is taken into account [Lut99]. If this displacement energy of about 25 eV is transfered from an incoming particle, a silicon atom can be removed from its lattice site [Lin80]. The process creates a Frenkel pair that consists of an interstitial silicon atom (I) and a vacancy (V). These can then combine to form other structures like di-vacancies and di-interstitials or create more complex defects by combining with impurities in the lattice like oxygen or carbon. Some examples are visualized in Fig. 4.1. A large number however recombines and does not cause permanent damage to the silicon [Shi90].

These so-called point defects can be acceptor or donor like. Acceptors are neutral and become negatively charged when occupied by an electron, whereas donors are neutral when occupied by an electron and positively charged otherwise. So-called shallow level defects have a level close to the band edges, whereas defects with a level close to the middle of the band gap are called deep defects.

If the transfered energy is high enough the PKA can itself remove silicon atoms from the lattice and lead to a cascade of point defects and ionizations. At the end of the path of these recoil atoms, when their velocity is already very low, the cross section for elastic scattering increases and a conglomeration of defects, a cluster, is formed (see Fig. 4.2). The minimum recoil energy needed for the creation of clusters is 5 keV [Lin80].

In the case of 1 MeV neutrons 50-70 keV are transferred to a silicon recoil atom that in turn can displace up to 1000 atoms within 0.1 μm [Lin80] [Spi05]. These neutrons form mainly long range cluster defects as can be seen in Fig. 4.4. In the same figure a simulation of the defect formation after irradiation with 10 MeV protons is shown. Here the Coulomb force enhances small energy transfer and therefore short distance defects, which leads to more point defects. As the energy increases the picture changes again and 24 GeV protons induce a mixture of point and cluster defects.

4.2 NIEL hypothesis

To be able to compare damage due to displacement of atoms in silicon caused by different types of radiation, the NIEL hypothesis can be used for normalization. It is assumed

---

[1] For electrons relativistic kinetics have to be used.

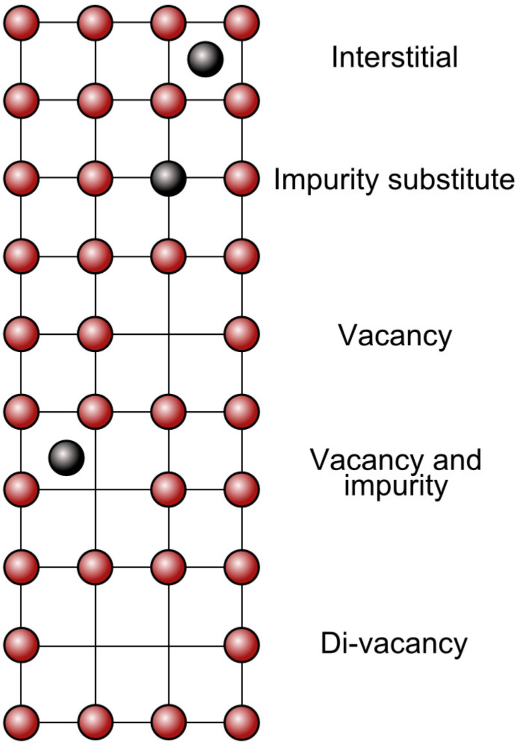

Figure 4.1: Examples of lattice defects that can be caused by irradiation of silicon.

that non ionizing energy loss (NIEL) scales linearly with the imparted energy and is independent of the spatial distribution of the defects caused by recoil atoms.

The displacement damage $D(E)$ can then be calculated via

$$D(E) = \sum_i \sigma_i(E_{kin}) \int_0^{E_{R,max}} f_i(E_{kin}, E_R) P(E_R) dE_R \tag{4.2}$$

where σ_i is the cross section, f_i describes the probability of a collision of a particle with E_{kin} transferring the energy E_R. The Lindhard partition function gives the fraction of the energy that goes into the displacement of a silicon atom, for 1 MeV neutrons $P(E_R) \approx 43\%$, for 24 GeV protons $P(E_R) \approx 42\%$. The 1 MeV neutron equivalent fluence Φ_{eq} with $D_{neutron}(1\,MeV)/cm^2 = 95\,MeVmb/cm^2$ is used as a standard [Har09]. If serveral different particle fluences are to be compared, they are scaled via the hardness factor κ

$$\kappa = \frac{\int D(E)\Phi(E)dE}{D(E = 1\,MeV) \cdot \Phi} = \frac{\int D(E)\Phi(E)dE}{95\,MeVmb \cdot \Phi} = \frac{\Phi_{eq}}{\Phi} \tag{4.3}$$

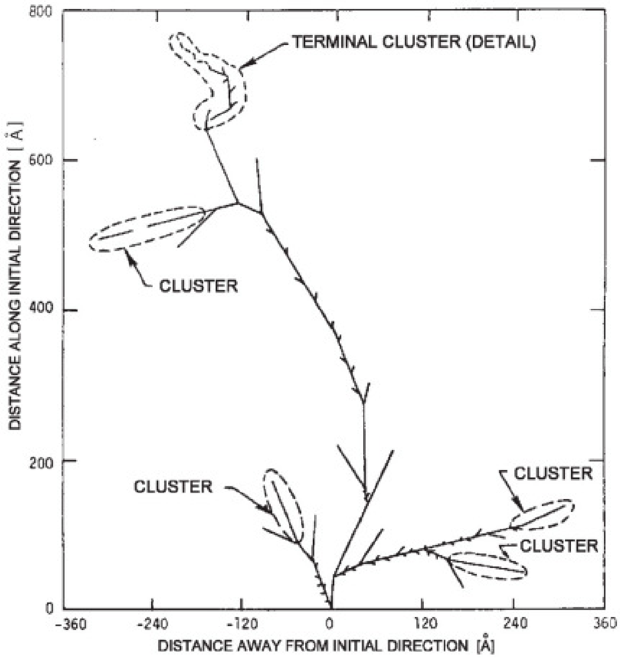

Figure 4.2: Simulation of the track created by a recoil-atom with $E_R = 50\ keV$, which is the energy $1\ MeV$ neutrons on average transfer to the primary knock-on atom [Lin80].

4.3 Damage effects

Microscopic damage in the form of various defect complexes influences the macroscopic properties of silicon detectors, in most cases degrading them. Three different mechanisms are at work:

- Mid-gap states are generated that make it easier for electrons to move from the valence band to the conduction band. This leads to increase in the leakage current.
- Defects can capture charge and re-emit it with a time delay, which decreases the charge collection efficiency.
- The charge density in the space charge region can be changed and space charge sign inversion can occur.

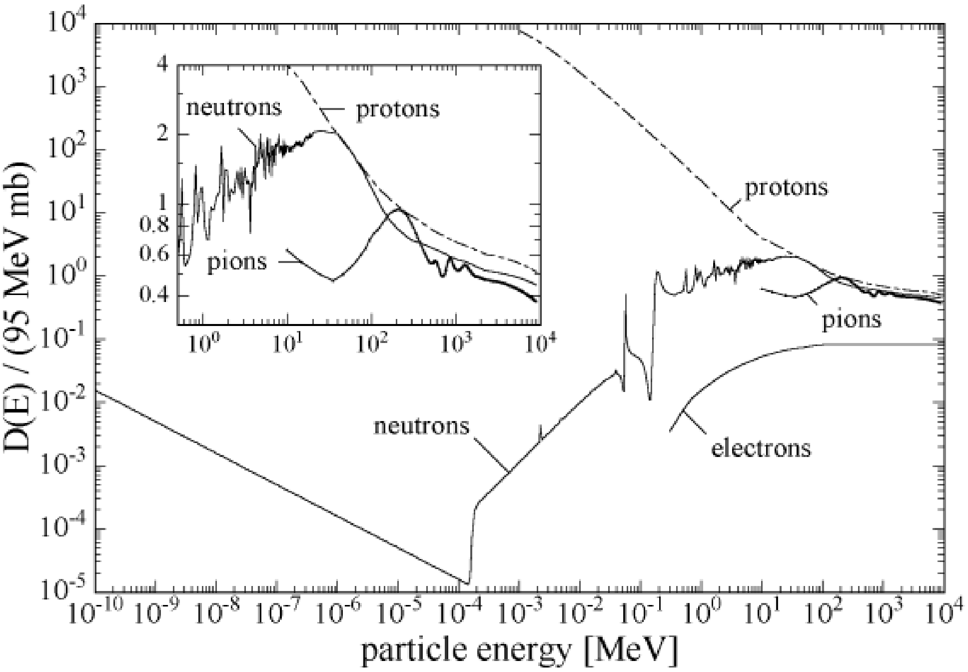

Figure 4.3: Displacement energy function D(E) as a function of the the particle energy normalized to 1 MeV neutrons for different particle types. The insert shows a zoom on the high energy region [Mol99].

Leakage current

Mid-gap states make it easier for charge carriers to move from the valence to the conduction band thereby increasing the leakage current in the reverse biased detector. An overview over emission and capture processes through these states is shown in Fig. 4.5. An electron from the valence band is first promoted to the defect level, which can also be viewed as an hole emission (a) and then emitted again from the defect (b). Similarly an electron from the conduction band can be caught by a defect (c) that then capture a hole from the valence band (d) and thereby reduces the number of free charge carriers (recombination). The transition probability that is an exponential function of the energy difference is greatly enhanced by these mid-gap states. In a diode in reverse bias the conduction band is empty therefore generation dominates over recombination.

The increase in leakage current caused by these processes scales linearly with the particle fluence [Mol99]:

$$\frac{\Delta I}{A \cdot d} = \alpha \cdot \Phi_{eq} \tag{4.4}$$

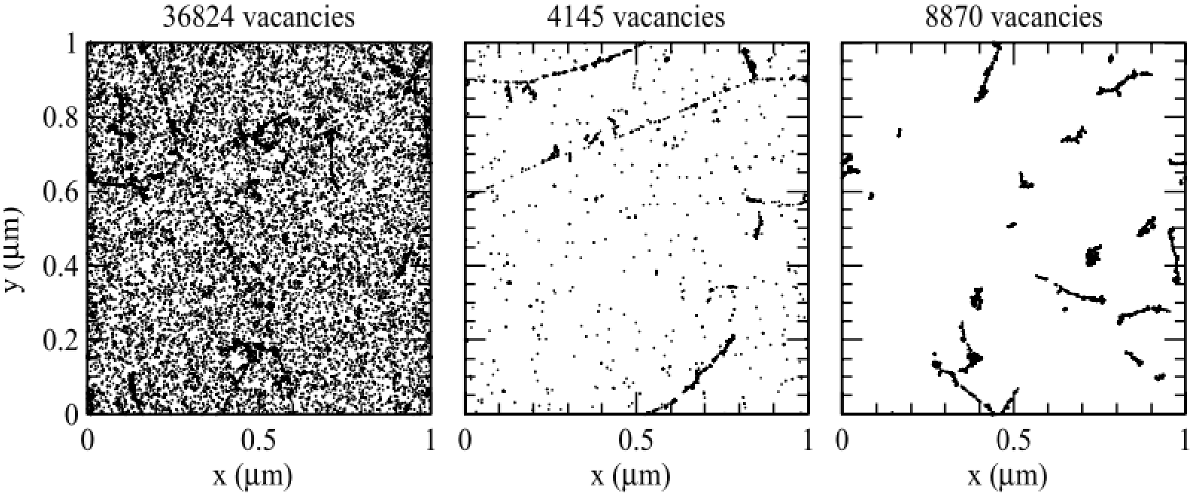

Figure 4.4: Distribution of vacancies produced by 10 MeV protons (left), 24 GeV protons (middle) and 1 MeV neutrons (right). Whereas low energy protons mainly produce homogenously distributed point defects, a mixture of point defects and clusters is created by 24 GeV protons. After irradiation with 1 MeV neutrons on the other hand cluster defects are predominant [Huh02].

where Δ I is the difference between the current before and after irradiation, A and d are the area and the thickness of the diode, respectively. α denotes the current related damage rate and Φ_{eq} the equivalent particle fluence (see chapter 4.2). α does not depend on the particle type or energy or even the silicon material used, i.e. it is the same for n- and p-type Fz, MCz and EPI. The leakage current that leads to increased energy consumption, noise and heating up of the diode can therefore not be influenced by changing material properties.

A point defect that is thought to be responsible for part of the increase in leakage current is the V_2O_i defect that is created by a combination of a VO_i defect with another vacancy [Pin03]. This acceptor-like defect near the middle of the band gap that also occurs after γ-irradiation also influences the doping characteristics of the silicon bulk. However after hadron irradiation cluster related defects play a major role. Examples are the E4 and E5 level at E_C-0.39 eV and E_C-0.45 eV respectively that are two different charge states of the same defect, interpreted as a tri-vacancy [Jun12].

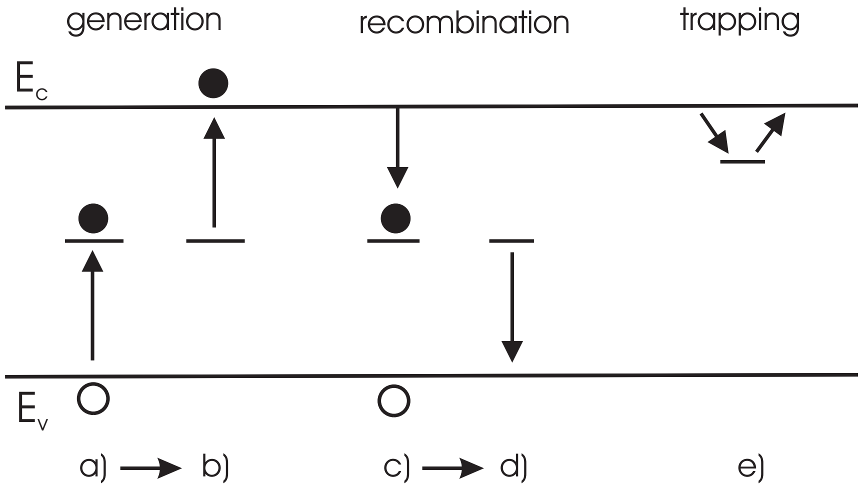

Figure 4.5: Emission and capture processes through defect levels. Generation: (a) electron capture from/hole emission to the valence band and (b) electron emission to the conduction band. Recombination: (c) electron capture from the conduction band and (d) hole capture from the valence band. Trapping: (e) capture and release.

Effective space charge

Defects can interact with dopants to make them electrically inactive and radiation can induce positively or negatively charged defects, which both change the effective space charge $N_{eff} = |N_D - N_A|$ that describes the difference between the number of charged donors and charged acceptors in the silicon bulk.

The development of the effective space charge with fluence strongly depends on the material used. In n-type material the positive space charge can be reduced by the introduction of acceptor states that can be populated with electrons and thereby add negative space charge. Depending on the material (see chapter 8) this can then lead to a change from positive to overall negative space charge in the diode, the so called 'type inversion' or 'Space Charge Sign Inversion' (since the material is only p-like, but not actually the same as p-type silicon) [Li94]. The effective space charge is determined by measuring the depletion voltage that correlates via

$$|N_{eff}| = \frac{V_{dep} 2\epsilon\epsilon_0}{q_0 d^2} \tag{2.6}$$

with $|N_{eff}|$, which means that no information about the space charge sign can be gained from these measurements. Additional measurement techniques, like Transient Current Technique, are therefore needed to give a complete picture of the development of the effective space charge after irradiation (compare chapter 5.3.2). The change of the effective space charge with irradiation can be defined as

$$\Delta N_{eff}(\Phi) = N_{eff,0} - N_{eff}(\Phi) \tag{4.5}$$

where $N_{eff,0}$ is its initial value before irradiation.

Its fluence dependence can be parameterized using equation 4.6

$$|\Delta N_{eff}| = |N_0|(1 - (exp^{-c\Phi})) + g_c\Phi \tag{4.6}$$

Here the first part describes the (incomplete) donor removal with the removal constant c and the second part the introduction of space charge. The effective introduction rate g_c is positive if acceptors are introduced at high fluences and negative in the case of donors.

One example for a point defect that changes the effective space charge after irradiation at low fluences is the VP_s defect or E-center. It is created by a combination of a phosphorus atom that was introduced to change the native silicon bulk to n-type with a vacancy created by displacing a silicon atom from the lattice. The shallow donor close to the conduction band ($E = E_C - 0.045\,eV$) that is positively charged at room temperature is thereby transformed to neutral mid-gap state with $E = E_C - 0.456$ [Bro82]. On a macroscopic level this process leads to donor removal in the device. This defect that is also visible after γ-irradiation is related to point defects. Other defects that influence $|N_{eff}|$ and only occur after hadron irradiation are related to the formation of clusters (compare Fig. 4.4). In recent years the impact of several deep level acceptors in the lower half of the band gap have been investigated that contribute negative space charge during annealing [Pin08] as well as a shallow donor that also influences $|N_{eff}|$ [Pin09].

Charge Collection efficiency

As described in chapter 2.3 the charge collection efficiency is reduced if charge is trapped by defects and lost for the signal read out (compare also Fig. 4.5 (e)). The effective trapping probability depends on the concentration of defects that can act as trapping centers and can be described by

$$\frac{1}{\tau_{eff}} = \sum_i N_i(1 - P_i)\sigma_i v_{th} \tag{4.7}$$

with the occupation probability P_i and the charge carrier cross section σ_i. The fluence dependence is linear [Kra01]

$$\frac{1}{\tau_{eff(e,h)}} = \beta_{e,h}\Phi_{eq} \tag{4.8}$$

The proportionality constant β is different for electrons and holes (compare chapter 8.1).

4.4 Annealing

Defects in silicon are not stable over time but can move through the silicon lattice and form new defect complexes, which influences the macroscopic detector properties during the annealing stage. These processes are temperature dependent and can be slowed down or stopped by keeping detectors at low temperatures. Several mechanisms on a microscopic level lead to changes in defect type and density [Har09]:

- Frenkel pair recombination, i.e. interstitials and vacancies recombine
- vacancies and interstitials combine, forming e.g. di-vacancies
- formation of more complex defects (longer time scale)

Annealing of the leakage current

For the leakage current annealing is always 'beneficial' i.e. the current is reduced, but it can stabilize after a long annealing time. Its behavior can be parametrized by [Mol99]:

$$\alpha = a_0 + \alpha_I e^{-\frac{t}{\tau_I}} - \beta ln(\frac{t}{t_0}) \tag{4.9}$$

as a sum of a constant damage parameter α_0, a first order process and a logarithmic term that is not directly based on a physical model. This parametrization can be used for annealing times between 1 min and 5000 min at 80°C. For shorter annealing times the logarithmic term can cause α to become negative, for longer annealing times a saturation is seen for which a new model is needed (compare e.g. [Lan08]).

Annealing of the effective space charge

The annealing of the effective space charge can be described by the so-called 'Hamburg model' [Mol99]:

$$\Delta N_{eff}(\Phi_{eq}, T, t) = N_C(\Phi_{eq}) + N_A(\Phi_{eq}, T, t) + N_Y(\Phi_{eq}, T, t) \tag{4.10}$$

In addition to the stable damage N_C, i.e. the effective space charge directly after irradiation as described in Eq. 4.6, there are two parts that add to the annealing curve: the short term annealing N_A, traditionally called beneficial annealing since it reduces $|N_{eff}|$ and therefore V_d in the predominantly used material, and the reverse annealing N_Y.

Short term/Beneficial annealing

The short term annealing is the change in effective space charge within the first hours compared to hundreds of days for the reverse annealing at room temperature that is of higher interest for HEP experiments. It can be parameterized as a first order process:

$$N_A(\Phi_{eq}, t) = N_A(\Phi_{eq}) e^{-\frac{t}{\tau_a}} \tag{4.11}$$

where $N_A(\Phi_{eq})$ is the short-term annealing amplitude and τ_a the temperature dependent time constant for the process.

Long term/Reverse annealing

Acceptor like states increase during the long term annealing and there are two ways to describe the behavior. A first order process as shown in equation 4.12 is the most likely physical description deduced from the defect kinetics, whereas a second order process shows the better least square fit to the data. A pragmatic parametrization like in equation 4.13 [Mol99] is therefore quite often chosen:

$$N_Y = N_{Y,\infty}(\Phi_{eq}) \cdot (1 - e^{-\frac{t}{\tau_Y}}) \tag{4.12}$$

$$N_Y = N_{Y,\infty}(\Phi_{eq}) \cdot (1 - \frac{1}{1 + \frac{t}{\tau_Y}}) \tag{4.13}$$

where $N_{Y,\infty}$ is the reverse annealing amplitude and τ_Y its timescale. An example for an annealing curve measured within this work and fitted with the two different approaches is shown in Fig. 4.6

In standard Fz material long term annealing increases the effective space charge and therefore the voltage needed to fully deplete the detector. Since lower temperatures slow down the annealing process these silicon devices should be cooled down at all times, especially also during maintenance periods.

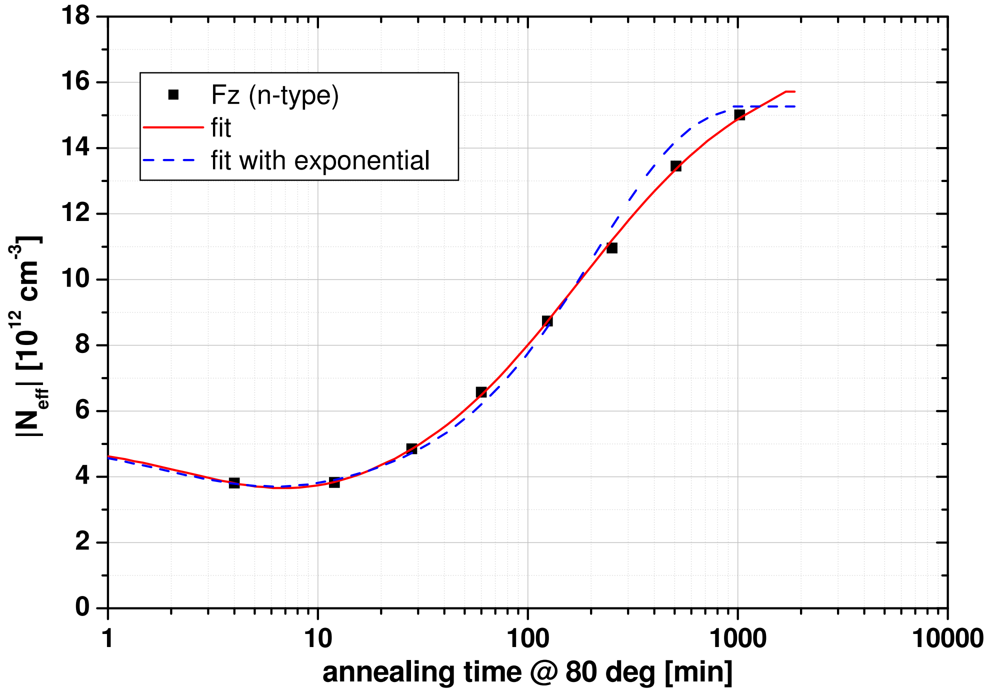

Figure 4.6: Isothermal annealing curve of the effective space charge at 80°C for a n-type FZ diode irradiated with 3.5 x 10^{14} p/cm^2. The two different fitting methods used are described in Eq. 4.12 and Eq. 4.13.

Chapter 5

Experimental Procedures and Setups

This chapter describes the experimental techniques and setups used in this work. First an overview about the materials and diodes used is given (chapter 5.1), followed by a description of the irradiation facilities for proton, neutron and pion irradiation in chapter 5.2. Chapter 5.3 describes the measurement methods and setups used to obtain the depletion voltage, the leakage current, the trapping time and the charge collection efficiency.

5.1 Diodes

This section describes the properties of the pad detectors before irradiation. FZ material was produced by Topsil (Copenhagen, Denmark), MCz by Okmetic (Vantaa, Finland) and Epitaxial by ITME (Institute for Electronics Material Technology, Warsaw, Poland). The major part of the samples was then processed to produce diodes by the Helsinki Institute of Physics (HIP) and CSIC Centro Nacional de Microelectronica (CNM) in Barcelona. The thickness of all FZ and MCz samples was 300 μm. For the epitaxial samples the relevant thickness is that of the epitaxial layer. In this work diodes with 150 μm, 75 μm and 50 μm layer thicknesses were used. The substrate for these samples was highly Sb doped Cz silicon ($\rho = 0.01\,\Omega cm$) for n-type and highly B doped ($\rho = 0.02\,\Omega cm$) for p-type with a thickness of 525 μm for 150 μm samples and 300 μm for the thinner EPI samples. The resistivity throughout the samples can be seen in Fig. 5.1.

All diodes had a guard ring structure around the contact pad on the front which was kept at ground potential (except for TCT measurements) in order to define the depleted volume and exclude lateral effects. Diodes produced by HIP and CNM had an opening in the front aluminum contact pad to allow laser illumination for TCT measurements. For the same reason the backside contact was not fully metalized but showed a grid structure. For an illustration of the diode structure see Fig. 5.2.

The resistivity ρ was determined from the effective doping concentration N_{eff} measured

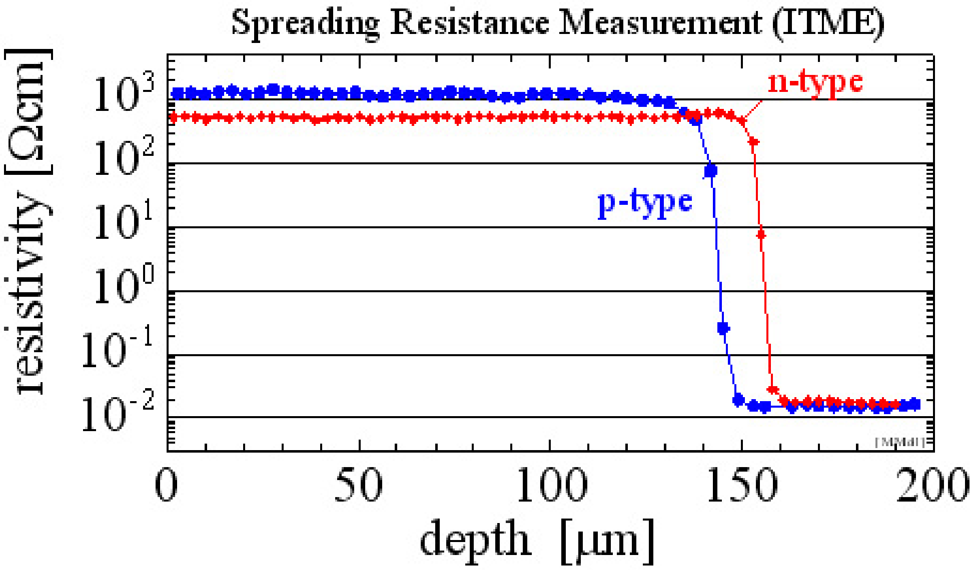

Figure 5.1: Spreading Resistance Measurement (ITME) for 150 μm EPI that shows the resistivity depth profile. Plot taken from [RD508].

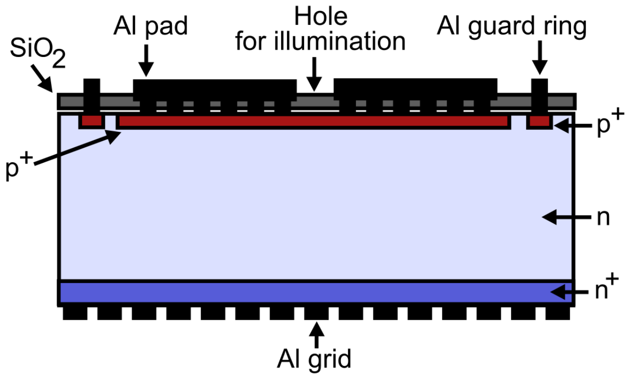

Figure 5.2: Schematics of the diode cross section with guard ring (n-type). A hole in the front aluminum contact and an aluminum grid on the back side allow laser illumination for TCT measurements.

before irradiation. The results are summarized in table 5.1, where the size refers to the active area of the diode.

type	series	producer crystal	producer diode	size $[mm]$	$\lvert N_{eff}\rvert$ $[10^{12} cm^{-3}]$	ρ $[k\Omega cm]$
FZ-n	HIP-002-C	TOPSIL	HIP	2.5x2.5	0.29 ±0.008	14.69 ±0.38
	HIP-002-B	TOPSIL		5x5		
FZ-n	CNM-03	TOPSIL	CNM	5x5	0.28 ±0.03	15.47 ±1.5
FZ-n	FCC14	Wacker	CiS	5x5	1.44 ±0.06	3.79 ±0.18
DOFZ-p	RD-50-05	TOPSIL	CNM	5x5	0.59 ±0.04	21.22 ±1.38
FZ-p	CNM-20	TOPSIL	CNM	5x5	0.031 ±0.002	401.06 ±24.38
FZ-p	F-2551	TOPSIL	Micron	5x5	0.86 ±0.05	14.44 ±0.86
MCz-n	HIP-003-C	Okmetic	HIP	2.5x2.5	4.27 ±0.16	1.01 ±0.04
	HIP-003-B			5x5		
MCz-n	HIP-MCz-01-n	Okmetic	HIP	5x5	4.7 ±0.8	0.92 ±0.02
MCz-n	Wxx-SMG	Okmetic	ITC-IRST	5x5		
MCz-n	M-8556	Okmetic	CiS	5x5	4.52 ±0.22	0.95 ±0.05
MCz-n	CNM-01-M	Okmetic	CNM	5x5	5.33 ±0.15	0.08 ±0.002
MCz-p	p069	Okmetic	HIP	5x5	1.68 ±0.06	7.53 ±0.27
MCz-p	p068	Okmetic	HIP	5x5	1.68 ±0.08	7.53 ±0.35
MCz-p	M-2553-14	Okmetic	Micron	2.5x2.5	9.44 ±0.07	1.32 ±0.01
EPI-n	HIP-004-C	ITME	HIP	2.5x2.5	9.21 ±0.44	0.46 ±0.021
EPI-n	CNM-11	ITME	CNM	5x5	8.62 ±0.21	0.50 ±0.012
EPI-p	CNM-22	ITME	CNM	5x5	12.49 ±0.74	0.99 ±0.056
EPI-p 75 μm	Wxx-xx	ITME	ITC-IRST	2.5x2.5	44.3 ±1.2	0.281 ±0.007
EPI-p 50 μm	Wxx-xx	ITME	ITC-IRST	2.5x2.5	59.55 ±0.7	0.209 ±0.003

Table 5.1: This table lists the names and producers as well as the sizes of all diodes used in this work. The thickness is 150 μm except for the last two entries. The effective space charge before irradiation was measured for all devices by extracting the depletion voltage from CV curves.

5.2 Irradiation facilities

Proton irradiations were performed at the IRRAD-1 facility at the T7 beam line of the CERN PS with a 24 GeV/c proton beam. The beam comes in 1-3 spills of about 400 ms that depend on the 14.4 s supercycle of the PS with a maximum beam intensity of (1-4) x 10^{11} p/spill. The average proton flux is (3-9) 10^{9} $p/cm^{2}/s$. The beam is spread out in order to achieve a uniform irradiation over a spot size of 2x2 cm^{2} [Gla99] [IRR]. Irradiation temperature was around 27 °C. The fluence was determined using aluminum foils irradiated together with the samples. Aluminum gets activated via the reaction $Al^{27}(p,3pn)Na^{24}$ and $Al^{27}(p,3p3n)Na^{22}$. The 1.37 and 2.75 MeV gamma lines from the decay of Na^{24} to Ca^{24} with a half life time of 4.96 h are measured shortly after irradiation with a NaI spectrometer (error of 7-9 %). The Na^{22} 1.27 MeV gamma line can be measured with a Ge spectrometer even long after irradiation due to the longer half life time ($\tau = 12.6\, a$). The hardness factor used for scaling fluences to the 1 MeV neutron equivalent fluence Φ_{eq} (compare chapter 4.2) was $\kappa = 0.62$.

The $\pi E1$ beam line at the Paul Scherer Institute (PSI) in Villigen, Switzerland [For97] was used for pion irradiations. The beam line provides a high intensity π and μ beams with a momentum range between 10 and 500 MeV/c. In the operation mode used for irradiations, the maximum momentum is 280 MeV/c with a low momentum resolution ($\Delta p/p = 0,8\%\, FWHM$), but higher flux. Irradiations temperatures varied between 22 and 23 °C. Also here the fluence was measured using aluminum activation but with an error of 20 % of the 1 MeV equivalent fluence due to uncertainties from determining the hardness factor (κ=1.14 [Kra10a]).

Neutron irradiations were performed in the 250 kW TRIGA reactor at the Jožef Stefan institute in Ljubljana, Slovenia [Rav03]. In this light-water reactor samples are irradiated using a tube occupying the place of a fuel rod in the core [Ž99]. The fluence was determined with gold foils within an error of 10 % [Cin00].

5.3 Experimental methods and setups

In this chapter the measurement procedures and setups for determining depletion voltage, leakage current (chapter 5.3.1), trapping time (chapter 5.3.2) and charge collection efficiency (chapter 5.3.3) are described.

5.3.1 CV-IV

For obtaining the depletion voltage V_{dep} and the leakage current above depletion capacitance-voltage (CV) and current-voltage (IV) measurements were performed.

An unirradiated reverse biased diode can be represented by a parallel circuit consisting of a resistor R_p and a capacitance C_p and an additional serial resistor R_s (see Fig. 5.3). R_p represents the leakage current in the device, whereas R_s stands for the resistance in the undepleted silicon bulk. R_s can be neglected due to the low resistivity in the undepleted bulk in an unirradiated diode. The device is then best represented by a parallel circuit with an admittance Y given by

$$Y = \frac{1}{R_p} + j\omega C_p$$

where $\omega/2\pi$ is the measurement frequency. The admittance depends primarily on the capacitance C_p since the leakage current in the silicon bulk is very low.

For irradiated devices the pictures becomes more complex: the high resistivity of the bulk

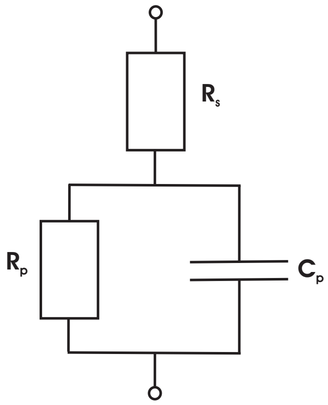

Figure 5.3: Equivalent circuit for a biased diode. The parallel resistor R_P represents the leakage current, the serial resistor R_S the resistivity of the bulk.

has to be represented by a serial resistor R_s, whereas for the increased leakage current adding a parallel resistor R_p is necessary. Since it is only possible to either measure the impedance Z depending on R_s and C_s in series or the admittance Y in a parallel circuit a method that best represents the actual device has to be decided on. For highly irradiated detectors furthermore an additional frequency dependence of the measurement is introduced by the presence of deep defects in the bulk [Dab89]. Since the emission coefficient for these radiation-induced traps is temperature dependent, the correct measurement frequency also depends on temperature [Pet07]. For easy comparison of measurement data from different groups it was therefore agreed within the RD50 community to use parallel mode with a frequency of 10 kHz for CV measurements at room temperature [Chi04], where the best agreement to the depletion voltage from CCE measurements is found.

For the CV and IV measurement the diodes were contacted with needles on the guard ring and the front pad, both of which were kept on ground potential. Bias was applied through the backside metalization. For CV measurements a Keithley 237 voltage source that also read out the total (backside) current was used. The compliance was kept to $1mA$ to ensure proper CV measurements without heating up of the diode which leads to thermal run-away, influencing the results. The signal was taken from the pad contact on the front with an Agilent 4263B LCR meter operating at 10 kHz in parallel mode with an amplitude of 500 mV. The DC bias voltage was decoupled from the AC voltage coming from the LCR meter by capacitors. The setup was calibrated to account for this additional capacitance of 65 pF.

Above depletion the capacitance of the diode only depends on its geometric properties (see chapter 2.2) and is therefore constant. To determine the depletion voltage straight lines were fitted in the $logV$ versus $logC$ plot before and after the the kink and the voltage at the intercept was extracted (see Fig. 5.4).

For IV measurements a Keithley 240 source meter and a Keithley 485 current meter

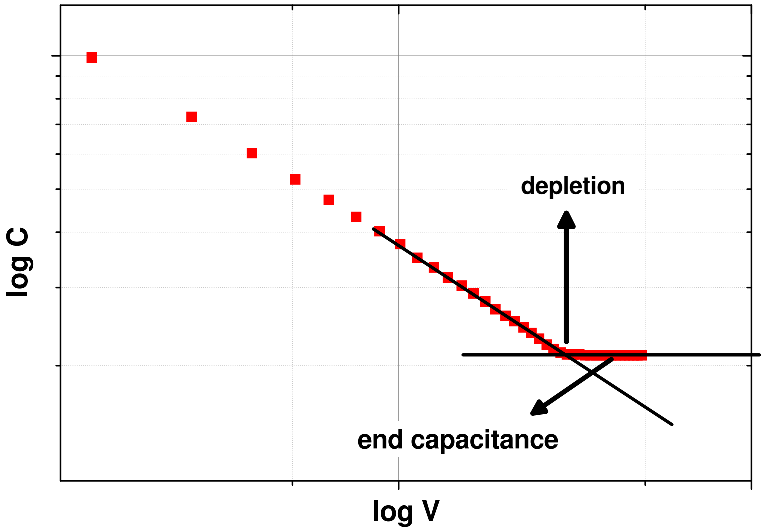

Figure 5.4: Determination of the depletion voltage using the $logV$ vs. $logC$ plot. V_{dep} is extracted from the intercept of the fits.

were used, again keeping the compliance at 1 mA for the total current. The depletion voltage was extracted from the $logV$ vs. $logI$ plot similar to the method used in the CV measurement and the leakage current was measured at around 50 V above depletion.

CV and IV measurements were performed at room temperature ranging from 20 to 22 °C measured on the metal support close to the diode. The current in the diode depends on the temperature according to equation 2.11 and was corrected to the value at 20 °C after all measurements.

5.3.2 TCT - Transient Current Technique

The Transient Current Technique looks at the current induced by charge carriers that drift through the diode after being created by incident particles or short laser pulses. Irradiation creates defects in silicon that can act as traps for charge carriers (see chapter 4.3), which leads to signal loss if the integration time is less than the time needed for de-trapping. TCT can be used for finding the effective trapping probability for charge transversing silicon by using the Charge Correction Method [Bro00], [Kra02]. By integrating over the signal to gain a QV plot also the depletion voltage can be determined. The shape of the TCT signal gives an indication on the sign of the space charge in the bulk by showing which side of the diode the dominant junction is at.

Signal Formation

The general principle used for TCT measurement is to look at the signal produced by the drift of electron-hole pairs that are created by an incident particle. They induce charge at the electrodes, which leads to a current flow in the attached circuit. This current is given by (compare chapter 2.3):

$$I_{e,h} = \pm \frac{q_0 N_{e,h}(t)}{d} v_{e,h}(t) \tag{5.1}$$

where the drift velocity $v_{e,h}(t)$ depends on the electric field and therefore on the position of the charge carrier in the device.

To look at the shape of the signal and therefore of the electric field in a pad detector it is useful to only have one type of charge carriers that are all produced at approximately the same time and depth in the device. This can be achieved by illuminating different sides of the diodes with a pulsed red laser. The absorption of light in silicon depends on the wave length, for 670 nm it is small compared to the thickness of the diode (3.3 μm [Das55]) compared to 300μm), so the charge carriers are created close to the surface and one type immediately reaches the electrode and thereby only minimally contributes to the signal. In the following the situation in $p^+ - n - n^+$ diodes that have not been type inverted due to irradiation (see chapter 4.3) will be described, for $n^+ - p - p^+$ devices the roles of electrons and holes are reversed.

In the TCT setup the n^+ side of the diode, in the following called 'back', is kept on ground potential, the p^+ side, in the following called 'front', on negative potential (Fig. 5.5). The main junction with the the highest electric field is therefore on the front side. If the laser shines onto the front side, the electron-hole pairs are created close to the negative electrode. The holes therefore immediately reach the electrode and barely contribute to the overall charge signal. The electrons on the other hand have to travel through the diode of thickness d, inducing a signal on the back electrode. If the applied bias voltage is below depletion, i.e. if the electric field does not extend through the whole device, they first drift in the high field region and then slowly diffuse. If the laser shines onto the backside before the bias voltage is high enough for depletion, the charge first reaches a region with no field and does not create a signal. Only at sufficiently high bias voltages, when the electric field comes close to the backside, a current is induced by the holes that now traverse the detector while the electrons are absorbed by the backside electrode. Since the holes are created in the low field region of the detector and move towards the high field region, the drift velocity increases with time and reaches its maximum when they arrive at the front electrode. The current signal is proportional to the drift velocity, therefore the signal height increases as the holes move through the detector. For electrons the opposite is true: after front side illumination, they are created in the high field region and move to the low field region, therefore the signal decreases with time. Furthermore the mobility of holes is only one third of the electron mobility, which makes the hole signal longer than the electron signal.

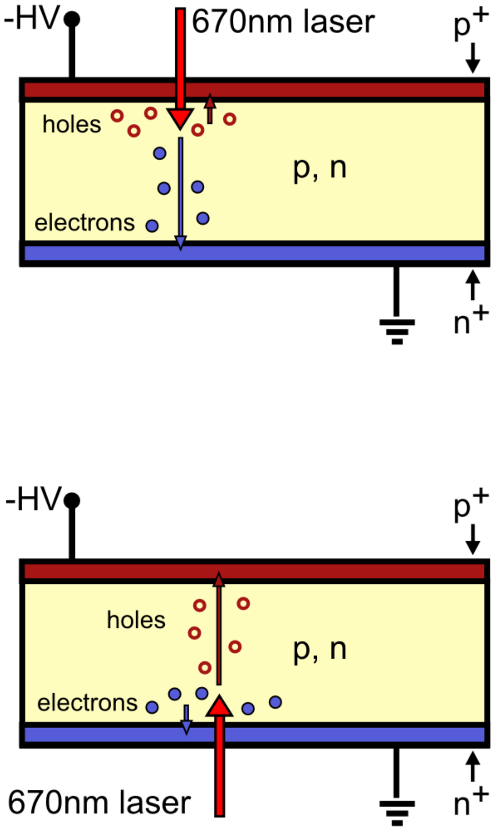

Figure 5.5: Schematics of TCT measurements. If the laser shines onto the n^+ side of the diodes, the holes reach the electrode immediately and the electrons produce the signal by drifting through the diode. If on the other hand the laser creates electron-hole pairs close to the p^+ side, mainly the holes contribute to the signal.

Examples of electron and hole signals at different bias voltages are shown in Fig. 5.6 and Fig. 5.7. At bias voltages below V_d, when the field reaches the backside of the diode, the holes still have to diffuse for a certain distance before the they drift in the field which leads to very long signals. At very high bias voltages, the drift velocity saturates, leading to similar signal shapes for electrons and holes. TCT can be used for determining where the dominant junction in a detector lies by looking at the signal shapes of electron and hole signals. For irradiated diodes, the signals have to be corrected for trapping, which can make the determination of the dominant junction difficult (see for instance the case of MCz in chapter 8.2.2).

QV method

As the applied bias voltage increases, the depletion zone extends further into the device and the collected charge increases. When depletion is reached, even if the applied voltage

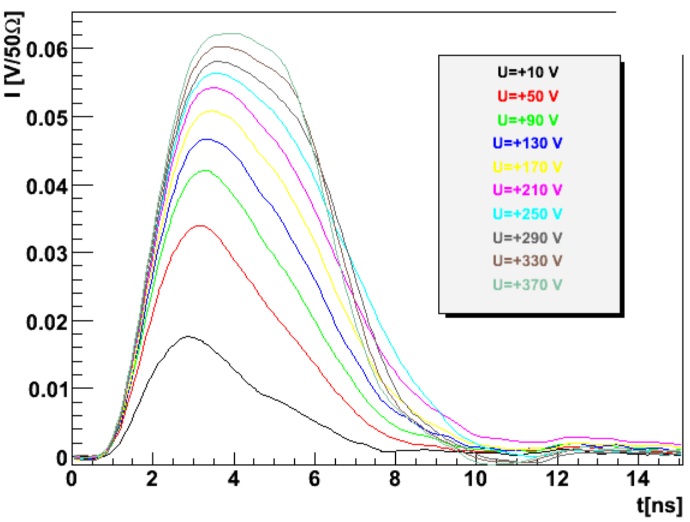

Figure 5.6: Electron signal at different bias voltages in n-type silicon. The laser shines on the front or p^+ side of the diode where the main junction with the highest electric field is situated. The electrons that are created in this region drift to the low field region.

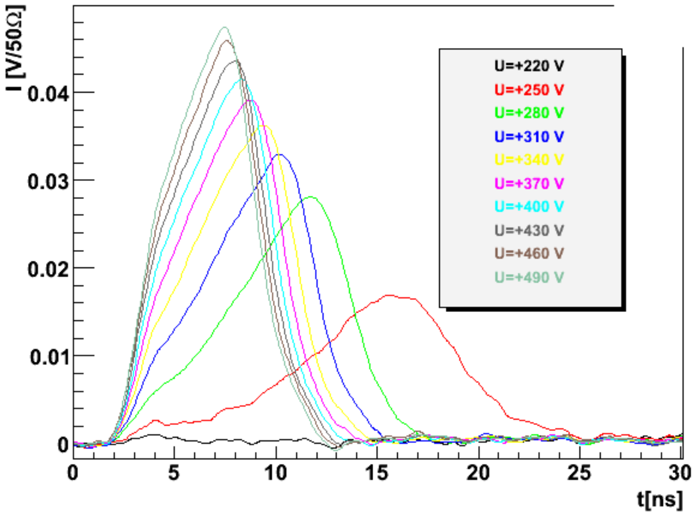

Figure 5.7: Hole signal at different bias voltages in n-type silicon. The laser shines on the back or n^+ side of the diode away from the main junction. The holes that are created in this low electric field region drift to the high field region.

is increased, the charge stays constant in an unirradiated detector. By fitting lines in the charge vs. voltage plot as shown in Fig. 5.8 this gives another method to determine the depletion voltage.

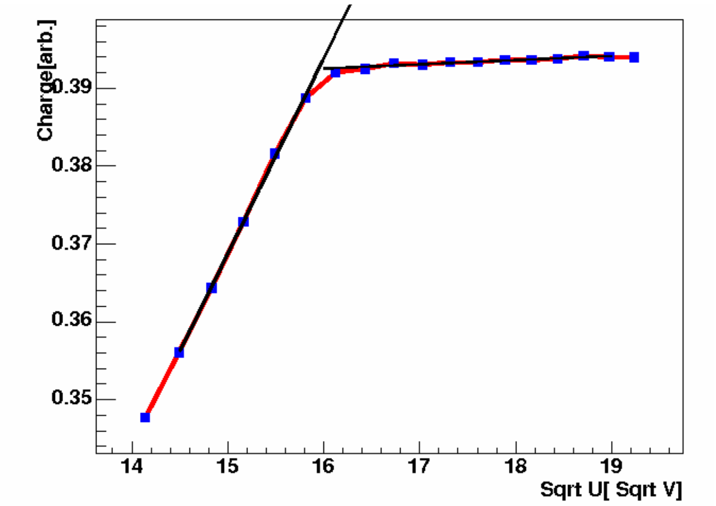

Figure 5.8: Determining the depletion voltage from the Q-V plot by looking at the intercept of two straight lines.

Charge Correction Method

In the presence of defects that can act as traps for charge going through the detector, the collected charge is reduced, if the time needed for de-trapping is longer than the read out time, which is the case in the LHC scenario with bunch crossing times of 25 ns. The number of charge carriers decays exponentially (compare chapter 2.3).

$$N_{e,h}(t) = N_{e,h}(t_0) \cdot exp(-\frac{t}{\tau_{eff_{e,h}}}) \tag{5.2}$$

where $\tau_{eff_{e,h}}$ is the *effective trapping time* that is defined via the effective trapping probability in equation 4.7. In irradiated devices even after depletion the charge increases with higher bias voltages, since the higher drift velocities make it less likely for the charge to be trapped due to shorter drift times in the diode.

To determine $\tau_{eff_{e,h}}$ the current integral above depletion can be used. The measured current $I_m(t)$ that is proportional to the number of charge carriers has to be corrected for trapping by multiplying it with the factor $exp(\frac{t-t_0}{\tau_{eff_{e,h}}})$, where t_0 is the carrier injection time:

$$I_c(t) = I_m(t) \cdot exp(\frac{t - t_0}{\tau_{trapping}}) \tag{5.3}$$

If the time integral over $I_c(t)$ at voltages above depletion is corrected with the right

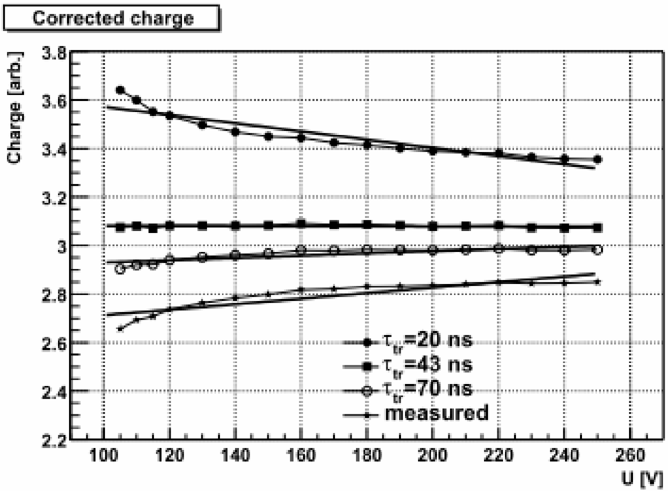

Figure 5.9: Application of the Charge Correction Method. The value for τ_{eff} is varied until the slope in the Q_{corr} vs. V plot is zero τ [Kra01].

value τ_{eff} for $\tau_{trapping}$(see Eq. 5.2), the charge thereby obtained should be constant and therefore the gradient in the charge vs. voltage plot should be zero.

In the so called *Charge Correction Method* [Bro00], [Kra02] the effective trapping time is hence determined by a linear fit to the Q_{corr} vs. V plot and evaluating the slope for various values of $\tau_{trapping}$ until at the correct trapping time it vanishes.

Fig. 5.9 shows the variation of the slope with τ_{eff}. If the trapping time used for correction is too high, i.e. the assumed trapping probability is too low, the slope is positive and the corrected charge at low voltages and therefore at low drift velocities is smaller than the actual charge and vice versa for high trapping probabilities above the correct value.

The following conditions have to be met for the method to be valid:

- All charge is lost due to trapping only.
- Only one trap with one trapping constant τ is responsible for the trapping.
- Integration times are shorter than the time needed for de-trapping.
- All the charge is injected at once, i.e. the laser pulse width is much shorter than the drift time.

TCT setup

The TCT setup was originally built by Alison Bates [Bat05a] in 2004 based on a design from the Jožef Stefan Institute in Ljubljana [Kra01], but was changed significantly as new equipment became available in the course of building a measurement station for strip detectors. The diodes were contacted using a Cu-Be needle (99 % copper) soldered to a PCB board (see Fig. 5.10). The bias voltage was supplied by a Keithley 2410 through the needle while the backside of the diode was kept on ground potential and the guard ring was left floating. A red 660 nm picosecond laser was used to induce the signal read out with a LeCroy wavepro 7100A oscilloscope. The signal was fed to the scope through an Picosecond Lab 5531 Bias-Tee with a capacitance of 2.2 nF for decoupling (see Fig. 5.11) and amplified with a Philips 6954 50x current sensitive 1 GHz amplifier. The length of the signal lines was chosen to find an optimum between removal of reflections and signal loss due to long cables. Laser irradiation was possible from the front side (through a hole in the aluminum layer) for most diodes, whereas back side illumination was limited partly due to the nature of the material, partly due to the complete covering of the back side with aluminum. The laser frequency was fixed to 170 Hz while the intensity, controlled by a shutter system, had to be varied due to losses of light on the back side aluminum grid.

The data taken with the LABVIEW control system was then evaluated using a ROOT software developed by G. Kramberger [Kra01].

Signal deconvolution

The measured signal is a convolution of the actual detector signal and the shaping of the electronics. From the TCT system transfer function the real deconvoluted current can be obtained using

$$I(t) = \frac{\tau_{TCT}}{R}\frac{dU_{Osc(t)}}{dt} + \frac{U_{Osc}}{R}$$

with

$$U_{Osc}(t) = \frac{AR}{\tau_{TCT}} exp(-\frac{t}{\tau_{TCT}}) \int_{-\infty}^{t} I(t^{'}) exp(\frac{t^{'}}{\tau_{TCT}}) dt^{'}$$

where R is the input impedance of the oscilloscope and $\tau_{TCT} = RC_d$ [Kra01]. The input detector capacity C_d varied according to detector area and thickness, but was always larger than the end capacitance obtained by the CV measurements. The guard ring was not connected for TCT measurements, which increases the active area.

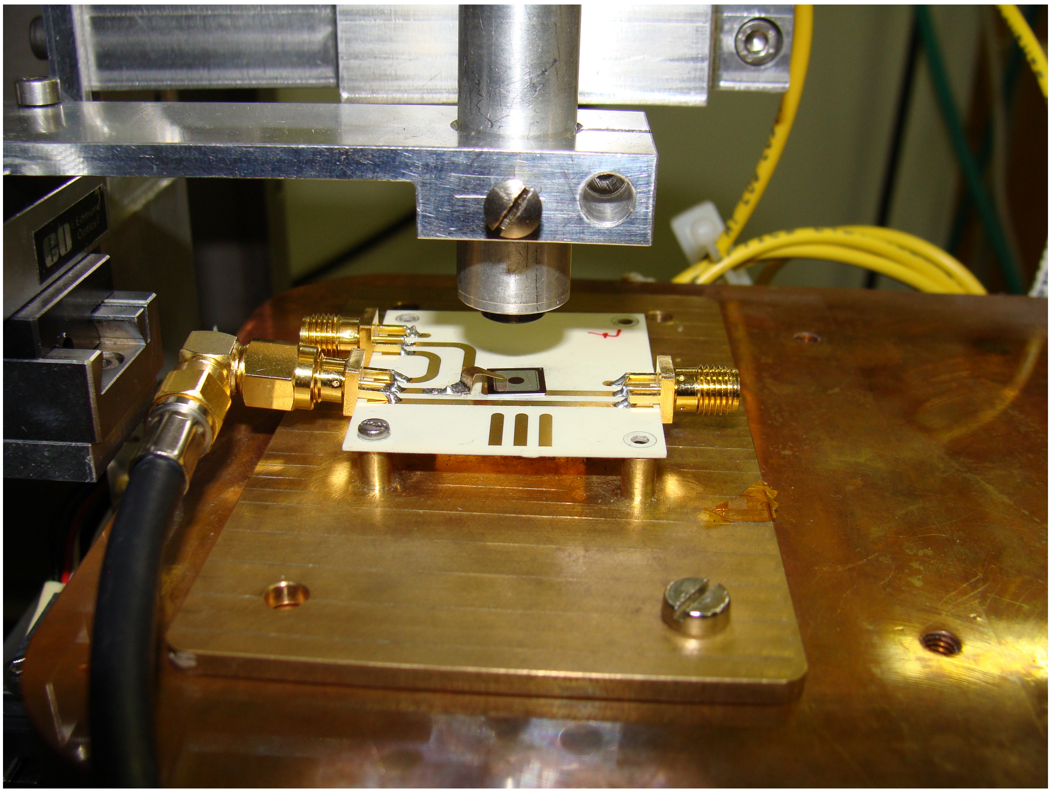

Figure 5.10: Diode contacted for TCT measurements with a Cu-Be needle with the laser shining in from the front. For a schematic of the setup box see [Pac11].

5.3.3 Determining the collected charge

The collected charge in irradiated diodes was determined using beta particles from a radioactive source in a dedicated setup. Electrons travel through the whole detector creating electron-hole pairs along the way. In the presence of defects introduced by irradiation of the sample, part of the charge is trapped, thus reducing the output signal of any silicon detector as described in chapter 5.3.2. Together with the depletion voltage, the charge collection efficiency, determined by comparing the collected charge in an irradiated device to that of an unirradiated one, is therefore one of the most important parameters for comparing the radiation hardness of different materials.

CCE setup

CCE measurements were performed with a system obtained from NIKHEF [NIK] that uses a ^{90}Sr source with an activity of 3.5 MBq to create a signal from electron-hole pairs produced in the biased diode. A tungsten collimator was used to focus the electrons to the center of the diode to avoid any effects from changes in the electric field close to the edges. The readout electronic was triggered with a scintillator-photomultiplier

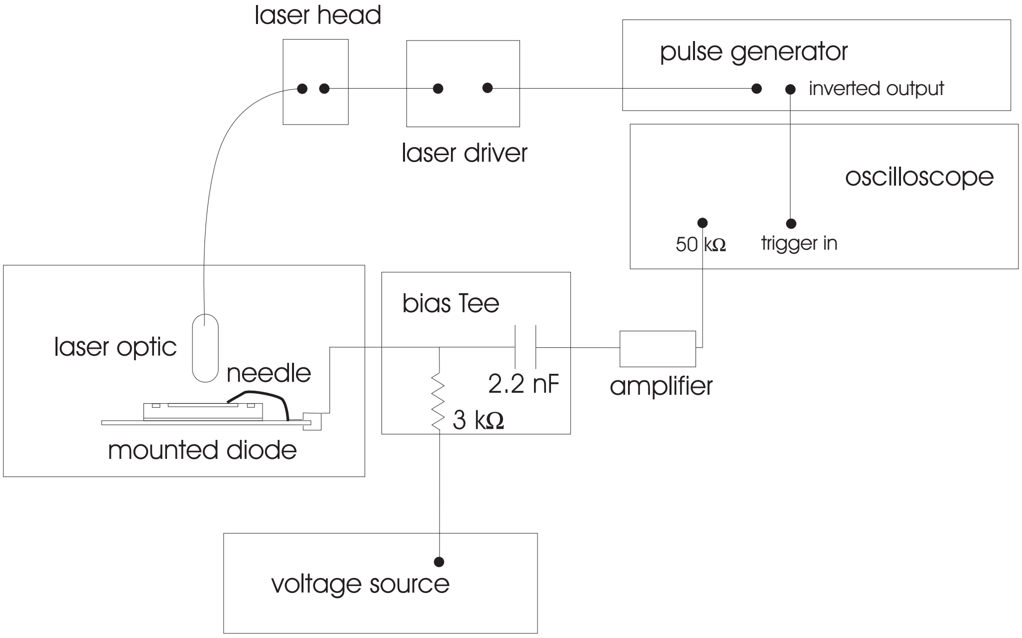

Figure 5.11: Schematic of the TCT setup at CERN.

combination placed underneath the diode (for a schematic of the setup see Fig. 5.12). The signal shaping time of the setup was 2.5 μs and the electronic noise was measured to be 309 e^- without a detector. The noise added by the presence of a detector depends on the capacitance of the diode according to 4.6 e^-/pF.

The diodes were glued to PCB boards with silver glue. Pad and guard ring contact were connected with bond wires. For all measurements at (-20 ± 1)°C the whole setup was put into a freezer and flushed with dry nitrogen to keep the humidity below 30 %. The temperature was measured by two thermistors on the backside of the PCB boards. A Sensirion SHT75 sensor in the setup provided huminity measurements.

The LABVIEW DAQ was provided by NIKHEF and measured the charge at a series of voltages, collecting a predefined number of events (usually 5000). A LABVIEW analysis program was used to plot a histogram and fit it with a Landau distribution. For a typical Landau distribution obtained with the NIKHEF setup see Fig. 5.13. An additional measurement was performed using an internal trigger rate of 50 Hz in order to be able to correct the data for the pedestal offset and deconvolute the Gaussian noise and the Landau distributed signal. Pedestal events amounted to 2-4 % of the total number of events.

Repeated measurements of the same diode with complete re-mounting of the sample could

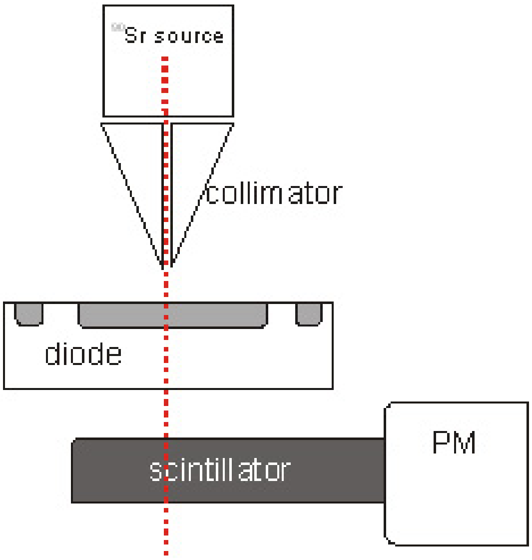

Figure 5.12: Schematic of the CCE setup from NIKHEF. Beta particles from a ^{90}Sr are focused by a tungsten collimator, pass through the silicon pad detector and trigger the read-out system via a scintillator-photomultiplier combination.

be reproduced within 1 % (see Fig. 5.14). If two samples from the same batch, irradiated at the same fluence are compared, the variation of the most probable value of the Landau distribution is around 3 % (Fig. 5.15).

Gain

For determining the gain factor a pulse generator signal was attenuated to a few mV and then fed into the dedicated test input of the system via an oscilloscope. The gain factor G can be calculated from the charge created by the test pulse by using

$$G = \frac{A(C_T + C_p) \cdot V_T}{V_m}$$

where A is a constant with a value of 6241 (provided by NIKHEF), V_T is the step height of the test pulse and V_m is the voltage measured by the system DAQ. C_T (2.2 pF) is the capacitance that converts the rising and falling edge of the pulse into a signal for the preamplifier and C_p represents the the parasitic capacitance of the board with a value of 0.11 pF [NIK]. The gain was determined at -22 °C for several input voltages between 6 and 1 mV, leading to an average value of $G = 247\, e^-/mV$.

Influence of sample size and collimator position

It was also tested whether the size of the diode or the positioning of the source influenced the result. Three unirradiated n-type diodes of different sizes produced by HIP from

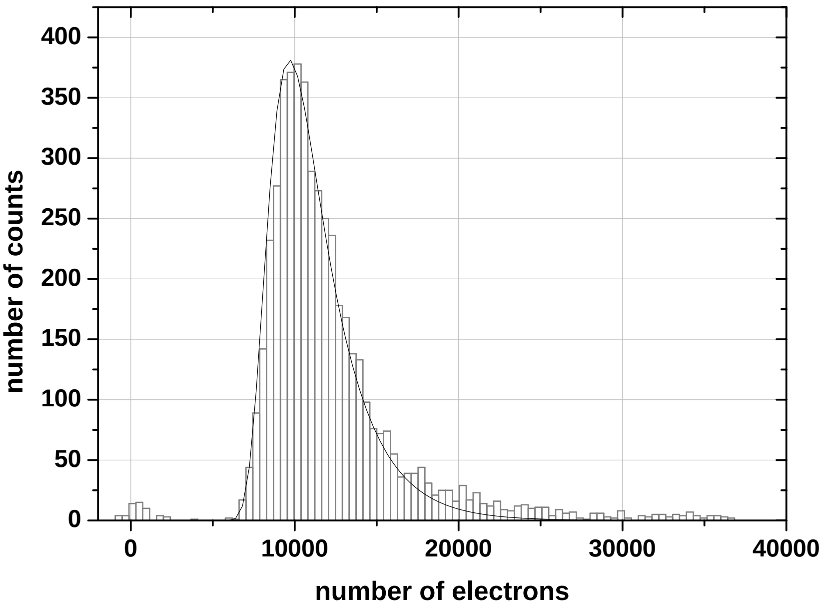

Figure 5.13: Typical Landau distribution obtained with the NIKHEF setup.

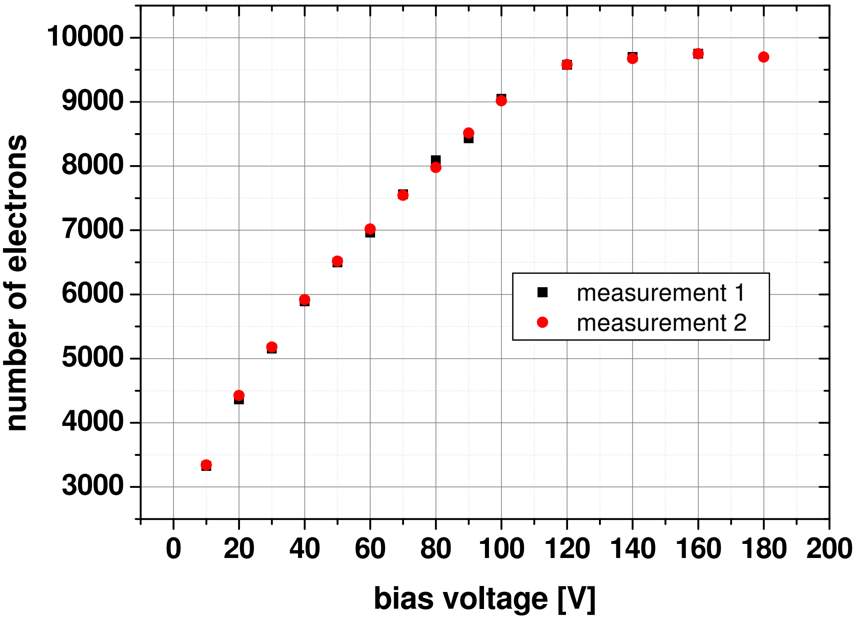

Figure 5.14: Repeated measurements with complete removal and re-mounting of a EPI-n diode irradiated with $1 \times 10^{13}\ n/cm^2$.

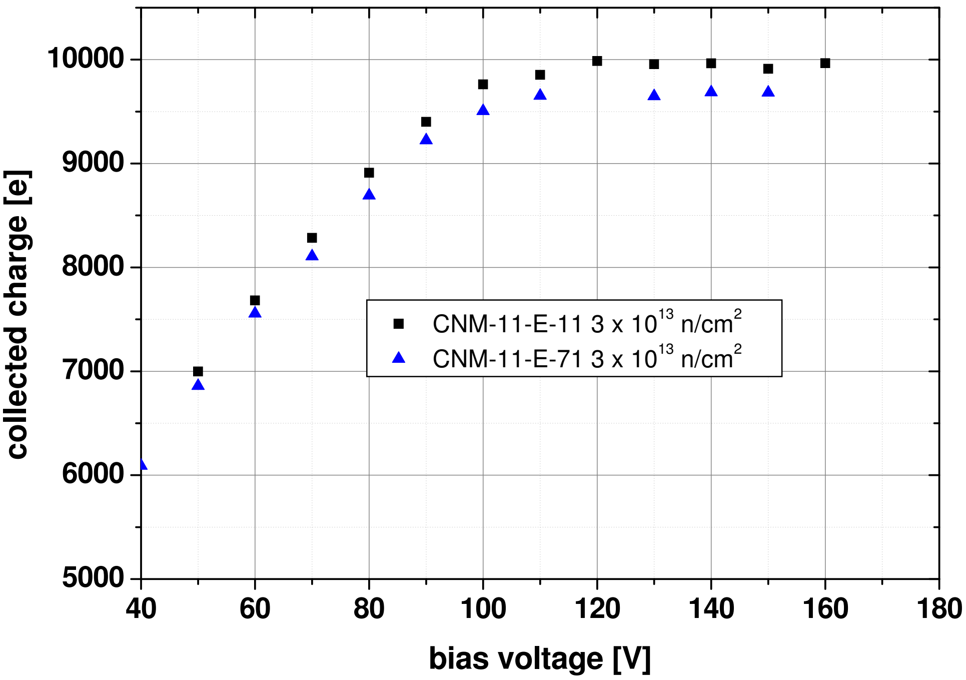

Figure 5.15: Comparison of the collected charge in two n-type EPI samples from the same batch irradiated to the same neutron fluence of 3 x 10^{13} n/cm^2.

the same wafer were measured. The biggest diode with an area of 10 x 10 mm^2 shows the lowest collected charge (Fig. 5.16(a)). The difference between the two diode sizes that were actually used for measurements, 2.5 x 2.5 mm^2 and 5 x 5 mm^2, is similar to variations between samples from the same wafer. Equally the collected charge in these two diode types irradiated with a neutron fluence of 1 x 10^{13} cm^{-2} is the same (Fig. 5.16(b)). At higher fluences however differences between small and big diodes, albeit not produced by the same company but from the same wafer material, become noticeable (compare chapter 7).

In addition measurements to determine the influence of the collimator position on the measured charge were performed. The collimator was moved from the middle position usually used for measurements to the outer edge of the diode in several steps. As can be seen in Fig. 5.17, no differences in the collected charge were found outside the small variations expected between measurements.

Silver glue vs. adhesive carbon pads

There was the suspicion that using different kinds of adhesives to fix the diodes to PCB boards could alter the measurement results, therefore a few comparative tests were conducted before starting the measurement program. An irradiated diode was first mounted to the PCB board using a carbon adhesive tab and measured under standard measure-

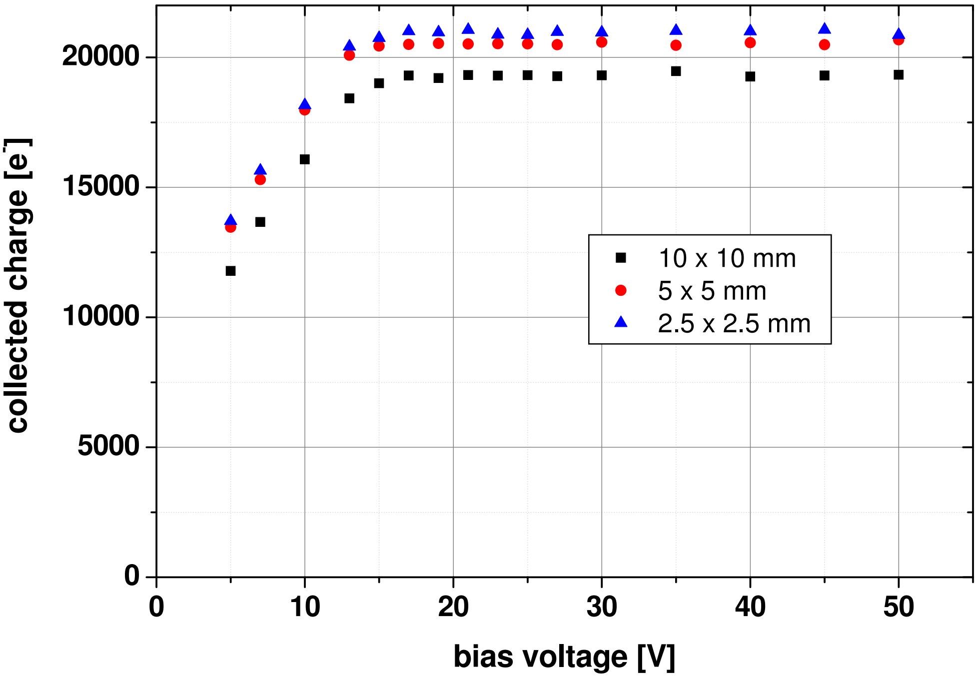

(a)

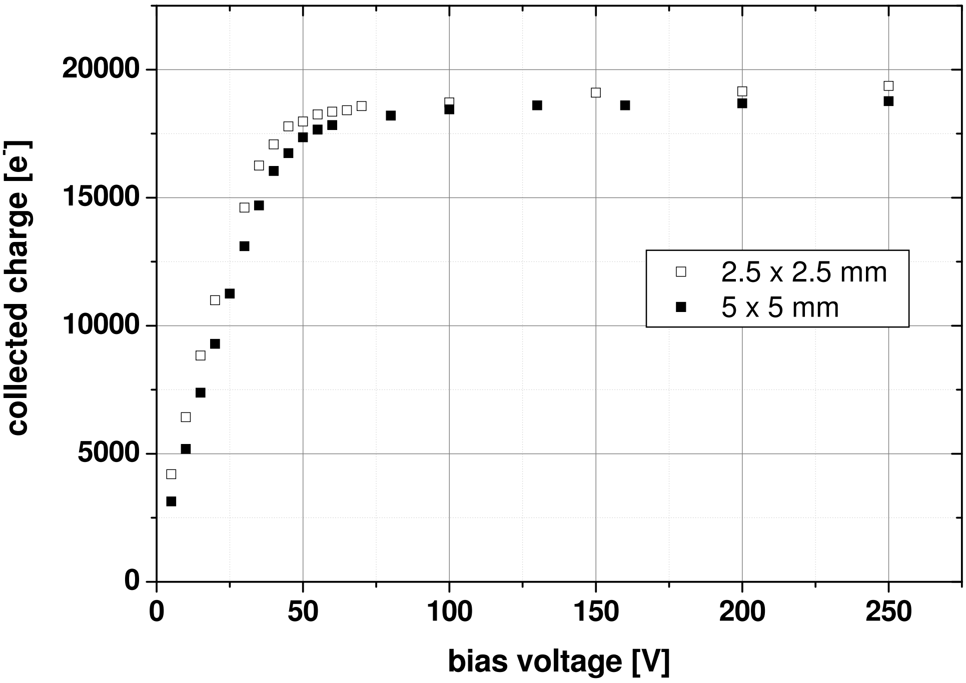

(b)

Figure 5.16: Influence of the diode size on the collected charge in (a) unirradiated and (b) neutron irradiated n-type FZ diodes (irradiation fluence: 1 x 10^{13} n/cm^2).

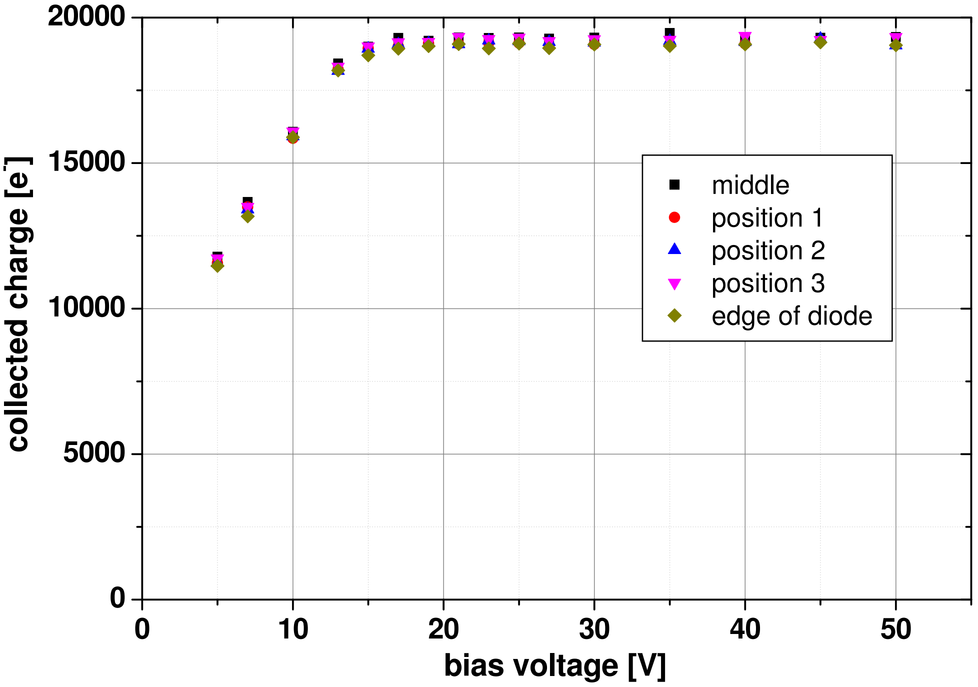

Figure 5.17: Influence of the collimator position on the collected charge. The collimator was moved from the center to the outer edge of the diode and the charge was measured at each point.

ment conditions. It was then removed and re-mounted using conductive silver glue. This second measurement showed around 10 % more collected charge as can be seen in Fig. 5.18. The reason for the different results remained unclear, however as the mounting of non-irradiated sensors using silver glue gave the expected results and there were also hints pointing towards worse reproducibiliy for the carbon adhesive tabs, all diodes were mounted using silver glue.

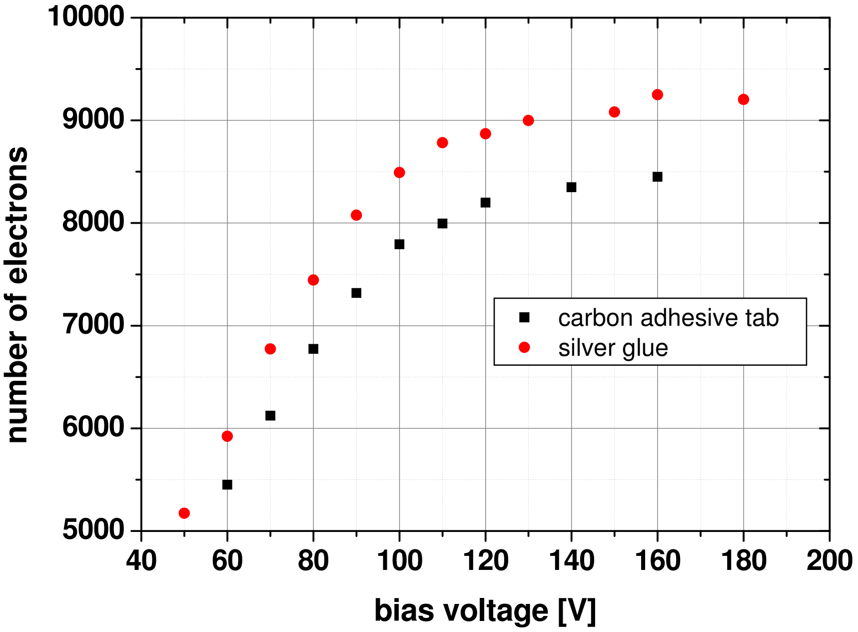

Figure 5.18: Comparison between silver glue and adhesive carbon pads using an EPI diode irradiated to $2.2 \times 10^{14}\ p/cm^2$. Temperature and humidity were the same for both measurements.

Chapter 6

Effective Space Charge Development

The development of the effective space charge $|N_{eff}|$ or depletion voltage V_d with fluence is one of the main criteria for the radiation hardness of silicon material. In this chapter first the effect of irradiation with 24 GeV/c protons, reactor neutrons and 200 MeV pions on this parameter is evaluated for FZ (chapter 6.1.1), MCz (chapter 6.1.2) and EPI of different thicknesses (chapter 6.1.3). Then these materials are compared for each particle type (chapters 6.2.1, 6.2.2 and 6.2.3).

6.1 Irradiation with different particle types

For comparing the behavior of different silicon materials after irradiation with various particle types while being able to exclude any effects from differences in the initial resistivity, oxygen content or processing, diodes with similar material properties were chosen for irradiation wherever possible. For n-type FZ and MCz material data after proton, neutron and pion irradiation was thus obtained, whereas for all other materials either wafers with different material properties had to be used, as was the case for p-type FZ, or no pion irradiation was performed, making therefore only comparison between 24 GeV/c protons and reactor neutrons possible.

The major part of the measurements was done on n-type FZ, MCz and EPI diodes from HIP and CNM. The material used by the two different companies for each of the different silicon types was the same, leading to similar effective space charge before and after irradiation (compare table 5.1 for the material properties). The sign of the space charge after the minimum of the $|N_{eff}|$ annealing curve and therefore the interpretation of g_c as effective donor or acceptor generation rate can not be deduced from CV measurements alone. It was however determined by TCT measurements as discussed in chapter 8.2.

6.1.1 FZ

Measurements on n-type FZ were limited by an increase in leakage current at relatively low voltages at fluences above 1 x $10^{14} cm^{-2}$. Some CNM and HIP diodes showed this behavior already at around 100 V, but generally the problem occurred at around 300 to 400 V. Fig. 6.1 shows a comparison of CV, IV and CCE curves to illustrate the effect. The diode has not yet fully reached depletion in the CV curve when the current starts to increase. This also leads to an increased noise in the CCE measurements which are performed at low temperature, making the correct determination of the collected charge impossible as can be seen by the spread of data points above 250 V. Similarly TCT measurements are only possible at low voltages. At first glance the CV curve looks undisturbed, but the correct end-capacitance is not reached and the capacitance decreases further with voltage above depletion. It is therefore not clear how reliable the effective space charge obtained from these diodes are.

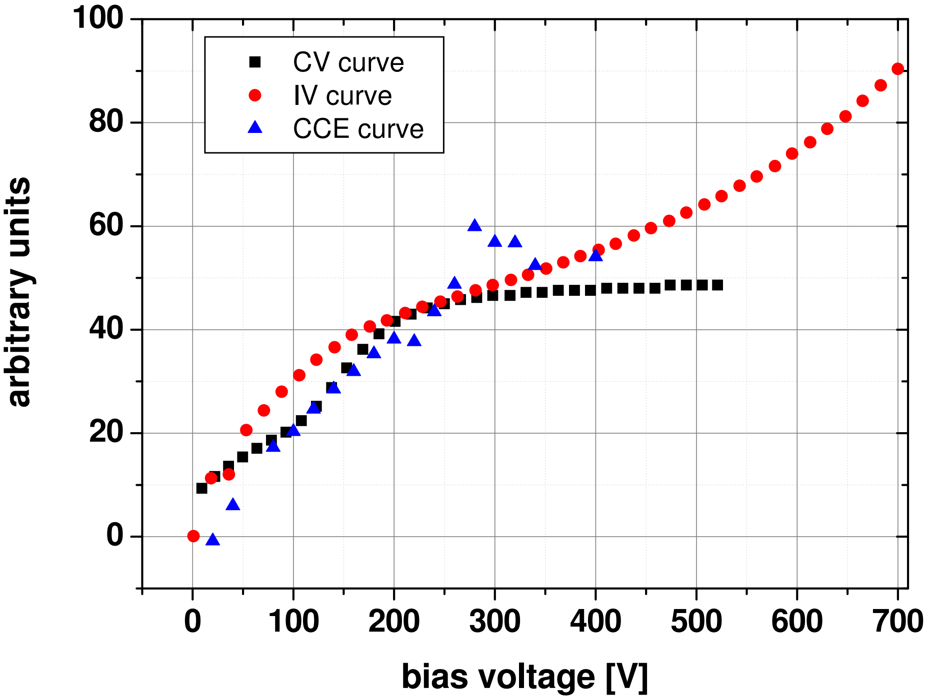

Figure 6.1: Comparison of 1/C, IV and CCE curves for n-type FZ irradiated with a proton fluence of 8.21 x $10^{14} p/cm^2$. The curves were normalized to make a comparison of the curve shape possible. The samples were annealed for 4 min at 80 °C before measurement.

In Fig. 6.2 the effective space charge in n-type FZ after irradiation with protons, neutrons and pions is shown for equivalent fluences below 3.5 x $10^{14} cm^{-2}$, where depletion voltages are still low enough to not be influenced by the increased current. No difference can be seen after proton and pion irradiation. The generation rate, obtained from the proton

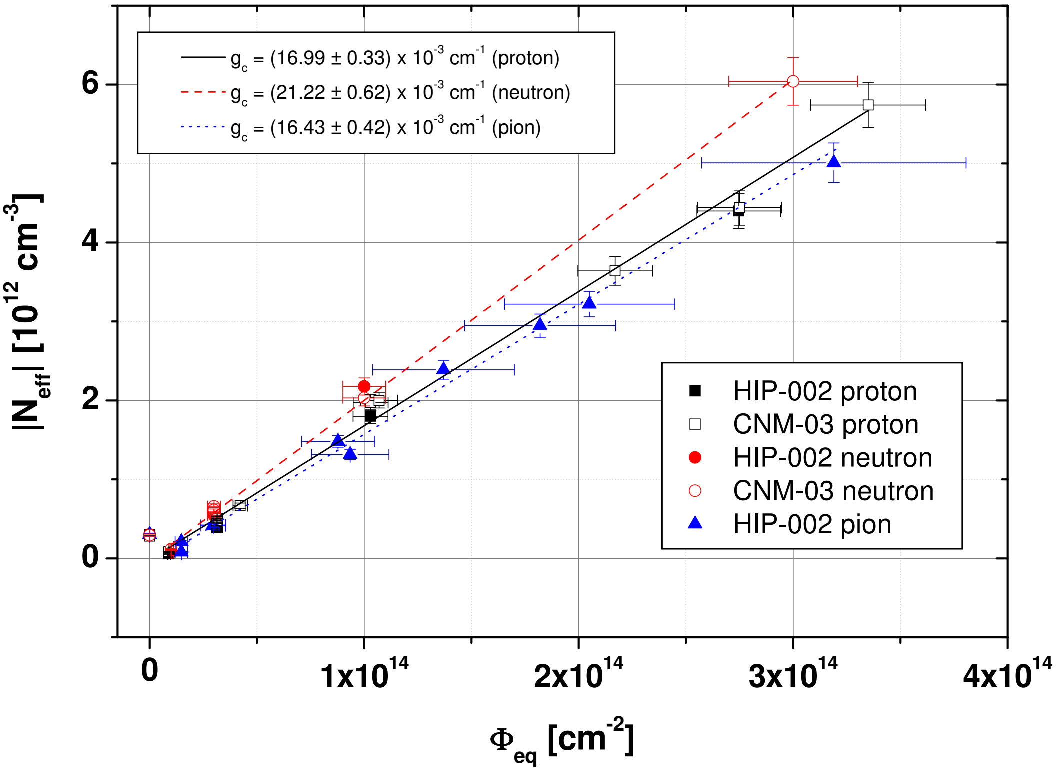

Figure 6.2: Development of the effective space charge in n-type FZ after 24 GeV/c proton, reactor neutron and 200 MeV pion irradiation. The samples were annealed for 4 min at 80 °C before measurement.

irradiated samples, is (16.99 ± 0.33) x $10^{-3}\,cm^{-1}$ whereas $g_c = (16.43 \pm 0.42)$ x $10^{-3}\,cm^{-1}$ for pion irradiated samples. Neutron irradiated samples on the other hand show a faster increase of the effective space charge with fluence ($g_c = (21.22 \pm 0.62)$ x $10^{-3}\,cm^{-1}$).

Two different sets of p-type FZ were irradiated with protons: 400 $k\Omega cm$ FZ diodes processed by CNM and 14 $k\Omega cm$ diodes processed by MICRON. In Fig. 6.3 it can be seen that the effective space charge shows a non-linear behavior at higher fluences. This has already been observed for MICRON diodes from the same production in [Kra10a], where a saturation was seen above 5 x $10^{14}\,p/cm^2$. That this behavior is not due to incorrect fluence determination via aluminum activation becomes obvious when looking at $\Delta I/V$ plotted against the equivalent fluence. The current increases linearly with fluence as expected, with a damage constant α of (4.03 ± 0.08) x $10^{17}\,A/cm$ (Fig. 6.4)[1]. Furthermore diodes made from other materials that were irradiated together with the FZ samples show the expected increase of the effective space charge with fluence. Comparing the depletion voltages obtained from CV, IV and CCE measurement as shown in Fig. 6.5 for p-type FZ, confirms this unexpected fluence dependence. In addition to the standard measurements after annealing of 4 min at 80 °C, the MICRON samples were also measured immediately

---

[1] The fluence obtained from the activation of aluminum foils was used in the fit (compare chapter 5.2) and the hardness factor was taken to be 0.62

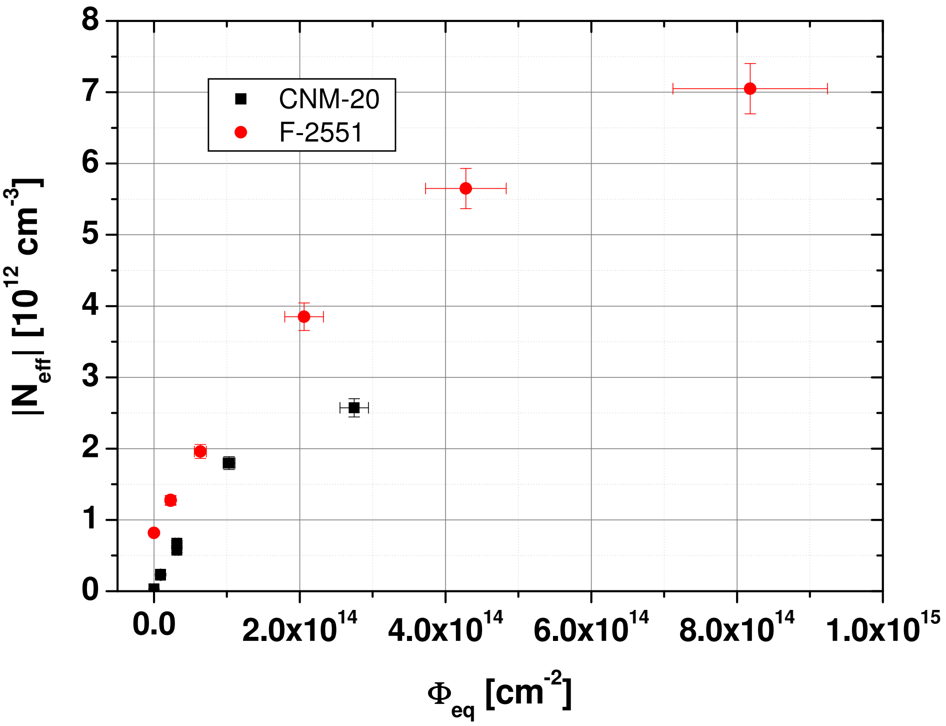

Figure 6.3: Development of the effective space charge in 400 $k\Omega cm$ (CNM) and 14 $k\Omega cm$ (Micron) p-type FZ after irradiation with 24 GeV/c protons measured after 4 min annealing at 80 °C.

after irradiation. As expected for p-type FZ after proton irradiation, the depletion voltage decreases during the so-called beneficial annealing phase (compare chapter 4.4), but, as can be seen in Fig. 6.6, the saturation at higher fluences is present before and after annealing.

In [Kra10a] the same behavior was also seen for n-type FZ at higher fluences. If n-type samples exhibiting a lower end capacitance than expected and an increase in current is visible at voltages close to the expected depletion voltage are included in the plot, a certain saturation becomes obvious also here (Fig. 6.7). It has to be stressed however that in p-type the behavior the leakage current and the end capacitance was as expected and it is therefore not clear if these two observations can be linked.

The effective space charge in both n- and p-type FZ after neutron irradiation shows a clear linear dependence on fluences, after the initial donor removal in n-type (Fig. 6.2 and 6.8). For fitting all 15 $k\Omega cm$ n-type FZ samples by different producers were combined, leading to an effective space charge generation rate g_c of (21.22 ± 0.62) x 10^{-3} cm^{-1} for n-type and (20.32 ± 0.24) x 10^{-3} cm^{-1} for p-type. Introduction rates for both FZ types are therefore the same, as is generally the case after neutron irradiation, where also no difference between 300 μm thick diodes made of different silicon types is found [RD510]

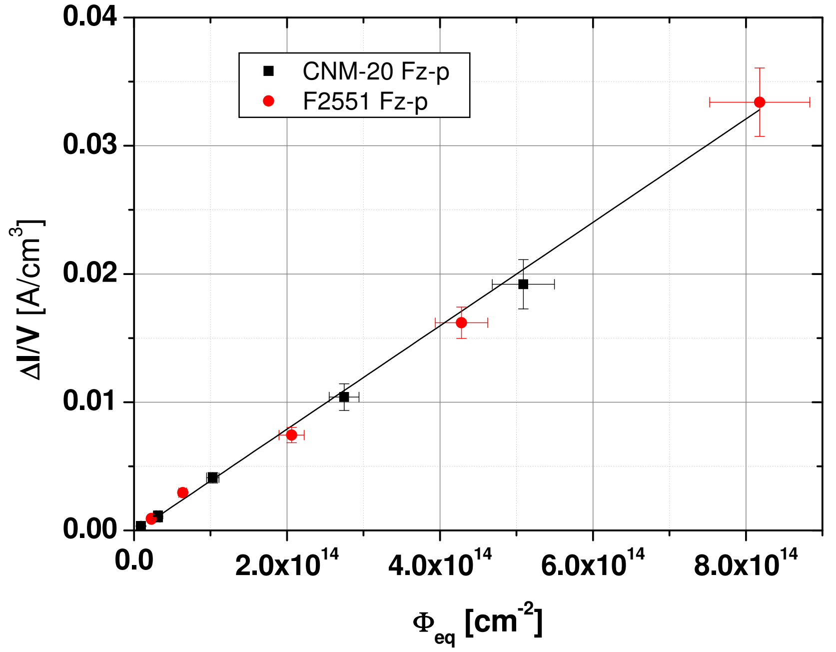

Figure 6.4: Fluence dependence of the reverse current in 400 $k\Omega cm$ (CNM) and 14 $k\Omega cm$ (Micron) p-type FZ after irradiation with 24 GeV/c protons measured after 4 min annealing at 80 °C.

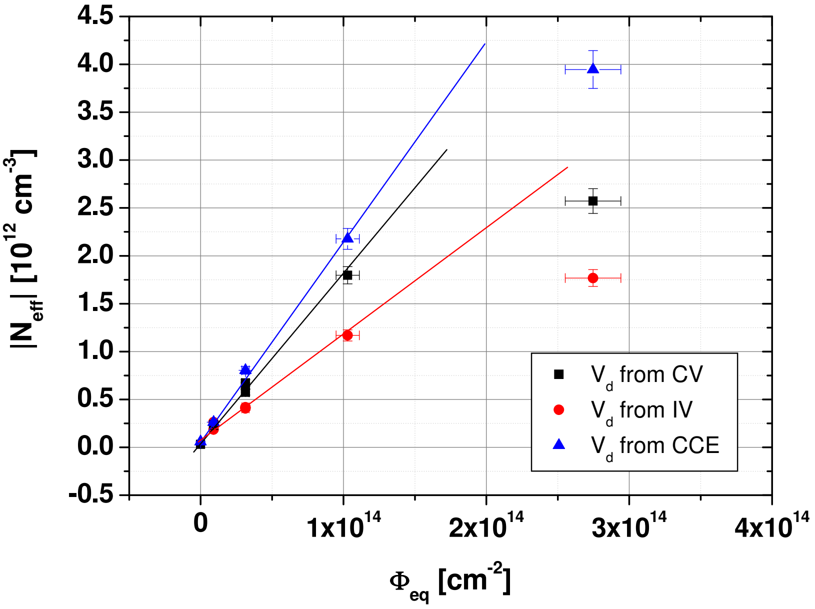

Figure 6.5: Comparison of the effective space charge obtained by CV, IV and CCE measurements for CNM FZ p-type samples irradiated with protons. The samples were annealed for 4 min at 80 °C before measurement.

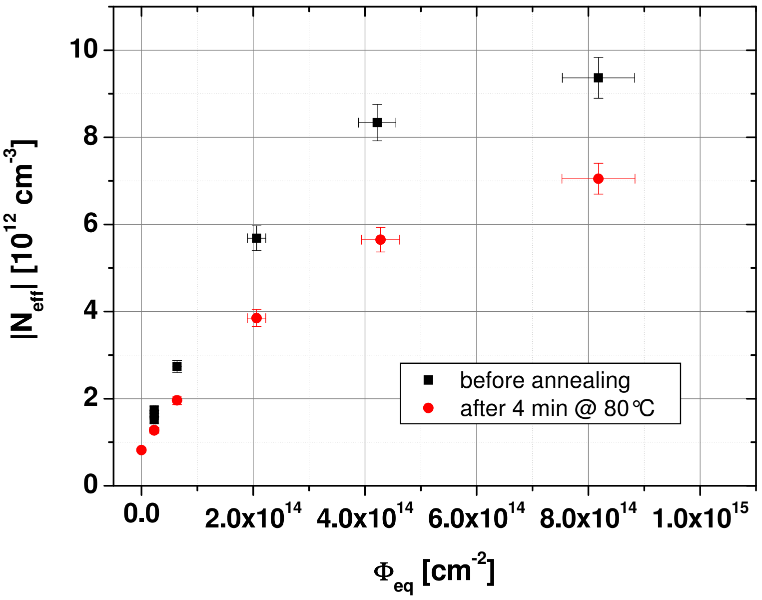

Figure 6.6: Effective space charge in FZ p-type processed by MICRON directly after irradiation with 24 GeV/c protons and after 4 min of annealing at 80 °C.

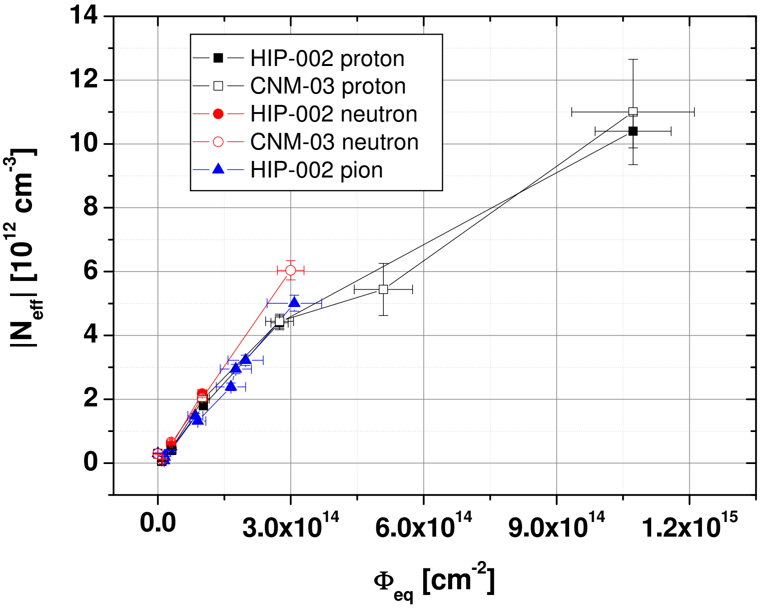

Figure 6.7: Development of the effective space charge with fluence in n-type FZ after 24 GeV/c proton, reactor neutron and 200 MeV pion irradiation measured after 4 min of annealing at 80 °C. The effective space charge in diodes irradiated to fluences higher than 5 x 10^{14} cm^{-2} is shown with a larger error bar due to uncertainties in determining the depletion voltage in samples with increased current (see text).

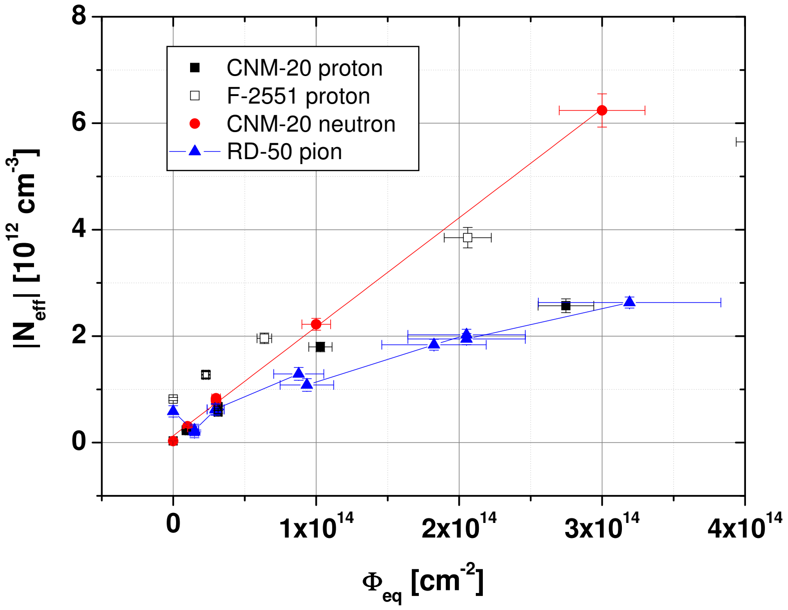

Figure 6.8: Development of the effective space charge with fluence in 400 $k\Omega cm$ and 14 $k\Omega cm$ p-type FZ after 24 GeV/c proton irradiation, 400 $k\Omega cm$ FZ p-type after irradiation with reactor neutrons and 22 $k\Omega cm$ p-type FZ after 200 MeV pion irradiation. All samples were measured after 4 min annealing at 80 °C.

(see also chapter 6.2).

For the pion irradiated FZ samples it was not possible to determine whether saturation occurs due to the low irradiation fluences. Previous measurements however showed a linear dependence of the effective space charge on fluence up to 9 x $10^{14}\pi/cm^2$ [Kra10a] [Pac10b]. The generation rate for n-type FZ of (16.43 ± 0.42) x 10^{-3} cm^{-1} agrees well with values found in [Kra10a]. The FZ p-type samples used had a higher oxygen content than standard FZ, which is reflected in the lower generation rate of (6.53 ± 0.22) x 10^{-3} cm^{-1} that is also lower than the generation rate found for DOFZ-p after proton irradiation [Cin07]. Acceptor removal is visible in DOFZ after pion irradiation, for proton irradiation no definite conclusion can be given due to the fluence range used in [Cin07], where the lowest irradiation fluence of about 5 x 10^{13} cm^{-2} is already too high to see the removal.

6.1.2 MCz

As can be seen in Figs. 6.9 and 6.10 n-type MCz diodes from different producers with a resistivity between 0.8 and 1.1 $k\Omega cm$ (compare also table 5.1) showed similar enough behavior to be able to combine the high fluence data points for obtaining the generation rate. The two p-type MCz wafers with a resistivity of 1.3 $k\Omega cm$ and 7.5 $k\Omega cm$ could equally be combined for determining g_c (compare Fig. 6.11).

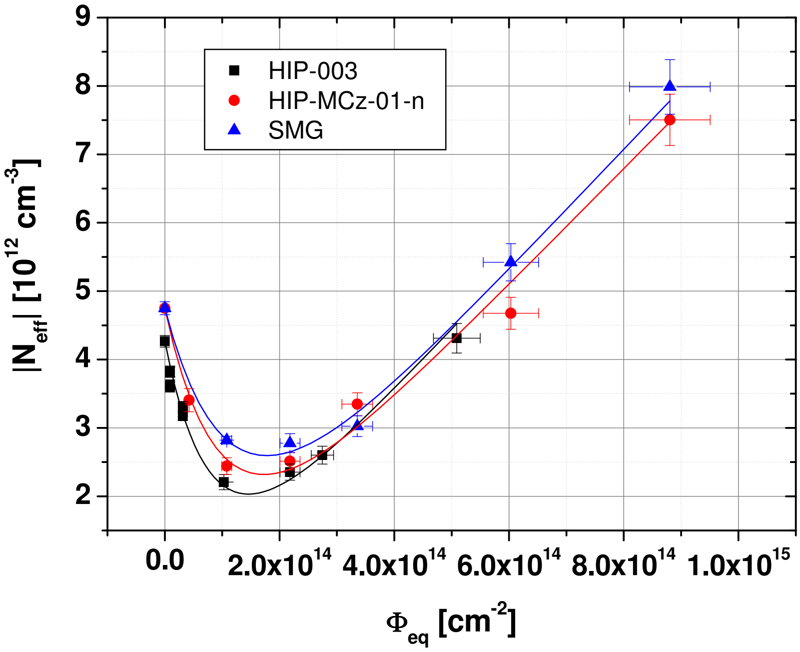

Figure 6.9: Comparison of the development of the effective space charge with fluence in n-type MCz diodes from different producers, but from the same wafer material, irradiated with 24 GeV/c protons. All samples were annealed for 4 min at 80°C before measurement.

The development of the effective space charge in MCz p-type after proton and neutron irradiation is shown in Fig. 6.12. The introduction rates are $|7.42 \pm 0.35|$ x $10^{-3}\,cm^{-1}$ and (22.04 ± 0.57) x $10^{-3}\,cm^{-1}$ respectively[2]. Here a direct comparison between samples processed by the same company from the same wafer material can be made. Strong acceptor removal is obvious after proton irradiation but not after neutron irradiation. For MICRON samples with a resistivity of 1.3 $k\Omega cm$, where the minimum of the effective space charge is reached at 2 x $10^{14}\,cm^{-1}$, a removal constant of (1.35 ± 0.03) x $10^{-14}\,cm^{-2}$ was obtained from the fit.

The generation rates of n-type MCz after neutron irradiation is (22.21 ± 1.1) x $10^{-3}\,cm^{-1}$ compared to $|8.55 \pm 0.35|$ x $10^{-3}\,cm^{-1}$ after proton irradiation. As shown in Fig. 6.13

---

[2] Since the sign of g_c in MCz after proton and pion irradiation is a matter of debate, only absolute values will be given throughout this work. Compare also chapter 8.2

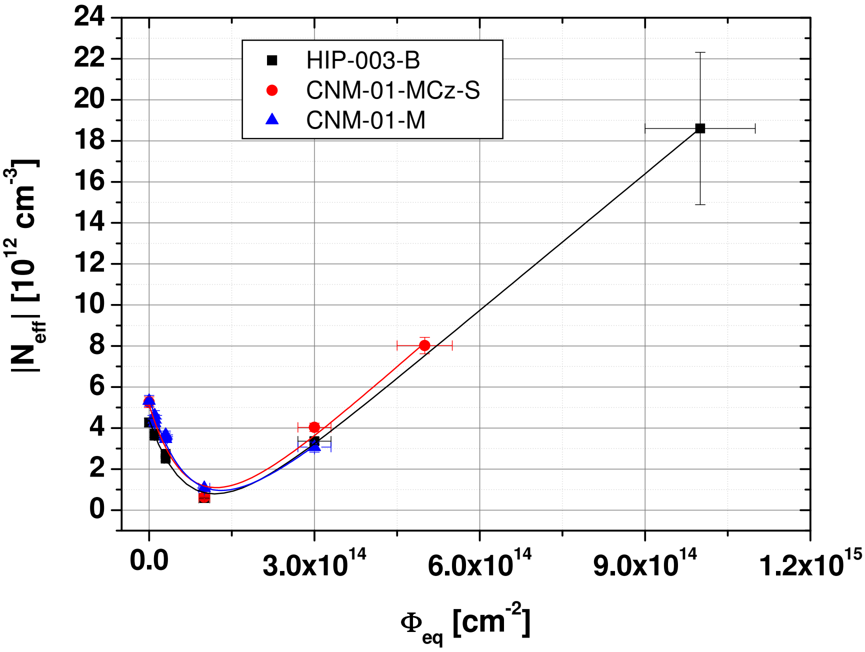

Figure 6.10: Comparison of the development of the effective space charge with fluence in n-type MCz diodes from different producers, but from the same wafer material, irradiated with reactor neutrons. All samples were annealed for 4 *min* at 80 °C before measurement.

the increase of N_{eff} with fluence is very similar in n- and p-type MCz.

Due to the limited fluence range the generation rate after pion irradiation can not clearly be determined since the donor removal phase is barely finished in MCz n-type at the highest irradiation fluence. The g_c value of |4.81 ± 1.45| x $10^{-3}\,cm^{-1}$ obtained from the available data seems however to be lower than what was seen after proton irradiation, which was also observed in [Kra10a]. For a comparison of the effect of these three particle types on n-type MCz see also Fig. 6.14.

For neutron irradiated samples g_c for MCz n- and p-type on the other hand is very similar to that of both FZ types. This agrees with most MCz data apart from results found in diodes produced by MICRON , where the introduction rate was 8 x $10^{-3}\,cm^{-1}$ [Kra10a] [Kra07]. Diodes from this company were used only for proton irradiation in this work, where no difference was seen to those produced by CNM or HIP. After both neutron and proton irradiation donor removal is visible with removal constants of (0.92 ± 0.08) x $10^{-14}\,cm^{-2}$ and (1.20 ± 0.04) x $10^{-14}\,cm^{-2}$ after proton irradiation for diodes from HIP and Smart respectively and (1.28 ± 0.12) x $10^{-14}\,cm^{-2}$ after neutron irradiation.

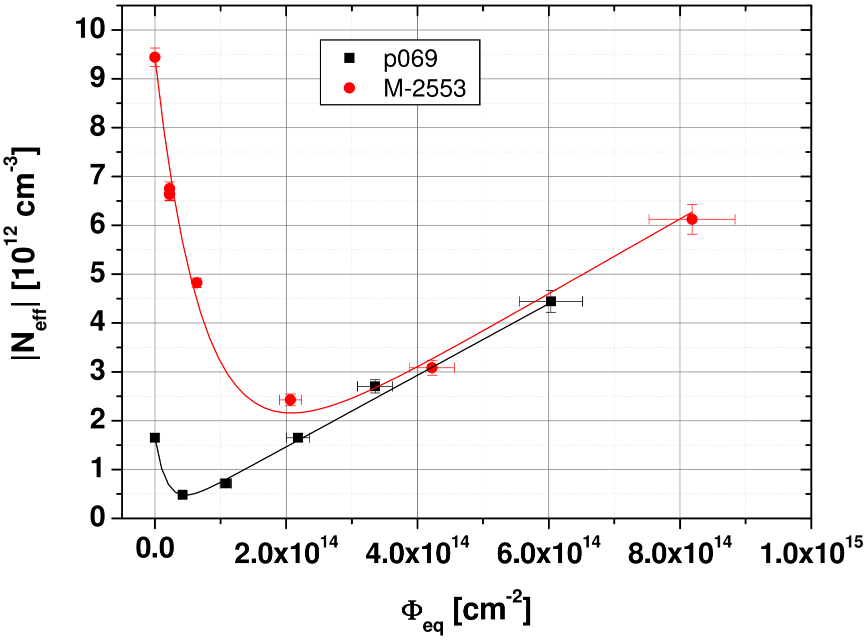

Figure 6.11: Comparison of the development of the effective space charge with fluence in p-type MCz diodes with different resistivity after irradiation with 24 GeV/c protons. All samples were annealed for 4 *min* at 80 °C before measurement.

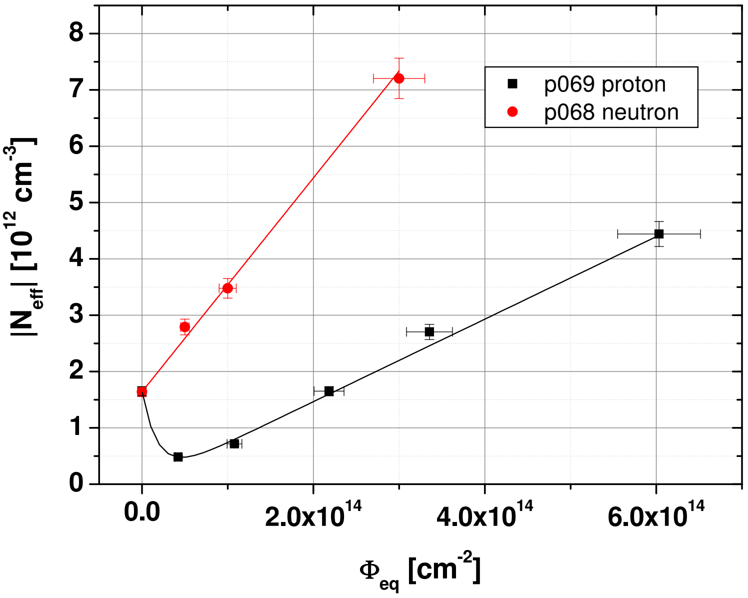

Figure 6.12: Development of the effective space charge with fluence in p-type MCz irradiated with 24 GeV/c protons and reactor neutrons. All samples were annealed for 4 *min* at 80 °C before measurement.

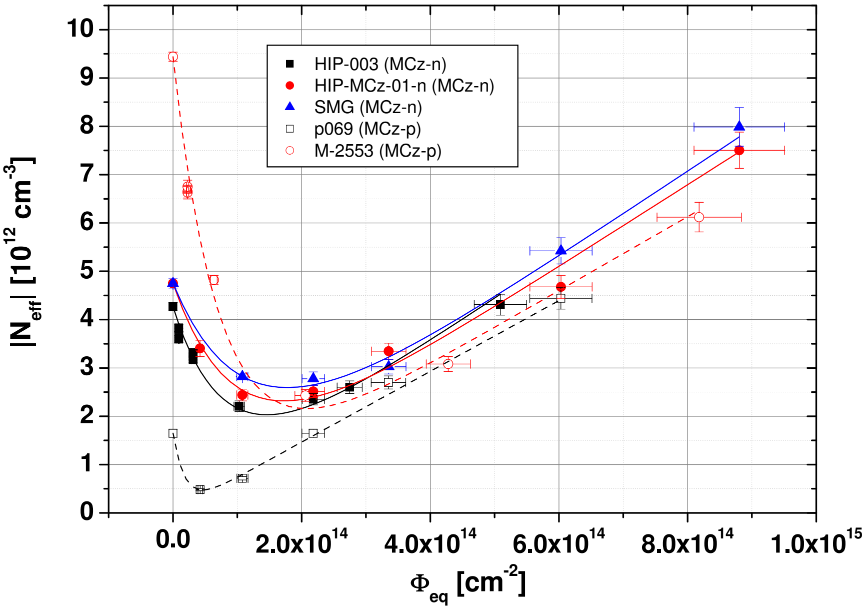

Figure 6.13: Comparison of the development of the effective space charge with fluence in n-type and p-type MCz diodes after irradiation with 24 *GeV/c* protons. All samples were annealed for 4 *min* at 80 °C before measurement.

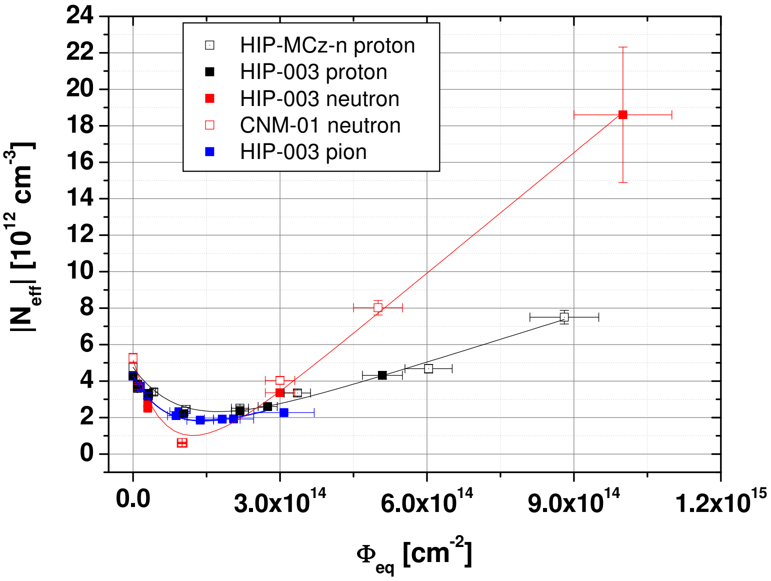

Figure 6.14: Development of the effective space charge with fluence in n-type MCz irradiated with 24 *GeV/c* protons, reactor neutrons and pions. All samples were annealed for 4 *min* at 80 °C before measurement.

6.1.3 EPI

Epitaxial silicon is produced by growing a silicon layer on a Cz substrate (compare chapter 3.4). The layer thicknesses investigated so far ranged between 25 and 150 μm for n-type EPI, whereas for p-type EPI mainly 150 μm samples were available.

Here 150 μm n- and p-type EPI samples irradiated with 24 GeV/c protons and reactor neutrons are compared to determine the influence of different particle types [3]. In addition 50 and 75 μm p-type EPI diodes were irradiated with protons to see if the development of the effective space charge with fluence was influenced by the layer thickness, as had been suggested for n-type material.

150 μm n- and p-type EPI

EPI n-type samples from CNM and HIP were combined for fitting as no difference in their response was seen. For p-type only one set of samples per particle type and thickness was available. Due to the smaller detector volume and therefore total current of EPI samples the fluence range extends to higher proton and neutron fluences of 2.99 x 10^{15} p/cm^2 and 3 x 10^{15} n/cm^2 respectively. As a sharp drop in charge collection efficiency was seen in n-type material after proton and neutron irradiation even at low fluences, additional samples irradiated with fluences below 1 x 10^{13} cm^{-2} were added (compare also chapter 7.1.3).

In all EPI samples the effective space charge decreased up to a fluence of (1-2) x $10^{14}\,cm^{-2}$ before showing an linear increase. The generation rate in p-type EPI after both proton and neutron irradiation is about 2/3 of that of n-type. At the highest available neutron fluence p- and n-type material show the same effective space charge, which was also observed by [Kho08a].

	$c\,[10^{-14}cm^{-2}]$	$g_c\,[10^{-3}cm^{-1}]$
neutron irradiated		
n-type	1.29 ± 0.09	$(+)5.8 \pm 0.2$
p-type	2.73 ± 0.51	$(+)3.7 \pm 0.2$
proton irradiated		
n-type	0.79 ± 0.02	$(-)15.6 \pm 0.2$
p-type	5.5 ± 0.04	$(-)10.5 \pm 0.5$

Table 6.1: Fit parameters for $|N_{eff}|$ as a function of fluence in n- and p-type 150 μm EPI irradiated with 24 GeV/c protons and reactor neutrons. The sign of the generation rate was determined from TCT measurements (see chapter 8.2.3). The samples were annealed for 4 min at 80 °C before measurement.

As can be seen in Fig. 6.15 and Fig. 6.16 absolute generation rates for 150 μm EPI

---

[3] These result were already published in [Kas10]

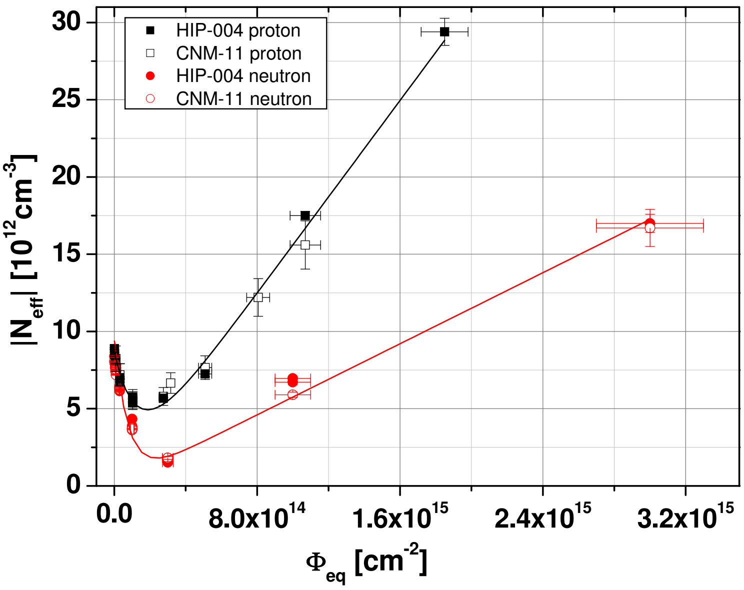

Figure 6.15: Development of the effective space charge with fluence in 150 μm EPI n-type after irradiation with 24 GeV/c protons and reactor neutrons, measured after 4 min of annealing at 80 °C.

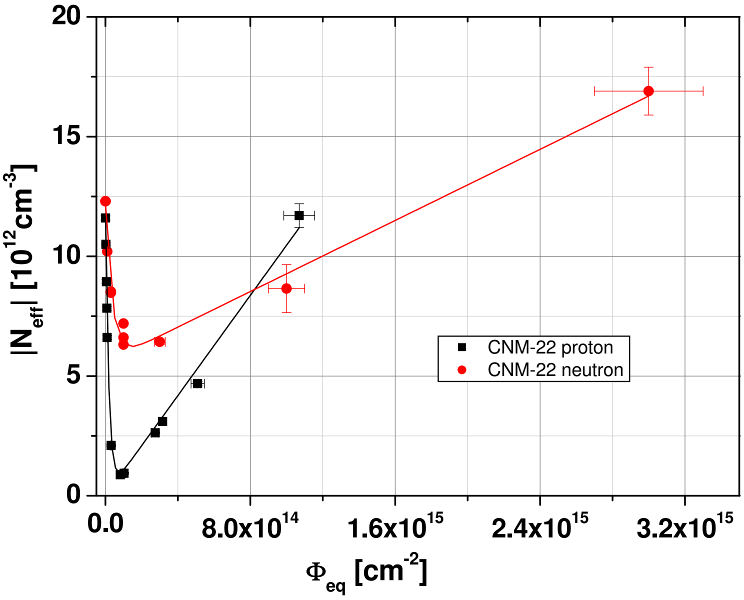

Figure 6.16: Development of the effective space charge with fluence in 150 μm EPI p-type after irradiation with 24 GeV/c protons and reactor neutrons, measured after 4 min of annealing at 80 °C.

samples are lower after neutron than after proton irradiation, where g_c is (-15.6 ± 0.2) x 10^{-3} cm^{-1} for n-type and (-10.5 ± 0.5) x 10^{-3} cm^{-1} for p-type. The values found after neutron irradiation, (5.8 ± 0.2) x 10^{-3} cm^{-1} for n-type and (3.7 ± 0.2) x 10^{-3} cm^{-1} for p-type, fit well to data from previous works [Kho08a] [Cre07]. All fitting parameters are summarized in Tab. 6.1 and all data from other publications can be found in Tabs. 6.3 and 6.4).

For 150 μm n-type EPI the generation rates after proton irradiation obtained by different groups varies between (7 - 24) x 10^{-3} cm^{-1} and are claimed to be similar to those after neutron irradiation in [Kho08a], where the CV data was taken after 8 minutes of annealing at 80 °C at 5 °C and 10 kHz and then scaled to 20 °C, compared to 10 kHz at 20 °C after 4 minutes of annealing at 80 °C in this work. Similar low values for g_c in n-type EPI after proton irradiation were however also found in [Lan08] where all samples were measured at 20 °C after 8 minutes at 80 °C. Therefore the difference in results cannot be explained by difficulties in temperature scaling for CV measurements. Looking at the annealing curves for 150 μm n- and p-type provided in [Kho08a], it seems unlikely that the difference in annealing - 4 vs. 8 min at 80 °C - could explain the lower values: at the relevant fluence and time range the annealing curve is nearly flat. Both of the above mentioned works however used diodes produced by CiS [CiS] while here and in [Hoe07] samples from CNM and HIP were measured. The latter study also included diodes from ITC-IRSTW [ITC] irradiated with protons, which showed a somewhat lower generation rate of g_c = -12.5 x 10^{-3} cm^{-1} than those of the other companies.

The differences in results obtained from diodes from different producers is likely due to out-diffusion of O_{2i} from the Cz substrate layer during the thermal treatment in the processing [RD510]. O_{2i} is believed to be the precursor of shallow bistable donors [Fre06] that are responsible for part of the observed generation rate in EPI [Pin05]. Different concentrations of O_{2i} in the diodes due to different thermal treatment could therefore explain the differences found between diodes from CiS and CNM/HIP. It has to be noted however that even though important steps towards the correlating of macroscopic and microscopic changes in silicon after hadron irradiation have recently been made [Pin09], still not all defects responsible have been fully identified. Further comparative measurements between the different diodes are therefore necessary to confirm this theory.

Dependence on EPI layer thickness

The major question in epitaxial silicon devices is whether and how the generation rate depends on the layer thickness. For n-type after proton irradiation two studies with EPI layer thicknesses of 25, 50 and 75 μm [Lin06b] and 75, 100 and 150 μm [Lan08] were performed on diodes obtained from CiS (all data is summarized in Tabs. 6.3 and 6.4). The generation rate was found to decrease significantly with increasing layer thickness in [Lin06b]. This behavior could not be explained by the different oxygen concentration depth profiles in the samples and although some defects were identified that could lie behind this phenomenon [Pin06] many questions remained open. Contrary to most other

CV data, all diodes had to be measured at 100 kHz due to problems with 75 μm diodes at 10 kHz [Lin06b].

To determine whether in 150 μm n-type epitaxial silicon the frequency of the CV measurement has an effect on the value of g_c, a set of 5 x 5 mm^2 CNM samples were measured at 100 and 10 kHz. After both proton and neutron irradiation the generation rate at 100 kHz is lower than at 10 kHz (compare Figs. 6.17 and 6.18 and Tab. 6.2). Examples of CV curves measured at 10 and 100 kHz at equivalent fluences of about 1 x $10^{13}\,cm^{-2}$ and 1 x 10^{15} cm^{-2} are given in Figs. 6.19 and 6.20.

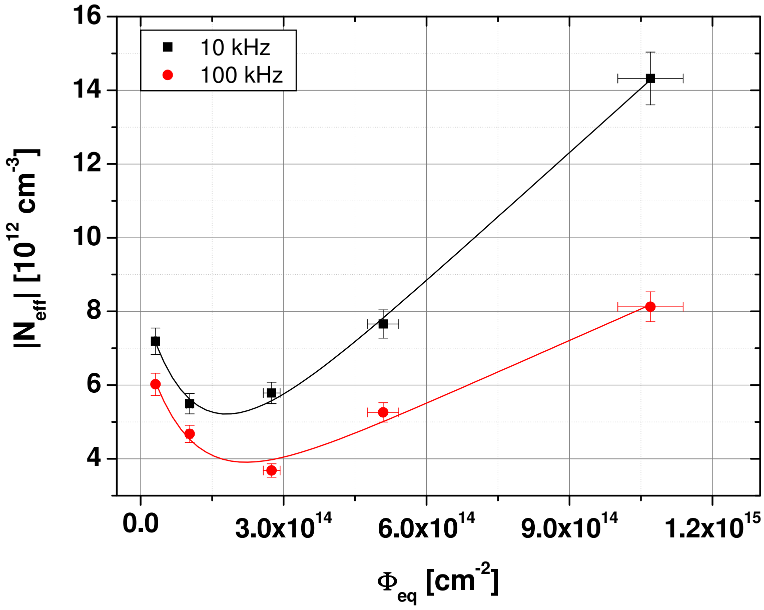

Figure 6.17: Development of the effective space charge in 150 μm EPI obtained from CV measurements at 10 and 100 kHz after irradiation with 24 GeV/c protons. All samples were annealed for 4 min at 80 °C before measurement.

parameter	10 kHz	100 kHz
proton irrad.		
c $[10^{-14}\,cm^{-2}]$	0.91 ± 0.3	1.00 ± 0.43
g_c $[10^{-3}\,cm^{-1}]$	-11.64 ± 0.93	-5.71 ± 0.87
neutron irrad.		
c $[10^{-14}\,cm^{-2}]$	1.21 ± 0.32	1.23 ± 0.30
g_c $[10^{-3}\,cm^{-1}]$	5.43 ± 0.28	3.99 ± 0.2

Table 6.2: Effective generation rates g_c and removal constants c obtained from CV measurements at 10 and 100 kHz for n-type EPI diodes processed by CNM after irradiation with 24 GeV/c protons and reactor neutrons. All samples were annealed for 4 min at 80 °C before measurement.

From this it becomes clear that a direct comparison between g_c values found at different

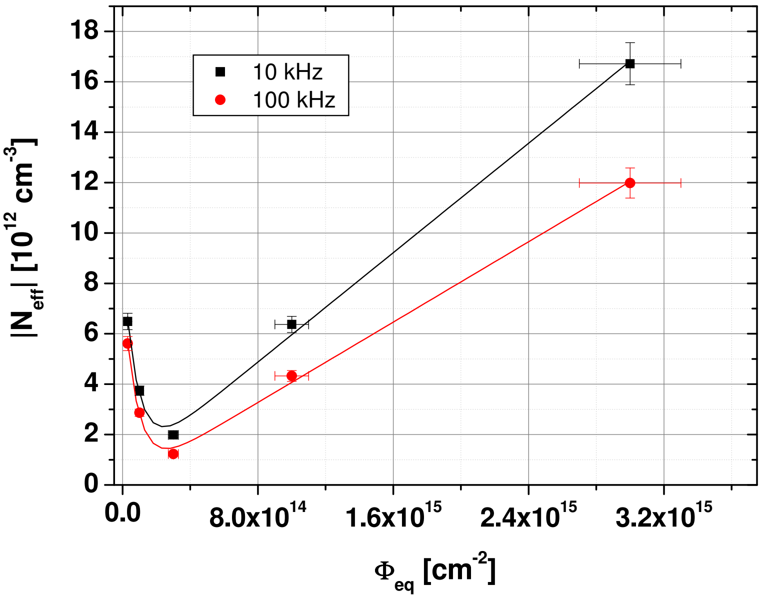

Figure 6.18: Development of the effective space charge in 150 μm EPI obtained from CV measurements at 10 and 100 kHz after irradiation with reactor neutrons. All samples were annealed for 4 *min* at 80 °C before measurement.

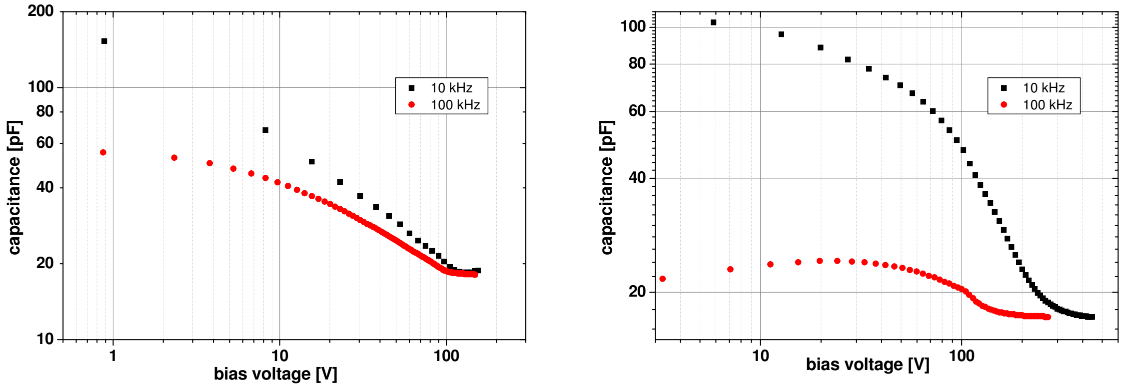

(a) (b)

Figure 6.19: CV curves at 10 kHz and 100 kHz measured in n-type EPI irradiated with a 24 GeV/c proton fluence of (a) 1.46 x 10^{13} p/cm^2 and (b) 1.73 x 10^{15} p/cm^2

.

frequencies is not possible. This could also explain why for 75 μm samples, where the two studies on the layer thickness dependence of g_c overlap, the value obtained in [Lan08] on diodes from the same producer is nearly seven times as high. For 50 μm EPI n-type another study also seems to indicate higher values for g_c ([Kra05], Fig. 1) than what is shown in [Lin06b] Fig. 4, but close to Fig. 6 in the same paper. It can be assumed that the different values for 50 μm in [Lin06b] are due to a change in the measurement

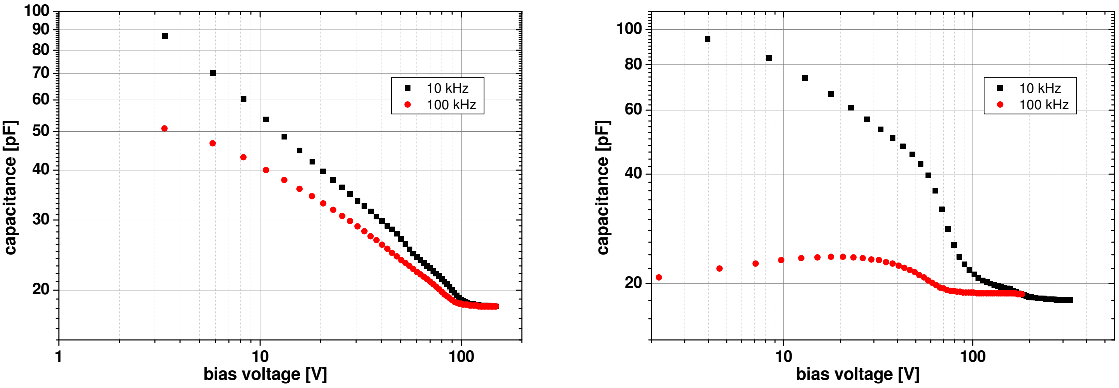

(a) (b)

Figure 6.20: CV curves at 10 kHz and 100 kHz measured in n-type EPI irradiated with a reactor neutron fluence of (a) 1 x 10^{13} n/cm^2 and (b) 1 x 10^{15} n/cm^2

.

frequencies even though this difference in procedure is not mentioned in the text. Since the ratio between the generation rates at the 10 and 100 kHz does not seem to be the same for 50, 75 and 150 μm n-type EPI samples, it is difficult to draw conclusions for the development of radiation hardness with layer thickness when using the standard measurement procedure at 10 kHz. In [Lan08] on the other hand, no clear dependence of the generation rate on thickness is found. There is a drop going from 75 μm to 100 μm, but 150 μm samples shows practically the same behavior as 100 μm ones and the generation rate of -7 x 10^{-3} cm^{-1} is close to that found for 50 μm thick samples at 100 kHz.

For p-type samples less comparison data is available and no previous study on the development of g_c with thickness was done. For 150 μm diodes the values found here are higher than what was reported in [Kho08a] for CiS diodes after proton irradiation, but compatible after neutron irradiation. This is similar to what was seen in n-type.

In addition to the 150 μm diodes from HIP and CNM, a set of p-type EPI samples with layer thicknesses of 50 and 75 μm produced by CiS was irradiated with proton fluences between 1.32 x 10^{13} p/cm^2 and 2.88 x 10^{15} p/cm^2. The generation rates for both sample types, (-15.8 ± 0.4) x 10^{-3} cm^{-1} and (-15.1 ± 0.4) x 10^{-3} cm^{-1} for 75 and 50 μm respectively, are the same and higher than those in the thickest sample type, where g_c = (-10.5 ± 0.5) x 10^{-3} cm^{-1} (compare Fig. 6.21). This might however be due to different thermal treatment by the different producers.

No clear dependence of the generation rate on the layer thickness can be seen seen here and overall the variation of the generation rate in p-type seems to be lower than in n-type.

Comparing p-type to n-type of the same thickness shows only small differences in 75 μm samples, where g_c = -15.2 x 10^{-3} cm^{-1} in n-type diodes from the same company [Lan08] measured at 10 kHz. For 50 μm n-type EPI samples results obtained at 10 kHz vary

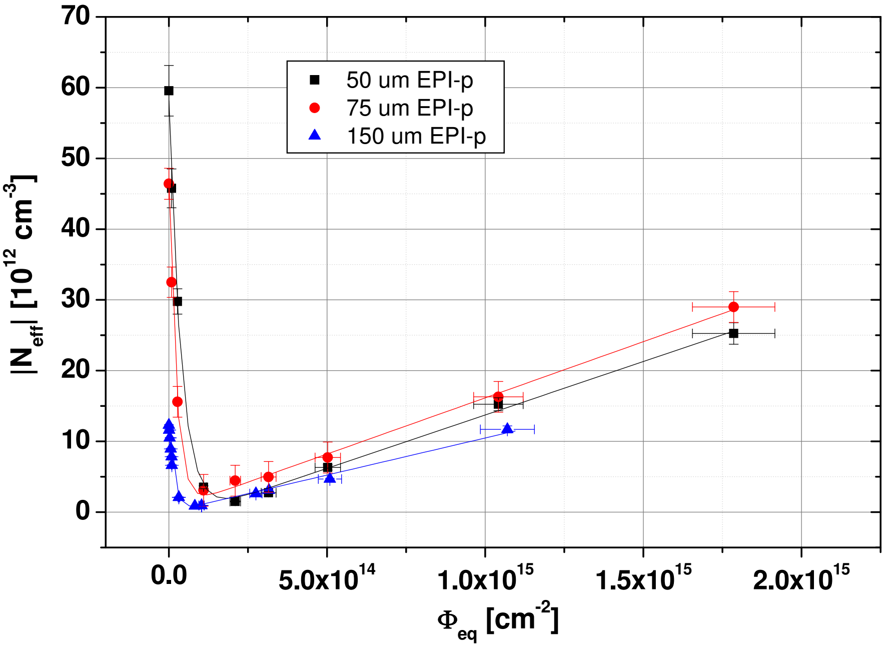

Figure 6.21: Development of the effective space charge in 150, 75 and 50 μm EPI p-type irradiated with 24 GeV/c protons after 4 min of annealing at 80 °C.

between -13.2 and -20 x $10^{-3}\, cm^{-1}$ (compare Tab. 6.4), which again is roughly similar to what was measured in p-type.

material	thickness [μm]	g_c [$10^{-3} cm^{-1}$]	space charge	reference
EPI	50	5	pos.	[Lin06b]
EPI	50	8	-	[Kho08b]
EPI	72	6	neg	[Fre07]
EPI	150	5.8	neg	this work
EPI	150	4.2	neg.	[Kho08a]
EPI	150	4.1	-	[Cre07]

Table 6.3: Effective space charge generation rate g_c for n-type EPI silicon sensors after irradiation with reactor neutrons. Samples in [Lin06b], [Cre07] and [Kho08b] were measured after 8 min annealing at 80 °C. Results from [Lin06b] were measured at 100 kHz. The space charge was either determined by TCT measurements or annealing studies with CV measurements.

material	thickness $[\mu m]$	g_c $[10^{-3} cm^{-1}]$	reference
EPI	25	19	[Lin06b]
EPI	25	38	[Lin06a]
EPI	50	7.8	[Lin06b]
EPI	50	15	[Lin06a]
EPI	50	20	[Kho08b]
EPI	50	13.2	[Kho06]
EPI-DO	75	20.8	[Lan08]
EPI	75	2.3	[Lin06b]
EPI	75	15.2	[Lan08]
EPI-DO	100	11.3	[Lan08]
EPI	100	7	[Lan08]
EPI-DO	150	13.6	[Lan08]
EPI	150	15.6	this work
EPI	150	19-24	[Hoe07]
EPI	150	7.5	[Kho08a]
EPI	150	7	[Lan08]

Table 6.4: Effective space charge generation rate g_c for n-type EPI and oxygen enriched EPI (EPI-DO [Fre07]) after irradiation with 24 GeV/c protons. Samples in [Hoe07] were measured after 4 min annealing at 80 °C, samples in [Lin06b], [Kho08b], [Kho06] and [Lan08] at the end of the beneficial annealing (8-10 min at 80 °C). Results from [Lin06b] were measured at 100 kHz. The space charge is positive in all samples.

6.2 Material comparison

The ultimate goal of the RD50 collaboration is to find radiation hard material that can withstand the expected fluences in the LHC luminosity upgrade. In this chapter the effective generation rates of all types of silicon investigated in this work will therefore be compared. All values of g_c obtained on FZ, MCz and EPI after proton, neutron and pion irradiation are collected in Tab. 6.5.

6.2.1 Proton irradiation

Fig. 6.22 shows the development of the effective space charge in all materials measured after irradiation with 24 GeV/c protons. The standard material used in the LHC is FZ, which is therefore a reference for all other materials. Due to increased currents in FZ n-type samples as discussed in chapter 6.1.1, the generation rate could only be determined up to a fluence of 3.5 x 10^{14} cm^{-2}. FZ p-type samples on the other hand showed an unexpected saturation at higher proton fluences, which made it impossible to determine g_c. Values found for FZ in other studies varied consideribly, with g_c between (10 - 20) x 10^{-3} cm^{-1} [RD510]. With a value of 16.99 x 10^{-3} cm^{-1} the generation rate observed for FZ n-type here lies well within this range.

Oxygen was found to have a positive effect on the radiation hardness of silicon [Fre05]. MCz silicon, with oxygen concentrations of several 10^{17} cm^{-3}, is therefore expected to show a lower generation rate. The exact values of g_c found so far however varies again strongly between $|4|$-$|10.1|$ x 10^{-3} cm^{-1} for n-type and $|7|$-$|10|$ x 10^{-3} cm^{-1} for p-type [RD510], [Kra10a]. The values obtained here, $|8.5|$ x 10^{-3} cm^{-1} and $|7.4|$ x 10^{-3} cm^{-1} for n- and p-type respectively, agree with previous results.

Compared to this, the effective space charge in 150 μm epitaxial silicon shows a significantly worse development with fluence for both n- and p-type. With generations rates of 15 x 10^{-3} cm^{-1} and 10 x 10^{-3} cm^{-1} respectively, it is similar to FZ. Also thinner 75 and 50 μm EPI p-type lies within this range with g_c = 15 x 10^{-3} cm^{-1}.

6.2.2 Neutron irradiation

Fig. 6.23 gives an overview over the development of the effective space charge with neutron fluence for all measured samples. It is obvious that EPI is more radiation hard than FZ and MCz. This agrees well with previous results, where no material dependence was found in 300 μm diodes (apart from one type of MCz by MICRON, as mentioned in chapter 6.1.2) and g_c was about 20 x 10^{-3} cm^{-1} [RD510]. Thinner samples with lower resistivity however showed less increase in space charge with fluence for all measured materials and thicknesses [Fre10].

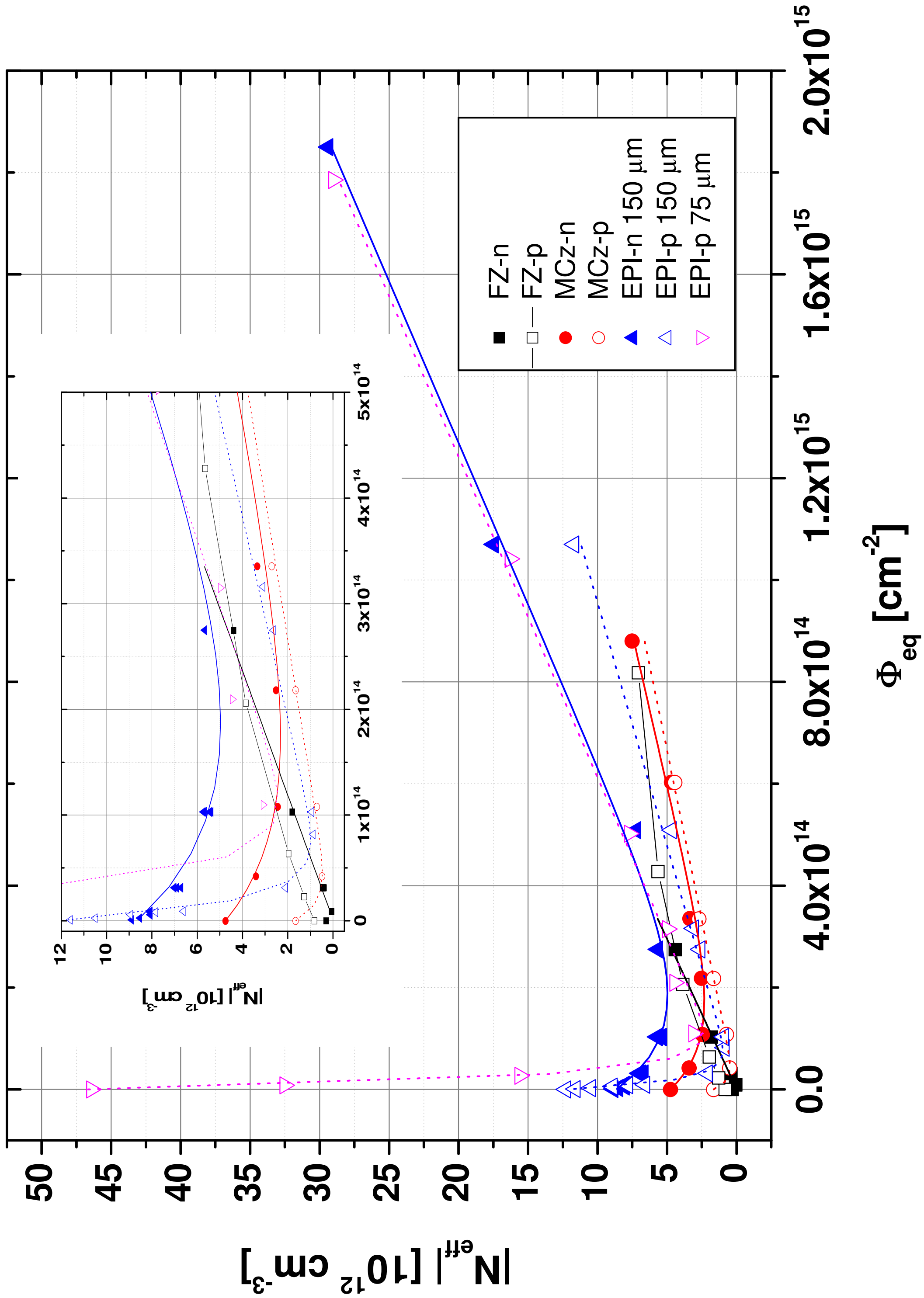

Figure 6.22: Development of the effective space charge with fluence in n- and p-type FZ, MCz and 150 μm EPI and 75 μm p-type EPI after irradiation with 24 GeV/c protons. No error bars are added for better visibility. The fluence error is about 8 %, the error of the effective space charge about 5 %. All samples were annealed for 4 min at 80 °C before measurement.

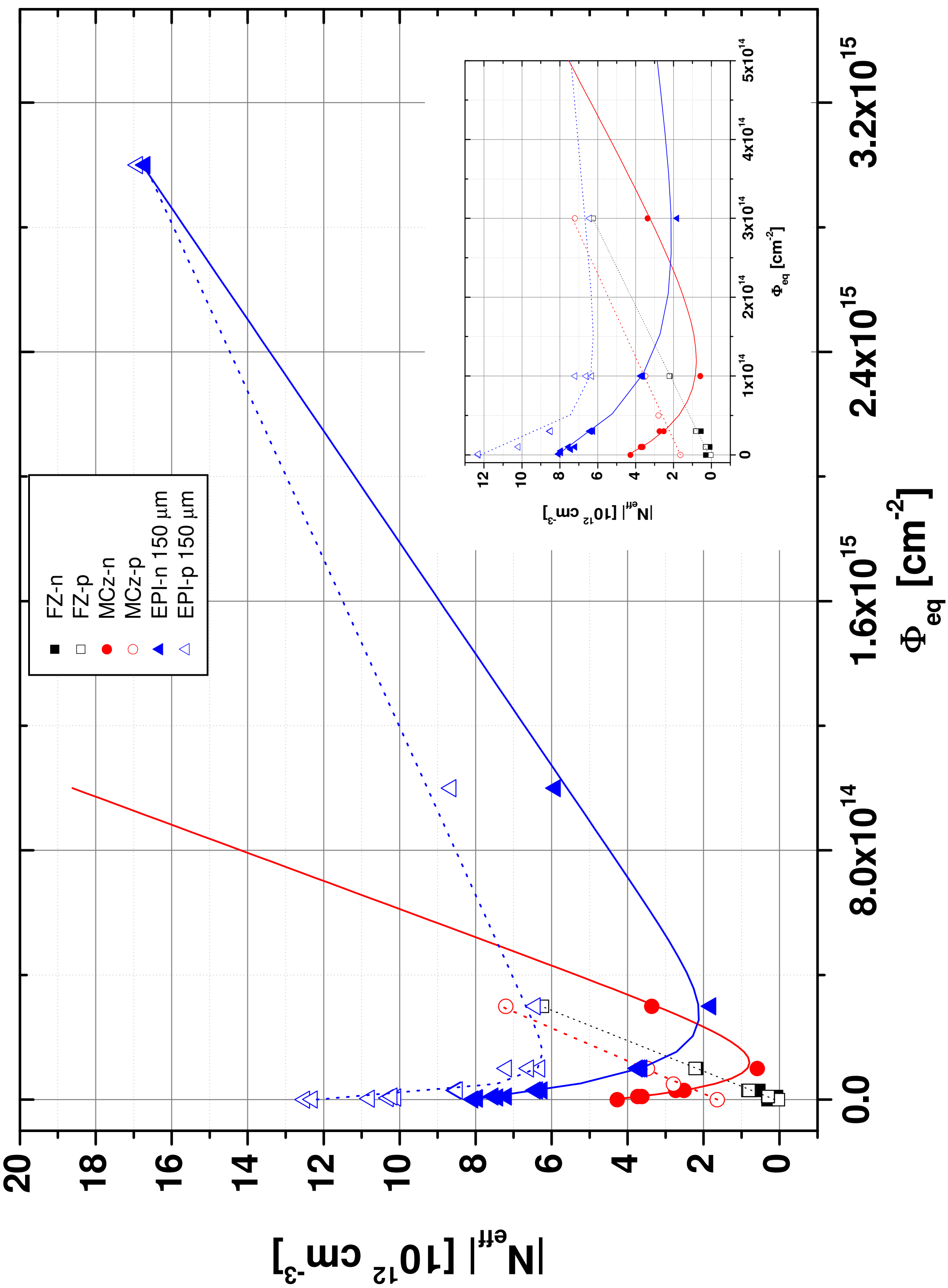

Figure 6.23: Development of the effective space charge with fluence in n- and p-type FZ, MCz and 150 μm EPI after irradiation with reactor neutrons. No error bars are added for better visibility. The fluence error is about 10 %, the error of the effective space charge about 5 %. All samples were annealed for 4 min at 80 °C before measurement.

6.2.3 Pion irradiation

Only MCz and FZ n-type and DOFZ p-type were irradiated with pions (Fig. 6.24). MCz and DOFZ show a similar increase of the effective space charge with fluence in this fluence range, but since not enough data points are available after the initial donor removal in MCz, no definite conclusion can be given. It can be clearly seen though that the generation rate in n-type standard FZ is higher than in both other materials with $g_c = 16 \text{ x } 10^{-3} cm^{-1}$ compared to g_c= 6.5 x 10^{-3} cm^{-1} for DOFZ-p and g_c= |4.8| x 10^{-3} cm^{-1} for MCz-n.

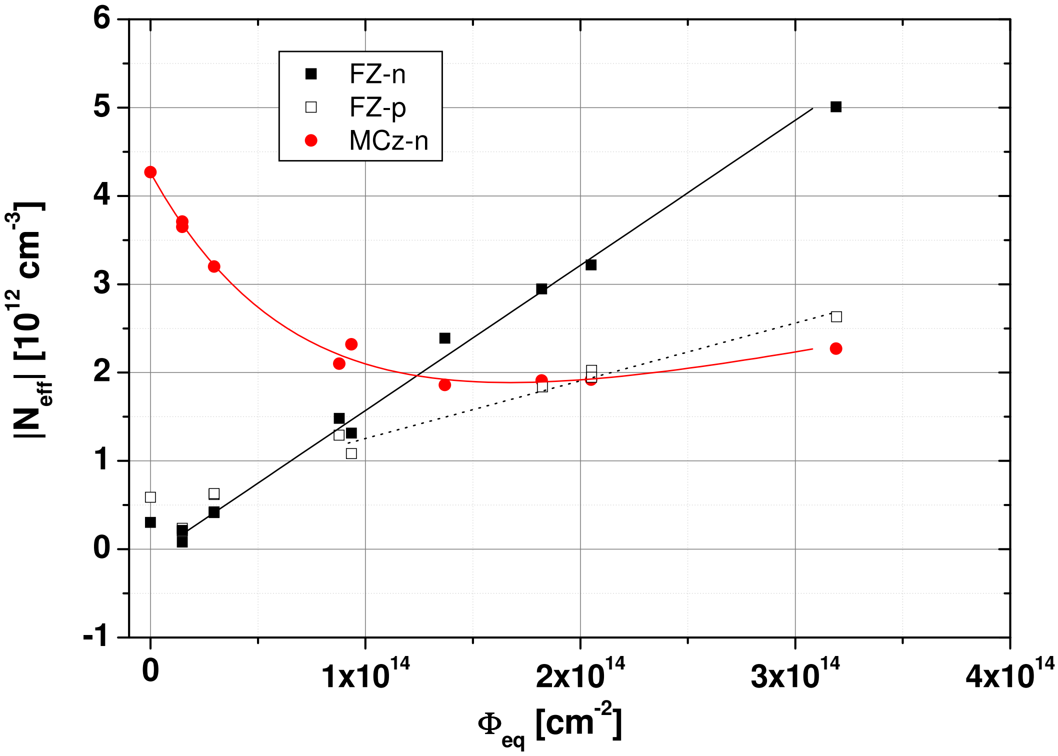

Figure 6.24: Development of the effective space charge with fluence in n- type FZ and MCz and p-type DOFZ after irradiation with 200 MeV pions. No error bars are added for better visibility. The fluence error is about 20 %, the error of the effective space charge about 5 %. All samples were annealed for 4 min at 80 °C before measurement.

silicon type	24 GeV/c protons $[10^{-3}\ cm^{-1}]$	reactor neutrons $[10^{-3}\ cm^{-1}]$	200 MeV pions $[10^{-3}\ cm^{-1}]$
FZ-n	16.99 ± 0.33	21.22 ± 0.62	16.43 ± 0.42
FZ-p	–	20.32 ± 0.24	–
DOFZ-p	–	–	6.53 ± 0.22
MCz-n	? 8.55 ± 0.35	22.21 ± 1.10	- 4.81 ± 1.45
MCz-p	? 7.42 ± 0.35	22.04 ± 0.57	–
150 μm EPI-n	-15.61 ± 0.21	5.80 ± 0.22	–
150 μm EPI-p	-10.52 ± 0.53	3.72 ± 0.24	–
75 μm EPI-p	-15.81 ± 0.44	–	–
50 μm EPI-p	-15.11 ± 0.42	–	–

Table 6.5: Effective generation rates for all materials and particle types measured in this work. The sign of g_c was determined via TCT measurements For MCz no conclusions for the sign of g_c could be drawn from standard TCT measurements as described in chapter 5.3.2.

Chapter 7

Collected Charge

The collected charge is the most important parameter for characterization of silicon materials. In the following FZ, MCz and 150 μm EPI samples irradiated with 24 GeV/c protons, reactor neutrons and 200 MeV pions are compared to investigate differences in the response to different particle types. Prior measurements have shown that in highly overdepleted detectors the collected charge is not material dependent [RD510]. At this point the drift velocity has reached saturation and the loss of charge is determined by the effective trapping probabilities. These in turn are not changed by varying material properties like resistivity, silicon type or wafer production method (compare also chapter 8.1). At lower voltages however the electric field in the detector, determined by the effective space charge, influences the output signal. As shown in chapter 6 the development of $|N_{eff}|$ with fluence is highly material dependent, leading to differences in the collected charge if silicon with different properties is compared at a fixed bias voltage. The collected charge was measured using beta particles from a ^{90}Sr source in a dedicated setup from NIKHEF. All measurements were performed at (-20 ± 1)°C in order to keep the reverse current low in irradiated diodes (compare chapter 5.3.3).

The decrease of collected charge with fluence in highly overdepleted devices will be shown in addition to the value at 300 V wherever high enough bias voltages could be reached. For all fluence steps also the development of the collected charge with bias voltage will be included.

The charge collection efficiency, i.e. the ratio between the deposited and the measured charge, is not temperature dependent since according to [Kra05] two mechanisms work against each other: the effective trapping probability, responsible for the loss of charge in irradiated detectors, increases with decreasing temperature, but at the same time the carrier mobility increases. Thus the overall amount of trapped charge stays constant. It has recently been shown however that at high pion fluences above 5 x 10^{14} cm^{-2} the development of collected charge with bias voltage changes and the depletion voltage shifts to lower values with decreasing temperature [Pac10b].

In Fig. 7.1(a) the development of the collected charge with voltage for all sample types before irradiation is shown. The difference between n- and p-type MCz is about 3 %, which is in the range of variations found between diodes from the same wafer. In FZ on the other hand the collected charge in p-type is considerably lower than in n-type. As can be seen in Fig. 7.1(b) already at the first fluence step however the collected charge reaches similar values in both materials and is higher than in unirradiated p-type.

Overall less charge is collected in unirradiated FZ than in MCz (about 7 % for n-type). Different detector thicknesses that would influence the number of charge carriers collected can be outruled by looking at the reverse current that is independent of material but dependent on sample thickness (and area): the temperature corrected current is the same for both materials.

Since the number of electron-hole pairs produced is linearly dependent on the thickness, unirradiated EPI samples with a thinner active layer of 150 μm compared to 300 μm in the other materials are expected to show only half of the collected charge. The thickness corrected collected charge in n-type EPI however is higher than what is found even in MCz n-type, where the highest value for all 300 μm thick detectors was measured. It has to be noted though that an unexpected drop in charge collection efficiency at very low fluences was observed in EPI-n, as discussed in section 7.1.3 in this chapter. Similar to what was found for FZ and MCz, less charge is collected in p-type EPI than in n-type. If scaled to 300 μm the agreement is within 5 % when compared to FZ, but the values are about 10 % lower than in MCz.

Overall, however, the charge measured here is lower than expected from the scaling factor of 79 $e^{-}/\mu m$ observed in [Kra05]. This does not influence the comparison of different materials in this work but has to be kept in mind comparing with results from other groups.

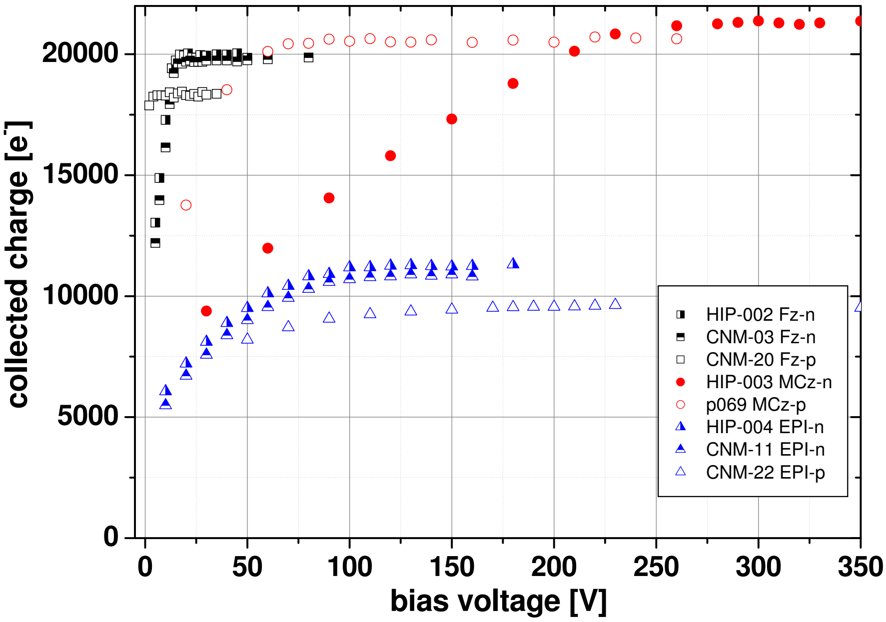

(a)

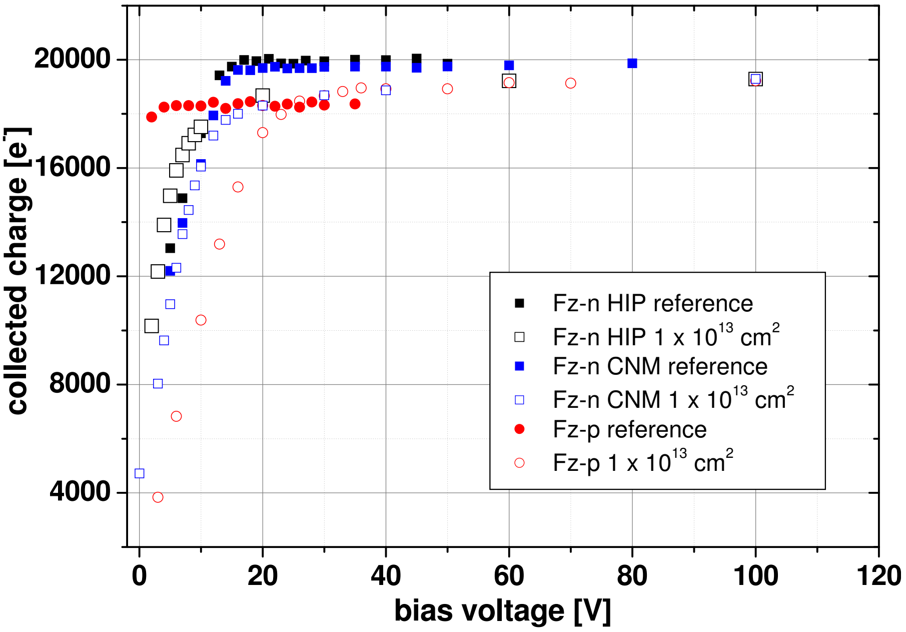

(b)

Figure 7.1: (a) Collected charge in unirradiated n- and p-type Fz, MCz and 150 μm EPI samples and (b) in n- and p-type FZ unirradiated and irradiated with 1 x 10^{13} n/cm^2.

7.1 Irradiation with different particle types

In this chapter the influence of different radiation types on the charge collection efficiency in 300 μm FZ and MCz and 150 μm EPI will be compared. All silicon types were irradiated with 24 GeV/c protons and reactor neutrons, n-type FZ and MCz samples in addition also with 200 MeV pions. The samples were annealed for 4 min at 80 °C before measurement. The collected charge was measured at (-20 ± 1) °C using beta particles from a ^{90}Sr source in a dedicated setup from NIKHEF (compare chapter 5.3.3).

7.1.1 FZ

Figs. 7.2 and 7.3 show the charge collected in n-type FZ after irradiation with protons, neutrons and pions. Where available samples processed by both CNM and HIP were used with active areas of 5 x 5 mm^2 and 2.5 x 2.5 mm^2 respectively for proton irradiation and 5 x 5 mm for neutron irradiation. After proton irradiation a difference in curve shapes is seen between diodes from the two producer at fluences of 1.66 x 10^{14} p/cm^2 and 4.43 x 10^{14} p/cm^2 that indicates shift in depletion voltage to higher values in CNM samples. The depletion voltage obtained from CV measurements however is the same for CNM and HIP samples (compare chapter 6.1.1). After neutron irradiation a full comparison is only possible up to 1 x 10^{14} n/cm^2 due to problems with high bias current in the sample from HIP. No significant differences were found.

Fig. 7.4 shows the development of the collected charge with bias voltage in p-type FZ for different proton and neutron fluences. As mentioned before, the collected charge at the first fluence step of 1.46 x 10^{13} p/cm^2 and 1 x 10^{13} n/cm^2 is higher than in the unirradiated sample. No reason for that behavior could be found by looking at the TCT curves.

In addition to the full charge vs. voltage curves at each fluence step, in Fig. 7.5 the dependence on fluence of the charge collected at 300 V is shown for all particle types. It decreases linearly in all FZ samples with a sudden drop at 3 x 10^{14} cm^{-2} where depletion is no longer reached. No differences between the different particle types are found in this representation. For a definite conclusion however the charge collected well above depletion, where only trapping is relevant, has to be looked at. Since these high bias voltage were not reached in all samples, in Fig. 7.6 the charge obtained at more than 200 V above depletion or at the highest available bias voltage had to be combined for a more limited comparison instead. No differences between proton and pion irradiation can be seen, which agrees with results obtained from TCT measurements: the effective trapping probabilities for these particle types are the same (compare also chapter 8.1). Neutrons on the other hand were found to be less damaging [Kra02], which would imply a higher collected charge in the neutron irradiated samples that is not visible in Fig. 7.5. The fluence range where high enough bias voltages could be reached in FZ irradiated with neutrons is however very limited, so no definite conclusion can be drawn.

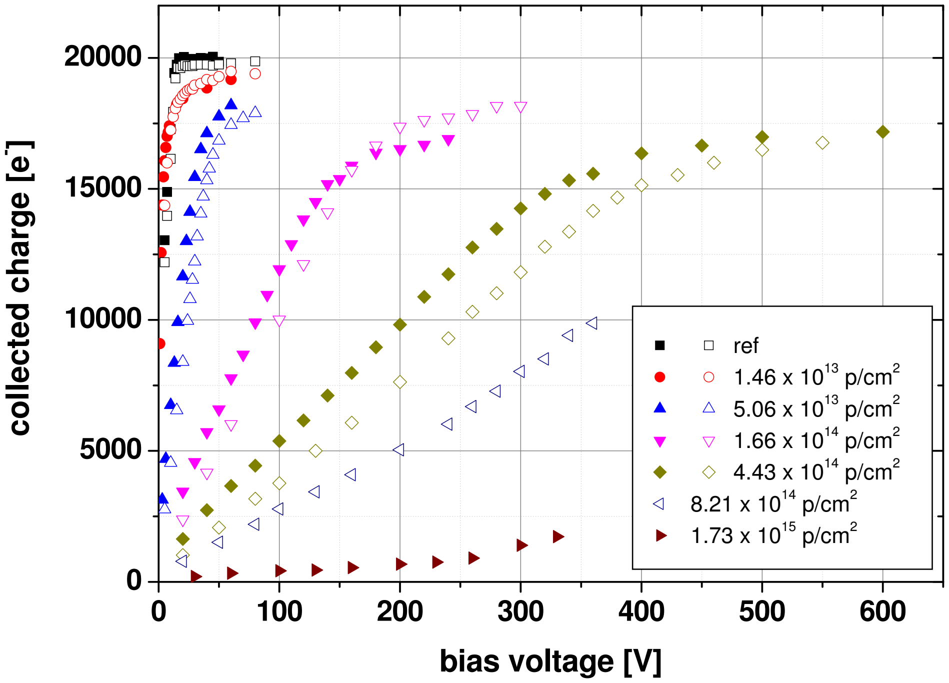

(a)

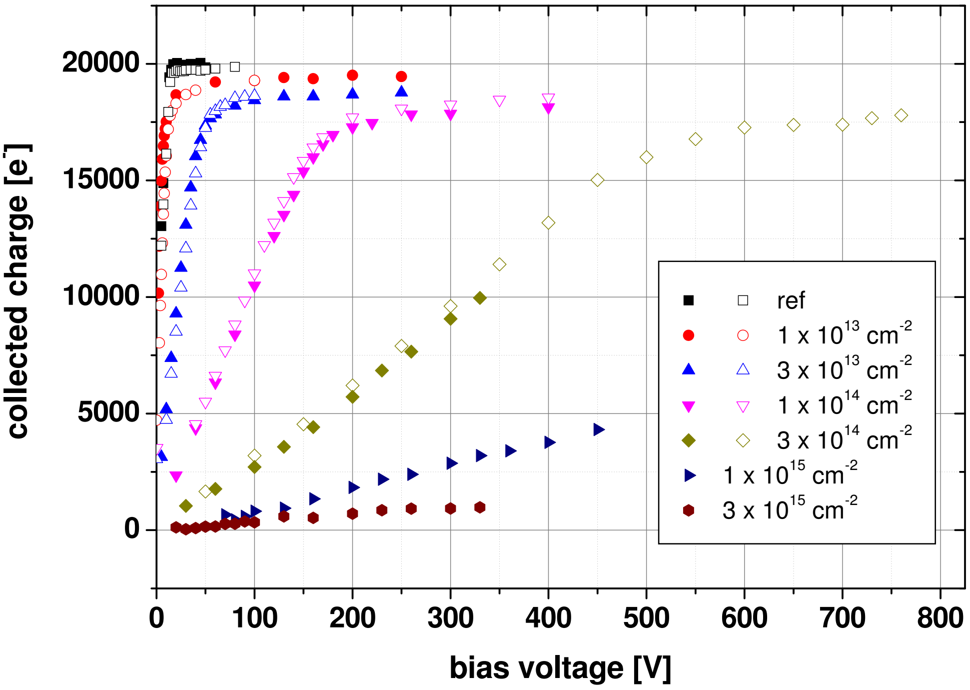

(b)

Figure 7.2: Collected charge in FZ n-type after irradiation with (a) 24 GeV/c protons and (b) reactor neutrons. Closed symbols refer to diodes from HIP, whereas open symbols denote samples processed by CNM from the same wafer material.

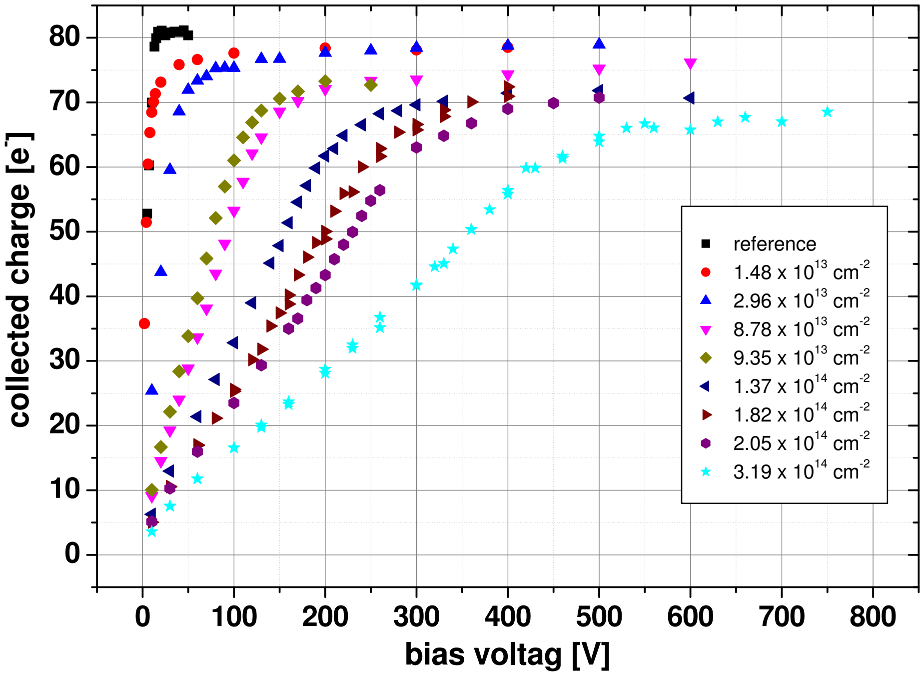

Figure 7.3: Collected charge in n-type FZ after irradiation with 200 MeV pions.

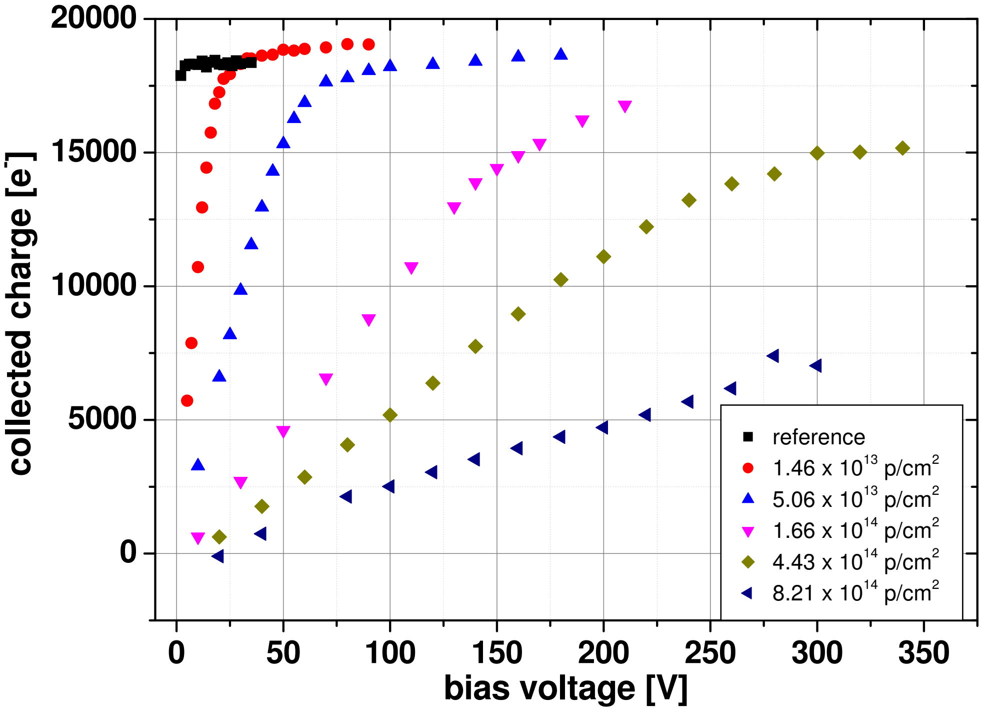

(a)

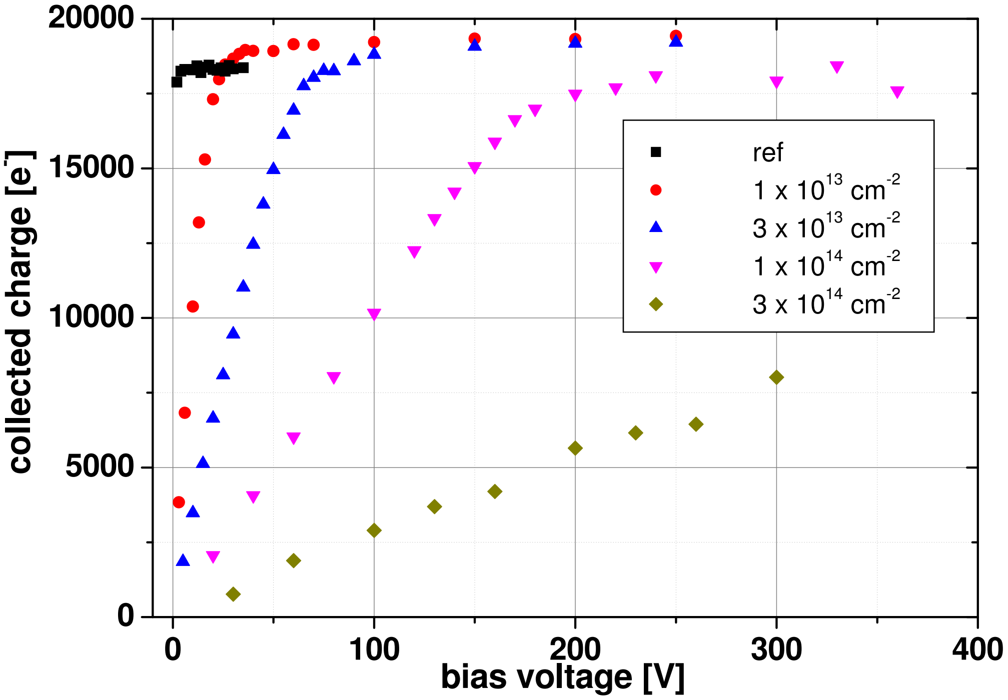

(b)

Figure 7.4: Collected charge in p-type FZ irradiated with (a) 24 GeV/c protons and (b) reactor neutrons.

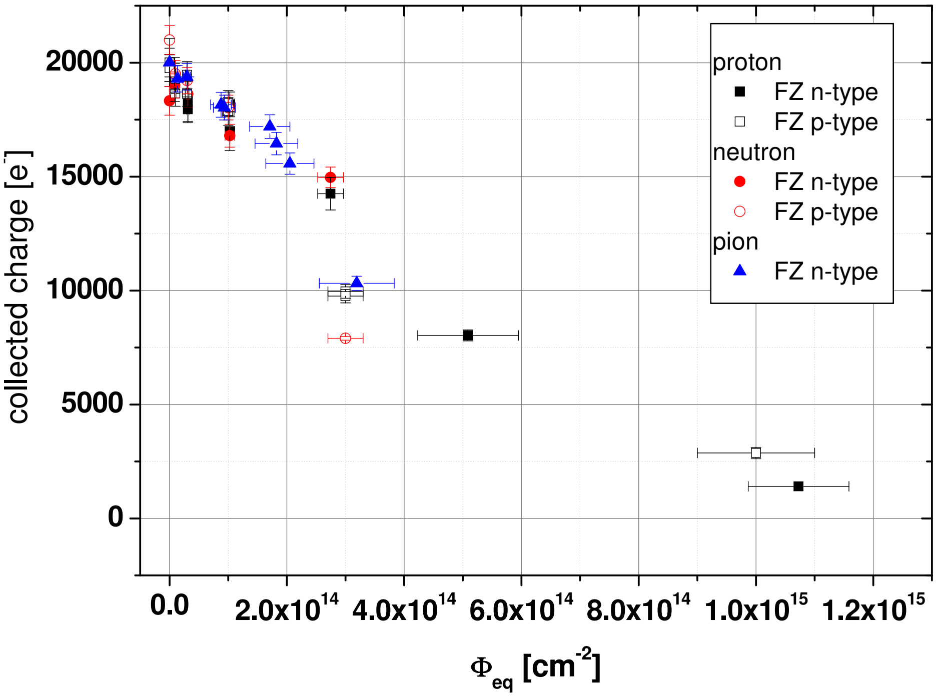

Figure 7.5: Collected charge at 300 V in n- and p-type FZ after irradiation with 24 GeV/c protons, reactor neutrons and 200 MeV pions.

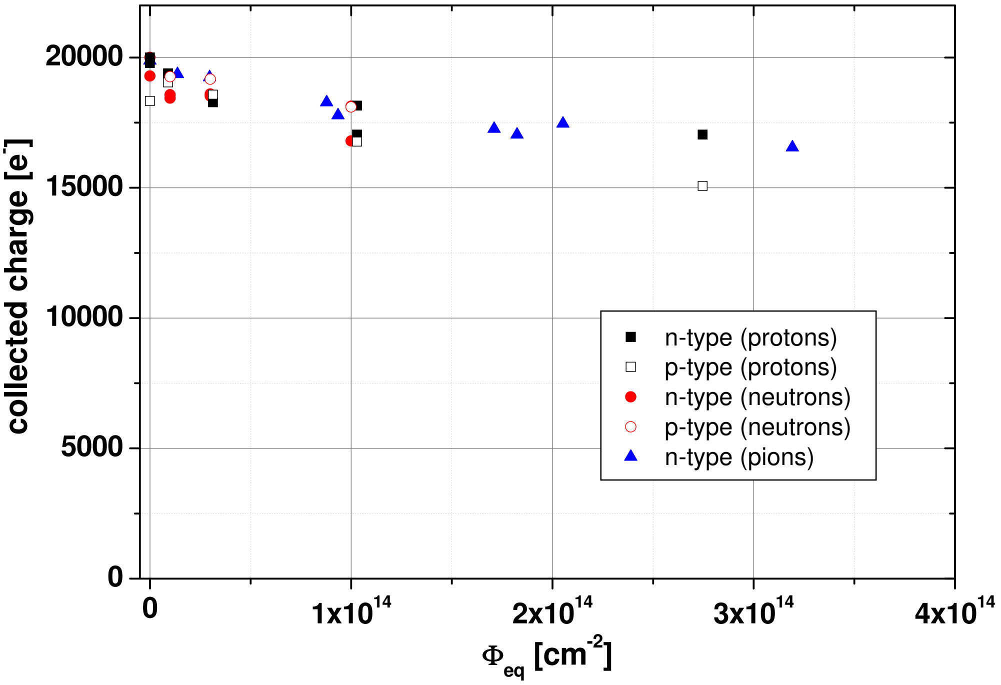

Figure 7.6: Maximum collected charge at $V > V_d + 200V$ above depletion or at the highest possible bias voltage in n- and p-type FZ after irradiation with 24 GeV/c protons, reactor neutrons and 200 MeV pions. No error bars were included for better visibility. The error in the collected charge is about 3 %.

7.1.2 MCz

Fig. 7.7 shows the development of collected charge with bias voltage for n- and p-type MCz irradiated with protons. p-type diodes were produced by HIP from a wafer with a resistivity of 7.53 $k\Omega cm$ and by MICRON from 1.32 $k\Omega cm$ material. Due to high noise in the samples from HIP, depletion could only be reached after low irradiation fluences. At these fluences the collected charge in samples from MICRON was significantly higher than in those processed by HIP (compare 7.7(b)). Different sample thicknesses that could explain the result can be excluded by looking at the pad current per volume (Fig. 7.8) calculated by using a thickness of 300 μm and the respective active area: no differences can be seen between the different sample types.

Since the development of depletion voltage with fluence is different in the two batches of p-type samples due to the wafer materials used, in Fig. 7.9 the maximum collected charge at voltages of 200 V or more above depletion where only a small increase with bias voltage is seen, is plotted instead of using a fixed voltage. The decrease is linearly dependent on fluence and can be parameterized by [Kra10a]:

$$Q_{V_d+200V}(\Phi_{eq}) = Q_{unirrad} - \delta_p \Phi_{eq}$$

where $Q_{unirrad}$ is the charge measured in an unirradiated detector and δ_p is the rate of charge decrease with fluence after proton irradiation. The decrease of charge with fluence in samples from HIP is faster than in those from MICRON, with δ_p equal to $(1920 \pm 296)\ e^-/10^{14}\ cm^{-2}$ compared to $(855 \pm 59)\ e^-/10^{14}\ cm^{-2}$. Only very few data points however are available for HIP samples and only up to a fluence of 1 x $10^{14}\ cm^{-2}$. A direct comparison of trapping times in the material is not possible since the diodes produced by MICRON have neither an opening the aluminum contact layer nor a mesh on the backside that would allow laser illumination necessary for TCT measurements. The trapping times in HIP samples on the other hand agree well with values measured in n-type (compare chapter 8.1).

In two different irradiation campaigns 2.5 x 2.5 mm^2 and 5 x 5 mm^2 n-type MCz samples from two different wafers with the same resistivity both processed by HIP were irradiated with 24 GeV/c protons. The fluence dependence of the maximum charge measured at $V > V_d + 200V$ is shown in Fig. 7.10. At the highest fluence point of 8.1 x $10^{14}\ cm^{-2}$ the maximum bias voltage that could be reached was only 150 V above depletion. The collected charge at this point is therefore quoted with a bigger error bar.

The rate of charge decrease δ_p of $889 \pm 65 e^-/10^{14}\ cm^{-2}$ agrees well with the rate found for MCz p-type from MICRON. Fig. 7.7(a) shows collected charge vs. bias voltage for both wafers, a direct comparison of the curves is however not possible due to different irradiation fluences. The development of the depletion voltage or effective space charge with fluence obtained from CCE curves is not the same in these two sample sizes: at fluences above 2 x $10^{14}\ p/cm^2$ 5 x 5 mm^2 diodes reach full depletion at higher bias voltages, contrary to

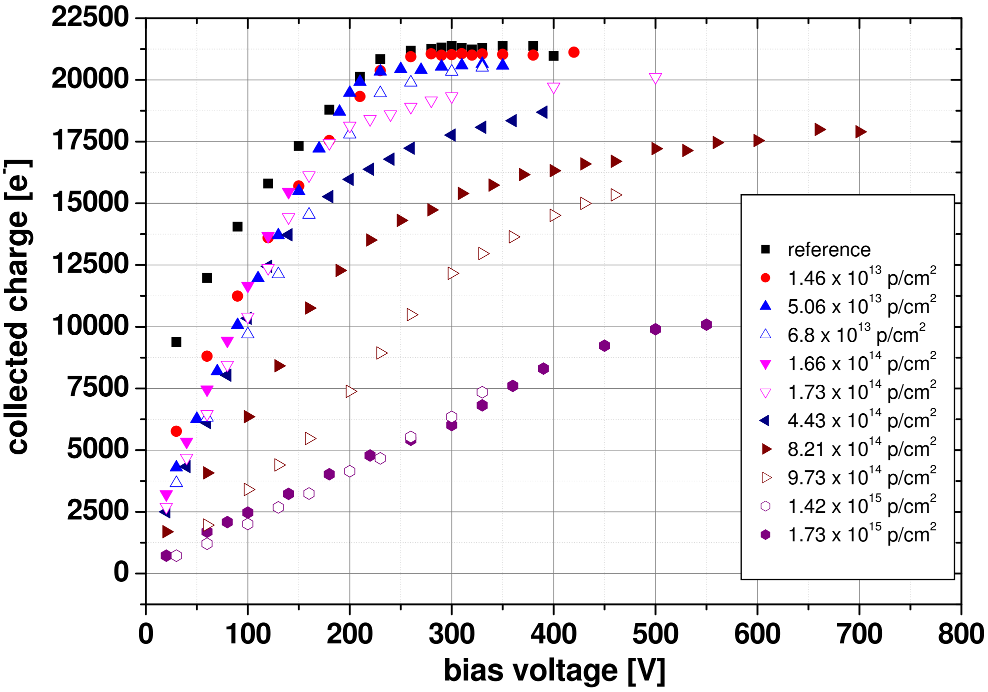

(a)

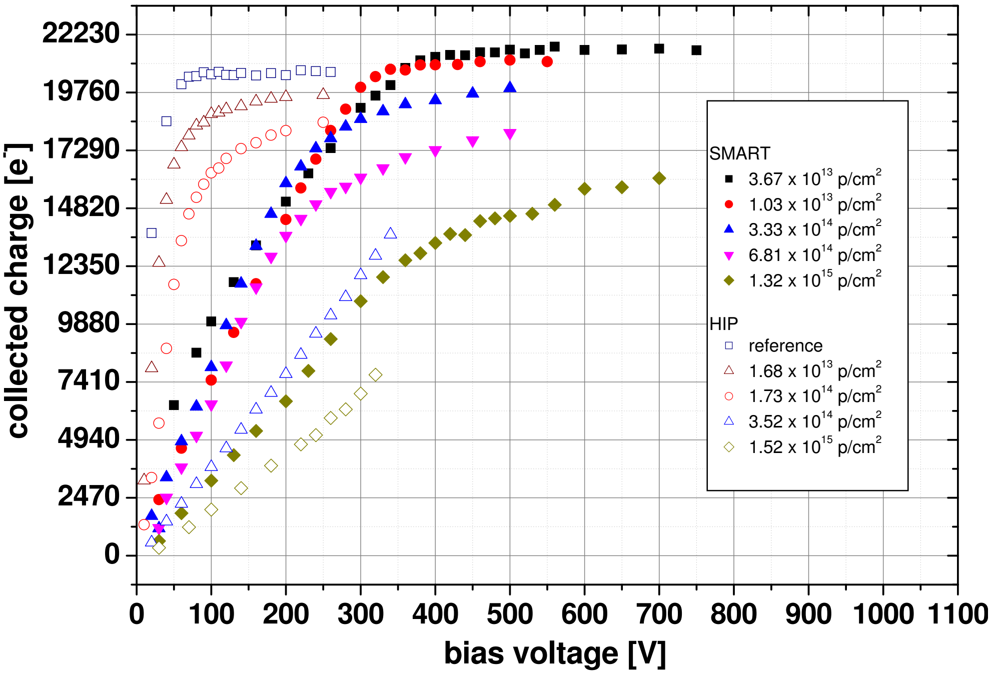

(b)

Figure 7.7: Collected charge in (a) n-type and (b) p-type MCz after irradiation with 24 GeV/c protons. Open symbols in (a) denote 5x5 mm samples, whereas closed symbols stand for 2.5 x 2.5 mm samples.

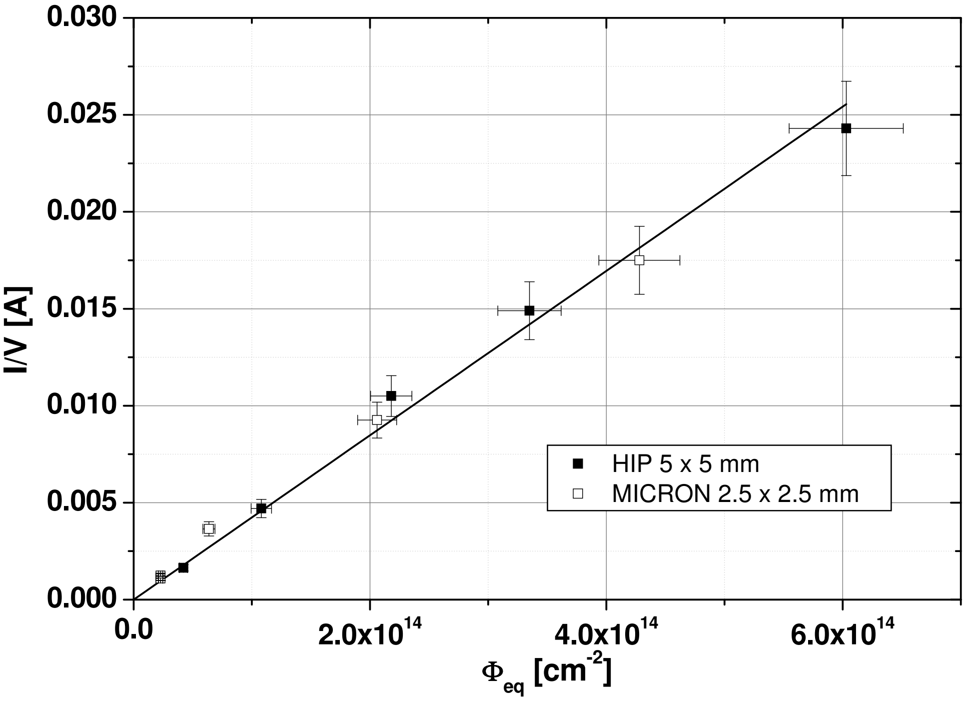

Figure 7.8: Reverse current per volume in p-type MCz irradiated with 24 GeV/c protons temperature corrected to 20°C.

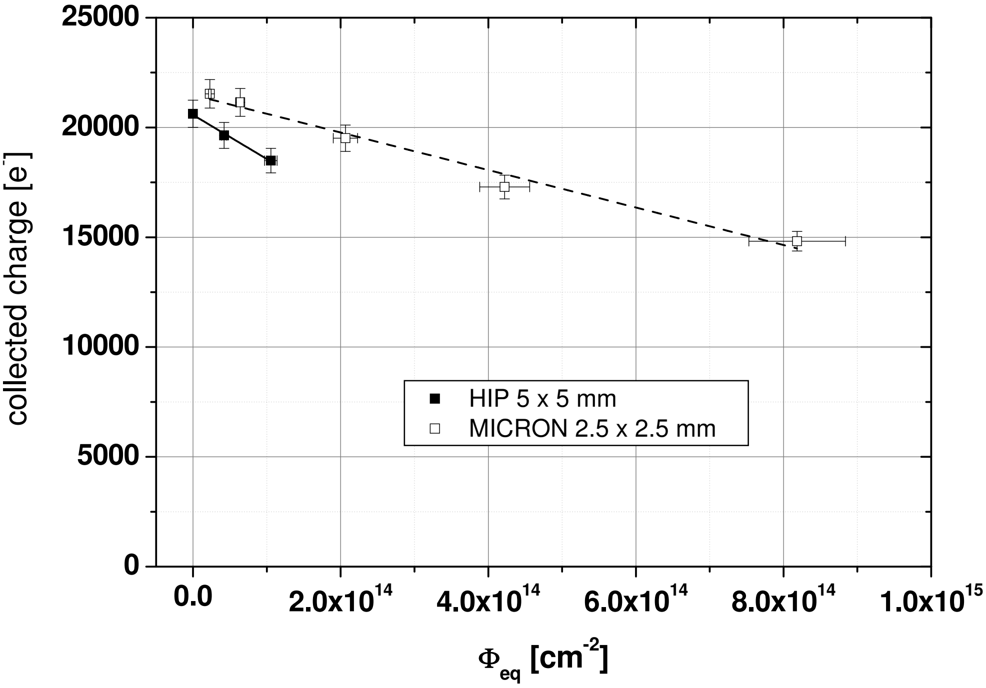

Figure 7.9: Maximum collected charge in p-type MCz with 1.32 $k\Omega cm$ (MICRON) and 7.53 $k\Omega cm$ (HIP) irradiated with 24 GeV/c protons.

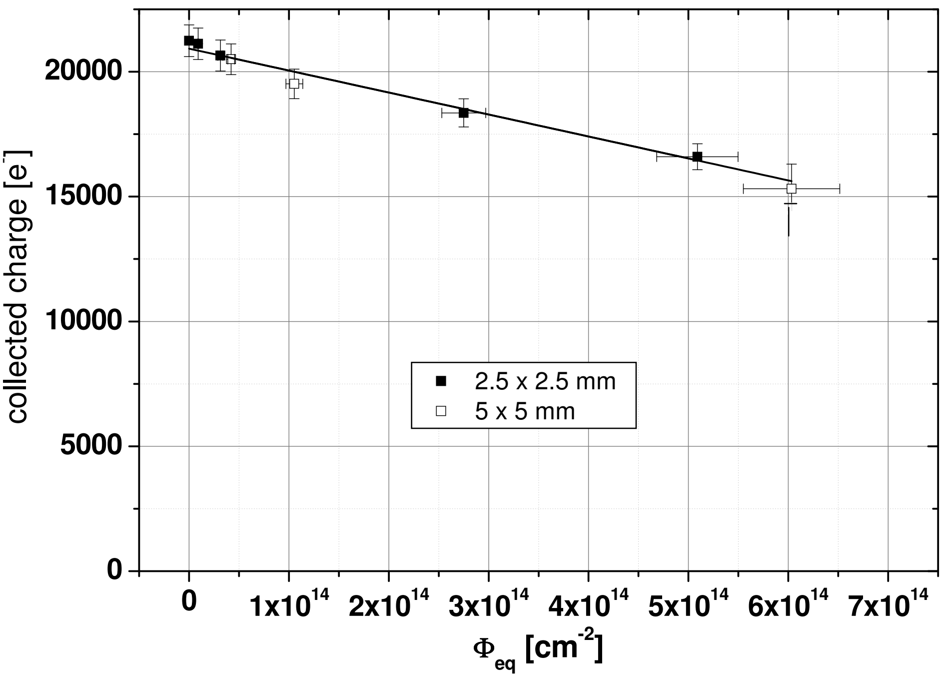

Figure 7.10: Maximum collected charge at $V > V_d + 200V$ in n-type MCz irradiated with 24 GeV/c protons.

results from CV measurements, where no differences were found (compare chapter 6.1.2).

A comparison of n- and p-type MCz after neutron irradiation shows the strong influence of the differences in the development of the depletion voltage on the collected charge at a fixed voltage (Fig. 7.11): in n-type the depletion voltage or effective space charge decreases up to a neutron fluence of 1 x 10^{14} cm^{-2} before increasing with a generation rate of 22 x $10^{-3} cm^{-1}$, whereas in p-type no acceptor removal and therefore no initial decrease is visible. Instead the depletion voltage increases linearly with fluence with approximately the same generation rate (compare chapter 6.1.2). When the depletion voltage minimum is reached in n-type, it is about 340 V lower than in p-type. At 300 V, the comparison voltage chosen in FZ, the charge collected in n-type is therefore significantly higher than in p-type (7.12): only around 8300 electrons are collected MCz-p, which is about 43 % of the maximum that was measured at 600 V in this sample. In n-type MCz at the same fluence step the collected charge is already at its maximum of 20000 electrons.

Overdepletion that would allow a direct material comparison was not possible due to the bad quality of the MCz p-type samples from HIP (no additional diodes from other producers were available). The rate of decrease of $1020 \pm 171\, e^-/10^{14}\, cm^{-2}$ in n-type after neutron irradiation however is similar to what is found in proton and also pion irradiated samples (Fig. 7.13, for pion irradiated samples see also Fig. 7.14), which, as in FZ, in this fluence range does not reflect the differences seen in the effective trapping probability.

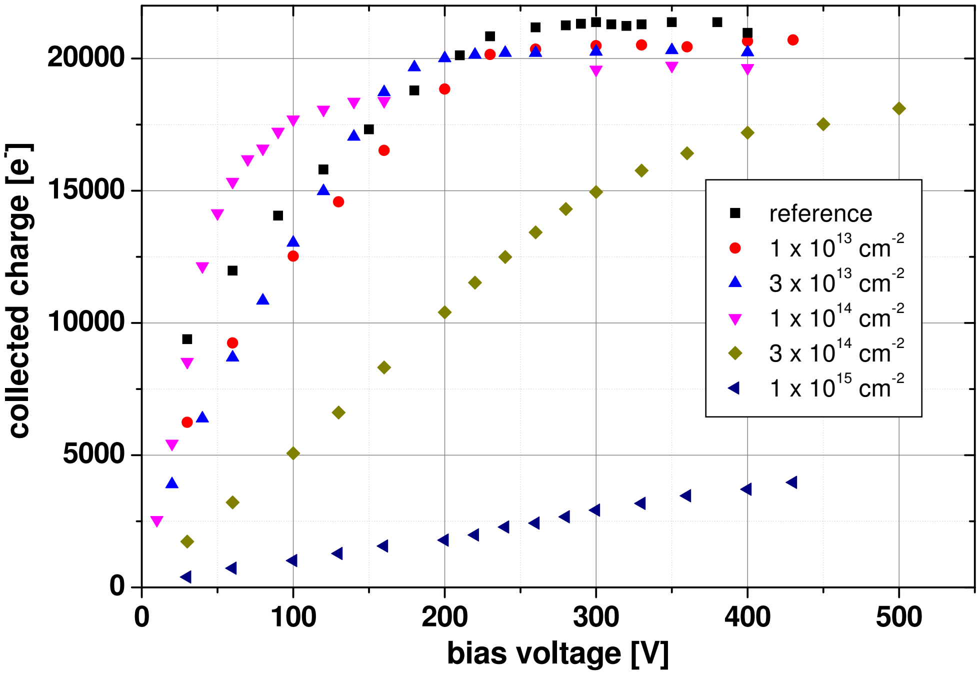

(a)

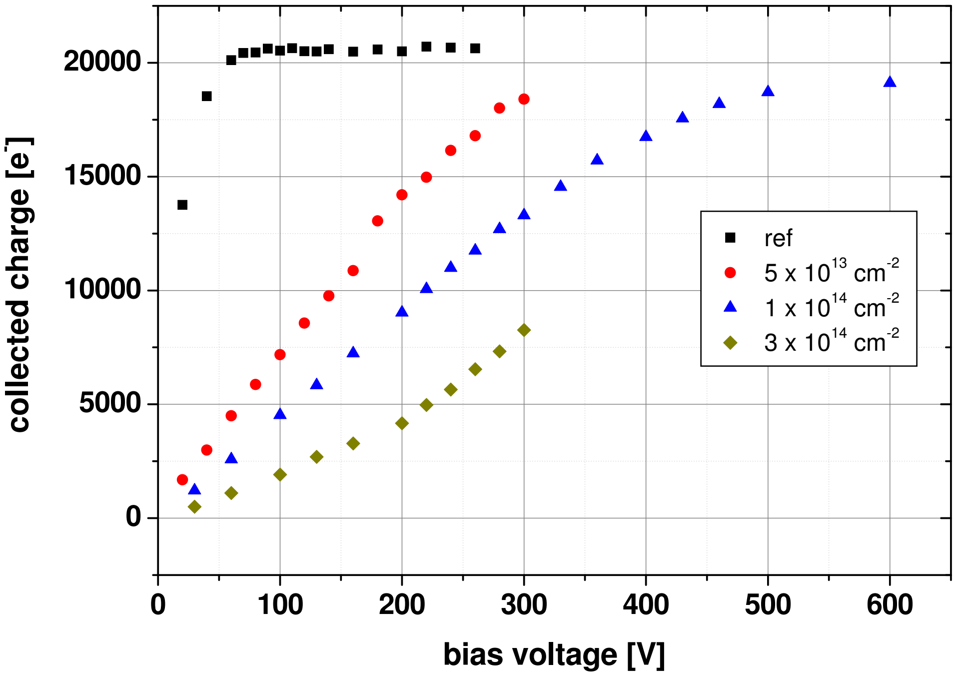

(b)

Figure 7.11: Collected charge in (a) n-type and (b) p-type MCz irradiated with reactor neutrons.

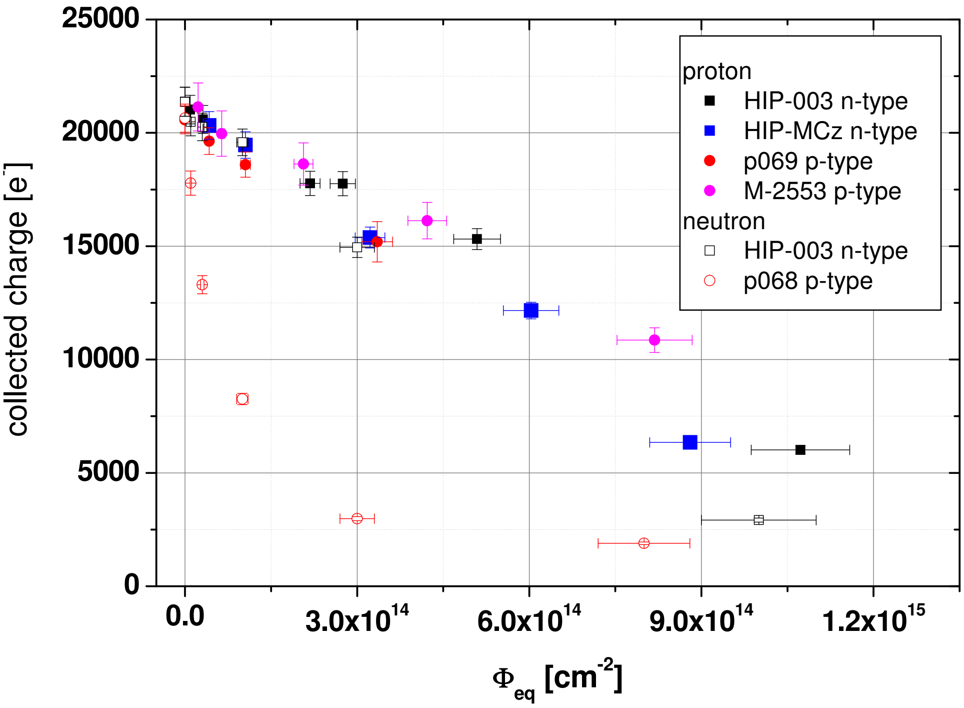

Figure 7.12: Collected charge at 300 V after irradiation with 24 GeV/c protons and reactor neutrons.

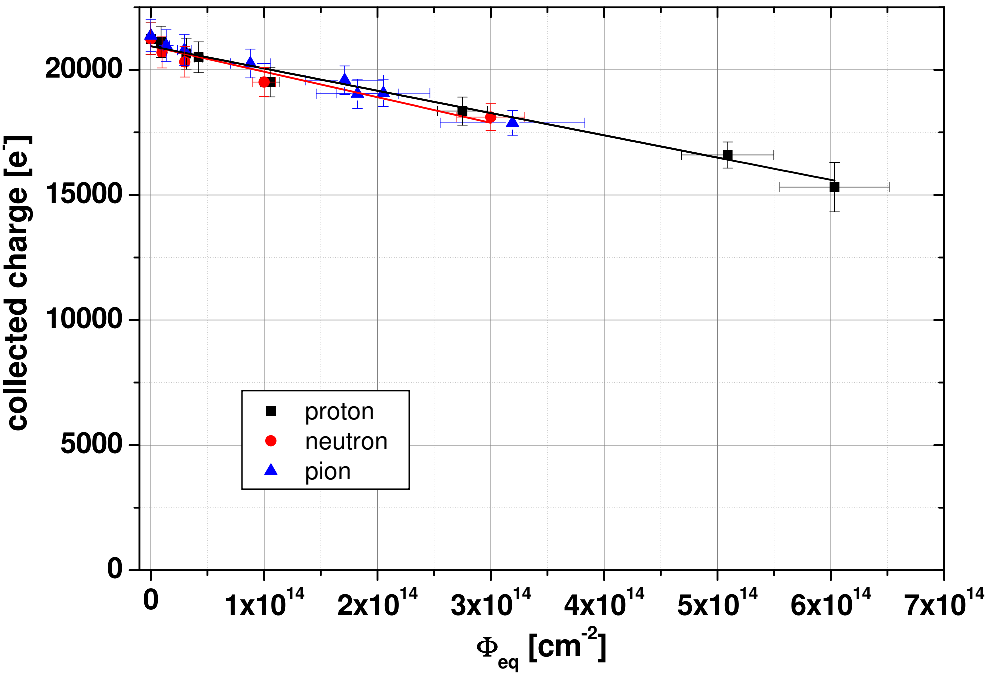

Figure 7.13: Maximum collected charge in n-type MCz irradiated with 24 GeV/c protons, reactor neutrons and 200 MeV pions.

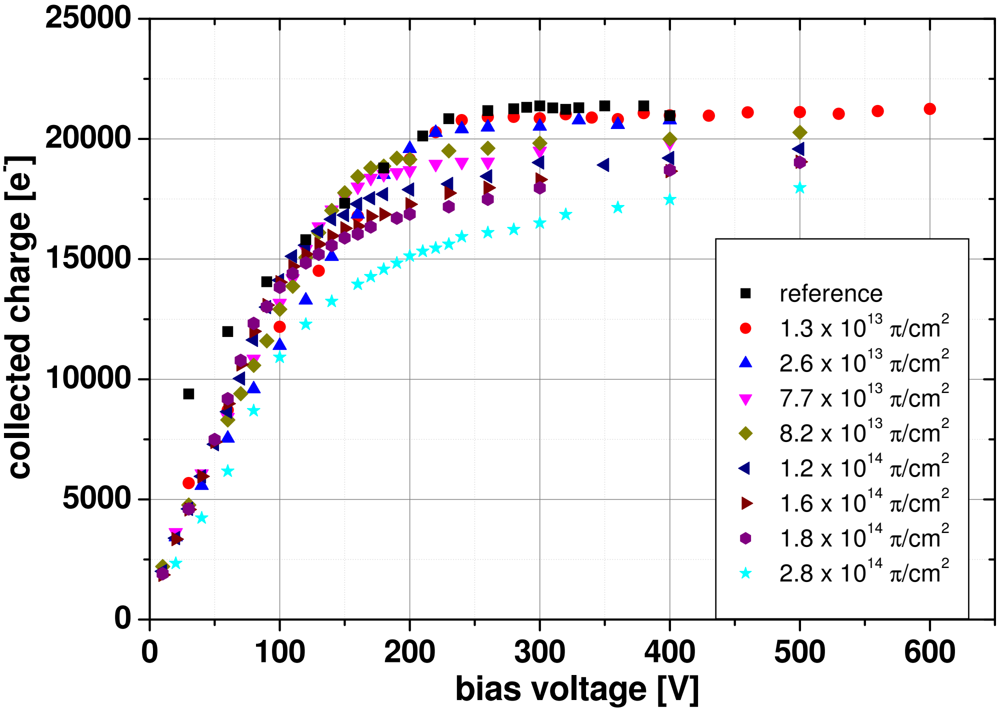

Figure 7.14: Collected charge in MCz n-type irradiated with 200 MeV pions.

	δ $[e^-/10^{-14}]$
24 GeV/c protons	
MCz-n MCz-p (HIP) MCz-p (MICRON)	889 ± 65 1920 ± 296 855 ± 59
reactor neutrons	
MCz-n MCz-p	1020 ± 171 not possible
200 MeV pion	
MCz-n	1092 ± 130

Table 7.1: Rate of decrease of the collected charge with fluence δ for MCz after 24 GeV/c proton, reactor neutron and 200 MeV pion irradiation.

7.1.3 EPI

In 150 μm n-type EPI samples a sharp drop in the charge collection efficiency was observed after irradiation with low proton fluences in [Hoe07]. To confirm the phenomenon and to investigate it further[1], n- and p-type EPI samples were irradiated with 24 GeV/c protons and reactor neutrons to equivalent fluences between 1 x 10^{12} cm^{-2} and 3 x 10^{15} cm^{-2}.

In Fig. 7.15 and Fig. 7.16 the dependence of the collected charge on the bias voltage is shown for n- and p-type EPI after irradiation with protons and neutrons. It is obvious that the above mentioned drop in charge at low fluences is visible in n-type irradiation with both particle types, whereas in p-type the differences between unirradiated samples and those irradiated to the first fluence step of about 1 x 10^{12} cm^{-2} are small. In [Hoe07] the charge collection efficiency after proton irradiation was also measured with a infrared laser setup, which confirmed the observed behavior. TCT measurements with a red laser that provide information about the electric field in the diode however could not explain the differences.

For both n- and p-type several reference samples and samples irradiated with low proton and neutron fluences of less than 1 x 10^{13} cm^{-2} were tested, a problem with single diodes can therefore be excluded.

Two different sample sizes, 2.5 x 2.5 mm^2 diodes processed by HIP and 5 x 5 mm^2 diodes processed by CNM from the same wafer material, can be compared after neutron irradiation. Before irradiation a difference of about 9 % in the collected charge was observed that was reduced to less than the average 3 % variation between samples from the same wafer already at 5 x 10^{12} cm^{-2}.

In Fig. 7.17 the charge collected at a bias voltage of 200 V in n- and p-type EPI is compared. Apart from the initial drop in n-type a linear development with fluence can be seen up to 3 x 10^{15} cm^{-2} for both sample types. At the highest neutron fluence of 8 x 10^{15} cm^{-2} however the collected charge is higher than expected if a linear decrease of the charge collection with fluence is assumed. No differences between irradiations with the two particle types are observed.

The collected charge in p-type EPI samples is lower than in n-type samples even before irradiation (compare Fig. 7.1(a)). In [Hoe07] no differences were found in the proton irradiated n- and p-type samples from the same wafers that were also used in this work (HIP-004 and CNM-22 in Fig. 4). This is the result of differences in sample preparation: conductive carbon pads were used to fix the n-type HIP samples on the CCE sample boards, whereas p-type samples were fixed with silver glue. As shown in chapter 5.3.3 using carbon pads leads to a lower collected charge, which makes a comparison impossible. Samples from the same two wafers measured with the same equipment but both fixed with silver glue show clear differences.

---

[1] These results have already been published in [Kas10]

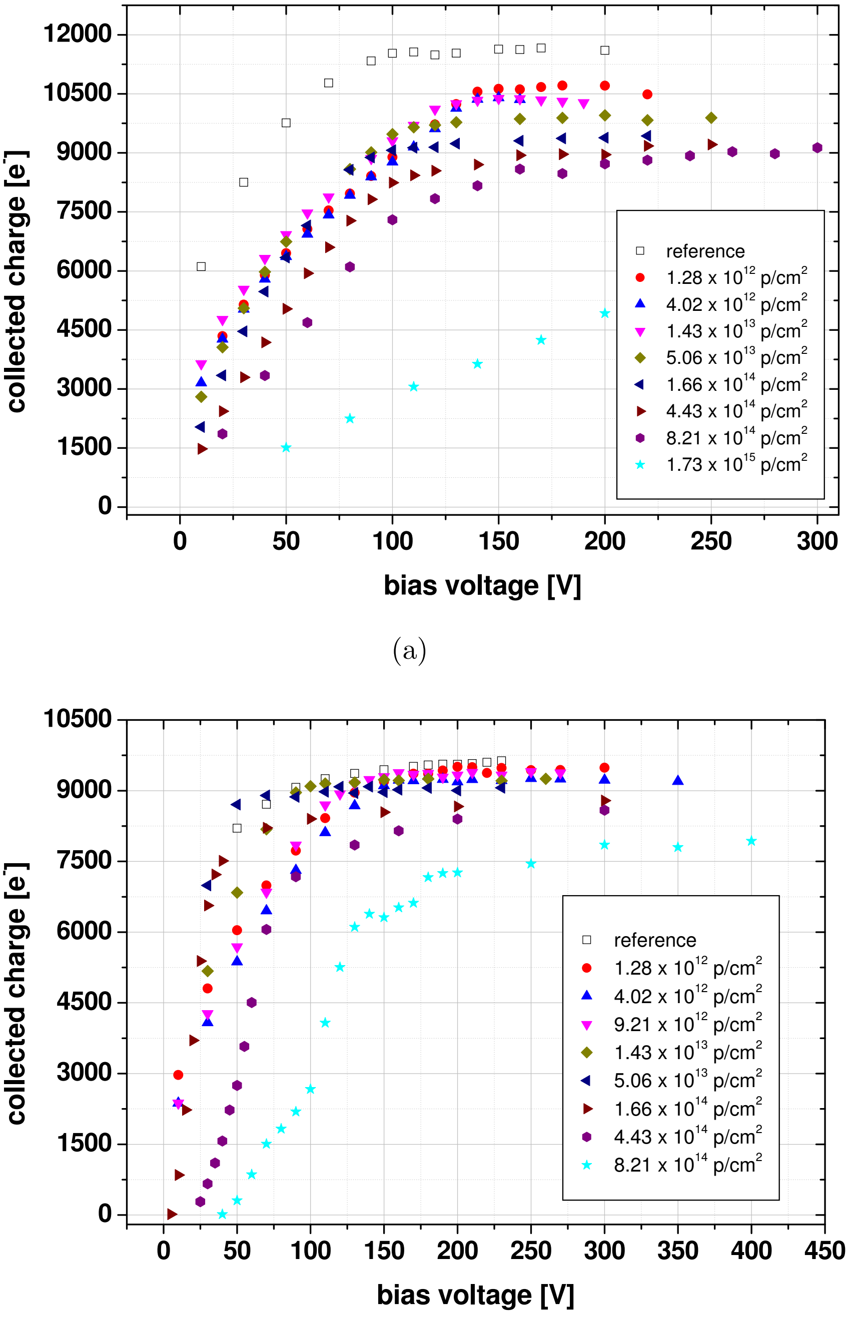

(a)

(b)

Figure 7.15: Collected charge in (a) n-type and (b) p-type 150 μm EPI irradiated with 24 GeV/c protons.

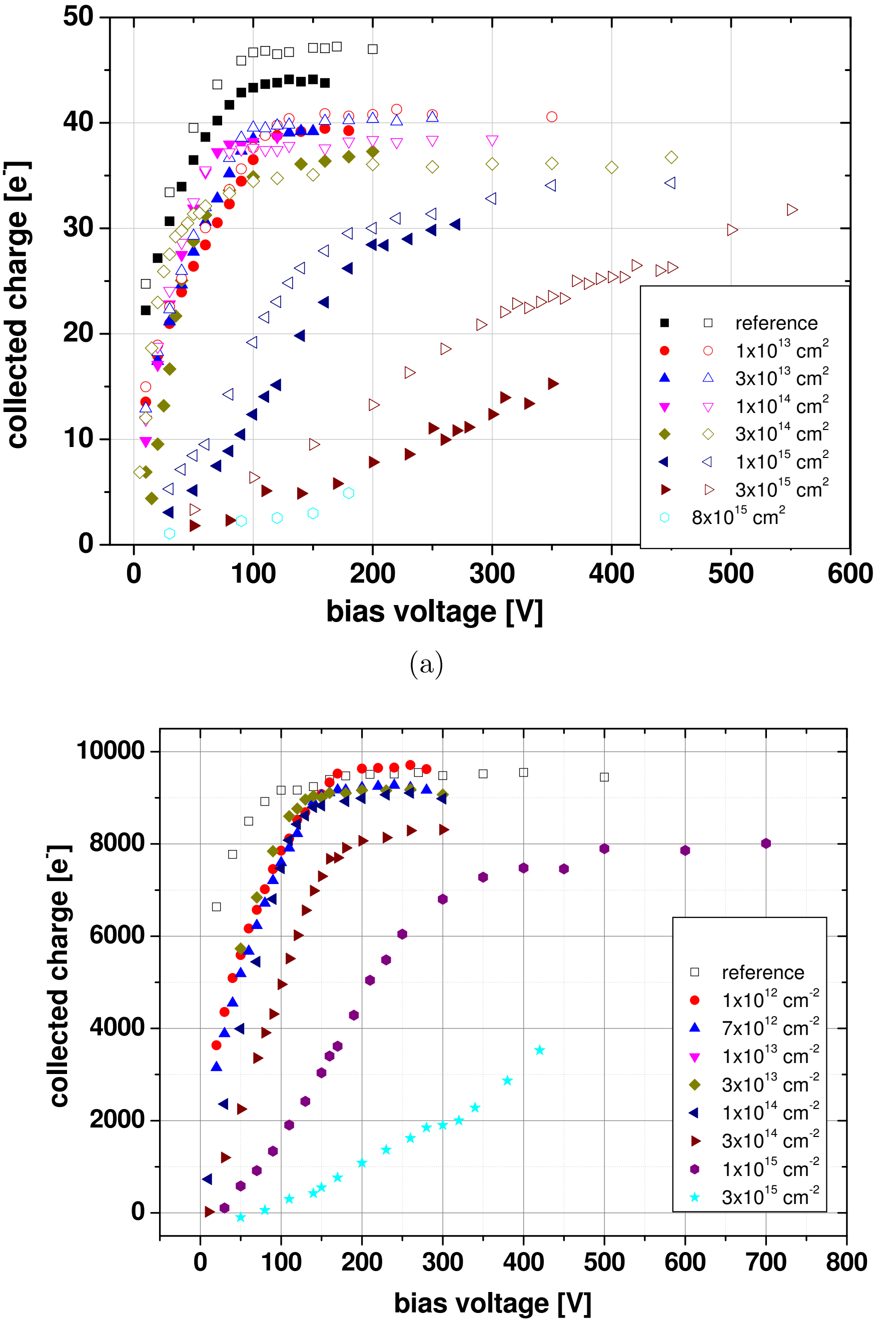

(a)

(b)

Figure 7.16: Collected charge in 150 μm EPI irradiated with reactor neutrons. For (a) n-type samples from CNM are denoted by closed symbols and HIP samples by open symbols. For (b) p-type only samples from CNM were available.

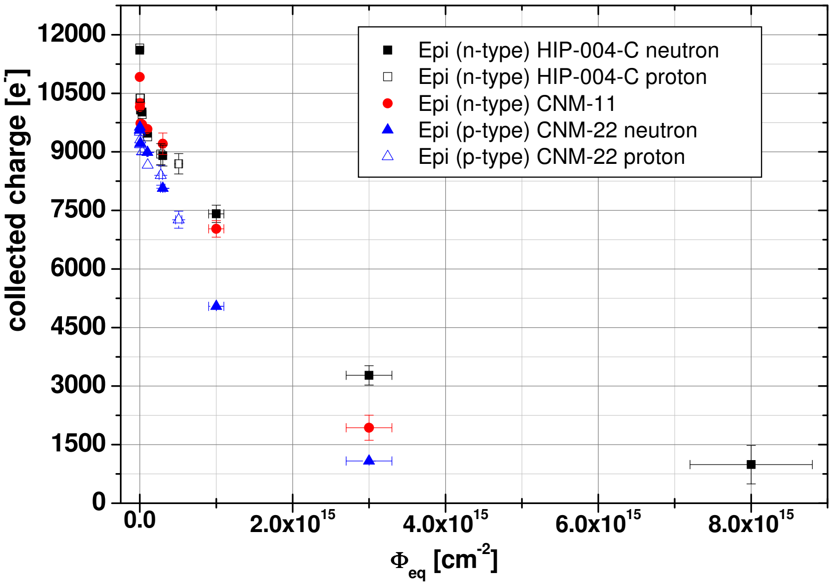

Figure 7.17: Development of the charge collected at 200 V with fluence for 150 μm n- and p-type EPI irradiated with 24 GeV/c protons and neutrons. The error bars are only shown at high fluences for better visibility. The error is around 3 % for all samples.

7.2 Material comparison

In the following the collected charge in n- and p-type Fz, MCz and 150 μm EPI after irradiation with different particle types will be compared at a fixed bias voltage of 300V.

7.2.1 Neutron irradiation

The charge collected in FZ, MCz and EPI samples after irradiation with neutrons is shown in Fig. 7.18. Bad sample quality as experienced in MCz p-type and to a certain extend in FZ (compare chapter 6.1) makes any comparison above 300 V impossible. This relatively low comparison voltage leads to differences in depletion voltage being strongly reflected in the development of collected charge with fluence. As shown in chapter 6.1 the generation rate in all 300 μm thick samples is rather high, ranging between 20 and 22 x $10^{-3} cm^{-1}$. If there is no initial removal of donors/acceptors, the charge at 300 V is then obtained in an underdepleted detector already at low fluences, explaining the quick drop in collected charge in MCz p-type (compare also section 7.1.2).

Since the number of charge carriers is linearly dependent on the thickness, at low fluences, where trapping is less relevant, less charge is collected in 150 μm EPI samples than in 300 μm thick FZ and MCz samples. At higher fluences, when more defects are created in the sample that potentially decrease the collected charge by trapping, the charge collection time becomes more important. In thinner samples, where the drift velocity is faster due to the higher electric field and the drift distance is smaller, an advantage over thicker devices can be expected. In addition the depletion voltage in EPI increases much more slowly with fluence than in Fz and MCz in neutron irradiated samples (compare chapter 6.1.3). At 300 V depletion is reached in all n- and p-type EPI samples and the collected charge is close to the maximum obtainable at the respective fluence step. Therefore already at 3 x 10^{14} cm^{-2} the collected charge in EPI is similar to that of FZ at 1 x 10^{15} cm^{-2} and at higher fluences EPI shows the least loss of charge of all materials.

7.2.2 Proton irradiation

In Fig. 7.19 the development of the charge collected at 300 V with fluence for all materials irradiated with 24 GeV/c protons is compared. Up to the highest irradiation fluence of 1.07 x 10^{14} cm^{-2} 300 μm MCz shows the highest charge signal of all materials. Above this fluence the charge in 2.5 x 2.5 mm^2 n-type samples from HIP and p-type samples from MICRON is higher than in 5 x 5 mm^2 diodes of both types produced by HIP. In n-type this is due to higher depletion voltages in the bigger samples and no differences are seen when the collected charge above depletion is compared (Fig. 7.10). In p-type however the collected charge is generally lower in the bigger diodes (compare Fig. 7.9).

For both n- and p-type FZ less charge is collected already before irradiation than in MCz

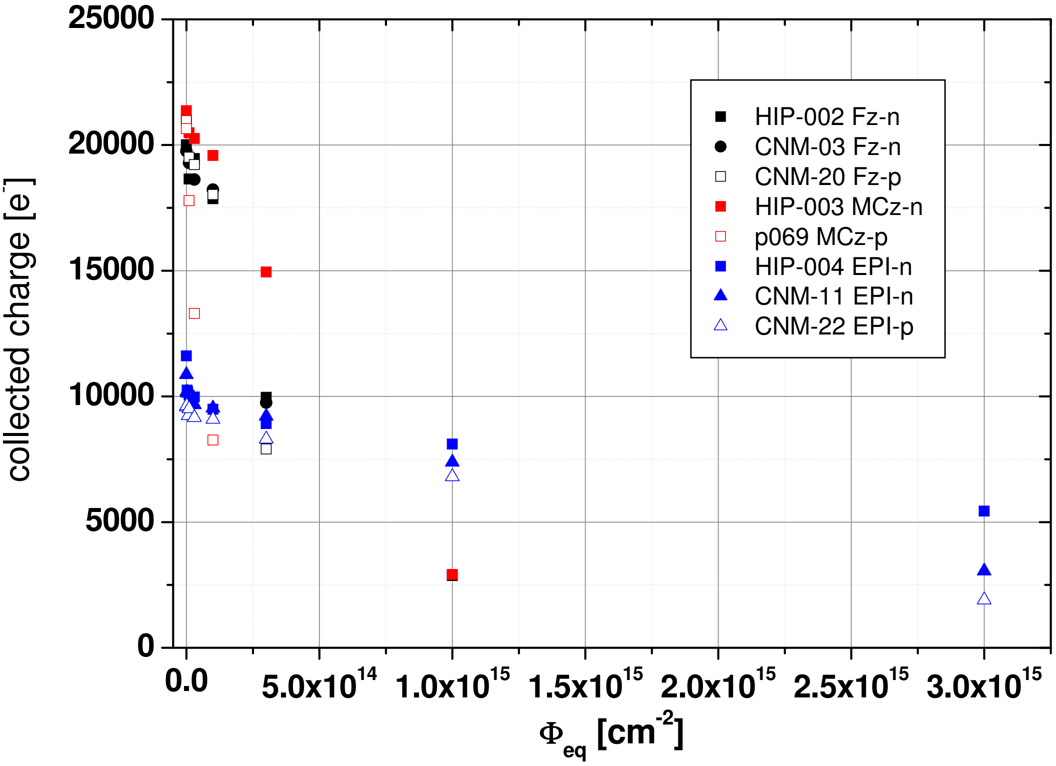

Figure 7.18: Collected charge measured at 300 V in n- and p-type FZ, MCz and EPI silicon samples irradiated with reactor neutrons. For better visibility error bars are not included. The error in the collected charge is about 3%.

and at the highest fluence the gap widens. With only a quarter of the charge that is collected in n-type MCz at a fluence of around 1.4 x 10^{15} cm^{-2}, FZ is the worst material investigated.

Contrary to neutron irradiation, no significant advantage is gained from the development of the space charge with fluence in proton irradiated EPI samples. Due to the lower collection time however EPI, whose collected charge is only about half that of FZ and MCz before irradiation, become compatible to n-type MCz and better than FZ at very high fluences.

7.2.3 Pion irradiation

The collected charge was measured in n-type FZ and MCz samples from HIP irradiated with pions up to an equivalent fluence of 3.2 x 10^{14} cm^{-2}. The decrease with fluence of the maximum collected charge well above depletion is linear for both material types and shows approximately the same rate of decrease with 1227 ± 110 and 1092 ± 130 electrons per 10^{14} cm^{-2} equivalent fluence for FZ and MCz respectively (see Fig. 7.20). This indicates similar response to irradiation in the measured fluence range as expected from

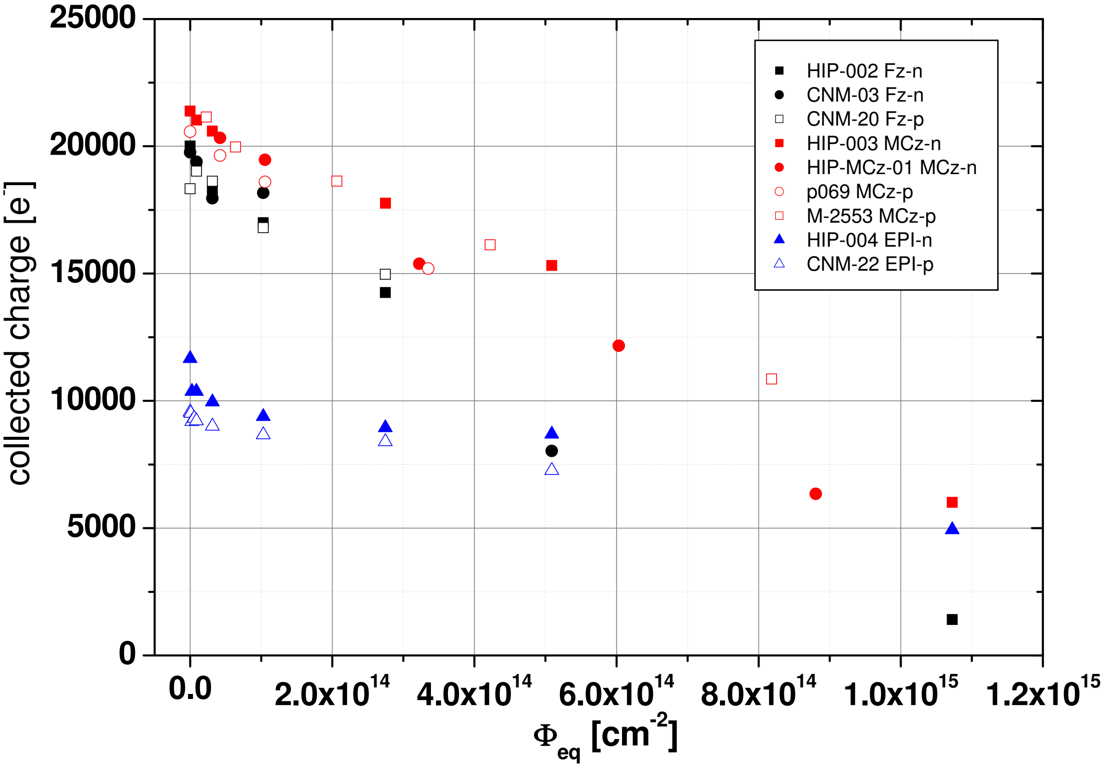

Figure 7.19: Collected charge measured at 300 V in n- and p-type FZ, MCz and EPI silicon samples irradiated with 24 GeV/c protons. For better visibility error bars are not included. The error in the collected charge is about 3%.

the effective trapping probabilities (compare chapter 8.1). For easier comparison with samples irradiated with protons and neutrons, in Fig. 7.21 also the charge collected at 300 V is added.

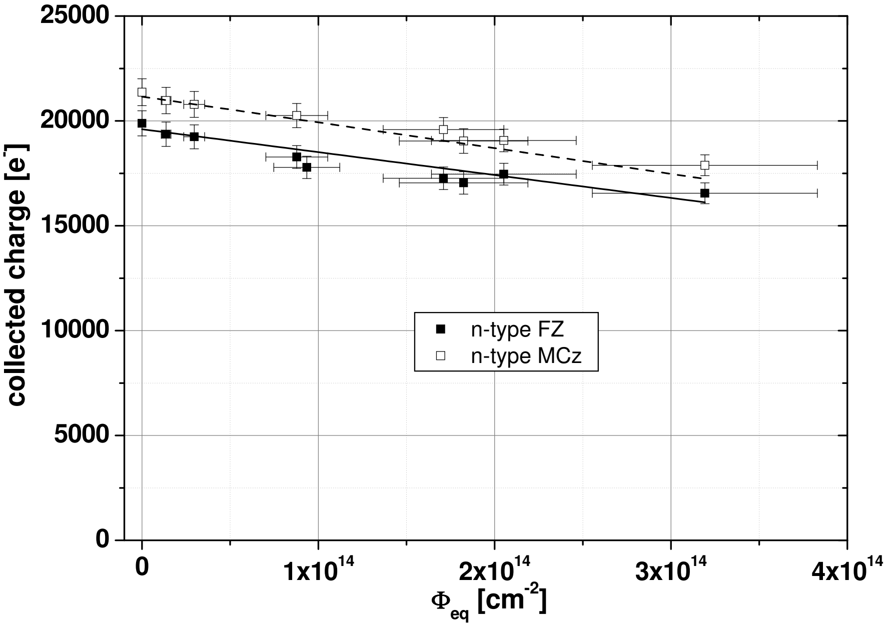

Figure 7.20: Maximum charge collected in n-type FZ and MCz irradiated with 200 MeV pions.

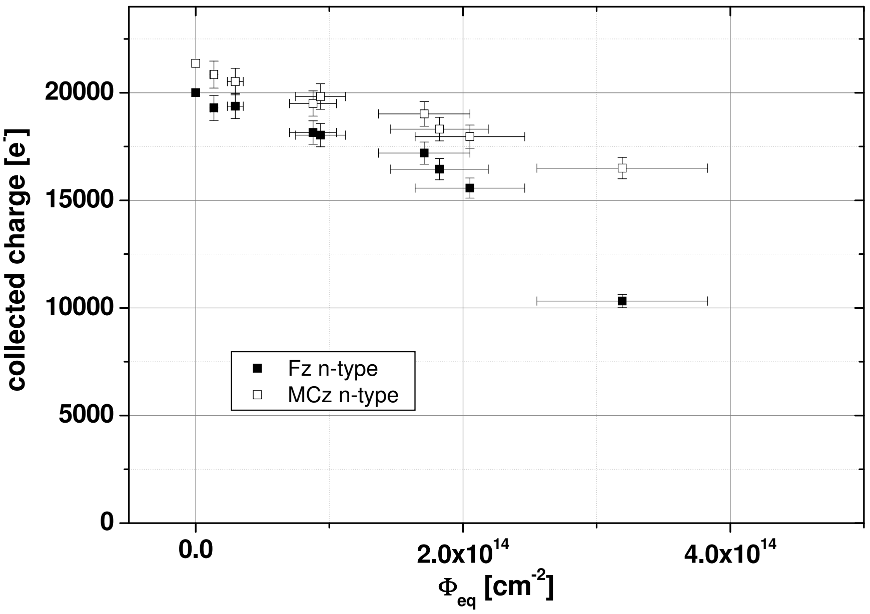

Figure 7.21: Charge collected at 300 V in n-type FZ and MCz irradiated with 200 MeV pions.

Chapter 8

TCT Measurements

In this chapter first the effective trapping times in MCz, FZ and 150 μm EPI measured by using the Transient Current Technique (TCT) is presented for samples irradiated with 24 GeV/c protons, reactor neutrons and 200 MeV pions (chapter 8.1). Then the TCT curves corrected for trapping with the values of τ_{eff} found for each diode is evaluated to determine the position of the dominant junction in the diode and thereby the sign of the space charge in the bulk (chapter 8.2), which in turn influences the sign of the effective generation rate g_c obtained from the development of the effective space charge with fluence (see chapter 6).

8.1 Effective trapping probability

The effective trapping probability, i.e. the inverse trapping time $1/\tau_{eff}$, increases linearly with fluence according to [Kra01]

$$\frac{1}{\tau_{eff,h,e}} = \beta_{h,e}\Phi_{eq} \tag{8.1}$$

.

β depends on annealing time and temperature. The measurement temperature influences the probability of trap occupation, the thermal velocity and the carrier capture cross section whose temperature dependence is poorly known. A simplified parametrization was therefore suggested after measurements of β between 223 and 293 K [Kra01]:

$$\beta_{e,h}(T) = \beta_{e,h}(T_0) \cdot (\frac{T}{T_0})^{\kappa_{e,h}} \tag{8.2}$$

with κ_e = (-0.86 ± 0.06) and κ_e = (-1.52 ± 0.07). Slightly higher values were found for a temperature range of 260-275 K in [Bat05b]. All measurements in this work were performed at room temperature (20-22 °C) and comparison values from literature were corrected to this measurement temperature using the values for κ found in [Kra01].

Annealing studies on the effective trapping probability have shown that for at least the first 60 min of annealing at 60 °C [Kra01] and 40 min at 80 °C [Bat05a] β does not change for both electrons and holes. Slightly different annealing steps at which the trapping time was measured, e.g. days at room temperature [Kra01], 30 min at 80 °C [Lan08], 4 min at 80 °C [Bat05a], do therefore not prohibit a direct comparison of the β values obtained. All samples in this work were annealed for 4 min at 80 °C and kept in the freezer between measurements.

The main source for uncertainty is not the measurement itself even though the position and intensity of the induced laser pulse varied, but the sensitivity of τ_{eff} to the integration interval and the range of bias voltages used to determine the slope of $Q(U)$ in the Charge Correction Method (compare chapter 5.3.2). Various time windows for the integration interval were therefore tested for each diode ranging from directly at the beginning and the end of the pulse to a few nanoseconds before and after. Similarly the bias voltages included in the fit were varied starting from a minimum of 40 V above depletion. From this the error in the effective trapping time for each diode was estimated. Overall it lies between 10 and 15 % with occasional higher uncertainties in diodes where the voltage range that could be used was limited due to diode break down and increased bias current. In general the determination of the effective trapping time in diodes irradiated with equivalent fluences below 3 x 10^{13} cm^{-2} is difficult since the trapping times are very long (or the trapping probilities very low) and the gradient in $Q(U)$ is barely noticeable already before correction. The trapping times from these samples were therefore only included for determining β if the results were stable with variation in both the integration interval and the bias voltage range used.

Similarly the determination of the effective trapping probability at an equivalent fluences of 3 x 10^{15} cm^{-2} and above was not possible. The bias current was too high to be able to reach depletion in 300 μm thick samples and additionally the trapping time at this fluence range is expected to be around 1 ns, which limits the measurement range in 150 μm EPI material. For these samples the active volume and therefore the bias current is lower and at least after neutron irradiation also the increase of the depletion voltage with fluence is slow, so the voltage range needed for the extraction of τ_{eff} could be reached. The trapping time however is in the order of the rise time of the signal and varies greatly with bias voltage range and integration interval used. Hence these values can also not be included when calculating β.

The proportionality constant β for electrons and holes was evaluated for n- and p-type FZ, MCz and EPI irradiated with protons, neutrons and pions separately (compare Tab. 8.1). Measurements of the hole signal in n-type and the electron signal in p-type were only possible in samples that allowed back side illumination, which was only the case in n-type FZ and MCz and p-type MCz produced by HIP. In EPI, due to the structure of the diode which consists of an active layer on a substrate, only the signal created on the front side of the diode could be measured. As mentioned in previous chapters, MCz p-type

	β_e $[10^{-16}cm^2ns^{-1}]$	β_h $[10^{-16}cm^2ns^{-1}]$
24 GeV/c **protons**		
FZ-n	4.95 ± 0.13	6.33 ± 0.21
FZ-p	–	5.97 ± 0.18
MCz-n	4.87 ± 0.14	5.84 ± 0.22
MCz-p	4.66 ± 0.18	5.62 ± 0.30
EPI-n	5.62 ± 0.33	–
EPI-p	–	6.15 ± 0.20
reactor neutrons		
FZ-n	3.66 ± 0.15	4.79 ± 0.18
FZ-p	–	4.68 ± 0.15
MCz-n	3.61 ± 0.15	4.61 ± 0.33
MCz-p	–	–
EPI-n	3.90 ± 0.25	–
EPI-p	–	4.35 ± 0.25
200 MeV **pion**		
FZ-n	5.08 ± 0.27	6.77 ± 0.42
MCz-n	4.72 ± 0.31	6.26 ± 0.34

Table 8.1: β for electrons and holes in n- and p-type FZ, MCz and 150 μm EPI samples irradiated with 24 GeV/c protons, reactor neutrons and 200 MeV pions. Measurements were taken at room temperature after 4 min of annealing at 80 °C. The determination of the electron signal in p-type FZ and EPI and the hole signal in n-type EPI was not possible since the diode structure allowed no back side illumination. Due to diode break through at 200-300 V no clear values for β could be obtained from neutron irradiated p-type MCz.

from HIP showed a strong increase in reverse current between 200 and 300 V. It was therefore not possible to reach high enough bias voltages to determine the trapping time after neutron irradiation with more than 1 x $10^{14}\,cm^{-2}$. In the two sample irradiated with lower neutron fluence τ_{eff} for electrons obtained by using the charge correction method is lower and therefore the trapping probability higher than in all other materials (compare Fig. 8.2(b)), whereas the trapping time for holes agrees with what was found for FZ and EPI. Due to the small number of measurement points it is however not clear whether this is an artifact caused by the poor diode quality or shows an actual difference in response to neutron irradiation.

As already established in previous studies, the effective trapping time does not depend on wafer production method or silicon type [RD510]. Only for proton irradiated n-type EPI β_e is slightly higher than what would be expected. It has to be kept in mind though that the electron signal in 150 μm EPI is the most challenging to measure due to the higher mobility of electrons compared to holes and the shorter drift length compared to 300 μm samples. This, especially at high bias voltages, results in a signal length that is close to the limits of the setup with respect to rise time and time resolution of the pulse. Other studies on the trapping time in 150 μm EPI and EPI-DO up to proton fluences of 3 x 10^{15} cm^{-2}

found no differences to FZ, with β_e equal to (4.9 ±0.4) x 10^{16} $cm^2\ ns^{-1}$ [Lan08].

	β_e $[10^{-16} cm^2 ns^{-1}]$	β_h $[10^{-16} cm^2 ns^{-1}]$
24 GeV/c protons		
without EPI-n	4.91 ± 0.08	6.09 ±0.1
with EPI-n	5.11 ± 0.11	
from literature	4.83 ± 0.46	5.6 ± 0.85
reactor neutrons		
without EPI-n	3.62 ± 0.10	4.44 ±0.08
with EPI-n	3.84 ± 0.09	
from literature	3.19 ± 0.55	3.99 ± 0.85
200 MeV pions		
	5.13 ± 0.80	6.28 ±0.11

Table 8.2: β for electrons and holes from a combined fit of all materials irradiated with 24 GeV/c protons, reactor neutrons and 200 MeV pions. Since β_e for n-type EPI was found to be higher than in other materials, also the β_e value obtained by combining only FZ and MCz is included (see text). The values from literature were taken from [RD510] but corrected to room temperature.

In Figs. 8.1, 8.2 and 8.3 that show τ_{eff} after irradiation with protons, neutrons and pions respectively, the results from FZ, MCz and 150 μm EPI samples are therefore combined and Tab. 8.2 lists the values of β from a combined fit to the effective trapping probabilities of electrons and holes measured in all silicon types. For β_e two values are quoted, the higher one includes data points from n-type EPI, whereas the lower one was obtained without these more uncertain measurements. β in samples irradiated with 24 GeV/c protons and 200 MeV pions is very similar, which agrees well with CCE measurements, where in this rather limited fluence range no difference in the decrease of collected charge after irradiation with these two hadron types is seen (compare chapter 7.1).

Neutron irradiated samples on the other hand show a slower increase of trapping probability with fluence for both electrons and holes. While this was also observed in [Kra02], where both irradiation types were compared, and is visible after combining the values for β from various groups (compare the values obtained from literature in Tab. 8.2), it is not reflected in the collected charge after irradiation with reactor neutrons. No significant differences to charged hadron irradiated diodes can be seen. In [Kra10a] however a larger fluence range was tested and the expected higher collected charge in neutron irradiated samples was observed.

The increase of trapping probability with fluence is between 20 and 30 % faster for holes than for electrons for both charged hadrons and neutrons. Only in 150 μm EPI no clear difference between β_e and β_h is seen mainly due to the high β_e mentioned before. A similar behaviour was indicated for neutron irradiated p-type MCz and FZ in [Cin09], where the differences between the two charge carriers were very small. In both cases however no clear conclusion can be drawn due to large errors in the fit.

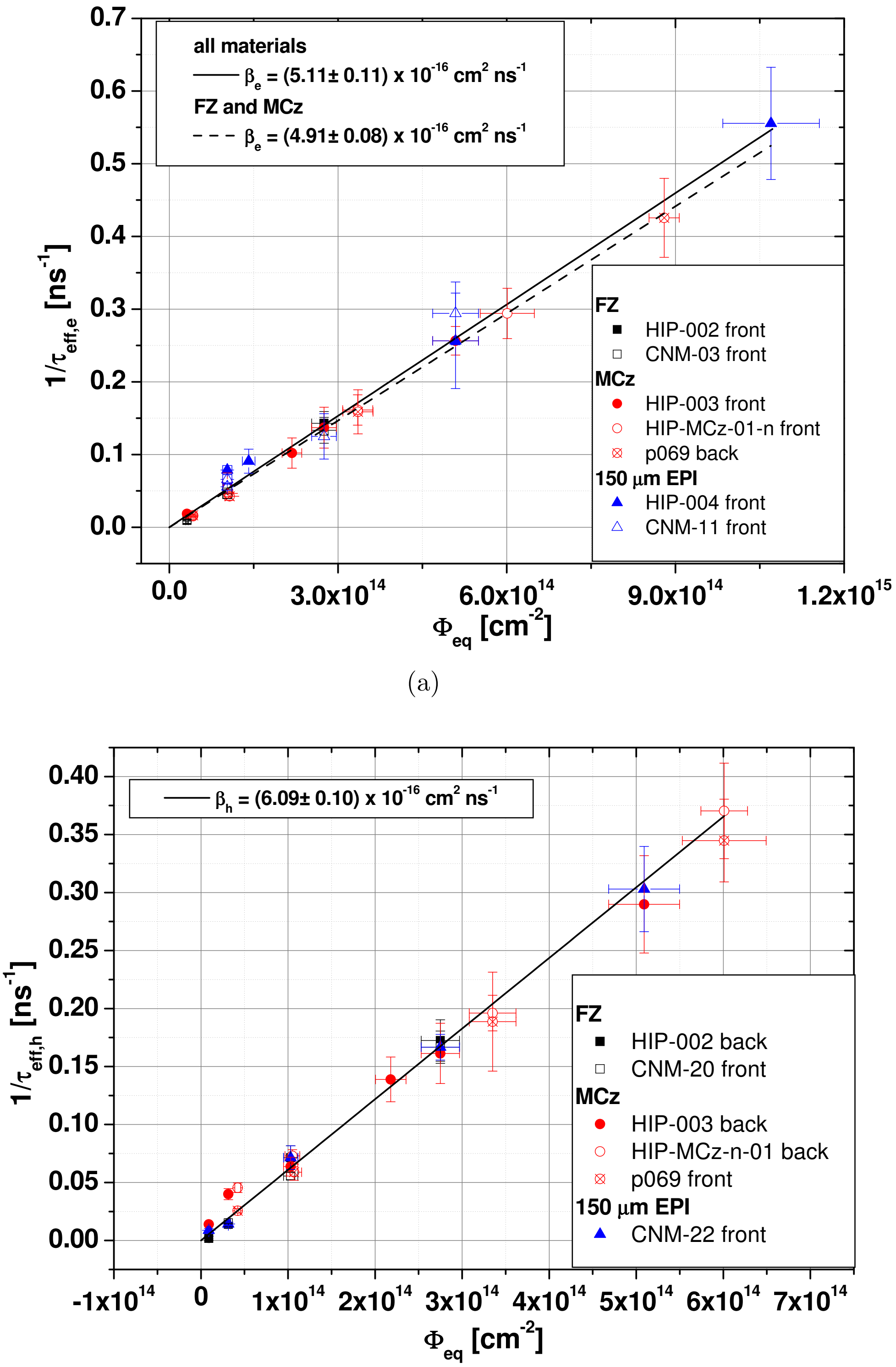

(a)

(b)

Figure 8.1: Fluence dependence of the effective trapping probability for (a) electrons and (b) holes in n- and p-type FZ, MCz and EPI irradiated with 24 GeV/c protons. τ_{eff} was measured at room temperature after annealing of 4 min at 80 °C.

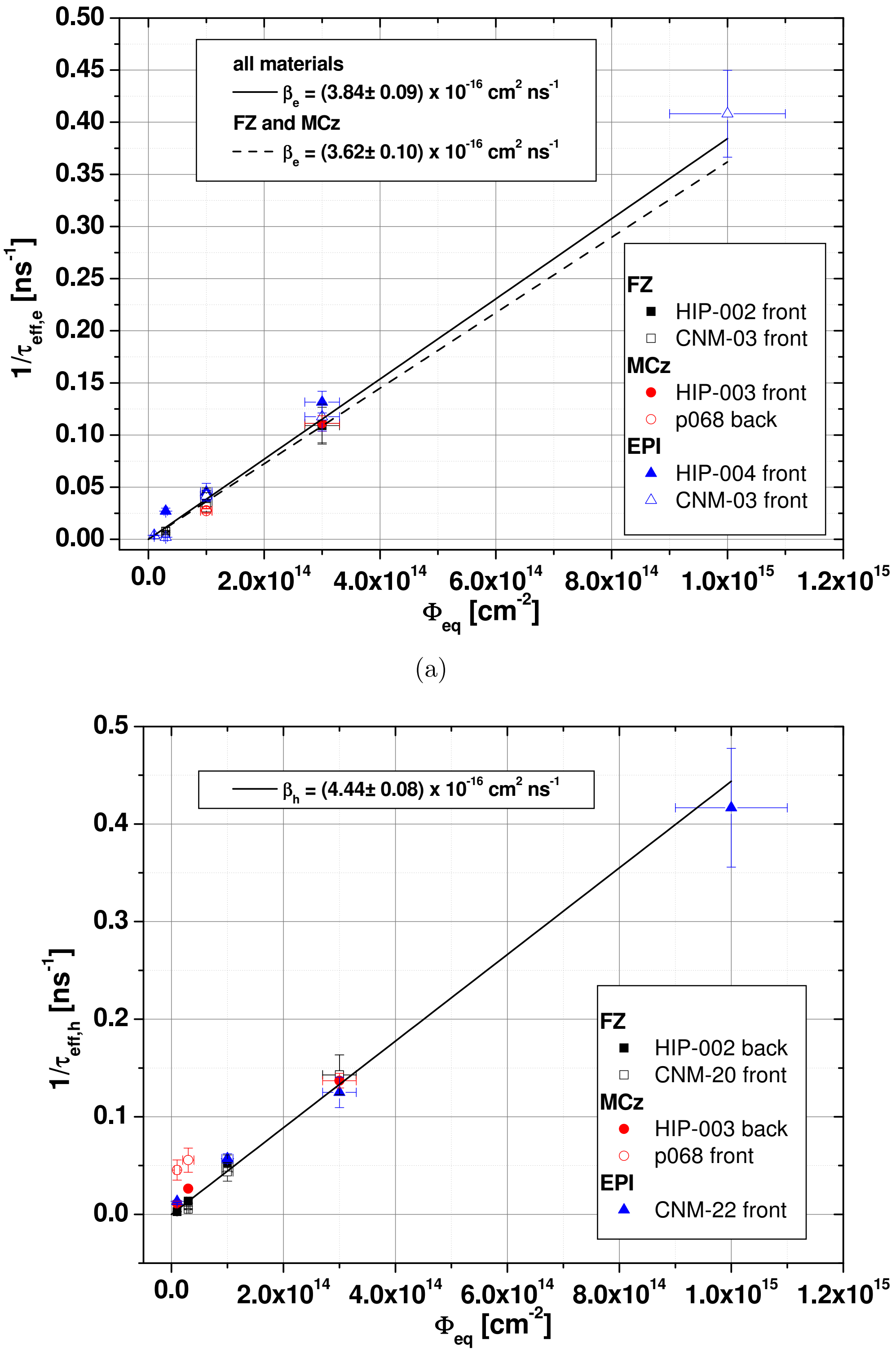

(a)

(b)

Figure 8.2: Fluence dependence of the effective trapping probability for (a) electrons and (b) holes in n- and p-type FZ, MCz and EPI irradiated with reactor neutrons. τ_{eff} was measured at room temperature after annealing of 4 *min* at 80 °C.

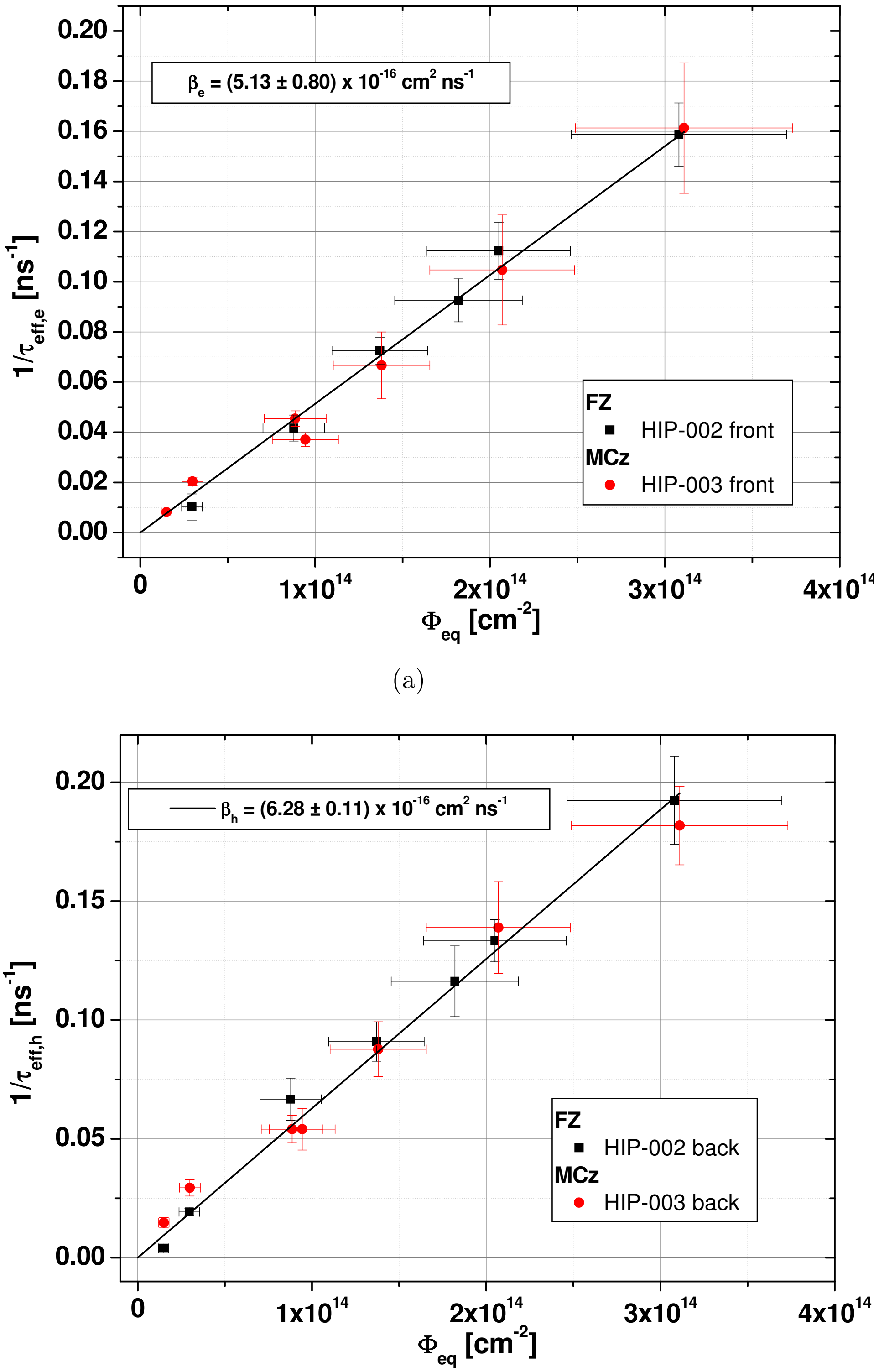

(a)

(b)

Figure 8.3: Fluence dependence of the effective trapping probability for (a) electrons and (b) holes in n-type FZ and MCz irradiated with 200 MeV pions. τ_{eff} was measured at room temperature after annealing of 4 min at 80 °C.

Correcting the values for β_e and β_h given in [RD510], obtained from combining the results from several publication, to room temperature as included in Tab. 8.2 shows that the trapping times found here lie at the higher end of the spectrum.

8.2 Space Charge Sign

As indicated in chapter 6, CV and IV measurements performed to determine the depletion voltage and thereby $|N_{eff}|$ do not give information on the sign of effective space charge after irradiation with various particle types that can introduce differently charged defects in the silicon bulk. In the following TCT measurements with a red laser will be used to look at the electric field in the diode and by examining the position of the dominant junction, the space charge will be determined.

Illumination of the p+ side in n-type and the n+ side in p-type material, i.e. the front side of the diode, leads to electron injection in n-type and hole injection in p-type material (see chapter 5.3.2). Illumination of the n+ side in n-type and the p+ side in p-type, i.e. the backside of the diode, on the other hand creates a hole signal in n-type and an electron signal in p-type. Whereas all detectors had a hole in in the aluminum layer on the front, backside illumination was only possible in few samples where instead of full backside metalization, a grid allowed the laser light to enter the active area of the diode.

Irradiation can cause a change in the space charge in the diode thereby shifting the dominant junction from the front side to the back of the diode. If this Space Charge Sign Inversion (SCSI) occurs n-type material with positive space charge becomes like p-type with negative space charge in the bulk and vice versa for p-type.

As soon as defects that can act as traps are introduced by irradiation, charge carriers are lost for the measurement on their way through the diode. Without correction for trapping the signal height diminishes with distance from the creation point of the charge carriers and no reliable conclusion on the electric field can be reached. The TCT signal measured from illuminating the front- or backside of the diode with a red laser pulse therefore has to be corrected for trapping with the appropriate value of τ_{eff} to simulate a trap-free detector, which increases the second peak in the signal and gives a more accurate picture of the position of the dominant junction (compare also chapter 5.3.2).

However, as shown in the previous chapter, trapping times measured by different groups vary to a great extent, which can lead to different interpretation of the electric field structure in diodes of the same material, irradiated together [Kas09] (see also section 8.2.2). Wherever advisable the uncorrected signal will therefore be shown in addition to the corrected curves. In cases where SCSI is obvious already from the uncorrected pulse, i.e. the dominant junction has clearly moved, no correction that would only enhance the dominant peak on the backside of the diode, will be applied.

FZ, MCz and 150 μm EPI will be discussed separately in chapters 8.2.1, 8.2.2 and 8.2.3, while a summary on the sign of the space obtained from TCT measurements is given in Tab. 8.3.

silicon type	**radiation**	**space charge**
Fz		
n-type	proton	pos. to neg.
n-type	neutron	pos. to neg.
n-type	pion	pos. to neg.
p-type	proton	stays neg.
p-type	neutron	stays neg.
MCz		
n-type	proton	?
n-type	neutron	pos. to neg.
n-type	pion	?
p-type	proton	?
p-type	neutron	stays neg.
150 μm EPI		
n-type	proton	stays pos.
n-type	neutron	pos. to neg.
p-type	proton	neg. to pos.
p-type	neutron	stays neg.

Table 8.3: Summary of TCT results on the sign of the space charge in FZ, MCz and 150 μm EPI irradiated with 24 GeV/c protons, reactor neutrons and 200 MeV pions. No clear conclusion could be reached for MCz irradiated with fast charged hadrons (for a discussion of this problem see chapter 8.2.2).

8.2.1 FZ

Already at low proton fluences of about 5 x 10^{13} cm^{-2} the prominent peak is on the backside of an n-type FZ diode even in the uncorrected electron signal (Fig. 8.4 (a)). The electrons therefore move from a low field region on the front to a high field region close to the back of the detector. This indicates that the dominant junction is now at the backside of the diode and space charge sign inversion has occurred. Likewise, when looking at the trapping corrected hole signal obtained by back side illumination, a decrease of the current with time is seen in the TCT curve, again showing that the high field region has moved to the back side (Fig. 8.4 (b)).

Irradiation with 24 GeV/c protons therefore introduces acceptors in FZ silicon that convert the positive space charge in n-type to 'p-type'. In p-type FZ, where the space charge is negative to begin with, more negative charge is introduced and no change in the position of the dominant junction is observed: the hole signal obtained by front side illumination decreases with time while the holes move from the high to the low field region (Fig. 8.5). The electron signal could not be measured since back side illumination was not possible.

FZ irradiated with a higher proton fluence of 4.43 x $10^{14} p/cm^2$ shows a pronounced double peak structure at voltages around depletion (Fig. 8.6). At higher bias voltages one peak becomes dominant again. This so called *double junction* has been observed in several materials (compare e.g. for EPI chapter 8.2.3). Its formation is thought to be due to high levels of reverse current and therefore large number of free charge carriers in these diodes [Ere02]: the overall current density throughout the diode is constant, but the ratio of electrons to holes that contribute to it varies locally. Deep level trapping centers close to the front- and backside can be occupied by these charge carriers, which in turn can cause local space charge sign inversion and the formation of a second p-n junction.

In Fig. 8.7 the electron and hole signal of a n-type FZ diode from the same wafer as presented in Fig. 8.4 but irradiated with pions instead of protons with an equivalent fluence of 2.96 x 10^{13} cm^{-2} is shown to make a comparison between these hadron types possible. As expected from previous results no differences in response can be seen. Also here SCSI is obvious from the uncorrected electron and the trapping corrected hole signal. The difference in signal height is caused by variations in the laser intensity that was controlled by a shutter system and not constant during the measurement series.

Neutron irradiation introduces negative space charge in nearly all silicon materials. As after pion and proton irradiation, n-type FZ again shows space charge sign inversion and a dominant peak on the backside of the diode (Fig. 8.8). Using Figs. 8.9 and 8.6 a direct comparison between n-type FZ samples irradiated to a similar equivalent fluence of about 3 x $10^{14} cm^{-2}$ with neutrons and protons is possible.

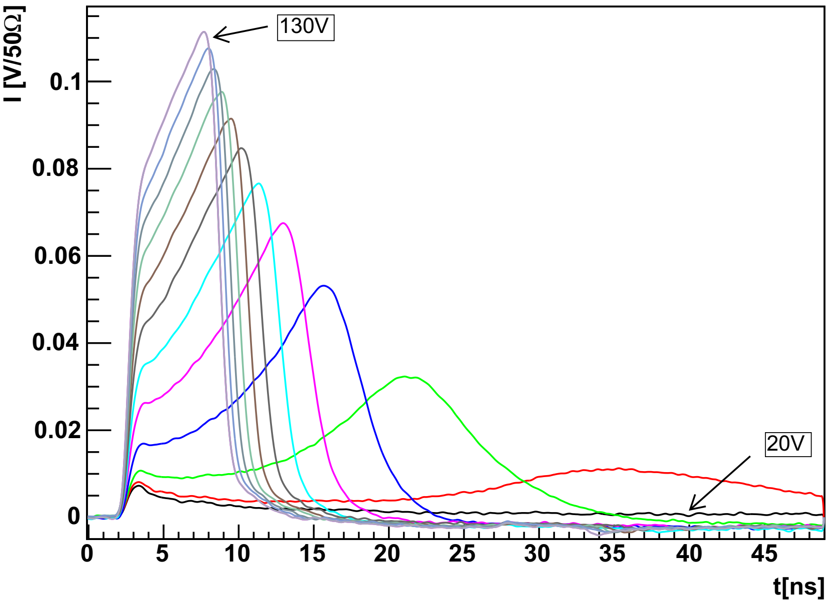

(a)

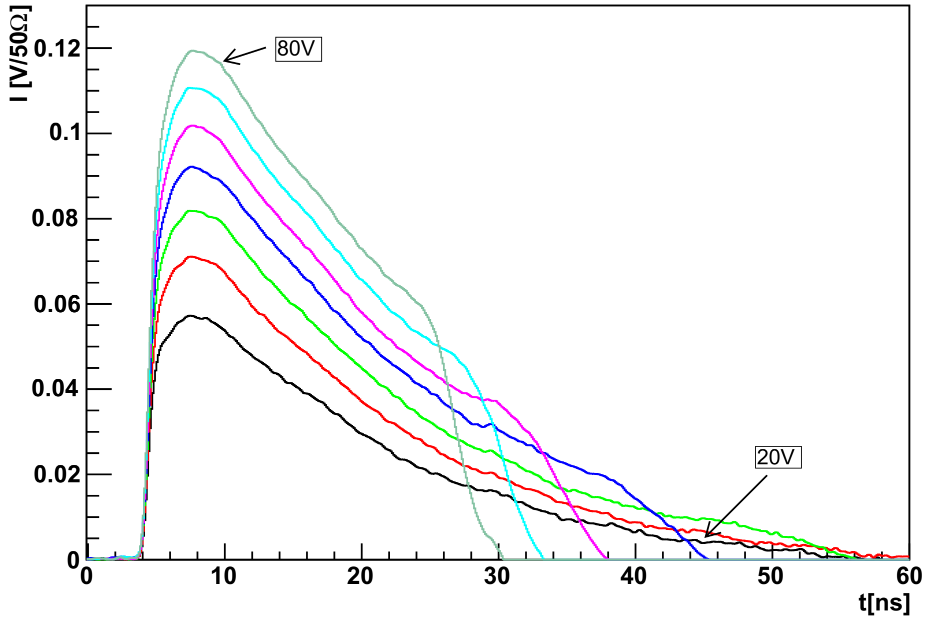

(b)

Figure 8.4: n-type FZ (HIP-002-C) irradiated with 5.06 x 10^{13} p/cm^{-2}. (a) Electron signal (front/p+ illumination), 10 V step size, no correction. V_{fd} as obtained from the Q(U) curve of the TCT signal is 41 V. (b) Hole signal (back/n+ illumination), 10 V step size , corrected with τ_{eff} = 72ns. V_{fd} = 46 V.

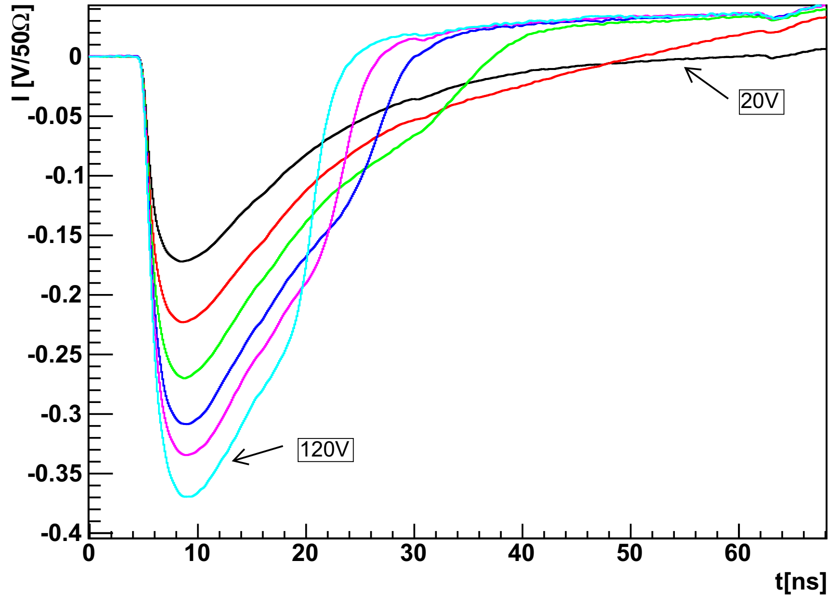

Figure 8.5: Hole signal (front/n+ illumination) in p-type FZ (CNM-20) irradiated with a proton fluence of 5.06 x $10^{13} p/cm^{-2}$ corrected with τ_{eff} = 66ns, 20 V steps. V_{fd} = 48 V.

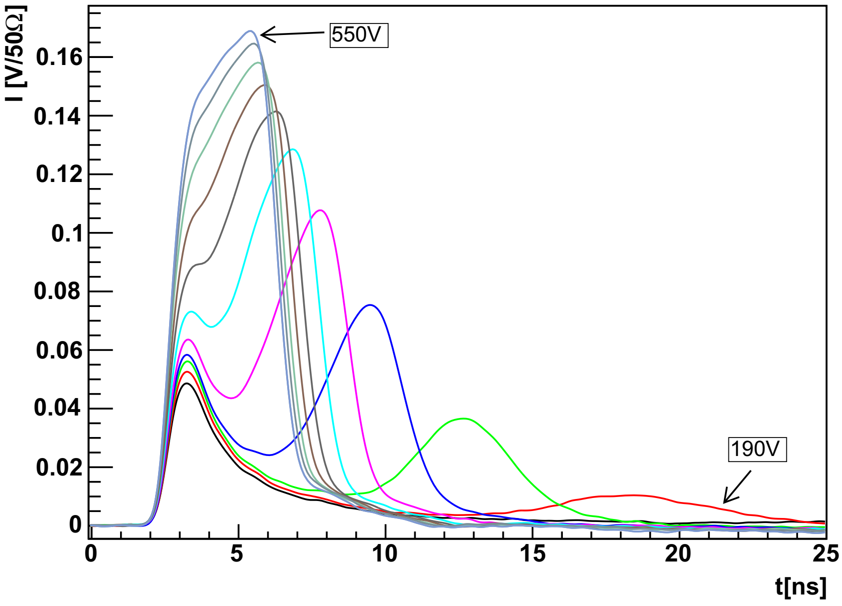

Figure 8.6: Electron signal (front/p+illumination) in n-type FZ (HIP-C) irradiated with a proton fluence of 4.43 x 10^{14} p/cm^2, no correction, 40 V steps, $V_{fd}(TCT) = 316$ V.

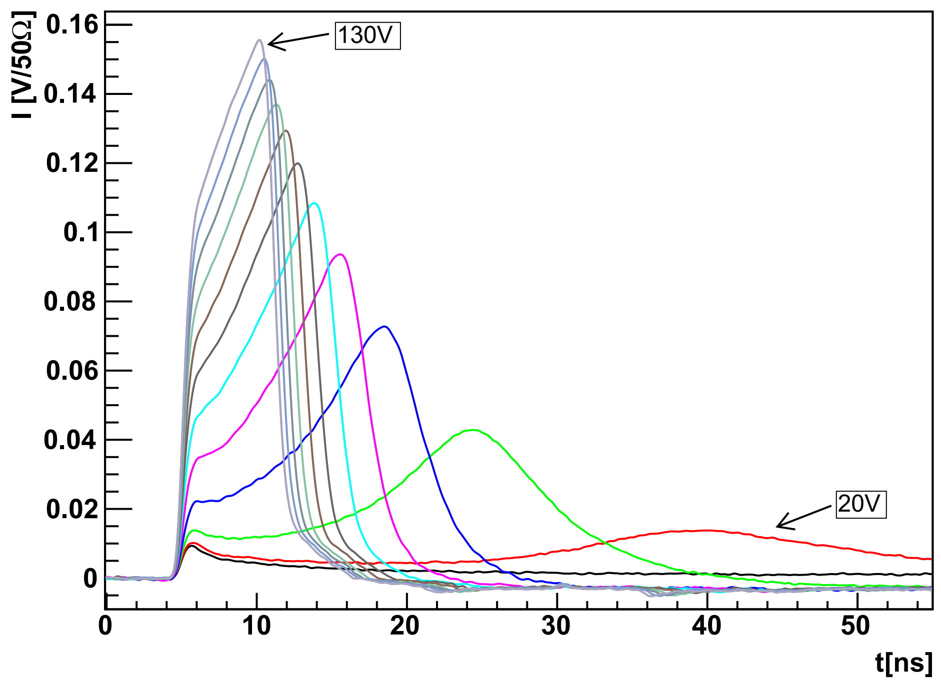

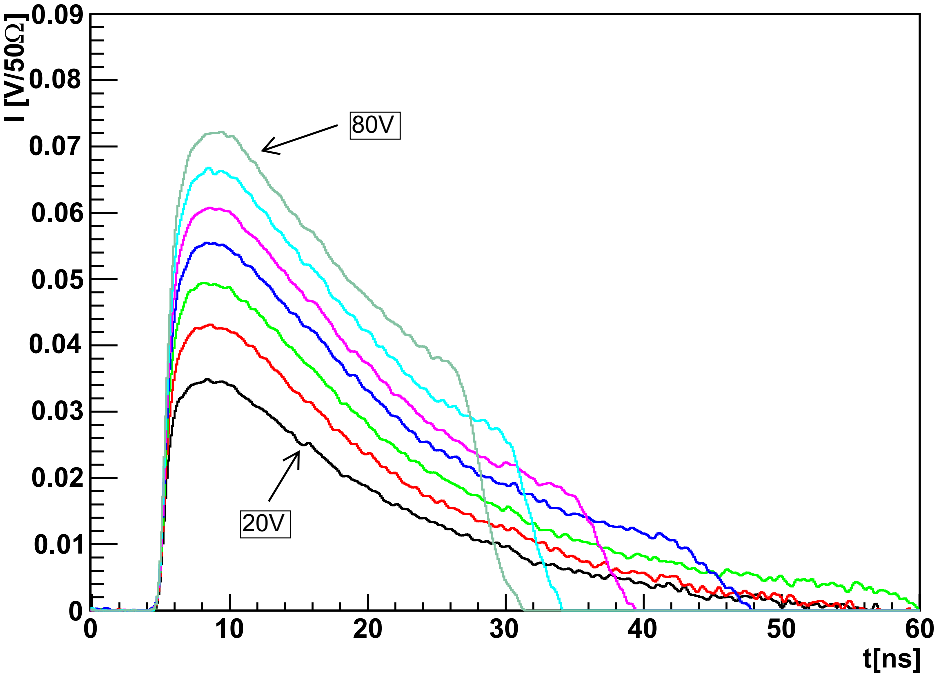

Figure 8.7: n-type FZ (HIP-C) irradiated with a pion fluence 2.6 x 10^{13} cm^{-2}. (a) Electron signal (front/p+ illumination), 10 V step size, no correction. V_{fd} as obtained from the Q(U) curve of the TCT signal is 42 V. (b) Hole signal (back/n+ illumination), 10 V step size , corrected with τ_{eff} = 52ns. V_{fd} = 44 V.

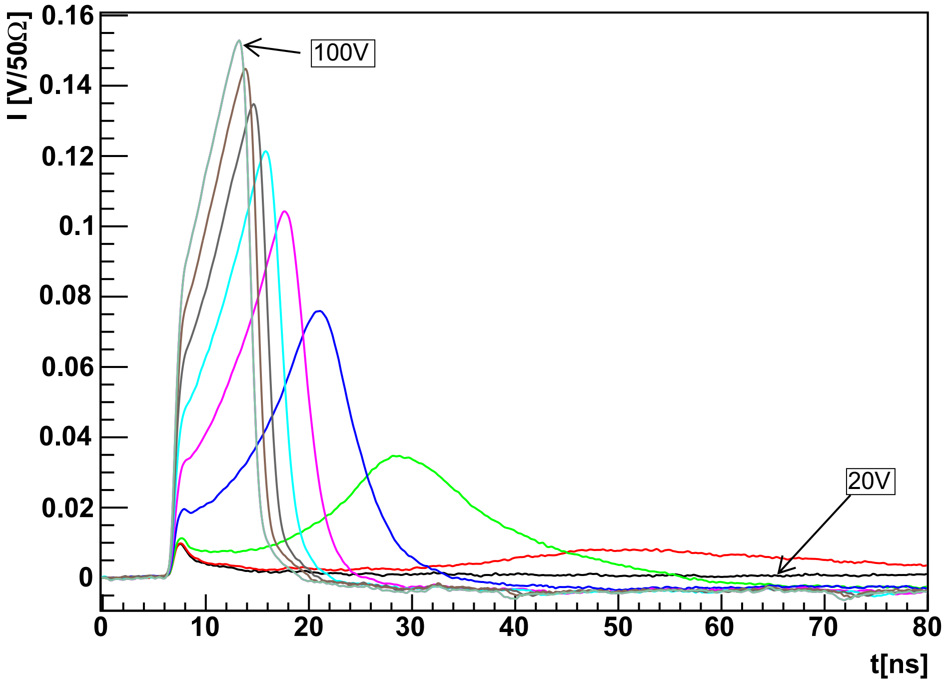

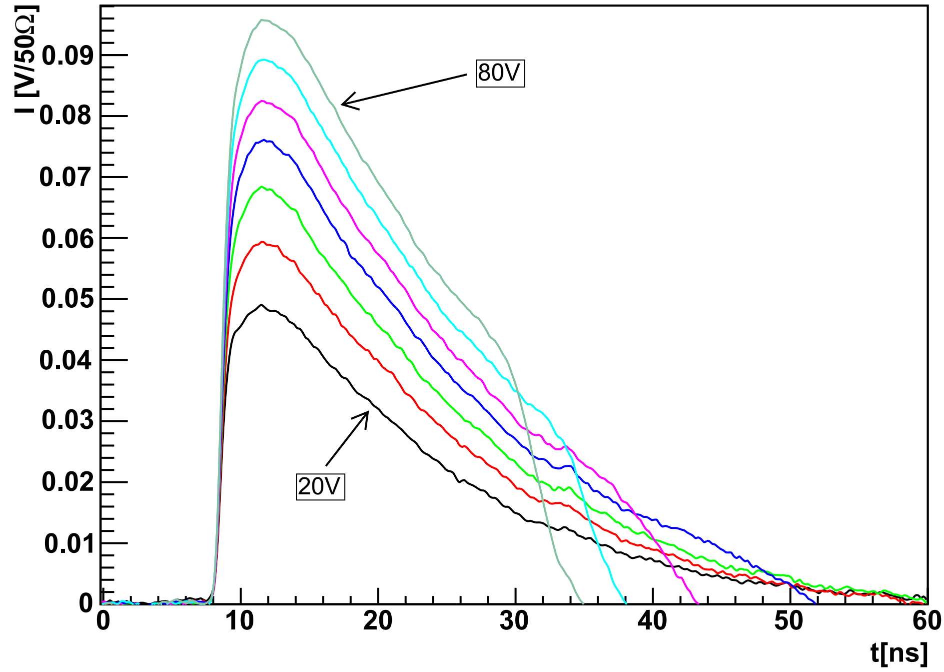

Figure 8.8: n-type FZ (HIP-C) irradiated with a neutron fluence of 1 x $10^{13}\ cm^{-2}$. (a) Electron signal (front/p+ illumination), 10 V step size, no correction. V_{fd} as obtained from the Q(U) curve of the TCT signal is 41 V. (b) Hole signal (back/n+ illumination), 10 V step size , corrected with τ_{eff} = 72ns. V_{fd} = 46 V.

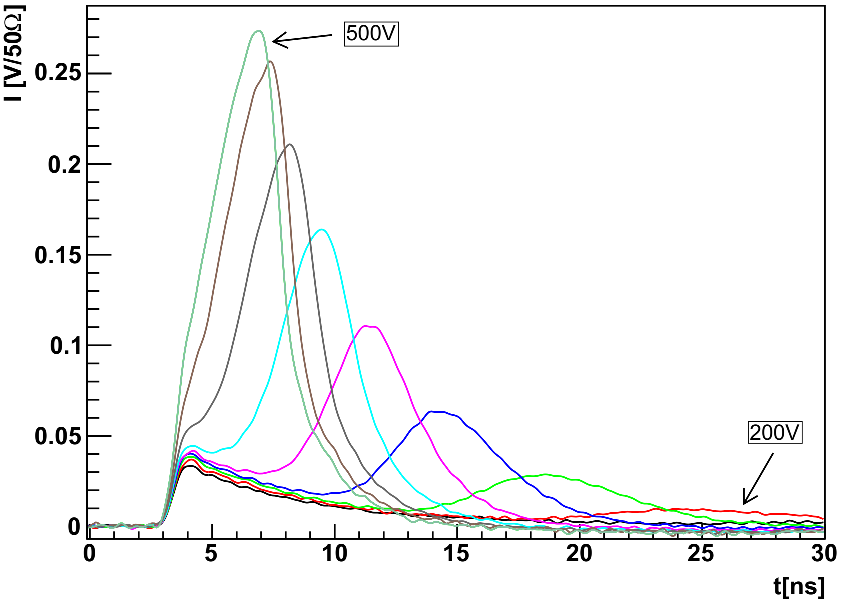

Figure 8.9: n-type FZ (HIP-B) irradiated with a neutron fluence of 3 x 10^{14} cm^{-2}, no correction, step size 20 V.

8.2.2 MCz

Whereas in both FZ and EPI the development of the dominant junction with fluence can quite clearly be determined from TCT measurements with red laser pulses, the results obtained for MCz by various groups have proven to be inconclusive and will therefore be discussed in more detail in the following. In addition also the sign of the space charge extracted from annealing studies will be taken into account, since especially at high fluences the interpretation of the electric field after trapping correction is very sensitive to small variations in the at this point already very low trapping times.

In order to clarify the situation and to determine the structure of the electric field in MCz after irradiation with fast hadrons, a batch of n- and p-type MCz samples from HIP and SMART were irradiated with 24 GeV/c protons and then distributed to different groups for measurements [Pac08], [Kas09], [Li 10], [Pac10a]. HIP samples could be illuminated from both sides, whereas SMART samples only had an opening on the front side of the diode. Since small variations in annealing times caused by transport and individual measurement procedures are not expected to influence the results, it should be assumed that all groups would reach similar conclusions from the distributed samples. However, while [Li 10] finds peaks of equal height on the front and back side of the diode for both n- and p-type material at fluences above 3 x $10^{14}\,p/cm^2$, [Pac08] also reports nearly equal peaks for n-type, but a dominant backside peak for p-type already at 5.4 x $10^{14}\,p/cm^2$.

To investigate the contradictions in the above mentioned studies further, one n- and one p-type MCz sample from the common irradiation project, irradiated with 9.73 x $10^{14}p/cm^2$ was chosen as a comparison point, since for this fluence [Li 10] provides both the uncorrected and trapping corrected TCT curve. By using this data it could be confirmed that the uncorrected electron and hole curves had the same shape when measured with different setups [Kas09]. No uncorrected TCT curves were included in [Pac10a].

At high fluences correction for trapping is necessary to ensure a correct interpretation of the TCT signal when determining the shape of the electric field in the diode. In [Li 10] an average τ_{eff} of 4.58 ns was chosen for both electrons and holes to correct for trapping at this fluence, which lead to a TCT signal with equal peaks on the front and back side of the diode for n- and p-type MCz samples processed by HIP. In [Pac08] for n-type, corrected with τ_{eff} = 3.9 ns, the result is similar, for p-type however, corrected with τ_{eff} = 3 ns, the backside peak is dominant. No backside illumination was possible in the samples produced by SMART that were used in this study.

In addition to correcting the TCT signal with different trapping times, the above mentioned studies do not include the same bias voltage range for the different silicon types. While [Li 10] only presents one hole and one electron signal close to depletion (for the bias voltages compare [Li 08]), [Pac08] extends the voltage range to a bias voltage of 500 V and therefore well above depletion.

For further investigations a closer look at the trapping times is necessary. For the two samples measured at CERN, trapping times of (3.4 ± 0.4) ns and (2.8 ± 0.3) ns for electrons and holes respectively were found. From the average values for β presented in [RD510] a range of 2.6-3.5 ns for holes and of 3.1-3.8 ns for electrons for this fluence is obtained. Both the trapping times found at CERN and in [Pac08] lie within this range, whereas $\tau_{eff} = 4.58$ ns as used in [Li 10] considerably higher.

Applying these different trapping times to the TCT curves measured at CERN while at the same time including several bias voltage steps gives further insight into the source of the discrepancies between the two above mentioned studies. Figs. 8.10 and 8.11 show the results for n- and p-type MCz respectively. In the first row the uncorrected TCT curves are presented. Here, as expected, the main peak is close to the front side of the diode and only a small peak is visible close to the backside. Correcting these curves with a trapping time of 4.58 ns shows an equal peak structure for the bias voltages used in [Li 10], but a dominant second peak for higher voltages. Similarly, if the lower trapping times presented in [Pac08] are used and the appropriate bias voltages are compared, the conclusions of this group can be reached. It is therefore obvious that the different interpretations of the data arise solely from corrections applied after measurement and variations in the presented bias voltage ranges, but not from actual differences in the raw measurement data. This implies that neither the processing of diodes by different companies nor the use of different measurement setups changes the outcome of the measurement, which in principle makes it possible to directly compare results from different groups as long as the raw data is also included in the publication and a range of possible trapping times are applied.

In the specific case of MCz however, further problems arise from correcting the data with the trapping times found here and in [Pac08]. The low trapping time or high trapping probability increases the second peak in the electron signal in n-type (front side illumination), indicating a strong negative space charge that becomes clearly dominant at very high bias voltages, where it gives a hint towards SCSI. In the hole signal on the other hand even before correction the second peak, close to the front side of the diode, is dominant, which would imply that the space charge stays mainly positive and the main junction on the front of the diode (compare Fig. 8.10). In p-type where the roles of electrons and holes are inverted, the results are similar (compare Fig. 8.11). Similar contradicting results however are also obtained with $\tau_{eff} = 4.58$ ns when looking at high bias voltages well above depletion, where the equal peak structure vanishes.

Another possibility for investigating the sign of the space charge in silicon samples is performing an annealing study, thereby looking at the development of the depletion voltage or $|N_{eff}|$ after several heating steps at a constant temperature. For 24 GeV/c proton irradiation annealing studies showed that n-type MCz behaves like samples with positive space charge up to a fluence of 2.59 x 10^{15} p/cm^2 [Pel05] [Pac10a]: the depletion voltage rises during the first annealing steps before decreasing again. One would therefore expect to find SCSI in p-type MCz due to the introduction of positive charge by effective donors similar to what is seen in 150 μm EPI. The annealing curves of p-type presented in [Pac10a] seem to show a different picture according to the interpretation of the author. Up to a fluence of 1.42 x 10^{15} p/cm^2 he sees typical p-type behavior with so-called beneficial annealing where the depletion voltage decreases in the early stages of the annealing process before increasing again. Only at the very highest fluence step of 2.59 x $10^{15}\,p/cm^2$ the annealing curve becomes similar to what is seen in n-type material, indicating SCSI. Measurements in this region are however limited by the high bias voltages, which makes it impossible to directly extract the depletion voltage from the CV curve without extrapolation. Overall this interpretation relies heavily on the very first annealing step, where the effective space charge visibly decreases in samples irradiated to fluences lower than 2.59 x $10^{15}\,p/cm^2$. However, $|N_{eff}|$ does stay practically constant up to about 50 min of annealing afterwards. This, together with an increase in effective space charge with fluence at a constant annealing time seems to indicate positive rather than negative space charge. It is therefore difficult to give a final evaluation of these annealing curves.

These results can be to compared to observations in MCz after mixed particle irradiation [Kra08a], [Kra08b] [Kra09]. If n-type MCz irradiated with charged hadrons is irradiated again but this time with neutrons that introduce negative space charge, the depletion voltage decreases as would be the case if the space charge was positive after the first irradiation step. In p-type MCz on the other hand the depletion voltage increases after neutron irradiation and therefore the space charge after the initial proton irradiation has to be negative. At the highest fluence step however the increase is smaller than expected from an additive damage. This could be explained by a double junction at high fluences, where the positive space charge region compensates the negative space charge introduced by neutron irradiation, which agrees with the fact that at very high fluences n-type like annealing behavior is seen in p-type MCz [Pac10a] [Kra09].

In 200 MeV pion irradiated n-type MCz also no clear determination of the dominant junction with TCT measurements is possible. As an example Fig. 8.12 shows the curve shapes for the highest available neutron equivalent pion fluence of 3.11 x $10^{14}\,cm^{-2}$ before and after correction for trapping. Like in proton irradiated samples, the electron signal indicates an equal peak structure around depletion with the second peak becoming dominant at higher bias voltages. The hole signal on the other hand, while also showing two peaks, points towards a dominant junction on the p+/front side of the diode.

Overall it looks as if the standard charge correction method does not provide valid results for MCz at high proton and pion fluences. The method relies on several assumptions (compare chapter 5.3.2) that could be violated in the case of MCz. Specifically it is possible that the trapping time is not constant in the whole detector and influenced by local field and space charge variations. Further investigations with other methods like edge-TCT [Kra10b] are therefore needed to explain the observed TCT curves.

Neutron irradiated MCz on the other hand clearly shows a predominance of negative space charge in both n- and p-type at fluences of 3 x $10^{14}cm^{-2}$ and above. The junction on the n+/back side in MCz-n is already dominant before correction for trapping of the electron signal and in agreement with this the first peak in the hole signal is still dominant after trapping correction (Fig. 8.13). In p-type MCz the dominant junction stays close to the n+/front side of the diode, again indicating the introduction of negative space charge into the already negatively charged bulk (Fig. 8.14).

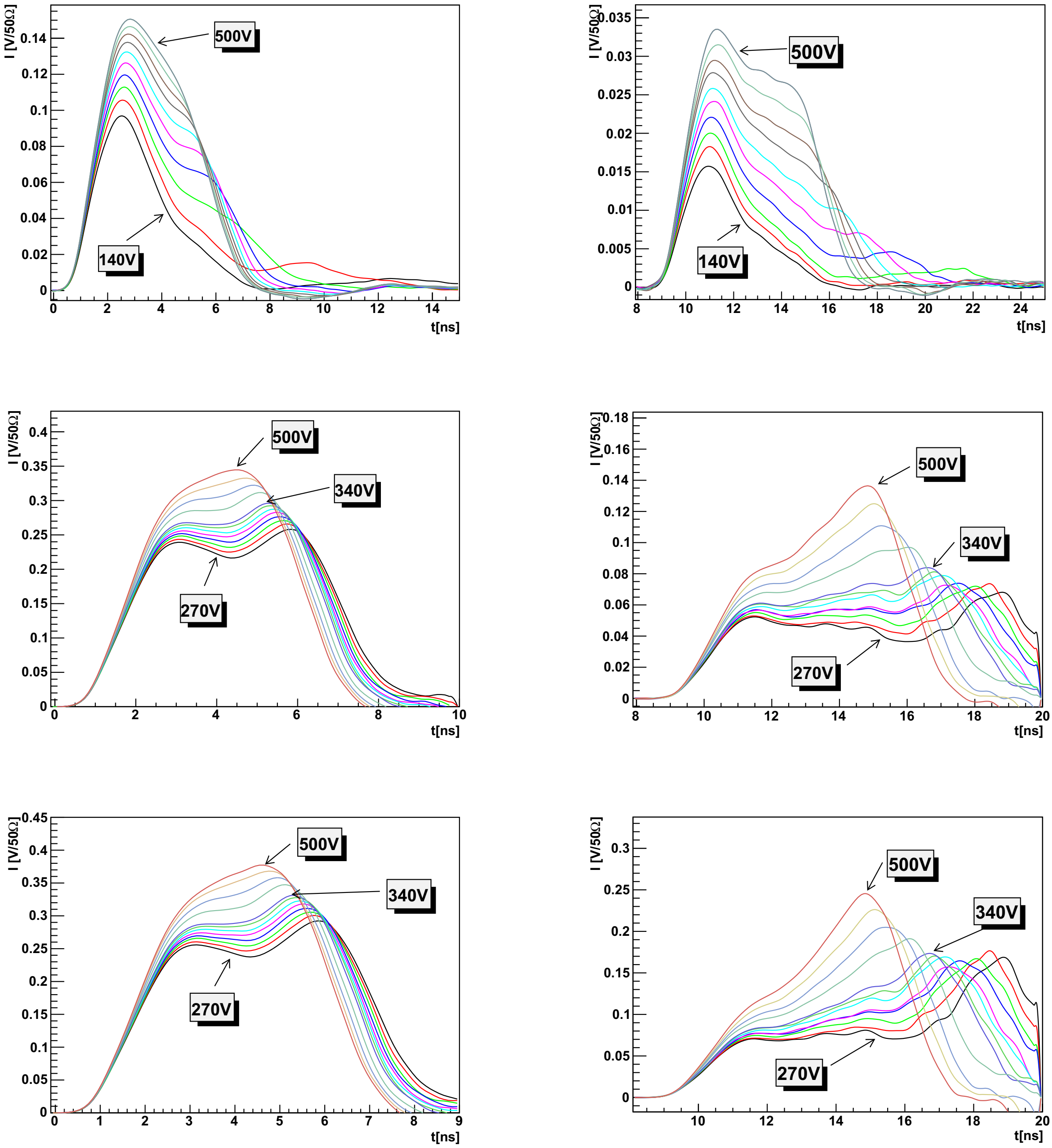

Figure 8.10: n-type MCz (HIP-MCz-01-n) irradiated with a 24 GeV/c proton fluence of 9.73 x $10^{14} p/cm^2$, measured at room temperature. Left column: electron signal (p+/front side illumination), right column hole signal (n+/back side illumination). The first row shows the signals as measured, the second row corrected with $\tau_{eff} = 4.58\ ns$ as used in [Li 10], the third row shows the same curves corrected with $\tau_{eff,e} = 3.9\ ns$ and $\tau_{eff,h} = 3\ ns$ from [Pac08]. In [Li 10] and [Li 08] the electron signal at $V_{fd} = 328\ V$ and the hole signal at $V_{fd} = 316\ V$ were presented, whereas in [Pac08] a voltage range of 300-500 V was chosen for the electron signal.

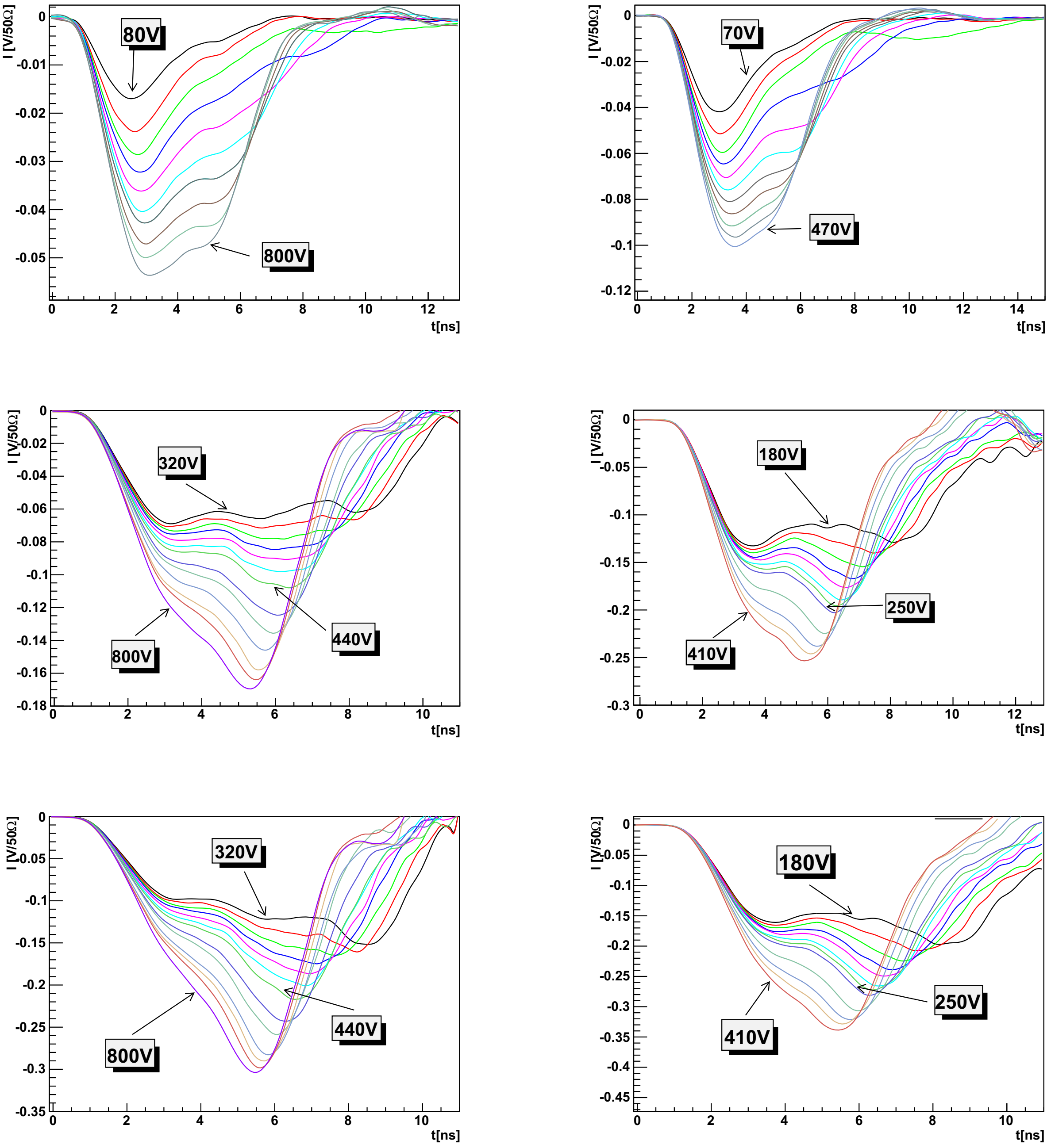

Figure 8.11: p-type MCz (HIP-MCz-01-n) irradiated with a 24 GeV/c proton fluence of 9.73 x 10^{14} p/cm^2, measured at room temperature. Left column: hole signal (n+/front side illumination), right column electron signal (p+/back side illumination). The first row shows the signals as measured, the second row corrected with $\tau_{eff} = 4.58$ ns as used in [Li 10], the third row shows the same curves corrected with $\tau_{eff,e} = 3.9$ ns and $\tau_{eff,h} = 3$ ns from [Pac08]. In [Li 10] and [Li 08] the hole signal at $V_{fd} = 345$ V and the electron signal at $V_{fd} = 254$ V were presented, whereas in [Pac08] a voltage range of 400-500 V was chosen for the hole signal.

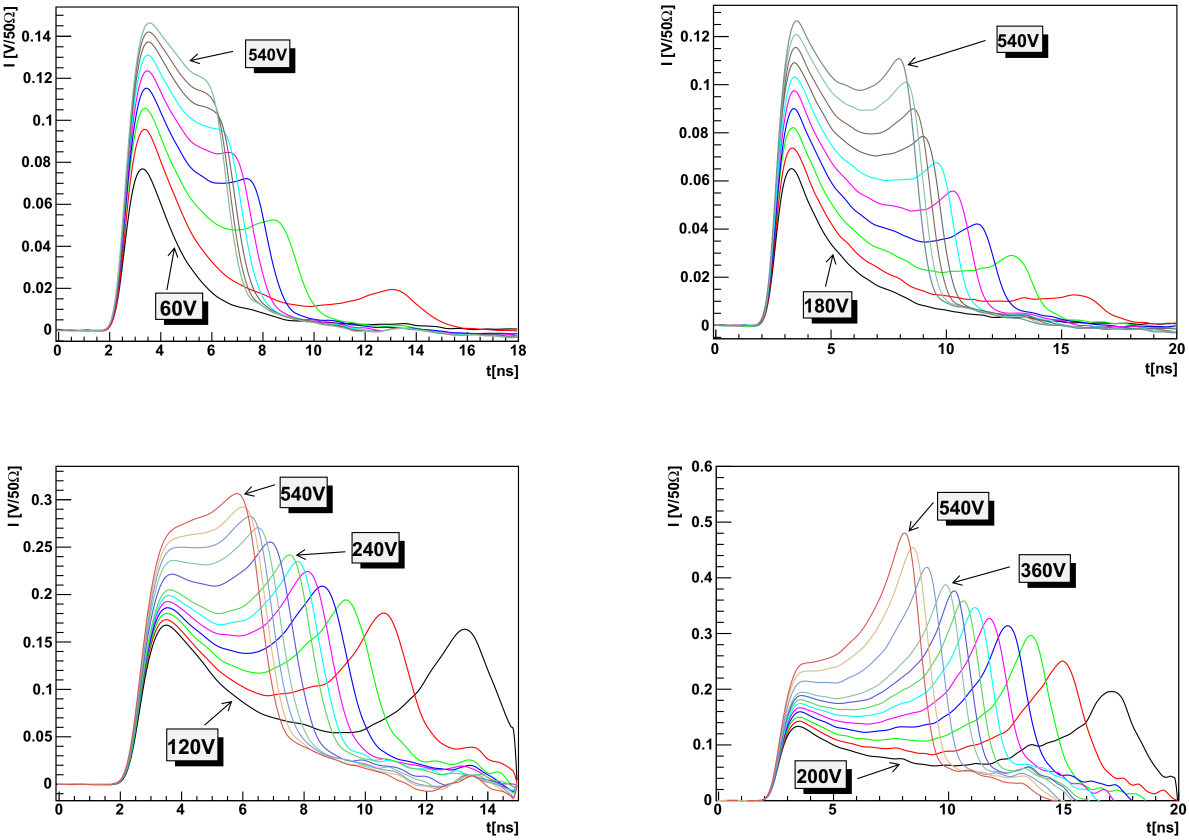

Figure 8.12: n-type MCz (HIP-003-C) irradiated with a neutron equivalent 200 MeV pion fluence of 3.11 x 10^{14} cm^{-2}, measured at room temperature. Left column: electron signal (p+/front side illumination), right column hole signal (n+/back side illumination). The first row shows the signals as measured, the second row shows the same curves corrected with $\tau_{eff,e} = 6.2$ ns and $\tau_{eff,h} = 5.5$ ns respectively.

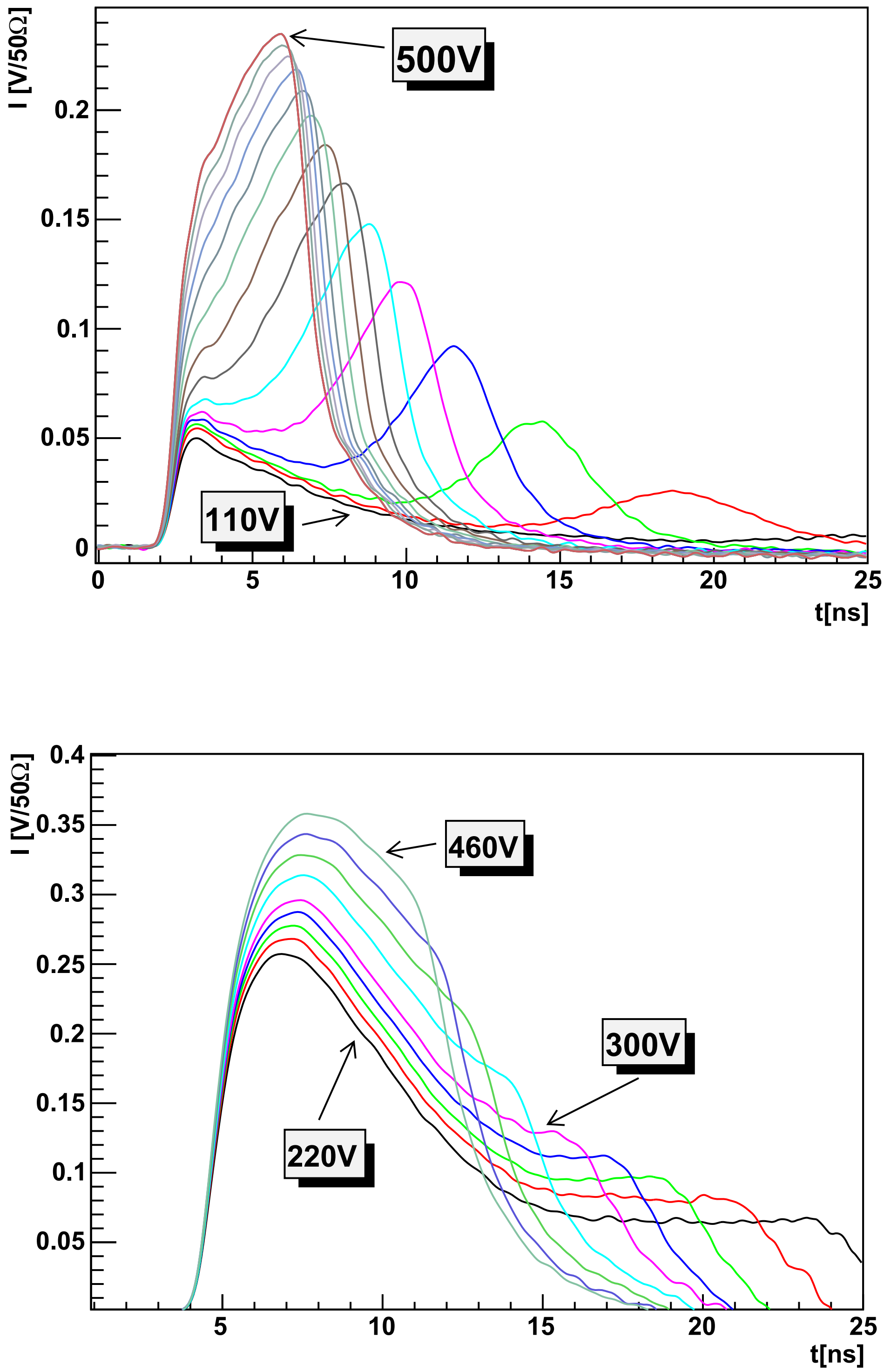

Figure 8.13: n-type MCz (HIP-003-B) irradiated with a neutron fluence of 3 x $10^{14}\,cm^{-2}$, measured at room temperature. (a) electron signal (p+/front side illumination), uncorrected. (b) hole signal (n+/back side illumination) corrected with $\tau_{eff,h}$ = 7.3 ns.

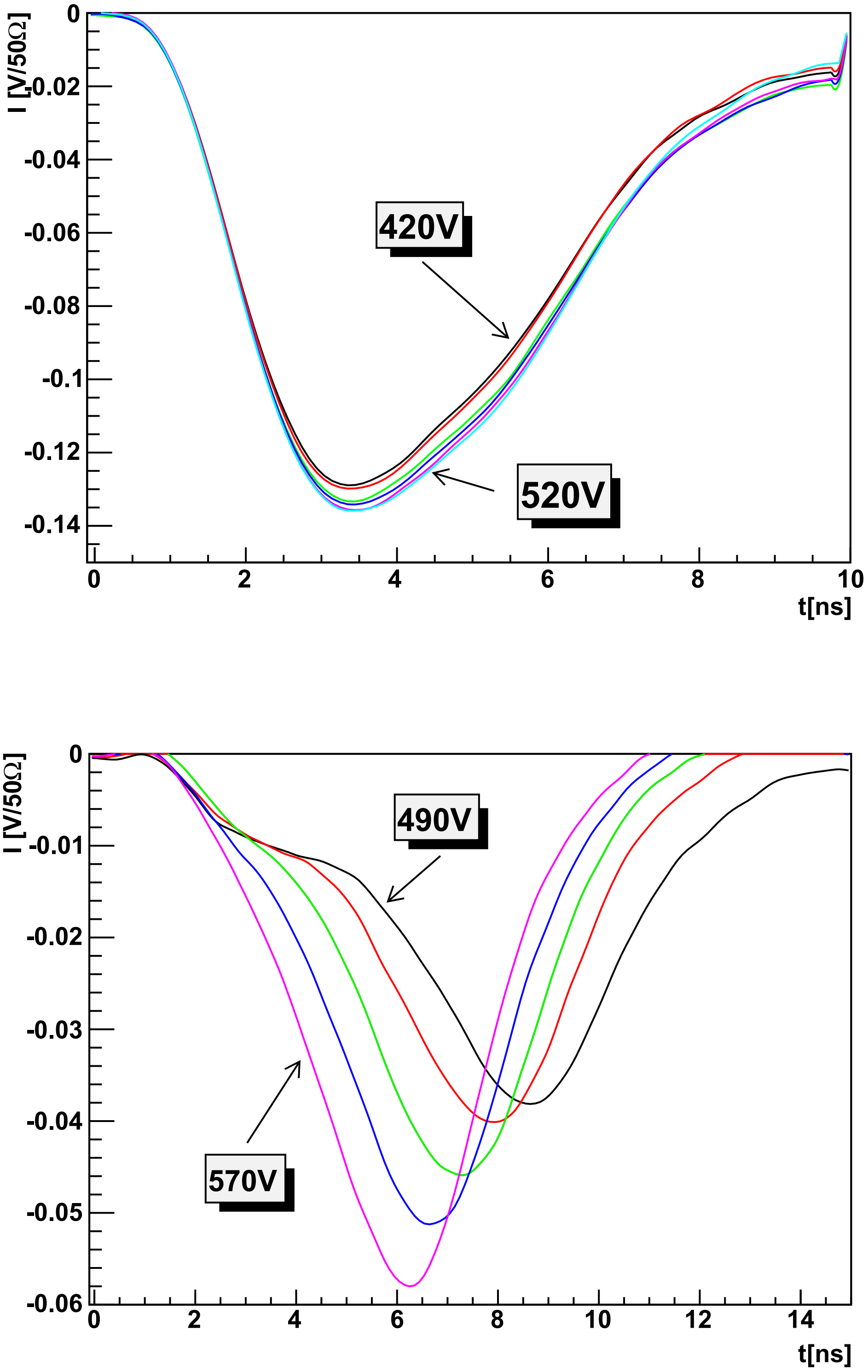

Figure 8.14: p-type MCz (p068) irradiated with a neutron fluence of 3 x 10^{14} cm^2, measured at room temperature. (a) hole signal (n+/front side illumination) corrected with $\tau_{eff,h} = 9$ ns. (b) electron signal (p+/back side illumination), uncorrected.

8.2.3 150 μm EPI

The development of the space charge sign in EPI silicon irradiated with 24 GeV/c protons is contrary to that in FZ material: p-type EPI converts to 'n-type' due to introduction of stable donors. In FZ SCSI is already visible at the lowest irradiation fluence of about 1 x $10^{13}\,cm^{-2}$, in EPI p-type irradiated to 5.06 x $10^{13}\,p/cm^{2}$ however the dominant junction is still at the front side of the diode even after correction for trapping indicating negative space charge in the diode bulk (compare Fig. 8.15 (a)). At the next available fluence step of 1.66 x $10^{14}\,cm^{-2}$ a clear SCSI is visible already in the uncorrected TCT curves (Fig. 8.15 (b)). This agrees with observations in the development of $|N_{eff}|$ in this fluence range: a minimum close to zero is reached at about this point after a decrease at lower fluences (Fig. 8.16).

Neutron irradiation introduces acceptors in EPI, like in all other investigated materials. The only exceptions to this found so far are thin, 50 and 75 μm, low resistivity n-type EPI samples, where donor generation prevails [Lin06b]. 150 μm p-type EPI however keeps its negative space charge (Fig. 8.18 (b)), while n-type EPI with originally positive space charge, changes to 'p-type'. SCSI occurs at fluences above 1 x $10^{14}\,cm^{-2}$ as indicated already by the minimum of $|N_{eff}|$ in Fig. 8.16 (compare Fig. 8.17). A clear double peak structure can be observed especially around depletion with one peak becoming dominant at higher bias voltages, similar to what is seen in FZ (compare chapter 8.2.1).

In Fig. 8.18 n-type and p-type EPI irradiated to an equivalent fluence of 1 x $10^{15}\,cm^{-2}$ protons and neutrons respectively is shown after correction for trapping. No SCSI is visible even at these high fluences, the space charge is still positive in n-type and still negative in p-type and the main junction is close to the front side of the diode.

For 50 and 75 μm p-type EPI samples whose effective space charge was evaluated in chapter 6.1.3, no full TCT study was performed within this work [1]. One sample of each series, irradiated with 24 GeV/c protons to a fluence of 5 x $10^{14}\,p/cm^{2}$ and 1.66 x $10^{15}\,p/cm^{2}$ respectively was however measured to determine the position of the dominant junction [Kas09]. Like in 150 μm p-type samples, SCSI is visible even before correction for trapping.

---

[1] For further investigations on these specific sample sets compare [Cas10]

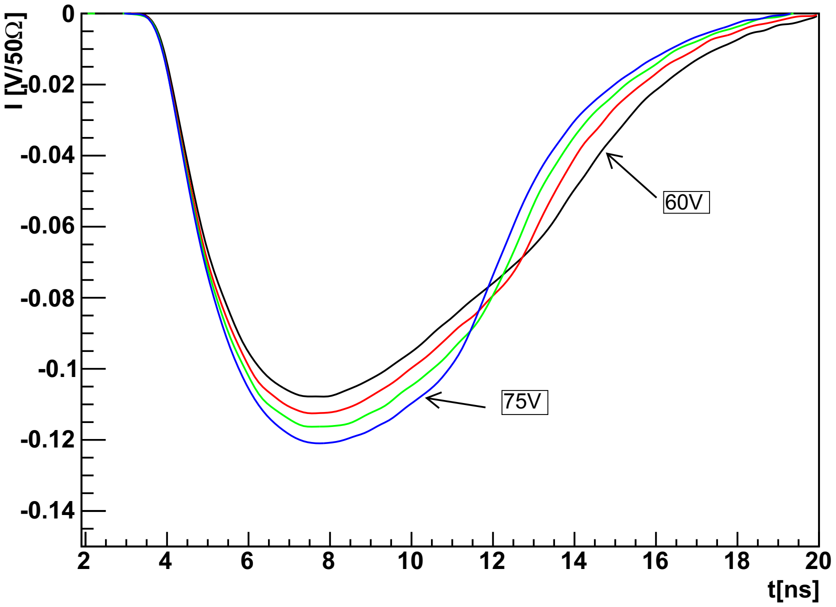

(a)

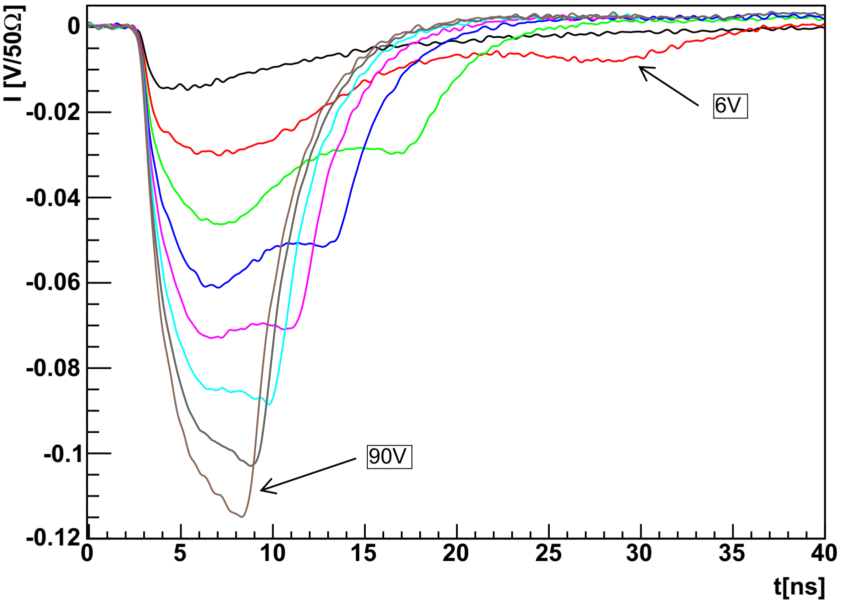

(b)

Figure 8.15: (a) p-type EPI (CNM-22) irradiated with a proton fluence of 5.06 x 10^{13} p/cm^2, corrected for trapping with $\tau_{eff} = 70$ ns, step size 5 V. (b) p-type EPI (CNM-22) irradiated with a proton fluence of 1.66 x 10^{14} p/cm^2, no correction, step size 12 V.

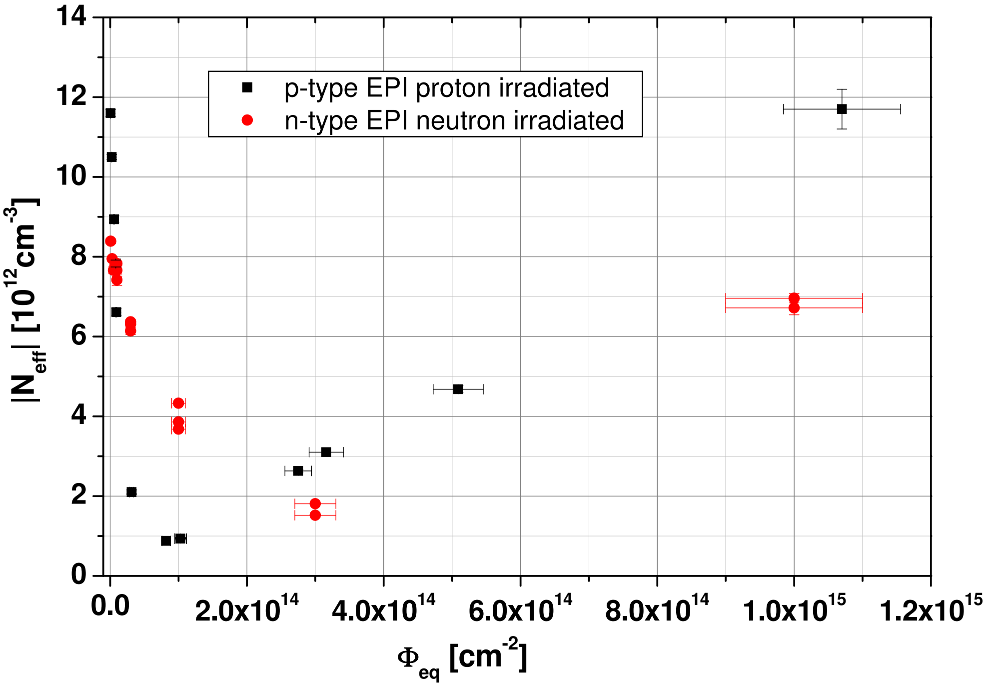

Figure 8.16: Development of the effective space charge in proton irradiated p-type and neutron irradiated n-type 150 μm EPI after annealing of 4 min at 80 °C (compare also chapter 6.1.3).

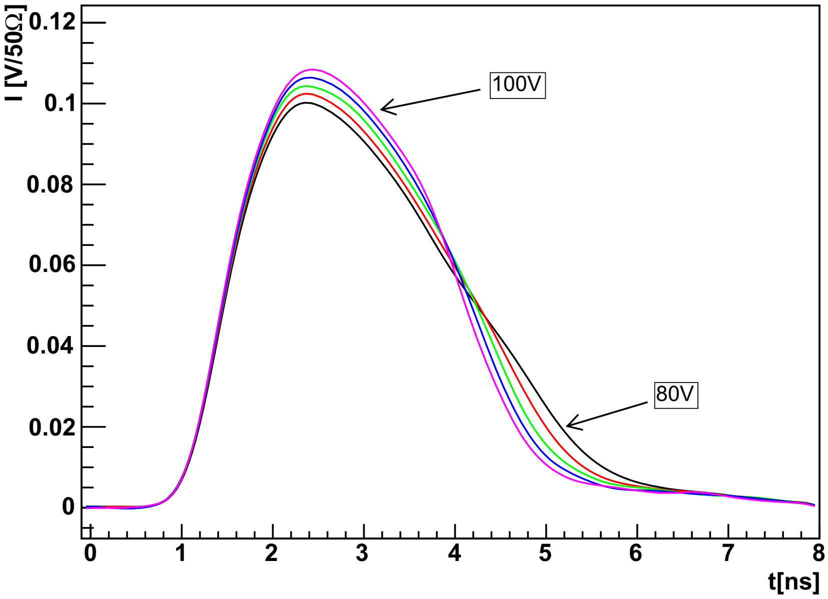

(a)

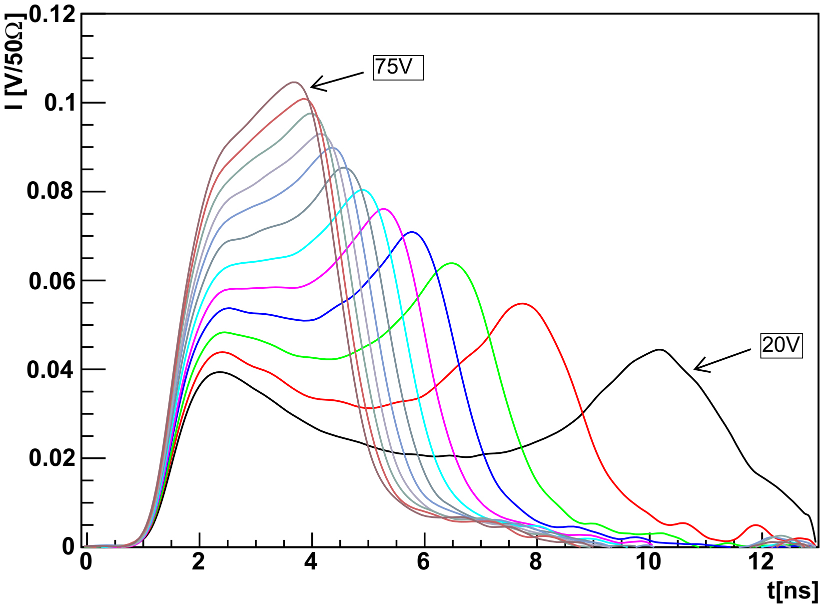

(b)

Figure 8.17: (a) n-type EPI (HIP-04-C) irradiated with a neutron fluence of 1 x 10^{14} cm^{-2}, corrected for trapping with τ_{eff} = 22 ns, step size 5 V. (b) n-type EPI (HIP-004-C) irradiated with a neutron fluence of 3 x 10^{14} cm^{-2}, corrected for trapping with $\tau_{eff} = 7.5$ ns, step size 5 V.

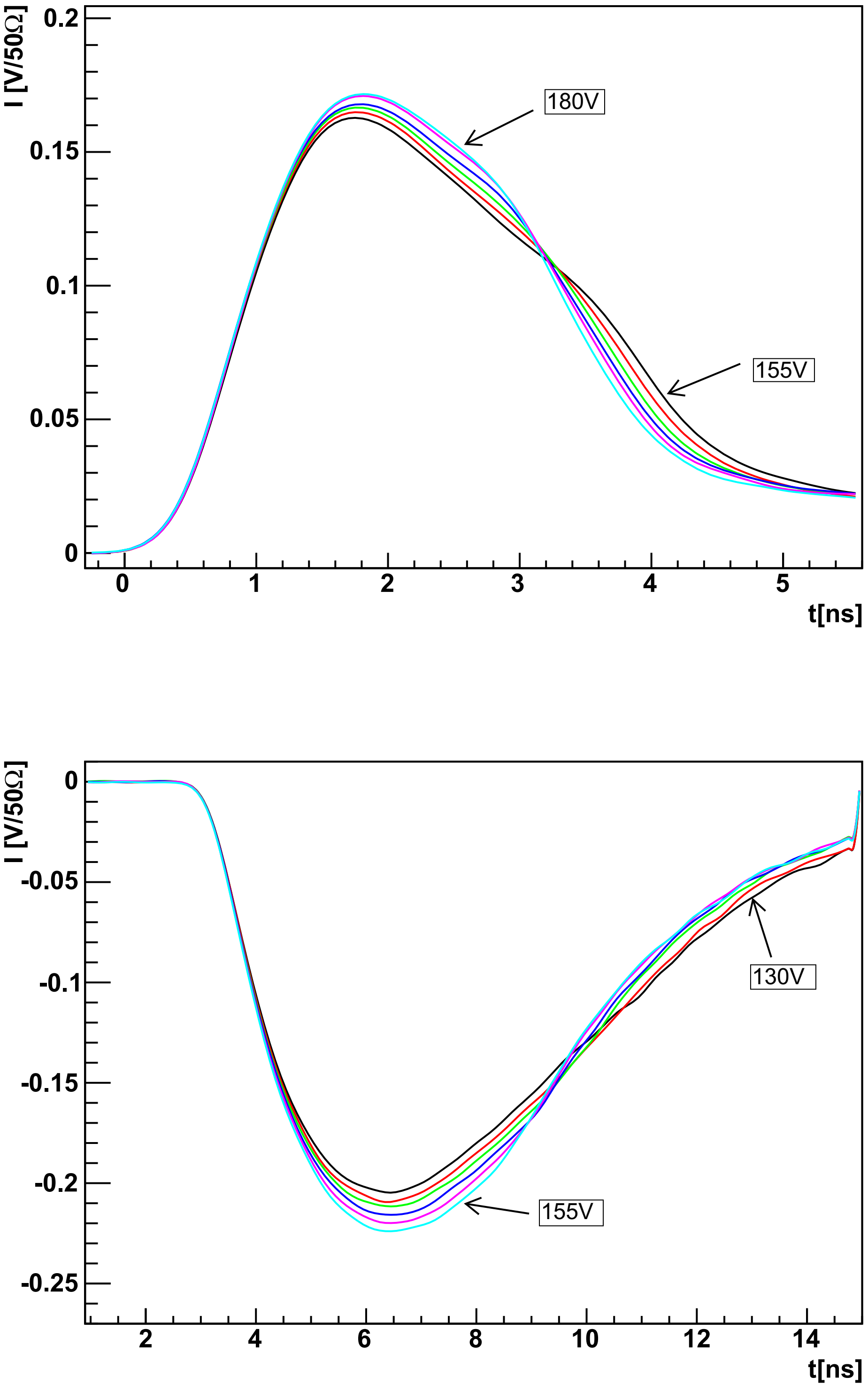

Figure 8.18: (a) n-type EPI (HIP-004-C) irradiated with a proton fluence of 1.73 x 10^{15} p/cm^2, corrected for trapping with τ_{eff} = 3.9 ns,5 V steps. (b) p-type EPI (CNM-22) irradiated with a neutron fluence of 1 x 10^{15} cm^{-2} corrected for trapping with τ_{eff} = 8 ns,5 V steps.

Chapter 9

Effective Space Charge Comparison

In the previous chapters four different measurements have been used to determine the detector parameters: using the development of the capacitance with bias voltage the voltage at which full depletion is reached in the detector has been extracted (i.e. the effective space charge), the reverse current was determined in a similar manner (IV measurement), while the collected charge was measured by looking at the response to beta particles (CCE measurement) and the position of the main junction in turn by evaluating the response to red laser light (TCT measurement). The measurement procedure in each of the methods included taking data at several bias voltage steps up to voltages well above depletion. It is therefore possible to extract the effective space charge also from IV, CCE and TCT measurements. In both CCE and TCT measurements the development of charge with bias voltage (QV plot) has to be used, which in the case of TCT measurements is extracted by integrating over the laser response curves. At low voltages, where the charge carriers drift through a large part of the bulk and a long integration time is necessary, it is however difficult to obtain a reliable value for the collected charge due to noise in the signal and signal reflections in the TCT setup. Since the same detector parameter - the collected charge - is examined in both CCE and TCT measurements, only QV plots produced by beta particles in the CCE setup will be taken into account in the following.

It has been stated that the depletion voltage or effective space charge extracted from QV plots agrees well with that determined from the kink in the CV curve, which is the standard measurement procedure [Kra08a]. Since this however was only shown for single measurements or single sample types, a more thorough comparison between the effective space charge obtained from CV, IV and CCE measurements is necessary.

The measurement procedures are described in detail in chapters 5.3.1 and 5.3.2, therefore only a short summary of the measurement conditions will be given here: In all cases the guard ring was connected to ground to limit the active volume of the detector. For CV measurements parallel mode and a frequency of 10 kHz was chosen. CV and IV measurements were performed at a room temperature of 20-22 °C, while for CCE measurements with a shaping time of 25 μs the sample was cooled to (-20±1)°C. Despite these differences the effective space charge obtained from all three measurement methods is very similar at low fluences, as the examples presented in Figs. 9.1, 9.2 and 9.3 show for n-type FZ, MCZ and EPI, respectively. That this however changes at higher fluences will be discussed in the following chapters for n- and p-type FZ, MCz and EPI samples irradiated with 24 GeV/c protons, reactor neutrons and where available 200 MeV pions.

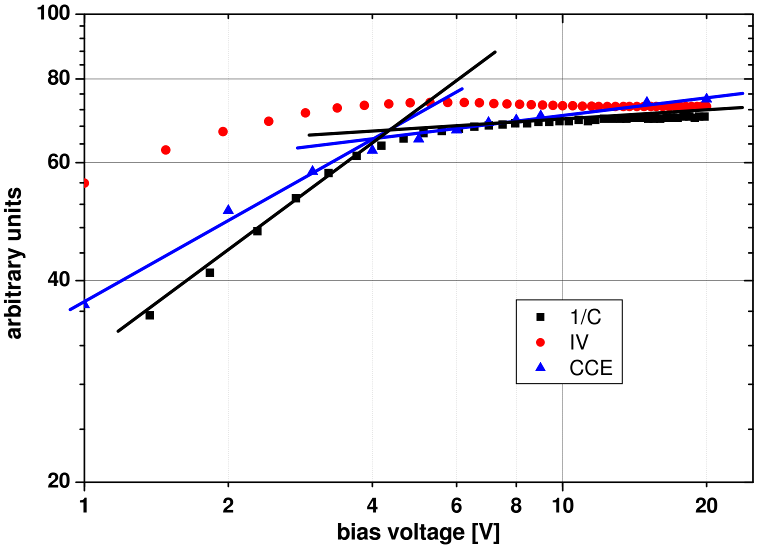

Figure 9.1: Development of $1/C$, I and the collected charge with bias voltage in n-type FZ irradiated with 24 GeV/c protons to an equivalent fluence of 1.46 x 10^{13} cm^{-2}. Values on the Y-axes were adjusted for better comparison of the curve shapes and do not reflect absolute measurement values. Straight lines are added to guide the eye and reflect the fitting process but are not actual fits used for determining the effective space charge. For the unexpected development of the current with bias voltage compare the text.

9.1 Comparison of the effective space charge in FZ

As Fig. 9.4 shows for detectors irradiated with 24 GeV/c protons, already in standard n-type FZ material differences in the effective space charge obtained by different measurement methods become obvious. At fluences above 3.5 x 10^{14} cm^{-2} increased current leads to uncertain results in n-type FZ (compare chapter 6.1.1), hence these data points were not taken into account. Each curve on its own shows the expected behavior for this material and this particle type, an initial decrease and later linear increase of the effective space charge (or depletion voltage) with fluence. The absolute values and the rate of the increase however differ with the effective space charge from IV showing the slowest increase.

In Fig. 9.5 the development of 1/C, I and Q with bias voltage is shown for the highest fluence point of 2.75 x 10^{14} cm^{-2} to emphasize that the differences in the effective space charge are not due to errors in fitting the curves. Since only the curve shape and not the

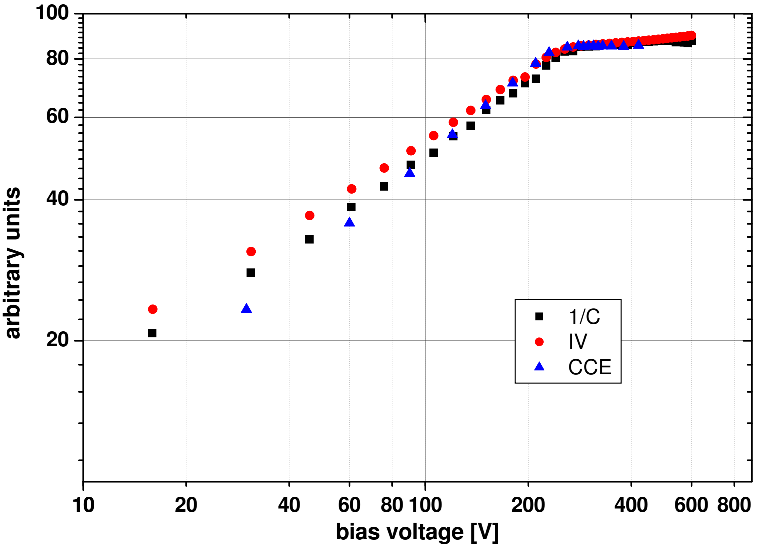

Figure 9.2: Development of $1/C$, I and the collected charge with bias voltage in n-type MCz irradiated with 24 GeV/c protons to an equivalent fluence of 1.46 x $10^{13}\,cm^{-2}$. Values on the Y-axes were adjusted for better comparison of the curve shapes and do not reflect absolute measurement values. Straight lines are added to guide the eye and reflect the fitting process but are not actual fits used for determining the effective space charge. For the unexpected development of the current with bias voltage compare the text.

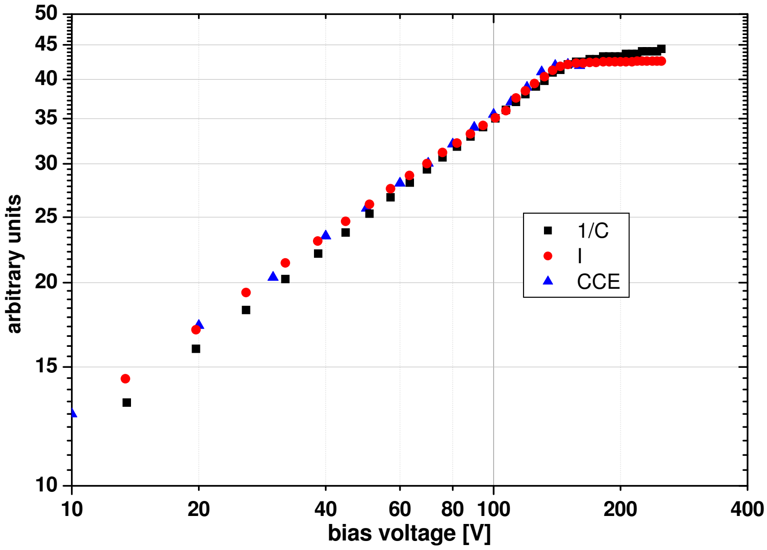

Figure 9.3: Development of $1/C$, I and the collected charge with bias voltage in n-type EPI irradiated with 24 GeV/c protons to an equivalent fluence of 1.33 x $10^{13}\,cm^{-2}$. Values on the Y-axes were adjusted for better comparison of the curve shapes and do not reflect absolute measurement values. Straight lines are added to guide the eye and reflect the fitting process but are not actual fits used for determining the effective space charge. For the unexpected development of the current with bias voltage compare the text.

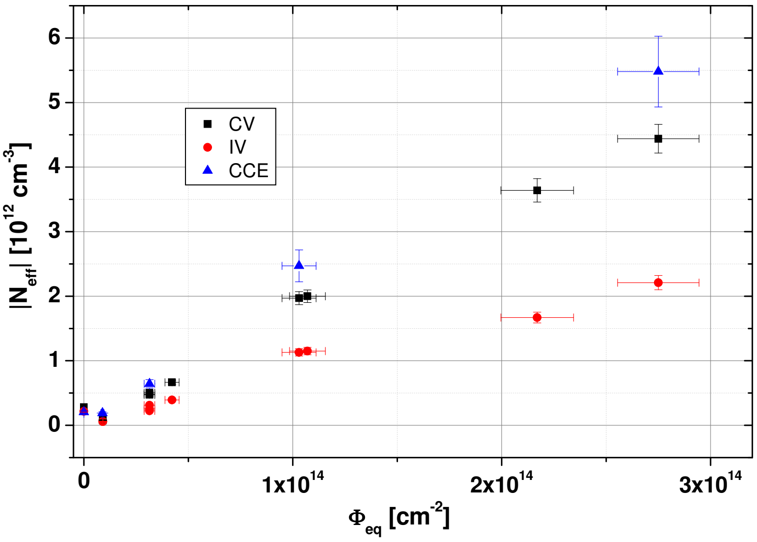

Figure 9.4: Comparison of the effective space charge in n-type FZ obtained from CV, IV and QV measurements after irradiation with 24 GeV/c protons. Larger errors in the effective space charge obtained from CCE measurements are due to less available data points.

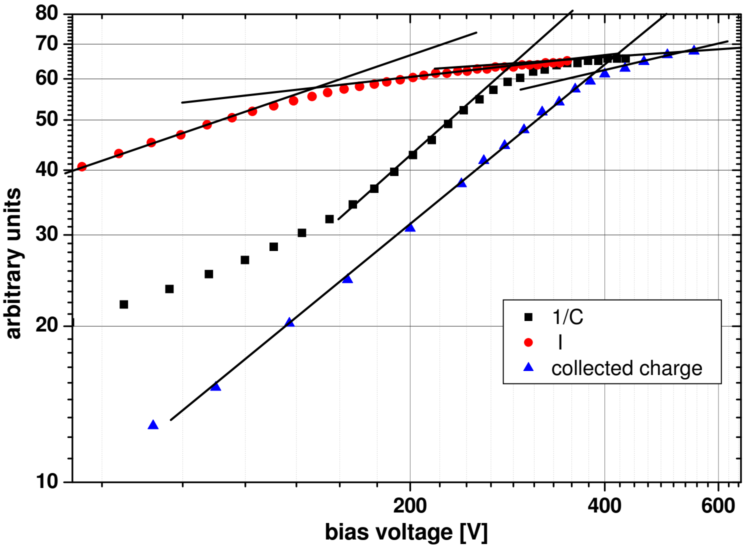

Figure 9.5: Development of $1/C$, I and the collected charge with bias voltage in n-type FZ irradiated with 24 GeV/c protons to an equivalent fluence of 2.75 x $10^{14}\,cm^{-2}$. Values on the Y-axes were adjusted for better comparison of the curve shapes and do not reflect absolute measurement values. Straight lines are added to guide the eye and reflect the fitting process but are not actual fits used for determining the effective space charge.

actual value at each bias voltage is of importance, the Y-axes was adjusted to make visual comparison easier.

A similar behavior can be observed in n-type FZ irradiated with reactor neutrons. Yet again the effective space charge obtained from QV plots shows the steepest increase with fluence while that from IV only slowly increases (Fig. 9.6). At the highest fluence point of 1 x $10^{14}\,cm^{-2}$ the difference in effective space charge between CCE and IV measurements amounts to 5.3 x $10^{12}\,cm^{-3}$ or around 370 V in this 300 μm thick sample (Fig. 9.7).

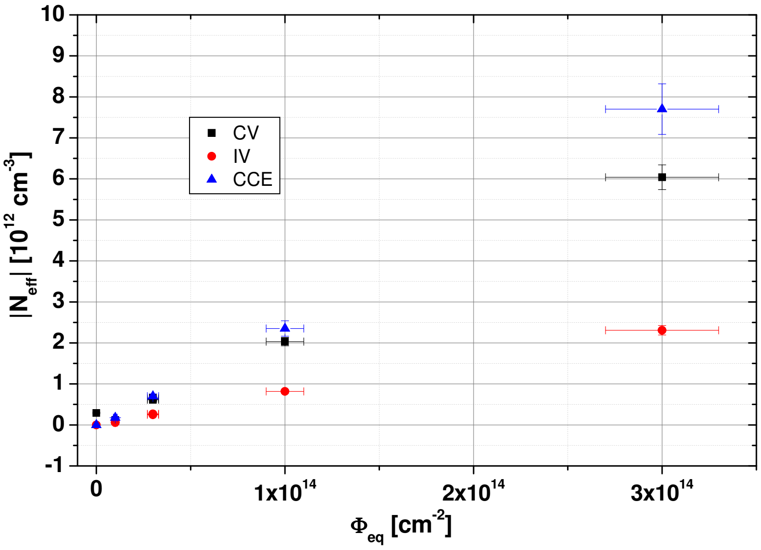

Figure 9.6: Comparison of the effective space charge in n-type FZ obtained from CV, IV and QV measurements after irradiation with reactor neutrons. Larger errors in the effective space charge obtained from CCE measurements are due to less available data points.

As described in chapter 6.1.1 the effective space charge in p-type FZ shows a non-linear behavior at high proton fluences independent of the measurement method used. As in n-type also here the highest values are obtained from QV and the lowest from IV curves (compare Fig. 6.5 in that chapter).

For neutron irradiated p-type only a limited comparison of $|N_{eff}|$ is possible since depletion is not reached at fluences above 1 x $10^{14}\,cm^{-2}$ (compare Fig. 7.4 (b) in chapter 7.1.1) and the effective space charge can not determined from IV curves due to fast increase in leakage current in this sample. From the available data however no difference can be seen to all other FZ samples presented so far.

As shown in chapter 6.1.1 differences between the effective space charge in n-type FZ after 24 GeV/c proton and 200 MeV pion irradiation as obtained from CV measurements are minimal. It can therefore be expected that also those obtained from other measurement methods would agree. While this is true for CCE measurements, as can be seen in Fig. 9.9, comparison of results from IV curves proof to be more difficult.

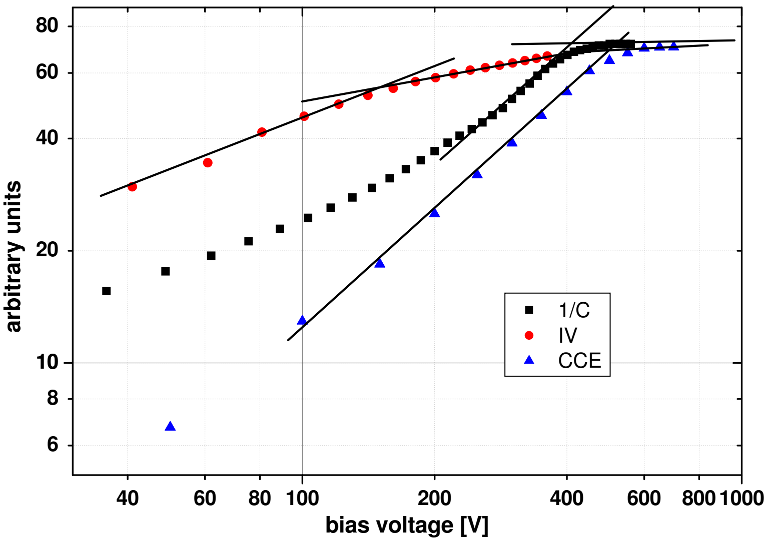

Figure 9.7: Development of 1/C, I and the collected charge with bias voltage in n-type FZ irradiated with reactor neutrons to an equivalent fluence of 1 x $10^{14} cm^{-2}$. Values on the Y-axes were adjusted for better comparison of the curve shapes and do not reflect absolute measurement values. Straight lines are added to guide the eye and reflect the fitting process but are not actual fits used for determining the effective space charge.

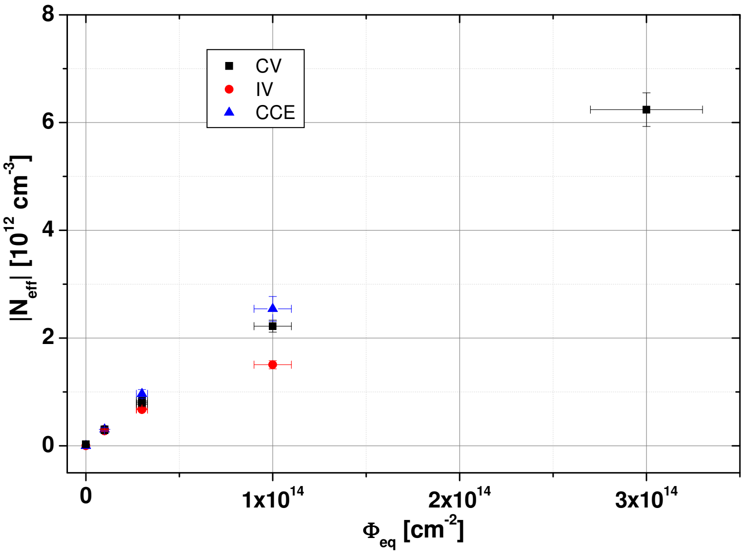

Figure 9.8: Comparison of the effective space charge in p-type FZ obtained from CV, IV and QV measurements after irradiation with reactor neutrons.

So far samples produced by CNM with a size of 5 x 5 mm^2 have been used for comparing the effective space charge. For pion irradiation however only 2.5 x 2.5 mm^2 produced by HIP were available. While no difference between these samples was seen when looking at the development of the effective space charged obtained from CV curves with fluence

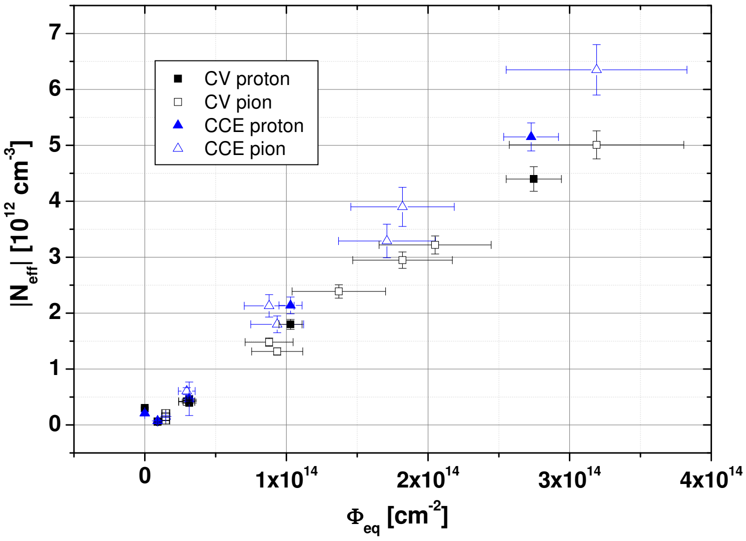

Figure 9.9: Comparison of the effective space charge in n-type FZ obtained from CV and measurements of the collected charge after irradiation with 24 GeV/c protons and 200 MeV pions.

(compare Fig. 6.2 in chapter 6.1.1) and differences in results from QV plots are small (Fig. 9.10) [1], the shape of the IV curves in the smaller samples make a comparison difficult. Instead of the expected linear increase with a change in slope as soon as depletion is reached, the current in this sample type decreases after an initial non-linear increase. In Fig. 9.11 a detector irradiated to a fluence of 1.66 x 10^{14} p/cm^2 is used to illustrate this unexpected behavior in comparison to a standard IV curve obtained from a bigger sample irradiated to the same fluence. Each curve represents the current per volume corrected to a reference temperature of 20 °C. As can be seen in the figure at higher voltage both curves are in agreement, which makes it unlikely that the differences are due to problems with IV measurements in general. This is further confirmed by looking at 2.5 x 2.5 mm^2 MCz and EPI samples: neither show a hill like structure in the IV curve, which also indicates that size itself is not the reason for the deviation.

After irradiation with reactor neutrons the picture does not change as the IV curves of two detectors irradiated to a fluence of 1 x 10^{13} cm^2 show (Fig. 9.12). Since in this case both samples were produced by the same company, differences in production methods can not explain the differences in the IV curves either.

The current values presented so far were taken on the front of the diode with the guard ring connected to ground (pad current), which limits and defines the active volume making comparisons more reliable [Mol99]. In comparison the total current measured on the backside of the diode through the bias voltage supply that acts as a current meter shows a more standard development with fluence (Fig. 9.13). It is therefore possible that the guard ring structure itself is the reason behind the deviation. FZ samples irradiated

---

[1] For a comparison of the actual QV curves compare Fig. 7.2 in chapter 7.1.1.

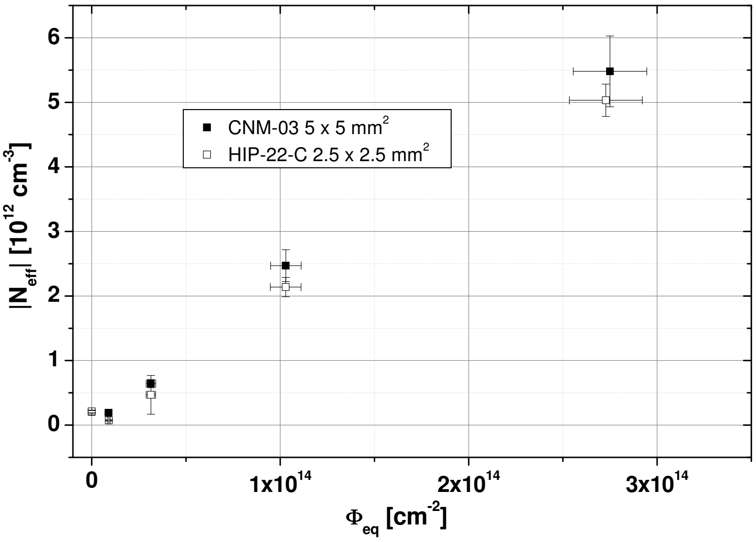

Figure 9.10: Comparison of the effective space charge in n-type FZ with an active area of 5 x 5 mm^2 (CNM-03) and 2.5 x 2.5 mm^2 (HIP-002-C) obtained from measurements of the collected charge after irradiation with 24 GeV/c protons.

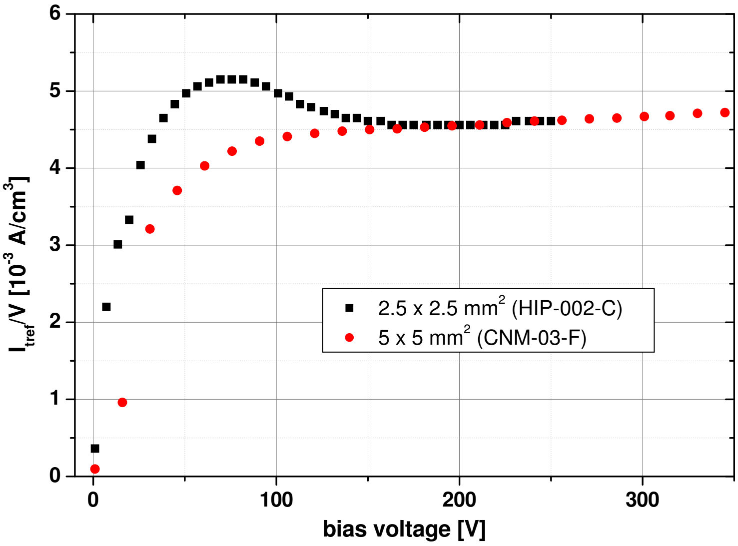

Figure 9.11: Comparison of the development of the reverse current per volume with bias voltage in 2.5x2.5 cm^2 (HIP-002-C) and 5x5 cm^2 (CNM-03-F) n-type FZ diodes irradiated with 24 GeV/c protons to a fluence of 1.66 x 10^{14} p/cm^2. Both curves were corrected to the reference temperature of 20 °C using Eq. 2.11.

with 24 GeV/c protons show space charge sign inversion even after irradiation with low fluences. When a bias voltage is applied, the electric field therefore starts growing from the back side. On the back side the implant covers the whole surface up to the edges of the sensor, which leads to surface currents generated there contributing to the overall

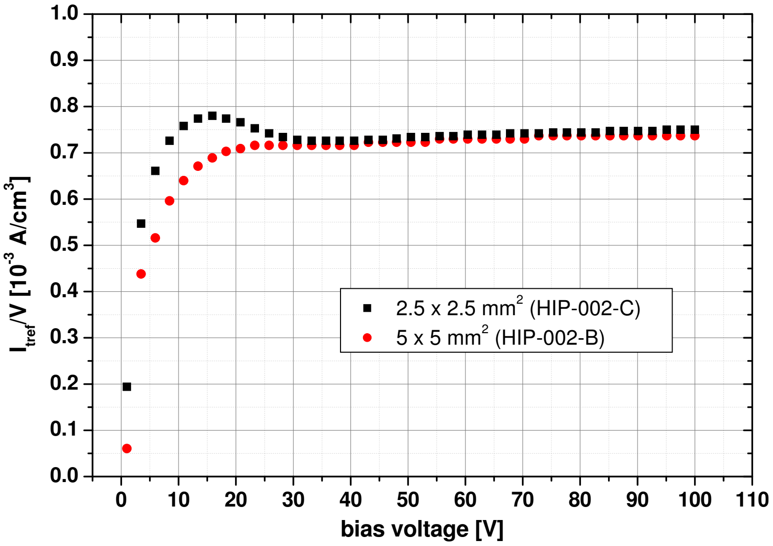

Figure 9.12: Comparison of the development of the reverse current per volume with bias voltage in 2.5x2.5 cm^2 (HIP-002-C) and 5x5 cm^2 (HIP-002-B) n-type FZ diodes irradiated with reactor neutrons to a fluence of 3 x 10^{13} cm^{-2}. Both curves were corrected to the reference temperature of 20 °C using Eq. 2.11.

current. At high bias voltages the electric field on the front side becomes relevant and therefore also the implanted guard ring structure that takes in the current from the edges, leaving the pad current as the main contribution to the current per volume.

A further hint that surface currents rather than currents from the active volume increased by irradiation lie behind the behavior might be given by a comparison of the reverse current per volume in unirradiated 2.5x2.5 cm^2 (HIP-002-C) and 5x5 cm^2 (CNM-03-F) samples. The smaller sample shows a higher reverse current already at this stage when compared to the bigger float zone sample (9.14). It has to be noted though that the total current from both samples is low (about 0.4 nA and 0.8 nA, respectively) and variations in the order of 0.5 nA are common when comparing samples from different positions on the wafer.

From TCT measurements no differences in the electric field between small and big samples can be seen, apart from higher rise times in 5 x 5 mm^2 diodes due to their higher capacitance. Since however the guard ring was not connected, relevant changes might not be visible due to this setup limitation. When comparing results from TCT measurements to those from CCE measurements one has to keep in mind that, while both methods use the same detector parameter - the collected charge vs. voltage - to determine the effective space charge, the measurement conditions were different: QV curves from CCE were obtained at a temperature of -20 °C after a long integration time in the order of μs, while TCT measurements were performed at room temperature of around 20 °C and the integration time was in the ns range. Nevertheless at least in the case of n-type Fz the values for the effective space charge obtained from integrating over these TCT curves are

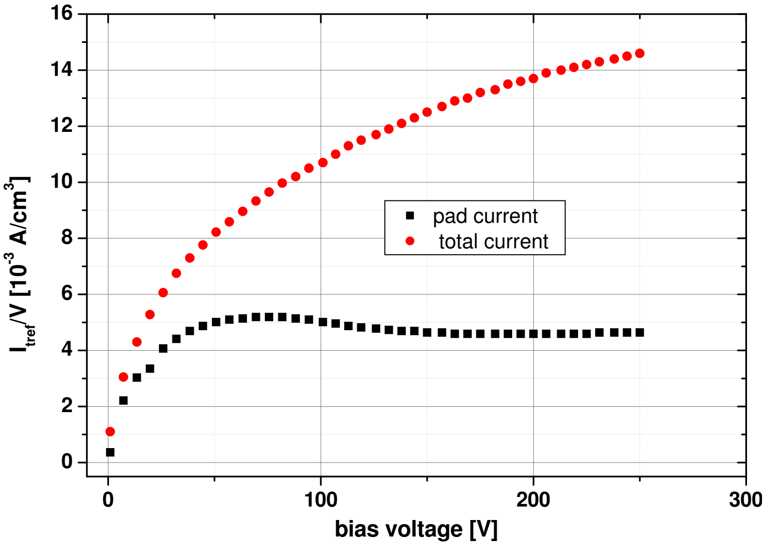

Figure 9.13: Pad current measured on the front of the diode with the guard ring connected to ground and back side total current in a 2.5x2.5 cm^2 n-type FZ diodes irradiated with 24 GeV/c to a fluence of 1.66 x 10^{14} p/cm^2.

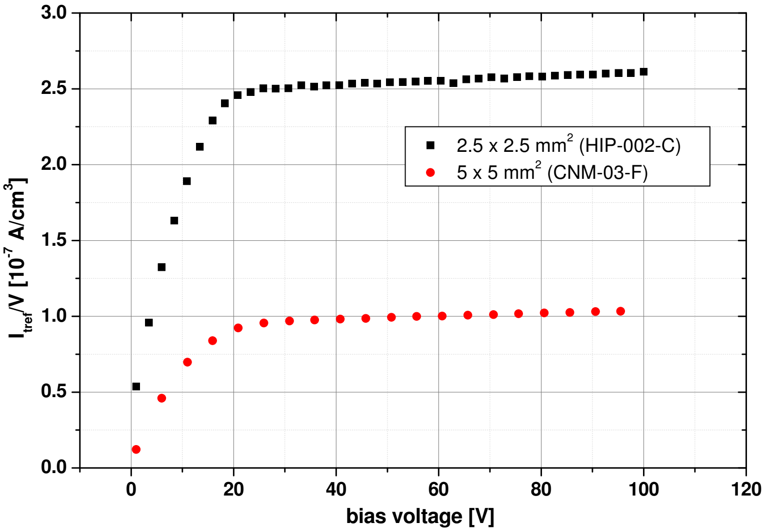

Figure 9.14: Comparison of the development of the reverse current per volume with bias voltage in 2.5x2.5 cm^2 (HIP-002-C) and 5x5 cm^2 (HIP-002-B) n-type FZ diodes before irradiation. Both curves were corrected to the reference temperature of 20 °C using Eq. 2.11.

only slightly higher than those found from CCE measurements with beta particles and therefore higher than those from both IV and CV measurements.

From what has been stated before for p-type FZ whose space charge stays negative after irradiation and thus the electric field grows from the front where the guard ring is situated, the effect should therefore not occur. Unfortunately no small p-type FZ samples were available to confirm this assumption. For MCz, where diodes produced with the same mask as used for the small HIP-002 samples were available, no definite conclusions on the sign of the effective space charge and therefore on the growth of the electric field can be drawn from the TCT results (compare chapter 8.2.2). None of the MCz samples shows any hill like structure though. The same is true for EPI silicon diodes. In EPI material however the build up of the field is different due the smaller thickness, only 150 μm compared to 300 μm, which makes a comparison difficult. Overall therefore more samples and further measurements are needed to give a final conclusion on the issue.

9.2 Comparison of the effective space charge in MCz

Similar to FZ, also in MCz the effective space charge obtained from CV, IV and CCE measurements does not agree. In this material however the values obtained from QV plots are not necessarily higher than what is seen in other evaluation methods as was the case in FZ. In n-type MCz irradiated with 24 GeV/c protons for instance IV and CCE measurements agree within the errors whereas values from CV measurements are higher from fluences of around 1 x 10^{14} cm^{-2} upwards (Fig. 9.15). In p-type MCz on the other hand, while $|N_{eff}|$ from IV measurements is still the lowest, the values obtained from CV and QV at high fluences are very similar (compare Figs. 9.16 and 9.17).

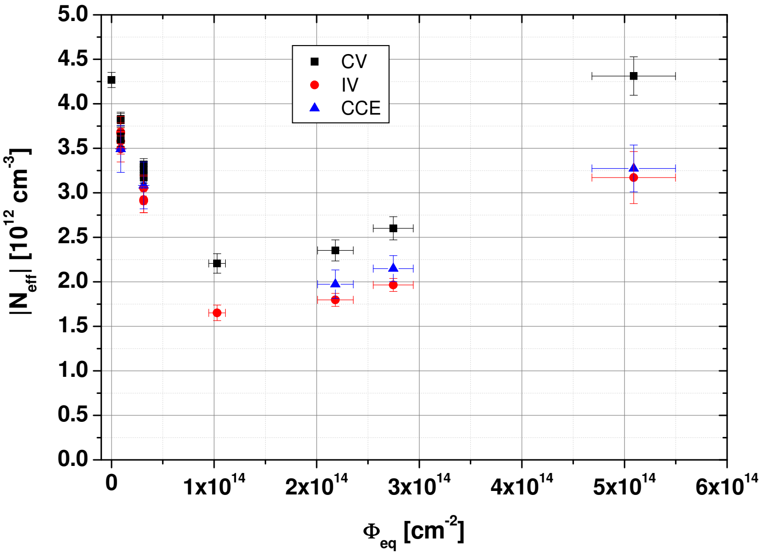

Figure 9.15: Comparison of the effective space charge obtained from CV, IV and QV measurements in n-type MCz after irradiation with 24 GeV/c protons.

It has to be noted that while donor removal is visible from CV measurements in p-type detectors with a resistivity of 7.53 ± 0.27 $k\Omega cm$ produced by HIP, from CCE measurements a straight increase of effective space charge with fluence is seen (Fig. 9.16). IV measurements did not produce a clear result in unirradiated diodes due to an early increase in current, but seem to indicate depletion at very low voltages. In lower resistivity p-type produced by MICRON ($\rho = 1.32 \pm 0.01$ $k\Omega cm$, Fig. 9.17), where the donor removal can be seen more clearly, it is obvious from all measurement methods.

Due to the fluence steps used donor removal in high resistivity material is only visible by a decrease in the effective space charge between the unirradiated sample and the first fluence step of 6.8 x 10^{13} p/cm^2. In the unirradiated sample however the effective space charge obtained from the QV plot is less than a fifth of that from the CV plot, while at the first fluence step both values agree. Both the development of 1/C and the collected charge with bias voltage in the unirradiated sample are shown in Fig. 9.18[2]. Since all unirradiated

---

[2] For low resistivity material produced by MICRON no reference sample was available.

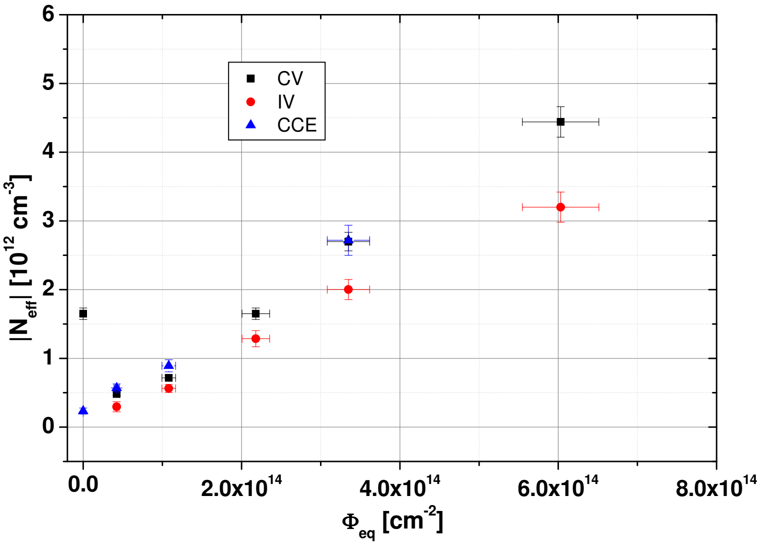

Figure 9.16: Comparison of the effective space charge obtained from CV, IV and QV measurements in p-type MCz with a resistivity of $7.53 \pm 0.27\ k\Omega cm$ (p069) after irradiation with 24 GeV/c protons.

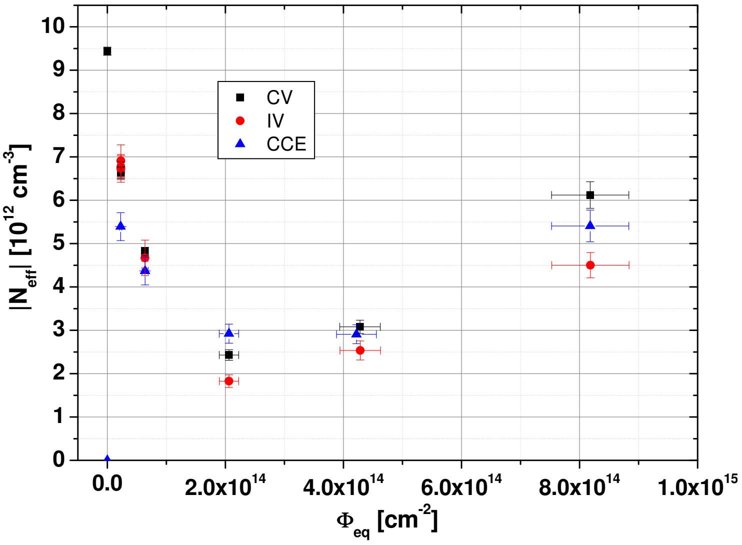

Figure 9.17: Comparison of the effective space charge obtained from CV, IV and QV measurements in p-type MCz with a resistivity of $1.32 \pm 0.01\ k\Omega cm$ (M-2553) after irradiation with 24 GeV/c protons.

MCz p-type samples show high reverse currents, further measurement points at various low fluences would therefore be necessary to verify that the apparent donor removal or lack thereof is not caused by problem arising from diode production. Similar low values for the effective space charge from QV plots in unirradiated material are however also observed in EPI samples with very low reverse currents (compare the following chapter).

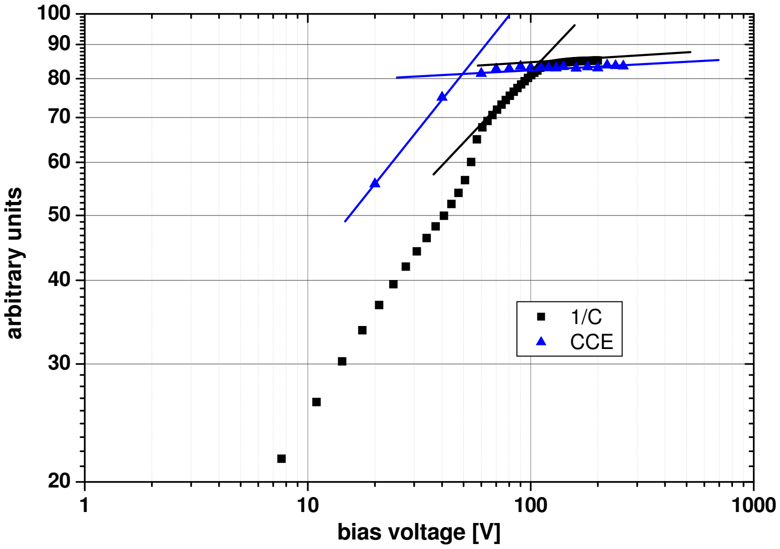

Figure 9.18: Development of 1/C, I and the collected charge with bias voltage in unirradiated p-type MCz with a resistivity of $\rho = 7.53 \pm 0.27\ k\Omega cm$(p069). Values on the Y-axes were adjusted for better comparison of the curve shapes and do not reflect absolute measurement values. Straight lines are added to guide the eye and reflect the fitting process but are not actual fits used for determining the effective space charge.

For neutron irradiated n-type MCz the situation is similar to what is seen in FZ: the effective space charge obtained from CCE measurements is higher than than from both CV and IV measurements (Fig. 9.19). No results could be obtained from p-type MCz after neutron irradiation due to bad sample quality.

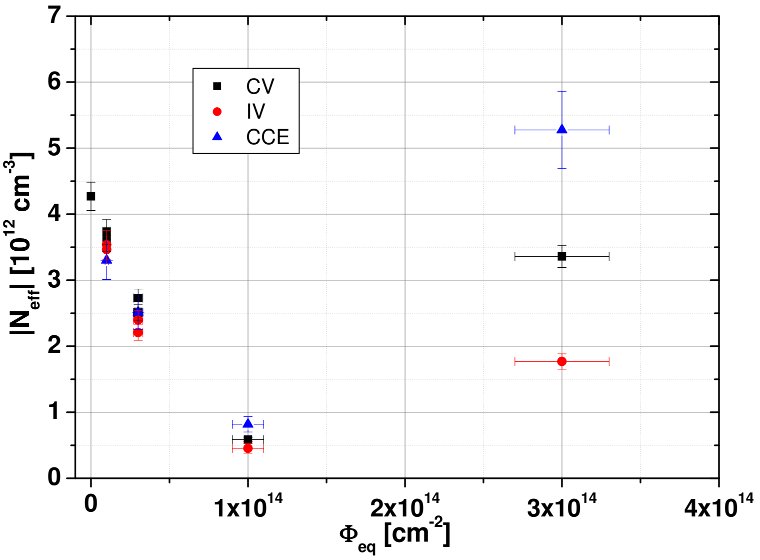

Figure 9.19: Comparison of the effective space charge obtained from CV, IV and QV measurements in n-type MCz after irradiation with reactor neutrons.

9.3 Comparison of the effective space charge in EPI

In epitaxial material at higher fluences a clear distinction between n- and p-type can be seen when comparing different measurement methods for the effective space charge. While in n-type EPI the effective space charge obtained from CV and QV curves is very similar after irradiation with both 24 GeV/c protons and reactor neutrons (Figs. 9.20 and 9.21), in p-type evaluation of IV and CV curves gives similar values, but lower than those from QV curves (Figs. 9.22 and 9.23).

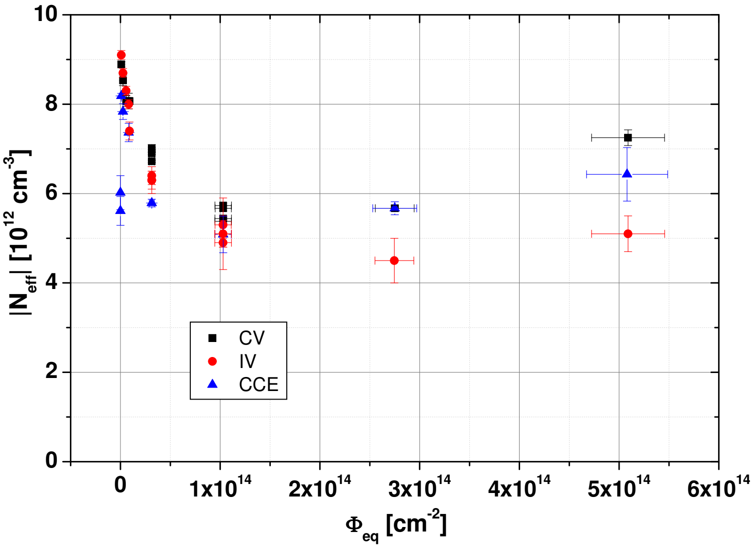

Figure 9.20: Comparison of the effective space charge obtained from CV, IV and QV measurements in n-type EPI after irradiation with 24 GeV/c protons.

In most curves presented so far the development of the effective space charge with fluence follows the expected pattern, with a decrease in the early stages of irradiation in case of donor removal followed by a linear increase. Differences between measurement methods only occurred with respect to absolute values and rate of increase.[3] While for the effective space charge obtained from CV measurements this also holds true for unirradiated EPI samples (compare also Figs. 6.15 and 6.16 in chapter 6.1.3), a deviation from the expected curve can be observed in the results from IV and QV plots. As an example the low fluence part of the $|N_{eff}|$ vs. V curve for p-type EPI irradiated with reactor neutrons is shown in Fig. 9.24, with the development of 1/C, I and Q with bias voltage in Fig. 9.25. Both CCE and IV measurements give values for the effective space charge in unirradiated samples that are far lower than those from CV measurements and furthermore not in agreement with predictions from equation 4.6 for this fluence range. Already at the first irradiation point of 1 x 10^{12} cm^{-2} however CV and IV results are in complete agreement again as is the case in other silicon types at this fluence. CCE results are still slightly lower but closer than in the unirradiated sample. Many of the p-type EPI samples produced by CNM that were used in this work exhibited an early increase in the reverse current

---

[3] For a possible exception see the results on p-type MCz in the previous chapter.

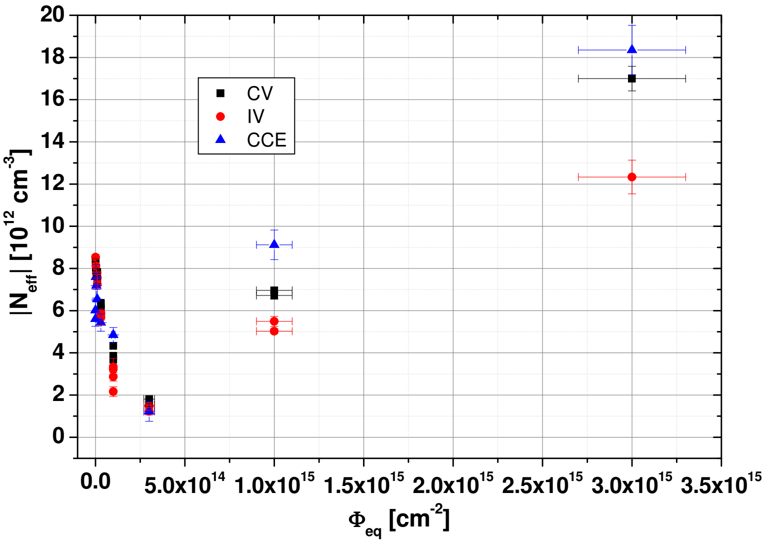

Figure 9.21: Comparison of the effective space charge obtained from CV, IV and QV measurements in n-type EPI after irradiation with reactor neutrons.

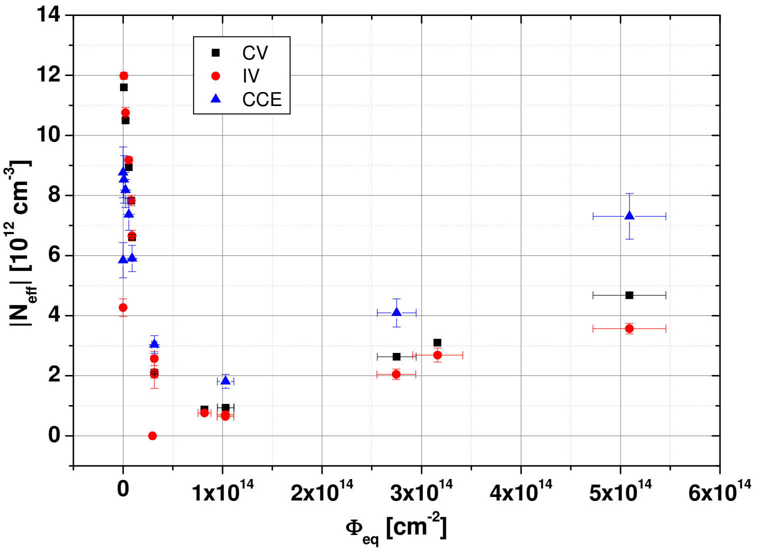

Figure 9.22: Comparison of the effective space charge obtained from CV, IV and QV measurements in p-type EPI after irradiation with 24 GeV/c protons.

before irradiation. Therefore, even though this was not visible in the samples used for determining the effective space charge, the possibility that an unusual development of the reverse current in this sample batch lies behind the deviation in the results from IV measurements can not be excluded. That however an abnormal reverse current in unirradiated samples is not the reason for the low depletion voltages obtained from CCE measurements is confirmed by n-type samples, where the same behavior can be observed, while IV and CV results agree (see also Fig. 9.26). To determine whether this behavior

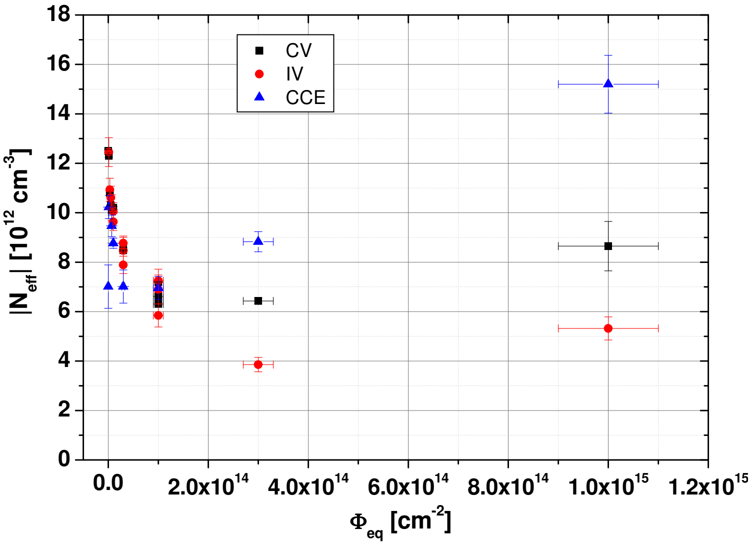

Figure 9.23: Comparison of the effective space charge obtained from CV, IV and QV measurements in p-type EPI after irradiation with reactor neutrons.

is related to what is seen in p-type MCz, more samples and measurements are necessary.

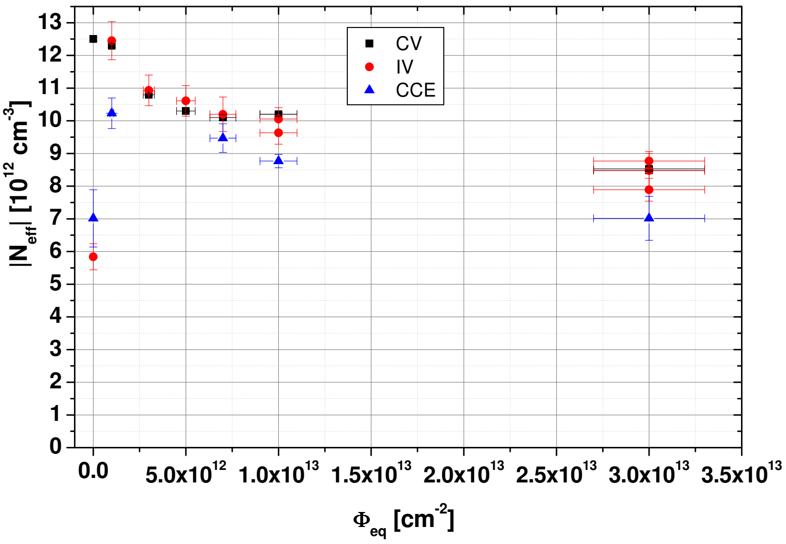

Figure 9.24: Comparison of the effective space charge in p-type EPI (CNM-22) obtained from CV, IV and measurements of the collected charge after irradiation with reactor neutrons at low fluences

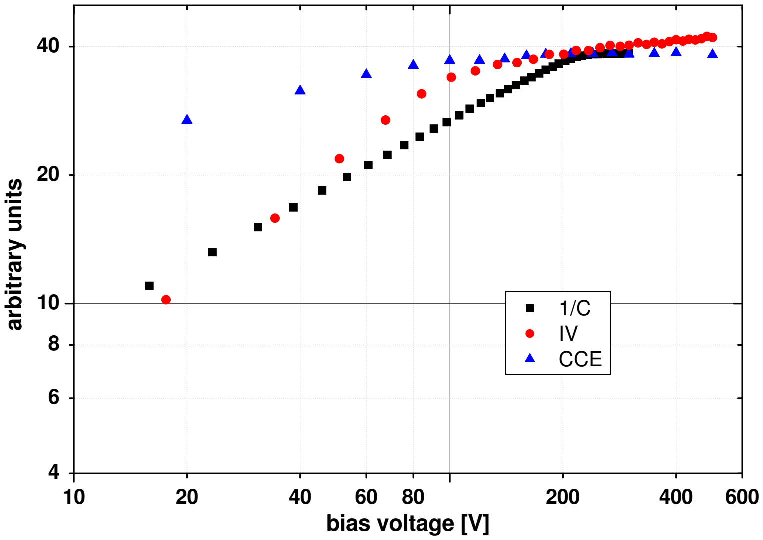

Figure 9.25: Development of 1/C, I and the collected charge with bias voltage in unirradiated p-type EPI. Values on the Y-axes were adjusted for better comparison of the curve shapes and do not reflect absolute measurement values.

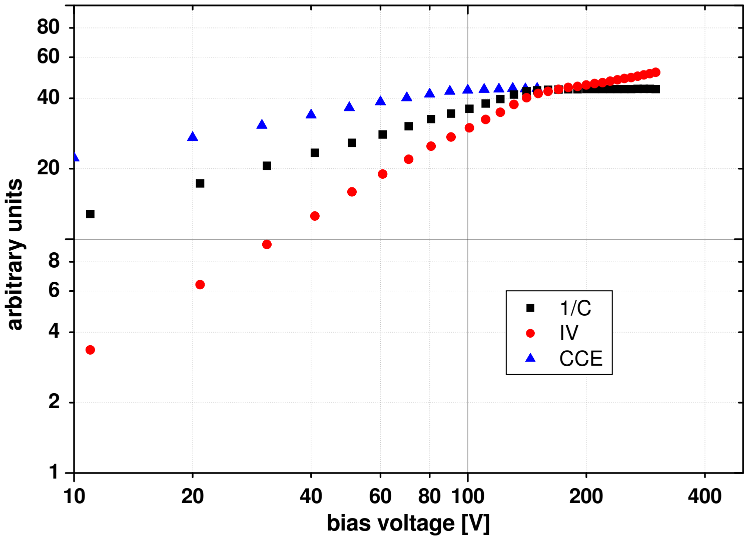

Figure 9.26: Development of 1/C, I and the collected charge with bias voltage in unirradiated n-type EPI. Values on the Y-axes were adjusted for better comparison of the curve shapes and do not reflect absolute measurement values.

9.4 Comparison of results

In the previous chapters it has been shown that effective space charge obtained by different measurement methods rarely agrees. In Tab. 9.1 the results are collected and it is indicated which measurement technique yields the highest and lowest value for the effective space charge. In all cases the effective space charge obtained from IV measurements is the lowest, whereas for CCE and CV results it is difficult to determine a clear general trend. In many sample types CCE measurements give considerably higher values, while for CV measurements this is only the case for n-type MCz irradiated with 24 GeV/c protons. There are also instances, like in n-type EPI irradiated with reactor neutrons or 24 GeV/c protons, where CCE and CV measurements nearly agree, as would be expected since both methods are used to determine the full depletion of the detector. This indicates that the shift in data is not due to the setups themselves or different measurement conditions.

However no correlation with material, material type, i.e. n- or p-type, or type of particle used for irradiation can be found. In Tab. 9.1 also the position of the main junction in the diode is included. If the sign of the space charge in the detector bulk is changed by irradiation, the main junction moves from the 'front' of the diode , i.e. the p+ side in n-type samples an the n+ side in p-type material, to the back side (n+ or p+ respectively). Yet again no correlation can be found between the position of the junction and the variation in the results for $|N_{eff}|$.

From the available data it is therefore not possible to determine the underlying mechanism of this behavior and further dedicated measurements, especially at fluences above $10^{14} cm^{-2}$ are necessary. Even without fully understanding the phenomenon, it is nevertheless an indicator that CV measurements for determining the depletion voltage might not be enough. At the given read-out voltage a sample that is clearly fully depleted when looking at the CV curve, might not have reached the maximum in the collected charge or read-out signal, which could overestimate the radiation hardness of certain materials.

silicon type	irradiation type	comparison	main junction
FZ-n	proton	CCE>CV>IV	back
FZ-n	neutron	CCE>CV>IV	back
FZ-p	proton	CCE>CV>IV	front
FZ-p	neutron	CCE≈CV>IV	front
MCz-n	proton	CV>CCE≈IV	?
MCz-n	neutron	CCE>CV>IV	back
MCz-p	proton	CV=CCE≥IV	?
MCz-p	neutron	not available	front
EPI-n	proton	CV≈CCE>IV	front
EPI-n	neutron	CV≈CCE>IV	back
EPI-p	proton	CCE>CV>IV	back
EPI-p	neutron	CCE>CV>IV	front

Table 9.1: Comparison of the development of the effective space charge with fluence in different sample types using different measurement methods. The irradiation types presented here are 24 GeV/c protons and reactor neutrons. The position of the junction was determined by TCT measurements, main junction on the back side points towards Space Charge Sign Inversion (compare chapter 8.2). It was not possible to measure p-type MCz sample irradiated with reactor neutrons due to bad sample quality. Two different p-type MCz samples were available for proton irradiation that showed slightly different behavior (compare chapter 9.2)

Chapter 10

Summary and Conclusions

A set of n- and p-type FZ, MCz and 150 μm EPI silicon was irradiated with 24 GeV/c protons, reactor neutrons and 200 MeV pions to allow a thorough investigation of the changes in macroscopic detector properties in high radiation environments. For proton and neutron irradiation fluences up to 1 x $10^{15}\,cm^{-2}$ were used, while for pion irradiation the maximum fluence available was about 3 x $10^{14}\,cm^{-2}$.

Effective Space Charge development

The development of the depletion voltage or effective space charge with fluence was first investigated for each material separately to compare the effect of irradiation with different particles. In a second step the different materials were compared for 24 GeV/c proton, reactor neutron and 200 MeV pion irradiation to determine the differences in radiation hardness.

For standard n-type FZ material the investigated fluence range was limited due to an increase in leakage current already at fluences of 1 x 10^{14} cm^{-2}. Up to this point the generation rate for protons (16.99 ± 0.33) x 10^{-3} cm^{-1} and pions is similar, but lower than after neutron irradiation ($g_c = (21.22 \pm 0.62)$ x $10^{-3}cm^{-1}$). Approximately the same value is obtained from neutron irradiated p-type samples, while for proton irradiated FZ-p no generation rate could be determined. Both the 400 $k\Omega cm$ FZ-p diodes processed by CNM and the 14 $k\Omega cm$ diodes processed by MICRON showed an unexpected sub-linear increase of the effective space charge with fluence above 1 x 10^{14} cm^{-2}. The effect persisted after short time annealing of 4 min at 80°C and was also visible in the effective space charge obtained from QV and IV plots. An explanation of this effect that was occasionally also observed by other groups has still to be found.

MCz n-type samples from three different producers with slightly different resistivity were combined to extract a generation rate of ($|8.55| \pm 0.35$) $10^{-3}cm^{-1}$ after proton irradiation compared to ($|7.42| \pm 0.35$) x 10^{-3} cm^{-1} obtained from MCz p-type, where similarly 1.3 $k\Omega cm$ and 7.5 $k\Omega cm$ material that showed the same increase of effective space charge with fluence once the acceptor removal phase was finished was used [1]. No initial decrease in effective space charge was measured in p-type irradiated with reactor neutrons, where, similar to n-type, the generation rate was about 22 x 10^{-3} cm^{-1}. Due to the limited irradiation range the generation rate could not be clearly determined from pion irradiated MCz-n (no MCz-p samples were available).

In EPI material not only the effect of 24 GeV/c proton and reactor neutron irradiation was investigated (no pion irradiated samples were available), but also the influence of the layer thickness on g_c. All samples show a decrease of the effective space charge in the early phases of the irradiation up to fluences of (1-2) x 10^{14} cm^{-2}. Clear difference between n-type and p-type can be observed: the generation rate of 150 μm after proton irradiation is (10.5 ± 0.5) x 10^{-3} cm^{-1} for p-type and (15.6 ± 0.2) x 10^{-3} cm^{-1} for n-type. After neutron irradiation again g_c for p-type material is only about 2/3 of what is obtained from n-type material: (3.7 ± 0.2) 10^{-3} cm^{-1} vs. (5.8 ± 0.2) 10^{-3} cm^{-1}.

For n-type material a decrease in g_c with increasing layer thickness was suggested in the literature. A thorough comparison of the values published by different groups however showed a strong variation in results. One of the reasons is most likely a difference in the out-diffusion of O_2 from the Cz substrate layer of EPI samples due to different thermal treatment. Other discrepancies are caused by using 100 kHz instead of the standard $10kHz$ for CV measurements in very thin samples. As comparative measurements show, using a higher frequency while keeping the temperature constant lowers the effective space charge in dependence of the particle type and irradiation fluence, thereby also lowering the value for g_c. The ratio between the generation rates obtained at 10 and 100 kHz is however not constant with layer thickness, making it therefore impossible to draw conclusions for the development of radiation hardness with layer thickness if different frequencies were used. Overall however it can be stated that no advantage is gained as far as the development of effective space charge is concerned when using 150 μm n-type EPI compared to thinner samples.

Between proton irradiated p-type EPI samples with a thickness of 50 and 75 μm no relevant variation of g_c were observed. The rate of increase of the effective space charge with fluence of around 15 x 10^{-3} cm^{-1} is higher than what was seen in 150 μm samples. This however might be due to different thermal treatment by different producers. Both thinner diode types were produced by CiS, while the thickest samples came from CNM. Overall, also taking values from literature into account, the variations between p-type EPI samples of different thickness is lower than for n-type.

When it comes to comparing the radiation hardness of various silicon types with respect to g_c, clear differences between irradiation with charged hadrons and neutrons can be observed. As expected oxygen was found to have a positive effect on the radiation hardness, making n- and p-type MCz superior to both standard FZ and EPI after 24 GeV/c proton irradiation. For reactor neutron irradiation EPI samples with their lower resistivity show a clear advantage over FZ and MCz that both have a similarly steep increase of g_c with

---

[1] Due to uncertainties regarding the sign of the space charge after proton irradiation, as discussed in Chapter 8.2.2, absolute values are used here.

fluence. Comparison after 200 MeV pion irradiation is limited by a lack of samples and low irradiation fluences. The overall picture is similar to what is seen after 24 GeV/c proton irradiation.

Collected charge

The maximum collected charge after full depletion of the detector is not material dependent. Since however the voltage that can be applied to a detector in practical use is limited, not the maximum, but the charge collected at a certain voltage is of interest when comparing different sample and particle types. Due to limitations in diode quality, the comparison voltage used in this work is 300 V to be able to include as many sample types as possible.

At low irradiation fluences 150 μm EPI samples are clearly inferior to both FZ and MCz due to their lower thickness that reduces the number of charge carriers that can be produced as a particle moves through the detector volume. At fluences above around 1 x $10^{15} cm^{-2}$ this shorter particle path on the other hand also reduces the possibility of charge carriers being trapped and therefore lost for the read-out signal. An additional advantage of thinner samples is the higher field at the same bias voltage that leads to higher carrier velocities, which yet again reduces the trapping probability. Even though therefore $|N_{eff}|$ in EPI samples irradiated to high proton fluences is considerably higher than in MCz and the sample is highly underdepleted at the comparison voltage of 300V, the collected charge of both materials is nevertheless very similar. After neutron irradiation, where EPI additionally shows a favorable development of the effective space charge with fluence, the thinner sample is superior to all other materials.

When looking at the development of the collected charge with fluence for various sample and particle types, a few unexpected effects can be observed in the early phases of the irradiation. Before irradiation the maximum collected charge in n-type FZ is higher than in p-type, which however changes already at the first fluence step where both types show identical values. At this stage the collected charge in p-type FZ is actually about 5 % higher than in unirradiated material.

In EPI n-type on the other hand, a sharp drop in the maximum collected charge can be observed already at fluences as low as 1 x $10^{12} cm^{-2}$, while no such drop is observed for p-type material. No explanation for this effect has so far been found since all other measurement on these particular samples did not show any deviation from the expected behaviour. It seems likely that for both cases the problem lies with the measurement of the unirradiated sample. In FZ-p the collected charge is clearly too low, while for EPI-n a comparison with FZ-n samples with a thickness of 300 μm seems to indicate a maximum charge that is higher than would be expected from a sample with a thickness of 150 μm.

Effective trapping probability

The effective trapping time was determined using the Charge Correction Method on QV curves measured by Transient Current Technique. Previous TCT studies have shown that electron and hole trapping times do not depend on the wafer production method or silicon type, but are influenced by the particle type used for irradiation. Values obtained from FZ, EPI and MCz irradiated up to equivalent fluences of 1 x 10^{15} cm^{-2} could therefore be combined to determine the proportionality constant β that describes the increase of the effective trapping probability with fluence. While it was not possible to measure both $\tau_{eff,e}$ and $\tau_{eff,h}$ for all samples due to constraints from the diode construction, nevertheless a large number of data points was thus available from samples irradiated with 24 GeV/c proton, reactor neutron and 200 MeV pions.

For all particle types β_h is about 20-30 % higher than β_e. No differences are seen in the response to proton and pion irradiation, where β_e is around 5.1 x 10^{-16} cm^2ns^{-1} and β_h around 6.1 x 10^{-16} cm^2ns^{-1}. Neutron irradiated samples showed a slower increase of trapping with fluence with $\beta_e = (3.84 \pm 0.09)$ x 10^{-16} cm^2ns^{-1} and $\beta_h = (4.44 \pm 0.08)$ x 10^{-16} cm^2ns^{-1}. These values lie within the range of results obtained by other groups, but are at the higher end of the relatively broad spectrum.

Space Charge Sign

CV and IV measurements can only provide the absolute value of the effective space charge, but give no information on its sign. Using TCT it is possible to determine the position of the main junction and thereby the space charge sign in a sample. Since charge carriers are trapped on their way through the detector, the signal obtained from illumination with a red laser has to be corrected for trapping with the trapping time extracted by the charge correction method before a valid interpretation can be given.

The development of the space charge sign with particle fluence is dependent on silicon material and particle type. In samples of all silicon types used in this study that were irradiated with a high enough fluence of reactor neutrons the space charge is negative. For n-type MCz and EPI (originally positive space charge) the resulting Space Charge Sign inversion happens at fluences of around 1-3 x 10^{14} cm^{-2}, where a minimum in the effective space charge obtained from CV measurements can be observed. For FZ it is already visible at fluences below 10^{13} cm^{-2}.

After irradiation with 24 GeV/c protons FZ and 150 μm EPI material respond in opposite ways: while negative space charge is introduced in FZ, the introduction of positive space charge leads to SCSI from p-type to 'n-type' in EPI. For 50 and 75 μm EPI-p no full TCT study was performed, first measurements however indicated a similar behaviour as observed in samples with a thicker EPI layer.

Of particular interest is the space charge sign in n- and p-type MCz material after irradiation with 24 GeV/c protons, where previous studies disagreed. In a dedicated effort to resolve the issue, MCz samples irradiated to the same fluence steps were measured by three different groups. First results from two groups showed yet again surprising differences: while for one batch of samples a space charge sign inversion from p-type to 'n-type' with a dominant peak on the backside was observed, for a second batch equal junctions on the front and back side of the p-type samples were reported. A detailed comparison of the raw data and the curves obtained after correction for trapping gave a hint towards the source of these discrepancies. Different trapping times were used to correct the TCT curves and different bias voltages were used to extract the position of the junction.

Measurements on a third batch of samples over a wider voltage range and a correction of the curves with values for τ_{eff} obtained in this study yielded inconclusive results. For p-type samples an evaluation of the hole signal (front side illumination) showed a dominant peak on the back side, indicating SCSI. In the electron signal measured by back side illumination of the same diode the dominant peak stayed on the front side of the sample. These contradicting results point towards local field and space charge variations that prohibit the application of the space charge correction method used to determine position of the main junction in the above mentioned works. Further measurements with other methods like edge-TCT are therefore necessary to determine the real field distribution in MCz.

Effective Space Charge Comparison

The effective space charge is in most cases determined by looking at the kink in the CV curve that indicates that full depletion is reached in the sample. Additionally it is also possible to determine $|N_{eff}|$ by evaluating the development of the current and the collected charge with bias voltage that similarly changes as soon as depletion is reached.

In unirradiated samples and those irradiated to low fluences all three methods yield the same results. With increased particle fluence however not only the absolute values, but also the increase of $|N_{eff}|$ with fluence differs and only few general trends can be observed. In all samples IV measurements give the lowest values for the effective space charge. The highest values are either obtained from CV or QV measurements that can sometimes also agree. The underlying mechanism has so far not been determined, since no correlation with material, material type (i.e. n- or p-type) or type of particle used for irradiation can be found. The findings nevertheless give an indication that CV measurements to determine the effective space charge might not be enough and can give an incorrect impression of the radiation hardness of different materials.

Conclusions and Outlook

In this work a vast amount of data has been collected on neutron, proton and pion irradiated silicon sensors made from different silicon material (MCz, EPI, FZ) and different conduction type (n- and p-type). The work was performed on simple devices (pad sensors) using CV, IV, TCT and CCE measurements to explore the radiation response of the various silicon materials. For all materials the generation rate of the space charge with particle fluence, the effective trapping times for holes and electrons and the internal electric field shape as represented by TCT curves was obtained. Sensors produced by different vendors deliver very similar results, thus reassuring that the material parameters are investigated in this work and not features introduced by different processing techniques.

It could be shown that 200 MeV pion and 24 GeV/c proton damage has almost identical impact on the detector performance if scaled to NIEL. The most challenging experimental results were obtained on the MCz materials after proton irradiation as the internal electric field structure as measured by TCT did not allow to clarify if the net effective space charge is positive or negative after high levels of irradiation. Other measurement techniques should therefore be investigated to gain a better understanding of the development of the space charge sign with fluende. Finally, it was demonstrated that the extraction of the depletion voltage from CV curves as a parameter for radiation hardness can be a misleading parameter for high particle fluences even more when taking into account that different measurement methods result in different depletion voltages. This effect might be even more significant when segmented devices like strip and pixel sensors are used where the charge sharing between the electrodes adds a further complication for charge collection.

Bibliography

[Amm84] W. v. Ammon, H. Herzer. The production and availability of high resistivity silicon for detector applications. *Nucl. Instr. & Meth. in Physics Research*, 226:94–102, 1984.

[ATL08] ATLAS Collaboration. The ATLAS experiment at the CERN Large Hadron Collider. *Journal of Instrumentation*, 3:S08003, 2008.

[Bat05a] A. Gouldwell Bates. *Development in Silicon Detectors and their impact on LHCb Measurements.* PhD thesis, University of Glasgow, 2005.

[Bat05b] A. Bates, M. Moll. A comparison between irradiated magnetic Czochralski and float zone silicon detectors using the transient current technique. *Nucl.Instr.& Meth.in Physics Research*, A 555:113–124, 2005.

[Bro82] S.D. Brotherton, P. Bradley. Defect roduction and lifetime control in electron and gamma irradiated silicon. *Journal of Applied Physics*, 53 (8):5720–5732, 1982.

[Bro00] T.J. Brodbeck, A. Chilingarov, T. Sloan, E. Fretwurst, M. Kuhnke, G. Lindstroem. A New Method of Carrier Trapping Time Measurement. *Nucl.Instr.& Meth.in Physics Research*, A 455:645–655, 2000.

[Cas10] E. del Castillo Sanchez, Manuel Fahrer, M. Moll, N. Pacifico. Study on 50, 75 and 150 μm thick p-type Epitaxial silicon pad detectors irradiated with protons and neutrons . *16th RD50 workshop, 31. May-2.June 2010, Barcelona, Spain*, 2010.

[Chi04] A. Chilingarov. Recommendations towards a standardisation of the macroscopic parameter measurements. *http://rd50.web.cern.ch/RD50/doc/Internal/rd50_2003_003_version_15-10-2004.doc*, 2004.

[Chi11] A. Chilingarov. Generation current temperature scaling. *http://rd50.web.cern.ch/RD50/doc/Internal/rd50_2011_001-I-T_scaling.pdf*, 2011.

[Chi13] G. Chilingarov. Temperature dependence of the current generated in Si bulk. *Journal of Instrumentation*, 8:P10003, 2013.

[Cin00] V. Cindro, G. Kramberger, M. Mikuž, M. Tadel, D. Žontar. Bias-dependent radiation damage in high-resistivity silicon diodes irradiated with heavy charged particles. *Nucl.Instr.& Meth.in Physics Research*, A 450:288–296, 2000.

[Cin07] V. Cindro, G. Kramberger, I. Mandić, M. Mikuž, M. Zavrtanik. P-type silicon irradiated with 24 GeV/c protons. *10th RD50 workshop, 3-6 June 2007, Vilnius, Lithuania*, 2007.

[Cin09] V. Cindro, G. Kramberger, M. Lozano, I. Mandić, M. Mikuž, G. Pellegrini, J. Pulko, M. Ullan, M. Zavrtanik. Radiation damage in p-type silicon irradiated with neutrons and protons. *Nucl.Instr.& Meth.in Physics Research*, A 599:60–65, 2009.

[CiS] CiS Institut für Mikrosensorik GmbH, Erfurt, Germany.

[CMS08] CMS Collaboration. The CMS experiment at the CERN LHC. *Journal of Instrumentation*, 3:S08004, 2008.

[Cre07] D. Creanza, D. Bassignana, L. Borrello, M. Boscardin, M. Bruzzi, M. de Palma, E. Focardi, A. Macchiolo, N. Manna, D. Menichelli, A. Messineo, C. Piemonte, A. Pozza, V. Radicci, M. Scaringella, N. Zorzi. Comparison of the radiation hardness of Magnetic Czochraslki and Epitaxial silicon substrates after 26 MeV proton and reactor neutron irradiation. *Nucl.Instr.& Meth.in Physics Research*, A 579:608–613, 2007.

[Czo18] J. Czochralski. Ein neues Verfahren zur Messung der Kristallisationsgeschwindigkeit der Metalle. *Zeitschrift für Physikalische Chemie*, 92:219–221, 1918.

[Dab89] W. Dabrowski and K. Kobel. Effects of deep imperfection levels on the capacitance of semiconductor detecotrs. *Nucl.Instr.& Meth.in Physics Research*, A 276:270–279, 1989.

[Das55] W. Dash and R. Newman. Intrinsic optical absorption in single-crystal germanium and silicon at 77K and 300K. *Physical Review*, 99:1151–1155, 1955.

[Eck08] D. Eckstein, L. Andricek, E. Fretwurst, J. Lange, G. Lindström, H.G. Moser, I. Pintilie, R. Richter, R. Röder. Comparison of proton damag in thin FZ, MCz and epitaxial silicon detectors. *12th RD50 workshop,2-4 June 2008, Ljubljana, Slovenia*, 2008.

[Ere02] V. Eremin, E. Verbitskaya, Z. Li. The origin of double peak electric field distribution in heavily irradiated silicon detectors. *Nucl.Instr.& Meth.in Physics Research*, A 476:556–564, 2002.

[Eva08] L. Evans, P. Bryant. LHC Machine. *Journal of Instrumentation*, 3:S08001, 2008.

[For97] F. Foroughi. $\pi E1$ secondary beamline. *http://aea.web.psi.ch/beam2lines/pie1.pdf*, 1997.

[Fre05] E. Fretwurst et. al. Recent advancements in the development of radiation hard semiconductor detectors for S-LHC. *Nucl.Instr.& Meth.in Physics Research*, A 552:7–19, 2005.

[Fre06] I. Fretwurst, G. Lindström, J. Stahl, I. Pintilie, Z. Li, J. Kierstead, E. Verbitskaya, R. Röder. Stable radiation-induced donor generation and its influence on the radtiation tolerance of silicon diodes. *Nucl.Instr.& Meth.in Physics Research*, A 556:197–208, 2006.

[Fre07] W. Fretwurst, F. Hönniger, G. Kramberger, G. Lindström, I. Pintilie, R. Röder. Radiation damage studies on MCz and standard and oxygen enriched epitaxial silicon devices. *Nucl.Instr.& Meth.in Physics Research*, A 583:58–63, 2007.

[Fre10] E. Fretwurst, L. Andricek, F. Hönniger, K. Koch, G. Kramberger, G. Lindström, H.G. Moser, I. Pintilie, R. Richter, R. Röder. Comparison of neutron damage in thin FZ, MCz and epitaxial silicon detectors. *10th RD50 workshop, 3-6 June 2007, Vilnius, Lithuania*, 2010.

[Gla99] M. Glaser, L. Durieu, F. Lemeilleur, M. Tavlet, C. Leroy, P. Roy. New irradiation zones at the CERN-PS. *Nucl.Instr.& Meth.in Physics Research*, A 426:72–77, 1999.

[Har09] F. Hartmann. *Evolution of Silicon Sensor Technology in Particle Physics.* Springer, 2009.

[Hoe07] H. Hoedlmoser, M. Moll, J. Haerkoenen, M. Kronberger, J. Trummer, P. Rodeghiero. Characterization of 150 μm thick epitaxial silicon detectors from different producers after proton irradiation. *Nucl.Instr.& Meth.in Physics Research*, A 580:1243–1249, 2007.

[Huh02] M. Huhtinen. Simulation of non-ionising energy loss and defect formation in silicon. *Nucl.Instr.& Meth.in Physics Research*, A 491:194–215, 2002.

[IRR] Information on IRRAD-1: https://irradiation.web.cern.ch/irradiation/irrad1_Info.htm.

[ITC] ITC-IRST Microsystems Division, Povo, Trento, Italy.

[ITM] Institute of Electronic Materials Technology (ITME), ul Wólczyńska 133, 01-919 Warsaw, Poland.

[Jun12] A. Junkes, I. Pintilie, E. Fretwurst, D. Eckstein. A contribution to the identification of the E5 defect level as tri-vacancy. *Physica B*, 407:3013–3015, 2012.

[Kas09] K. Kaska, M. Moll. TCT measurements on MCz n- and p-type after proton and neutron irradiation . *15th RD50 workshop, 16-8 November 2009, CERN, Geneva, Switzerland*, 2009.

[Kas10] K. Kaska, M. Moll, M. Fahrer. Study on 150 μm thick n- and p-type epitaxial silicon sensors irradiated with 24 GeV/c protons and reactor neutrons. *Nucl.Instr.& Meth.in Physics Research*, A 612:482–487, 2010.

[Kho06] V. Khomenkov, D. Bisello, M. Bruzzi, A. Candelori, A. Litovchenko, C. Piemonte, R. Rando, F. Ravotti, N. Zorzi. Irradiation effects on thin epitaxial silicon detectors. *Nucl.Instr.& Meth.in Physics Research*, A 568:61–65, 2006.

[Kho08a] V. Khomenkov, D. Bisello, A. Candelori, G. Kramberger, M. Moll. Radiation tolerance of epitaxial silicon after fast hadron irradiation. *IEEE Nuclear Science Symposium Conference Record*, N30 408:2550–2552, 2008.

[Kho08b] V. Khomenkov, D. Bisello, G. Kramberger. Electrical characterization of p- and n-type 150 μm EPI-Si diodes irradiated with protons and neutrons. *12th RD50 workshop, 2-4 June 2008, Ljubljana, Slowenia*, 2008.

[Kra01] G. Kramberger. *Signal development in irradiated silicon detectors.* PhD thesis, University of Ljubljana, 2001.

[Kra02] G. Kramberger, V. Cindro, I. Mandić, M. Mikuž, M. Zavrtanik. Determination of effective trapping times for electrons and holes in irradiated silicon. *Nucl.Instr.& Meth.in Physics Research*, A 476:645–651, 2002.

[Kra05] G. Kramberger, V. Cindro, I. Dolenc, E. Fretwurst, G. Lindströ m, I. Mandić, M. Mikuž, M. Zavrtanik. Charge collection properties of heavily irradiated epitaxial silicon detectors. *Nucl.Instr.& Meth.in Physics Research*, A 554:212–219, 2005.

[Kra07] G. Kramberger. Charge collection measurements on MICRON RD50 detectors. *ATLAS Tracker Upgrade Workshop, 11-14 December 2007, Valencia, Spain*, 2007.

[Kra08a] G. Kramberger, V. Cindro, I. Dolenc, I. Mandić, M. Mikuž, M. Zavrtanik . Annealing studies of mixed irradiated MICRON diodes. *13th RD50 workshop, 10.-12. November 2008, CERN, Geneva, Switzerland*, 2008.

[Kra08b] G. Kramberger, V. Cindro, I. Dolenc, I. Mandić, M. Mikuž, M. Zavrtanik . CV/IV and CCE measurements of MCz and FZ p and n type diodes after mixed irradiations. *12th RD50 workshop,2-4 June 2008, Ljubljana, Slovenia*, 2008.

[Kra09] G. Kramberger, V. Cindro, I. Dolenc, I. Mandić, M. Mikuž, M. Zavrtanik. Performance of silicon pad detectors after mixed irradiations with neutrons and fast charged hadrons. *Nucl.Instr.& Meth.in Physics Research*, A 609:142–148, 2009.

[Kra10a] G. Kramberger, V. Cindro, I. Dolenc, I. Mandić, M. Mikuž, M. Zavrtanik. Comparison of Pad Detectors produced on different silicon materials after irradiation with neutrons, protons and pions. *Nucl.Instr.& Meth.in Physics Research*, A612:288–295, 2010.

[Kra10b] G. Kramberger, V. Cindro, I. Mandić, M. Mikuž, M. Milovanović, M. Zavrtanik, K. Žagar. Investigation of Irradiated Silicon Detectors by Edge-TCT. *IEEE Trans. Nucl. Sci. NS*, 57-54:2294 – 2302, 2010.

[Lan08] J. Lange. Radiation Damage in Proton-Irradiated Epitaxial Silicon Detectors. Diploma thesis, Universität Hamburg, 2008.

[Li 08] Z. Li , G. Carini, W. Chen, V. Eremin, J. Harkonen, P. Luukka, E. Tuominen, E. Tuovinen, E. Verbitskaya. Systematic TCT Investigation of Equal-Double-Junctions in 24 GeV Proton Irradiated MCZ n and p-type Si Detectors. *7th International Conference on Radiation Effects on Semiconductor Materials Detectors and Devices, 15.-18. October 2008, Florence, Italy*, 2008.

[Li 10] Z. Li , W. Chen, V. Eremin, R. Gul, Y.H. Guo, J. Harkonen, P. Luukka, E. Tuovinen, E. Verbitskaya. Equal-double junctions in 24 GeV/c proton-irradiated MCZ n- and p-type Si detectors: A systematic transient current technique investigation. *Nucl.Instr.& Meth.in Physics Research*, A 612:539–548, 2010.

[Li94] Z. Li. Modeling and simulation of neutron induced changes and temperature annealing of N_{eff} and changes in resistivity in high resistivity silicon detectors. *Nucl.Instr.& Meth.in Physics Research*, A 342:105–118, 1994.

[Lin80] V.A.J.van Lindt, T.M. Flanagan, R.E. Leadon, J.A. Naber, V.C. Roger. *Mechanisms of Radiation Effects in Electronic Materials.* John Wiley & Sons, 1980.

[Lin01a] G. Lindström et. al. . Development for radiation hard silicon detectors by defect engineering - results by the CERN RD48 (ROSE) collaboration. *Nucl.Instr.& Meth.in Physics Research*, A 465:60–69, 2001.

[Lin01b] G. Lindström et. al. . Radiation hard silicon detectors - developments by the CERN RD48 (ROSE) collaboration. *Nucl.Instr.& Meth.in Physics Research*, A 466:308–326, 2001.

[Lin06a] G. Lindström, E. Fretwurst, F. Hönniger, G. Kramberger, M. Möller-Ivens, I. Pintilie, A. Schramm. Radiation tolerance of epitaxial siliconi detectors at very large proton fluences. *Nucl.Instr.& Meth.in Physics Research*, A 556:451–458, 2006.

[Lin06b] G. Lindström, I. Dolenc, E. Fretwurst, F. Ḧ'onniger, G. Kramberger, M. Moll, E. Nossarzewska, I. Pintilie, R. Röder. Epitaxial silicon detectors for particle tracking-Radiation tolerance at extreme hadron fluences. *Nucl.Instr.& Meth.in Physics Research*, A 568:66–71, 2006.

[Lut99] G. Lutz. *Semiconductor Radiation Detectors. Device Physics.* Springer, 1999.

[Mol99] M. Moll. *Radiation Damage in Silicon Particle Detectors-miscroscopic defects and macroscopic properties.* PhD thesis, Universität Hamburg, 1999.

[Mol07] M. Moll. Radiation Tolerant Sensors for Solid State Tracking Detectors. *Seminar Talk, Laboratory for High Energy Physics at the EPFL, 29 January 2007, Lausanne, Switzerland*, 2007.

[NIK] Description and manual of the NIKHEF CCE setup: http://www.nikhef.nl/i56/Manual.pdf.

[Pac08] N. Pacifico, D. Creanza, M. DePalma, N. Manna, A. Messineo, G. Kramberger, I. Mandic. First observation of SCSI in MCz silicon after irradiation with 24 GeV/c protons . *7th International Conference on Radiation Effects on Semiconductor Materials Detectors and Devices, 15.-18. October 2008, Florence, Italy*, 2008.

[Pac10a] N. Pacifico, D. Creanza, M. de Palma, N. Manna, G. Kramberger, M. Moll. A TCT and annealing study on Magnetic Czochralski silicon detectors irradiated with neutrons and 24 GeV/c protons. *Nucl.Instr.& Meth.in Physics Research*, A 612:549–554, 2010.

[Pac10b] N. Pacifico, I. Dolenc Kittelmann, M. Gabrysch, M. Moll. Field and Charge Collection Studies on pion irradiated p-type Float Zone strip detectors. *18th RD50 workshop, 23-25 May 2011, Liverpool, GB*, 2010.

[Pac11] N. Pacifico, I. Dolenc Kittelmann, M. Fahrer, M. Moll, O. Miliatru. Characterization of proton and neutron irradiated low resistivity p-on-n magnetic Czochralski ministrip sensors and diodes. *Nucl.Instr.& Meth.in Physics Research*, A 658:55–60, 2011.

[Pel05] G. Pellegrini, M. Ullán, J.M. Rafí, C. Fleta, F. Campabadal, M. Lozano. Annealing Studies of mangetic Czochralski silicon radiation detectors. *Nucl.Instr.& Meth.in Physics Research*, A 552:27–33, 2005.

[Pet07] M.K. Petterson, H.F.-W. Sadrozinski, C. Betancourt, M. Bruzzi, M. Scaringella, C. Tosi, A. Macchiolo, N. Manna, D. Creanza, M. Boscardin, C. Piemonte, N. Zorzi, L. Borrello, A. Messineo, G.F. Dalla Betta. Charge collection and capacitance-voltage analysis in irradiated n-type magnetic Czochralski silicon detectors. *Nucl.Instr.& Meth.in Physics Research*, A 583:189:194, 2007.

[Pin03] I. Pintilie, E. Fretwurst, G. Lindström, J. Stahl. Results on defects induced by 60-Co gamma irradiation in standard and oygen-enriched silicon. *Nucl.Instr.& Meth.in Physics Research*, A 514:18–24, 2003.

[Pin05] I. Pintilie, M. Buda, E. Fretwurst, F. Hönniger, G. Lindström, J. Stahl. Radiation-induced donor generation in epitaxial and Cz diodes. *Nucl.Instr.& Meth.in Physics Research*, A 552:56–60, 2005.

[Pin06] I. Pintilie, M. Buda, E. Fretwurst, F. Hönniger, G. Lindström, J. Stahl. Stable radiation-induced donor generation and its influence on the radtiation tolerance of silicon diodes. *Nucl.Instr.& Meth.in Physics Research*, A 556:197–208, 2006.

[Pin08] I. Pintilie, E. Fretwurst, G. Lindström. Cluster related hole traps with enhanced-field-emission - the source for long term annealing in hadron irradiated Si. diodes. *Applied Physics Letters*, 92:024101, 2008.

[Pin09] I. Pintilie, G. Lindström, A. Junkes, E. Fretwurstl. Radiation-induced point- and cluster-related defects with strong impact on damage properties of silicon detectors. *Nucl.Instr.& Meth.in Physics Research*, A 611:52–68, 2009.

[Rav03] M. Ravnik and R. Jeraj. Research Reactor Benchmarks,. *Nuclear Science and Engineering*, Vol. 145:145, 2003.

[RD408] RD48 Collaboration. 3rd RD 48 Status Report. The ROSE Collaboration. Research and Development On Silicon for future Experiments. *CERN-LHCC-2000-009/LEB Status Report/RD48*, 2008.

[RD502] RD50 Collaboration. RD 50 Status Report. Radiation hard semiconductor devices for very high luminosity colliders. *CERN-LHCC-2002-003/P6, 15.2.2002.*, 2002.

[RD508] RD50 Collaboration. RD 50 Status Report. Radiation hard semiconductor devices for very high luminosity colliders. *CERN-LHCC-2008-001/LHCC-RD-015*, 2008.

[RD510] RD50 Collaboration. RD 50 Status Report. Radiation hard semiconductor devices for very high luminosity colliders. *CERN-LHCC-2010-012/LHCC-SR-003*, 2010.

[RD511] RD50 Collaboration. Silicon detectors for the sLHCr. *Nucl.Instr.& Meth.in Physics Research*, A 658:11–16, 2011.

[Shi90] Y. Shi, D.X.Shen, F.M. Wu, K.J. Cheng. A numerical study of cluster center formation in neutron-irradiated silicon. *J. Appl. Phys*, 67:1116–118, 1990.

[Spi05] H. Spieler. *Semiconductor Detector Systems.* Oxford Science Publications, 2005.

[Sze81] S.M. Sze. *Physics of semiconductor devices.* John Wiley & Sons, 2^{nd} edition, 1981.

[Sze85] S.M. Sze. *SEMICONDUCTOR DEVICES Physics and Technology.* John Wiley & Sons, 1985.

[Tea50] G.K. Teal and J.B.Little. Growth of Germanium Single Crystals. *Physical Review*, 78:647, 1950.

[The62] H.C. Theuerer. U.S. patent. *3,060,123*, 1962.

[Ž98] D. Žontar. *Study of radiation damage in silicon detectors for high luminosity experiments at LHC.* PhD thesis, University of Ljubljana, 1998.

[Ž99] D. Žontar, V. Cindro, G. Kramberger, M. Mikuž. Time development and flux dependence of neutron-irradiation induced defects in silicon pad detectors . *Nucl.Instr.& Meth.in Physics Research*, A 426:51–55, 1999.

CURRICULUM VITAE

PERSONAL INFORMATION

Name	**Dipl.-Ing. Mag. Katharina Kaska, MA**
Address	**Bindergasse 3/11**
	1090 Wien
	Österreich
Telephone	**+43 2742 881913**
E-Mail	**Katharina.kaska@univie.ac.at**
Nationality	Austrian
Date of birth	27.02.1982

EDUCATION

Period	Since October 2013
University	University of Vienna
	Universitätsring 1
	1010 Vienna
Field of Study	PhD in History
	Project: *Texttransfer und Buchaustausch – Netzwerke monastischer Handschriftenproduktion am Beispiel des Zisterzienserstifts Baumgartenberg in Oberösterreich*
Period	October 2010-April 2014
University	University of Vienna
	Universitätsring 1
	1010 Vienna
Field of Study	Masters degree programme in Historical research, auxiliary sciences and archival studies
	MA Thesis: *Untersuchungen zum mittelalterlichen Buch- und Bibliothekswesen im Zisterzienserstift Heiligenkreuz*
Period	Oktober 2001-September 2010
University	University of Vienna
	Universitätsring 1
	1010 Vienna
Field of Study	MA (Mag.) Classics-Ancient Greek
	MA-Thesis/Diplomarbeit: *Theophrast „De Signis“ - Interpretation ausgewählter Partien*
Period	since October 2006
University	University of Technology
	Karlsplatz 13
	1040 Vienna
Field of Study	PhD in physics
Period	Jänner 2004 – Mai 2004
University	Umeå Universitet
	Universitetsområdet
	SE-901 87 Umeå
	Schweden
	Erasmus-Semester

Period	October 2000 – April 2006
University	University of Technology Karlsplatz 13 1040 Vienna
Field of Study	MSc Physics (Dipl.-Ing.) Ma-Thesis/Diplomarbeit: *Scanning tunneling microscopic investigations of potential sputtering of hydrogen-terminated silicon (111) surfaces*

WORK EXPERIENCE

Period	Since October 2013
Employer	History department University of Vienna Universitätsring 1 1010 Vienna Prae-doc as part of the uni:doc program
Period	January 2013-August 2013
Employer	Netzwerk Geschichte Archivist
Period	April 2007-September 2009
Employer	CERN CH-1211 Geneva 23 Switzerland DOC-student

PUBLICATIONS

Paper	Zerteilt und zerstört. Zu einem Fragment des Magnum Legendarium Austriacum in Heiligenkreuz. *Mitteilungen des Instituts für Österreichische Geschichtsforschung* 122 (2014) 91-98.
Paper	„Ein neugefundenes Traditionskodexfragment aus Stift Heiligenkreuz“ *Mitteilungen des Instituts für Österreichische Geschichtsforschung* 121 (2013) 91-98
Paper	„Ordnen, Finden, Benutzen – die Stiftsbibliothek Heiligenkreuz im Mittelalter“ Tagungsband zum Österreichischen Historikertag 2012 (in print)
Paper	„How to know where to look – usage and interpretation of late medieval book lists in Heiligenkreuz“ „Les Cisterciens et la transmission des textes, XIIe-XVIIIe siècle“, Troyes, 22-23 Nov. 2012. (Bibliothèque d'histoire culturelle du Moyen Âge, ed. Anne-Marie Turcan-Verkerk, in print)
Paper	Katharina Kaska, Michael Moll and Manuel Fahrer, Study on 150 µm thick n- and p-type epitaxial silicon sensors irradiated with 24 GeV/ c protons and 1 MeV neutrons. *NIMA* 612 (2010) 482-487

SKILLS AND QUALIFICATIONS

Mother Tongue	German
Other languages	English: fluent French: basic Italian: basic
	Latin: fluent Ancient Greek: fluent
Computer skills	Windows, Linux, Mac OS, MS Office, LateX, Labview